

2013

Dynamic Response of Aerospace Materials under Extreme Environments

Sandeep Abotula
University of Rhode Island, abotula.sandeep@gmail.com

Follow this and additional works at: https://digitalcommons.uri.edu/oa_diss

Terms of Use

All rights reserved under copyright.

Recommended Citation

Abotula, Sandeep, "Dynamic Response of Aerospace Materials under Extreme Environments" (2013).
Open Access Dissertations. Paper 31.
https://digitalcommons.uri.edu/oa_diss/31

This Dissertation is brought to you by the University of Rhode Island. It has been accepted for inclusion in Open Access Dissertations by an authorized administrator of DigitalCommons@URI. For more information, please contact digitalcommons-group@uri.edu. For permission to reuse copyrighted content, contact the author directly.

DYNAMIC RESPONSE OF AEROSPACE MATERIALS
UNDER EXTREME ENVIRONMENTS

BY

SANDEEP ABOTULA

A DISSERTATION SUBMITTED IN PARTIAL FULFILLMENT OF THE
REQUIREMENTS FOR THE DEGREE OF
DOCTOR OF PHILOSOPHY
IN
MECHANICAL, INDUSTRIAL AND SYSTEMS ENGINEERING

UNIVERSITY OF RHODE ISLAND

2013

DOCTOR OF PHILOSOPHY DISSERTATION

BY

SANDEEP ABOTULA

APPROVED:

Thesis Committee:

Major Professor

Dr. Arun Shukla

Dr. Martin H. Sadd

Dr. David G. Taggart

Dr. Richard Brown

Nasser H. Zawia

DEAN OF THE GRADUATE SCHOOL

UNIVERSITY OF RHODE ISLAND

2013

ABSTRACT

To improve the performance and safety of future aerospace vehicles, worldwide efforts are being directed towards the development of novel aerospace materials which exhibit superior structural and multifunctional capabilities in extreme environments. Fundamental investigation into the thermo-mechanical response and dynamic failure of the materials is paramount before they can be incorporated into the design of future space access vehicles that can operate reliably in combined, extreme environments. For this purpose, a comprehensive study was conducted to evaluate the performance of variety of aerospace materials such as Functionally Graded Materials (FGMs), Ti_2AlC , and Hastelloy X under extreme thermo-mechanical loadings.

Starting from the first principles, analytical analyses were conducted to develop thermo-mechanical stress fields for mixed mode dynamic curving cracks in functionally graded materials (FGMs) under steady-state and transient loading conditions. Asymptotic analysis was used in conjunction with displacement potentials to develop the stress fields around propagating cracks in FGMs. Asymptotic temperature fields were developed first for the exponential variation of thermal conductivity and later these temperature fields were used to derive thermo-mechanical stress fields for a curving crack in FGMs. Using these thermo-mechanical stress fields, various components of the stresses were developed and the effect of curvature parameters, transient parameters, temperature and gradation on these stresses were discussed. Finally, using the minimum strain energy density criterion, the effect of curvature parameters, transient parameters, crack-tip speeds, non-homogeneity values and temperature gradients on crack growth directions were determined and discussed.

Experimental studies were then conducted to evaluate two different materials, namely, Nanolayered Titanium Aluminum Carbide (a MAX phase material) and Hastelloy X under varying rates of loading and at different temperatures. The dynamic behavior of nanolaminated ternary carbide, Ti_2AlC , was characterized under dynamic loading using Split Hopkinson Pressure Bar (SHPB) compression apparatus. The dynamic loading experiments were performed in the strain-rate range of $1500-4200s^{-1}$ and at temperatures ranging from room temperature (RT) to $1150^{\circ}C$. At room temperature, the failure stress and strain show little dependence on strain rate, whereas the failure stress drops considerably at temperatures above $900^{\circ}C$. At all strain rates and temperatures, Ti_2AlC exhibits softening after failure initiation and a more graceful failure due to delamination and kink band (KB) formation. At temperatures higher than $900^{\circ}C$, grain boundary decohesion is suggested to contribute towards the decrease in the failure stress.

The dynamic constitutive behavior of Hastelloy X (AMS 5754) was studied at room and elevated temperatures under varying rates of loading. A split Hopkinson pressure bar (SHPB) apparatus was used in conjunction with an induction coil heating system for applying dynamic loads at elevated temperatures. Experiments were carried out at different temperatures ranging from room temperature ($25^{\circ}C$) to $1100^{\circ}C$ at an average strain rate of $5000s^{-1}$. Room temperature experiments were carried out at varying strain rates from $1000s^{-1}$ to $4000s^{-1}$. The results show that as the strain rate increases from quasi-static to $4000s^{-1}$, the yield strength increases by approximately 50%. Also, under dynamic loading, the yield stress decreases with temperature up to $700^{\circ}C$, after which it (yield strength) shows a peak at $900^{\circ}C$ before beginning to

decrease again as the temperature is further increased. The Johnson-Cook model was used to predict the dynamic plastic response under varying rates of loading and at different temperatures.

A series of experiments were conducted to study the dynamic response of rectangular Hastelloy X plates at room and elevated temperatures when subjected to shock wave loading. The shock tube apparatus was modified and validated for testing Hastelloy X at elevated temperatures. Propane gas was used as the heating source and it was directed onto the sample via four nozzles. A cooling system was also implemented to prevent the shock tube from reaching high temperatures. High-speed photography coupled with the optical technique of Digital Image Correlation (DIC) technique was used to record the real-time deformation of the specimen under shock wave loading. The DIC technique was used in conjunction with band pass optical filters and a high intensity light source to record the full-field deformation images under shock loading at high temperatures up to 900 °C. In addition, a high speed camera was utilized to record the side-view deformation images. The high temperature DIC system has been validated by comparing with the mid-point deflections obtained from the side-view camera. The dynamic response of Hastelloy X was evaluated as a function of temperature under shock wave loading.

ACKNOWLEDGMENTS

First and foremost I would like to thank Dr. Arun Shukla for his continuous guidance and support throughout this research. His patience and adamant work ethic have truly been inspiring and motivating throughout my doctoral research. He is not only an outstanding professor and mentor, but a truly inspirational human being. It has been an honor for me to be one of his Ph.D. students.

I would also like to sincerely thank Dr. Martin H. Sadd, Dr. David G. Taggart, Dr. Carl-Ernst Rousseau, Dr. Richard Brown, and Dr. K. Wayne Lee for agreeing to serve as my committee members.

The help and encouragement from my friends and colleagues are greatly appreciated. I would like to thank all of my lab mates in the Dynamic Photomechanics Laboratory that have been by my side and influenced me along the way: Addis Kidane, Erheng Wang, Puneet Kumar, James LeBlanc, Nate Gardner, Sachin Gupta, Nicholas Heeder, Ryan Sekac, Jefferson Wright, Daniel Gracia, Alexander Escher, Prathmesh Parrikar, Chris O'Connell, Emad Makki, Payam Fahr, Murat Yazici, Frank LiVolsi, Chris Shillings, Kyle Kossak and Abayomi N. Yussuf. The time spent with everyone has made it an incredible experience, as well as provided me with many great friendships. In addition, I would like to thank Joe Gomez, Dave Ferriera, Jim Byrnes, Rob D'Ambrosca, Jen Cerullo, Nancy Dubee, Sally Marinelli, Brittany Mathews and the rest of the mechanical engineering department faculty and staff.

I would like to acknowledge the financial support provided by Dr. David S. Stargel under the Air Force Office of Scientific research (AFOSR) Grant No. FA9550-09-1-0639. A special thanks to Dr. Otto J. Gregory for providing the Scanning

Electron Microscope (SEM) facility used in obtaining the images of Ti_2AlC specimens.

Last but not least, I would like to thank my parents Rama Rao and Sushila, my sister Sujana, my brother in-law Sukumar, my fiancée Neha and the rest of my extended family for their understanding nature and endless support throughout my studies.

PREFACE

Theoretical and experimental studies have been conducted to study the thermo-mechanical response of materials under extreme environments. Fundamental investigation into the thermo-mechanical response and dynamic failure of the materials is paramount before they can be incorporated into the design of future space access vehicles that can operate reliably in combined, extreme environments. This dissertation addresses the dynamic behaviors and the failure mechanisms of aerospace materials under extreme thermo-mechanical loadings. This dissertation is prepared using the manuscript format.

Chapter 1 provides an overview of previous and current published literature of subject matter relevant to this dissertation. Topics include a brief background on materials tested and their mechanisms and how they can be useful in improving the design of future space access vehicles as well as the idea of utilizing various functionally graded materials. This chapter serves to provide an overview of the relevant research in literature, the possible data gaps that exist, as well as an introduction to the studies within this dissertation.

Chapter 2 focuses on analytical development of thermo-mechanical stress fields for a mixed-mode dynamic crack growth along an arbitrarily smoothly varying path in functionally graded materials (FGMs). The property gradation in FGMs was considered by varying shear-modulus, mass density, thermal conductivity and coefficient of thermal expansion exponentially along the gradation direction. Asymptotic analysis in conjunction with displacement potentials was used to develop the stress fields around propagating cracks in FGMs. Asymptotic temperature fields

are developed first for the exponential variation of thermal conductivity and later these temperature fields were used to derive thermo-mechanical stress fields for a curving crack in FGMs. Using these thermo-mechanical stress fields, various components of the stresses were developed and the effect of curvature parameters, temperature and gradation on these stresses were discussed. Finally, using the minimum strain energy density criterion, the effect of curvature parameters, crack-tip speeds, non-homogeneity values and temperature gradients on crack growth directions were determined and discussed. This chapter follows the formatting guidelines specified by the *International Journal of Solids and Structures*.

Chapter 3 provides the details of developing transient thermo-mechanical stress fields for a mixed-mode dynamic crack growth behavior along an arbitrarily smoothly varying path in functionally graded materials (FGMs). Similar approach as explained in chapter 2 was used in developing the stress fields. Asymptotic analysis in conjunction with displacement potentials was used to develop transient thermo-mechanical stress fields around the propagating crack-tip. Asymptotic temperature field equations are derived for exponentially varying thermal properties, and later these equations were used to derive transient thermo-mechanical stress fields for a curving crack in FGMs. The effect of transient parameters (loading rate, crack-tip acceleration, and temperature change) and temperature gradient on the maximum principal stress and circumferential stress associated with the propagating crack-tip was discussed. Finally, using the minimum strain energy density criterion, the effect of temperature gradient, crack-tip speeds and T-stress on crack growth directions were

determined and discussed. This chapter follows the formatting guidelines specified by *Acta Mechanica*.

Chapter 4 details the experimental study conducted on nanolaminated ternary carbide, Ti_2AlC , was characterized under dynamic loading using Split Hopkinson Pressure Bar (SHPB) compression apparatus. The dynamic loading experiments were performed in the strain-rate range of $1500-4200s^{-1}$ and at temperatures ranging from room temperature (RT) to $1150^{\circ}C$. At room temperature, the failure stress and strain show little dependence on strain rate, whereas the failure stress drops considerably at temperatures above $900^{\circ}C$. At all strain rates and temperatures, Ti_2AlC exhibits softening after failure initiation and a more graceful failure due to delamination and kink band (KB) formation. At temperatures higher than $900^{\circ}C$, grain boundary decohesion is suggested to contribute towards the decrease in the failure stress. This chapter will follow the formatting guidelines specified by the *Acta Materialia*.

Chapter 5 details the experimental study conducted on the dynamic constitutive behavior of Hastelloy X (AMS 5754) at room and elevated temperatures under varying rates of loading. A split Hopkinson pressure bar (SHPB) apparatus was used in conjunction with an induction coil heating system for applying dynamic loads at elevated temperatures. Experiments were carried out at different temperatures ranging from room temperature ($25^{\circ}C$) to $1100^{\circ}C$ at an average strain rate of $5000s^{-1}$. Room temperature experiments were carried out at varying strain rates from $1000s^{-1}$ to $4000s^{-1}$. The results show that as the strain rate increases from quasi-static to $4000s^{-1}$, the yield strength increases by approximately 50%. Also, under dynamic loading, the yield stress decreases with temperature up to $700^{\circ}C$, after which it shows a peak at

900°C before beginning to decrease again as the temperature is further increased. The Johnson-Cook model was used to predict the dynamic plastic response under varying rates of loading and at different temperatures. This chapter follows the formatting guidelines specified by *Journal of Materials Science*.

Chapter 6 details the design of novel experimental set up for testing materials under shock loading at extreme temperatures. The shock tube apparatus was modified and validated for testing Hastelloy X at elevated temperatures. Propane gas was used as the heating source and it was directed onto the sample via four nozzles. A cooling system was also implemented to prevent the shock tube from reaching high temperatures. A series of experiments were conducted to study the dynamic response of rectangular Hastelloy X plates at room and elevated temperatures when subjected to shock wave loading. High-speed photography coupled with the optical technique of Digital Image Correlation (DIC) technique was used to record the real-time deformation of the specimen under shock wave loading. The DIC technique was used in conjunction with band pass optical filters and a high intensity light source to record the full-field deformation images under shock loading at high temperatures up to 900 °C. In addition, a high speed camera was utilized to record the side-view deformation images. The high temperature DIC system has been validated by comparing with the mid-point deflections obtained from the side-view camera. The dynamic response of Hastelloy X was evaluated as a function of temperature under shock wave loading. This chapter follows the formatting guidelines specified by *Mechanics of Materials*.

Chapter 7 provides a summary of the major experimental findings obtained during the investigation of various aerospace materials under high rates of loading and at extreme temperatures. Suggestions for future designs, as well as experiments and analysis will also be provided.

TABLE OF CONTENTS

ABSTRACT	ii
ACKNOWLEDGMENTS	v
PREFACE	vii
TABLE OF CONTENTS	xii
LIST OF TABLES	xvii
LIST OF FIGURES	xviii
CHAPTER 1	1
INTRODUCTION AND LITERATURE REVIEW	1
REFERENCES	7
CHAPTER 2	13
DYNAMIC CURVING CRACKS IN FUNCTIONALLY GRADED MATERIALS UNDER THERMO-MECHANICAL LOADING	13
Abstract	14
1. Introduction	14
2. Theoretical Formulation.....	18
2.1 Temperature Fields around the Crack-tip.....	24
2.2 Asymptotic Expansion of Crack-tip Stress Fields.....	28
3. Results and Discussion.....	35
3.1 Variation of Stress Components near the Crack-tip.....	37
3.1.1 Effect of Curvature of the Crack path	37
3.1.2 Effect of Temperature.....	44

3.1.3 Effect of Non homogeneity	46
3.2 Crack Extension Angle.....	47
3.3 Minimum Strain-Energy Density (MSED) Criterion.....	48
3.3.1 Effect of Crack-tip Velocity	50
3.3.2 Effect of Non homogeneity	51
3.3.3 Effect of Temperature.....	52
3.3.4 Effect of Curvature	54
3.4 Effect of T-stress on Curvature and Temperature	56
4. Conclusions	59
Acknowledgements	61
References	61
Appendix A	70
CHAPTER 3	76
TRANSIENT THERMO-MECHANICAL ANALYSIS OF DYNAMIC	
CURVING CRACKS IN FUNCTIONALLY GRADED MATERIALS	76
Abstract	77
1. Introduction	77
2. Theoretical Formulation.....	80
2.1 Temperature Field around the Crack-tip	86
2.2 Asymptotic Expansion of Crack-tip Stress Fields.....	91
3. Results and Discussion.....	101
3.1 Effect of Transient Terms on the Maximum Principal Stress	103
3.2 Effect of Transient Terms on the Circumferential Tensile Stress	104

3.3 Effects of Temperature	106
3.4 Effect of Temperature gradient and Crack-tip Velocity on the Crack Extension Angle	107
3.5 Effects of T-stress on the Crack Extension Angle	109
4. Concluding Remarks	110
Acknowledgement.....	111
References	112
CHAPTER 4	117
EFFECT OF STRAIN-RATE AND TEMPERATURE ON DYNAMIC DEFORMATION OF NANOLAMINATED Ti₂AlC.....	117
Abstract	118
1. Introduction	118
2. Experimental Details	120
3. Results and Discussion.....	121
4. Conclusions	127
Acknowledgements	127
References	127
CHAPTER 5	130
Abstract	131
1. Introduction	131
2. Material and Specimen Geometry.....	133
3. Experimental Details.....	134
3.1 Quasi-Static Characterization.....	134

3.2 Dynamic Characterization.....	134
3.3 Johnson Cook Constitutive Model	138
3.3.1 Model Description	138
3.3.2 Determination of Parameters of Model	139
4. Experimental Results	141
4.1 Quasi-Static Response.....	141
4.2 Dynamic Constitutive Response at Room Temperature	142
4.3 Dynamic Constitutive Response at Elevated Temperatures	144
4.4 Johnson Cook Constitutive Model Response.....	146
5. Conclusions	150
Acknowledgements	151
References	151
CHAPTER 6	155
DYNAMIC THERMO-MECHANICAL RESPONSE OF HASTELLOY X	
UNDER SHOCK WAVE LOADING	155
Abstract	156
1. Introduction	157
2. Material and Specimen Geometry.....	160
3. Experimental Procedures	161
3.1 Shock Tube.....	162
3.2 High Temperature Shock Tube Setup	163
3.3 High Speed Photography Systems	167
3.3.1 High Temperature DIC System under Dynamic Loading.....	168

4. Experimental Results & Discussion.....	172
4.1 Pressure profile & Impulse.....	172
4.2 Real-time Deformation Images	174
4.3 Digital Image Correlation Analysis.....	175
4.4 Deformation Energy Evaluation.....	183
4.5 Post-mortem Analysis	184
5. Conclusions	185
Acknowledgements	186
References	186
CHAPTER 7	190
CONCLUSIONS AND FUTURE WORKS	190
1. Conclusions	190
2. Future Work	193
APPENDICES	196
APPENDIX A: STANDARD OPERATING PROCEDURES (SOP)	196
APPENDIX B: MORE DETAILS OF CHAPTER 4.....	222
APPENDIX C: SAFETY GUIDELINES FOR EXPERIMENTAL EQUIPMENT.	226
APPENDIX D: MATLAB Code.....	230
APPENDIX E: ASTM STANDARDS	250
BIBLIOGRAPHY	251

LIST OF TABLES

CHAPTER 5

Table 1. Chemical composition of Hastelloy X [1]	133
Table 2. Johnson-Cook material parameters of Hastelloy X	141
Table 3. Predictability of the model for the dynamic plastic response of Hastelloy X at room temperature under various strain rates	148
Table 4. Predictability of the model for the dynamic plastic response of Hastelloy X at different temperatures.	149

CHAPTER 6

Table 1. Chemical composition of Hastelloy X	160
--	-----

LIST OF FIGURES

CHAPTER 2

Fig. 1 Propagating curved crack orientation with respect to property gradation direction and temperature gradient.....	19
Fig. 2 Comparison of normalized maximum shear stress for a straight and curved crack around the crack-tip for a mixed-mode loading in an FGM with and without temperature field ($K_{IID}/K_{ID} = 0.2$, $c/c_s = 0.5$, $\gamma_2 = 1$, $r = 0.002m$).....	38
Fig. 3 Comparison of normalized maximum principal stress for a straight and curved crack around the crack-tip for a mixed-mode loading in an FGM with and without temperature field ($K_{IID}/K_{ID} = 0.2$, $c/c_s = 0.5$, $\gamma_2 = 1$, $r = 0.002m$).....	39
Fig. 4 Comparison of normalized maximum circumferential stress for a straight and curved crack around the crack-tip for a mixed-mode loading in an FGM with and without temperature field ($K_{IID}/K_{ID} = 0.2$, $c/c_s = 0.5$, $\gamma_2 = 1$, $r = 0.002m$)	40
Fig. 5 Effect of curvature on normalized (a) maximum principal stress, (b) the circumferential tensile stress, and (c) maximum shear stress around the crack-tip for a mixed-mode loading in an FGM with temperature field ($K_{IID}/K_{ID} = 0.2$, $c/c_s = 0.5$, $\gamma_2 = 1$, $\zeta = -1$, $q_0 = 100$, $r = 0.002m$).....	41
Fig. 6 Effect of curvature parameters on the contours of maximum shear stress around the crack-tip for a mixed-mode loading in an FGM with no temperature field ($K_{IID}/K_{ID} = 0.2$, $c/c_s = 0.5$, $\zeta = -1$)	42

Fig. 7 Variation of normalized (a) maximum principal stress, (b) the circumferential tensile stress, and (c) maximum shear stress around the crack–tip for a mixed-mode thermo-mechanical loading in an FGM for several values of temperature coefficients ($K_{IID}/K_{ID} = 0.2, c/c_s = 0.5, \gamma_2 = 1, \zeta = -1, k = 20, \beta = 20^\circ, r = 0.002m$).....45

Fig. 8 Effect of property gradation for a curved crack on the contours of for maximum shear stress around the crack–tip for a mixed-mode loading in an FGM with no temperature field ($K_{IID}/K_{ID} = 0.2, c/c_s = 0.5, k = 20, \beta = 20^\circ$).....46

Fig. 9 Effect of (a) temperature, (b) curvature and (c) non-homogeneity on strain energy density around the crack–tip for a mixed mode thermo-mechanical loading in an FGM ($K_{IID}/K_{ID} = 0.2, c/c_s = 0.5, \gamma_2 = 1, r = 0.002m$).....48

Fig. 10 Crack extension angle as a function of crack-tip velocity for a mixed-mode thermo-mechanical loading in homogeneous material using MSED criterion ($\zeta = 0, k = 20, \beta = 20^\circ, r = 0.002m$).....50

Fig. 11 Crack extension angle as a function of non-homogeneity parameter for a mixed- mode crack with temperature field ($c/c_s = 0.5, k = 20, \beta = 20^\circ, r = 0.002m$) ..51

Fig. 12 Effect of temperature on the crack extension angle for a mixed-mode thermo-mechanical loading in FGM for different non-homogeneity values using MSED criterion ($K_{IID}/K_{ID} = 0.2, c/c_s = 0.5, k = 20, \beta = 20^\circ, \gamma_2 = 1, r = 0.002m$)52

Fig. 13 Crack extension angle as a function of crack-tip velocity for a mixed-mode thermo-mechanical loading at different temperature fields using MSED criterion ($K_{IID}/K_{ID} = 0.2, k = 20, \beta = 20^\circ, \gamma_2 = 1, r = 0.002m$).....53

Fig. 14 Effect of curvature on the crack extension angle for a mixed-mode thermo-mechanical loading in FGM for different non-homogeneity factors using MSED criterion ($K_{IID}/K_{ID}=0.2, c/c_s=0.5, q_0 = 100, \beta = 20^\circ, \gamma_2 = 1, r=0.002m$).....54

Fig. 15 Crack extension angle as a function of crack-tip velocity for a mixed-mode thermo-mechanical loading for various curvature parameters using MSED criterion ($K_{IID}/K_{ID}=0.2, q_0 = 100, \gamma_2 = 1, r=0.002m$)55

Fig. 16 Effect of T-stress on the crack extension angle for different values of curvature and temperature for a mixed-mode thermo-mechanical loading in FGM for different non-homogeneity factors using MSED criterion ($\sigma_{\alpha} = (-3/4 * K_{ID})m^{-1/2}, K_{IID}/K_{ID} = 0.2, c/c_s=0.5, \gamma_2 = 1, r=0.002m$)57

CHAPTER 3

Fig. 1 Propagating curved crack orientation with respect to property gradation direction and temperature gradient.....82

Fig. 2 Effect of transient terms on the contours of maximum principal stress around the crack-tip for mixed mode loading in an FGM ($\zeta = -2, \gamma_1 = 0.2, \gamma_2 = 0.5, c/c_s = 0.5, k(t) = 20 \text{ rad/m}, \beta(t) = 20^\circ, K_{ID} = 5 \text{ MPa}\cdot\text{m}^{1/2}, K_{IID} = 1 \text{ MPa}\cdot\text{m}^{1/2}$)..... 103

Fig. 3 Effect of transient terms on the contours of circumferential stress around the crack-tip for mixed mode loading in an FGM ($\zeta = -2, \gamma_1 = 0.2, \gamma_2 = 0.5, c/c_s = 0.5, k(t) = 20 \text{ rad/m}, \beta(t) = 20^\circ, K_{ID} = 5 \text{ MPa}\cdot\text{m}^{1/2}, K_{IID} = 1 \text{ MPa}\cdot\text{m}^{1/2}$)..... 105

Fig. 4 Variation of normalized (a) maximum principal stress, and (b) the circumferential tensile stress, around the crack-tip for a mixed-mode thermo-

mechanical loading in an FGM for several values of temperature coefficients ($\zeta = -2$, $\gamma_1 = 0.2$, $\gamma_2 = 0.5$, $c/c_s = 0.5$, $k(t) = 20$ rad/m, $\beta(t) = 20^\circ$, $K_{ID} = 5$ MPa-m^{1/2}, $K_{IID} = 1$ MPa-m^{1/2}, $\dot{K}_{ID} = 1 \times 10^8$ MPa- m^{1/2}-s⁻¹, $\dot{K}_{IID} = 2 \times 10^7$ MPa- m^{1/2}-s⁻¹, $\dot{c} = 1 \times 10^7$ m/s, $q_1(t) = q_2(t) = 50^\circ\text{C}\cdot\text{m}^{-1/2}$, $\dot{q}_0(t) = 100^\circ\text{C}\cdot\text{m}^{-1/2}\cdot\text{s}^{-1}$ and a typical value for radius, $r = 0.002\text{m}$) 106

Fig. 5 Effect of temperature on the crack extension angle for a mixed-mode thermo-mechanical loading in an FGM ($\zeta = -2$, $\gamma_1 = 0.2$, $\gamma_2 = 0.5$, $c/c_s = 0.5$, $k(t) = 20$ rad/m, $\beta(t) = 20^\circ$, $K_{ID} = 5$ MPa-m^{1/2}, $K_{IID} = 1$ MPa-m^{1/2}, $\dot{K}_{ID} = 1 \times 10^8$ MPa- m^{1/2}-s⁻¹, $\dot{K}_{IID} = 2 \times 10^7$ MPa- m^{1/2}-s⁻¹, $\dot{c} = 1 \times 10^7$ m/s, $q_1(t) = q_2(t) = 50^\circ\text{C}\cdot\text{m}^{-1/2}$, $\dot{q}_0(t) = 100^\circ\text{C}\cdot\text{m}^{-1/2}\cdot\text{s}^{-1}$)..... 108

Fig. 6 Crack extension angle as a function of crack-tip velocity for different values of temperature gradient for a mixed-mode thermo-mechanical loading in FGM ($\zeta = -2$, $\gamma_1 = 0.2$, $\gamma_2 = 0.5$, $c/c_s = 0.5$, $k(t) = 20$ rad/m, $\beta(t) = 20^\circ$, $K_{ID} = 5$ MPa-m^{1/2}, $K_{IID} = 1$ MPa-m^{1/2}, $\dot{K}_{ID} = 1 \times 10^8$ MPa- m^{1/2}-s⁻¹, $\dot{K}_{IID} = 2 \times 10^7$ MPa- m^{1/2}-s⁻¹, $\dot{c} = 1 \times 10^7$ m/s, $q_1(t) = q_2(t) = 50^\circ\text{C}\cdot\text{m}^{-1/2}$, $\dot{q}_0(t) = 100^\circ\text{C}\cdot\text{m}^{-1/2}\cdot\text{s}^{-1}$)108

Fig. 7 Effect of T-stress on the crack extension angle for different values of temperature gradient for a mixed-mode thermo-mechanical loading in FGM $\zeta = -2$, $\gamma_1 = 0.2$, $\gamma_2 = 0.5$, $c/c_s = 0.5$, $k(t) = 20$ rad/m, $\beta(t) = 20^\circ$, $K_{ID} = 5$ MPa-m^{1/2}, $K_{IID} = 1$ MPa-m^{1/2}, $\dot{K}_{ID} = 1 \times 10^8$ MPa- m^{1/2}-s⁻¹, $\dot{K}_{IID} = 2 \times 10^7$ MPa- m^{1/2}-s⁻¹, $\dot{c} = 1 \times 10^7$ m/s, $q_1(t) = q_2(t) = 50^\circ\text{C}\cdot\text{m}^{-1/2}$, $\dot{q}_0(t) = 100^\circ\text{C}\cdot\text{m}^{-1/2}\cdot\text{s}^{-1}$)109

CHAPTER 4

Fig. 1 (a) Dynamic stress-strain response of bulk Ti ₂ AlC at room temperature for different strain rates. Inserts show the samples tested at strain rates of 2300/s and 2800/s. Results of Scanning Electron Microscopy, SEM, show extensive kink band formation and delamination for the samples tested at strain-rates of (b) 2300/s and (c) 2800/s	122
Fig. 2 (a) Dynamic stress-strain response of bulk Ti ₂ AlC at different temperatures at a strain-rate of 3500/s. Inserts show the samples tested at 500 and 1150°C. Results of Scanning Electron Microscopy, SEM, show deformation kinking along the fracture surfaces of samples tested at (b) 500°C and (c) 1150°C, respectively	124
Fig. 3 Effect of temperature on the maximum stress during the dynamic deformation of Ti ₂ AlC. The quasi-static compressive strengths at different temperatures, from Ref. 10, are also plotted for comparison	125

CHAPTER 5

Fig. 1 Experimental setup of SPHB	134
Fig. 2 Experimental setup of SHPB apparatus with induction coil heating system....	137
Fig. 3 True compressive stress-strain curve of Hastelloy X under quasi-static loading	141
Fig. 4 Typical real-time strain pulses obtained from strain gages mounted on the bars for an average strain rate of 2500/s	142
Fig. 5 Typical force equilibrium conditions at the specimen-bar interface at an average strain rate of 2500/s	142

Fig. 6 True compressive stress-strain curve of Hastelloy X under dynamic loading at room temperature	143
Fig. 7 True compressive stress-strain curve of Hastelloy X under dynamic loading at elevated temperatures and a strain rate of about 5000/s	144
Fig. 8 Effect of temperature on the yield strength under dynamic loading at an average strain rate of 5000/s	144
Fig. 9 Experimental data and model prediction of Hastelloy X under dynamic loading at different strain rates.....	147
Fig. 10 Experimental data and model prediction of Hastelloy X under dynamic loading at different temperatures	149

CHAPTER 6

Fig. 1 True compressive stress-strain curve of Hastelloy X under dynamic loading at elevated temperatures	161
Fig. 2 Shock tube apparatus	162
Fig. 3 Front-view of the modified shock tube set up	164
Fig. 4 Calibration curves for 360 °C, 700 °C and 900 °C temperatures	164
Fig. 5 Side-view of the modified shock tube set up with cooling set up.	165
Fig. 6 Temperature vs. time plot for 360 °C, 700 °C and 900 °C experiments	166
Fig. 7 High-speed photography systems	167
Fig. 8 Captured image of the specimen (Hastelloy X) at 900 °C using an ordinary DIC system.....	169

Fig. 9 Complete experimental set up with bandpass filters, high speed cameras and the high energy flash unit.....	171
Fig. 10 Images captured at 25 °C and 900 °C using the proposed DIC system in conjunction with the optical band pass filters and high intensity light source energy flash unit.....	171
Fig. 11 (a) Pressure profiles measured for different temperatures (b) Pressure profile and deflection curve for 25 °C experiment	172
Fig. 12 Impulse imparted on the specimen for different temperatures	173
Fig. 13 Real-time side-view deformation images of the specimen for different temperatures	174
Fig. 14 Comparison of mid-point deflections obtained from the DIC technique with the side-view high speed images.....	176
Fig. 15 Deflection of back face during fluid structure interaction time for different temperatures	177
Fig. 16 Normalized standard deviation of the back face deflections along the center line as a function of time.....	177
Fig. 17 Back face deflections of the specimen for different temperatures.....	179
Fig. 18 Full-field out-of-plane deflection images for 25 °C, 360 °C, 700 °C and 900 °C experiments	180
Fig. 19 Back face in-plane strains at the center of the specimen for different temperatures	182
Fig. 20 Back face out-of-plane velocities at the center of the specimen for different temperatures	182

Fig. 21 Deformation energy of the specimens for different temperatures184

Fig. 22 Post-mortem images of the specimens tested at 25 °C, 360 °C, 700 °C and 900 °C under blast loading.....185

CHAPTER 1

INTRODUCTION AND LITERATURE REVIEW

To improve the performance and safety of future aerospace vehicles, worldwide efforts are being directed towards the development of novel aerospace materials which exhibit superior structural and multifunctional capabilities in extreme environments. Central to this proposed study is to enable revolutionary advances in future Air Force technologies through the development of new flight structures that fly in the hypersonic flow regime and can sustain severe environments. It was observed that the surface of an aircraft travelling at mach 5 speeds can experience temperatures above 1000°C. In addition to high temperature and high convective fluxes, the materials must be able to withstand high mechanical stresses associated with shock loading, vibrations at launch, acoustic-frequency vibrations and structural movement of the vehicle, as well as landing impact. Fundamental investigation into the thermo-mechanical response and dynamic failure of the materials is paramount before they can be incorporated into the design of future space access vehicles that can operate reliably in combined, extreme environments. To date there has been little research on thermo-mechanical characterization of aerospace materials. For this purpose, a variety of aerospace materials such as Functionally Graded Materials (FGMs), Ti_2AlC , and Hastelloy X were investigated to study their response under extreme thermo-mechanical loadings.

It was identified that reusable space access vehicles which must withstand launches and re-entries into Earth's atmosphere require efficient external thermal protection system (TPS) which are usually in the form of rigid surfaces in areas of

high or moderate working temperature. FGMs are identified as the potential candidates to be used as integrated hot structure in space access vehicles as the material combination and the composition gradation in these materials can be tailored to optimize their performance to meet multiple functions like thermal resistance, structural integrity etc. The fundamental factor that governs the nature of damage progression, stable or unstable, in any material is the relative dominance of the energy release rate and the material toughness over each other. Therefore, it is very important to understand the effect of crack-tip stress fields for propagating cracks in FGMs under thermo-mechanical loading.

Functionally Graded Materials (FGMs) are non-homogeneous composites which have spatially varying microstructure and mechanical/thermal properties to meet desired functional performance [1, 2]. FGMs used in high temperature applications have metals and ceramics as their constituents and thus have both thermal and mechanical non-homogeneities. These materials can withstand high temperatures effectively due to superior thermal properties of ceramics, and at the same time high strength can be achieved with the presence of metal. Several studies on the superior in-service advantages of FGMs over traditional duplex coatings under high temperature and high thermal cycling conditions have been reported. In their studies, Kawasaki and Wananabe [3], and Drake et al. [4] reported that the thermal residual stresses are relaxed in metal-ceramic layered materials by inserting a functionally graded interface layer between the metal and ceramic. Kudora et al. [5] and Takahashi et al. [6] reported that FGM coatings suffer significantly less damage than conventional ceramic coatings, under thermal shock condition.

Several studies on the quasi-static fracture behavior of FGMs under thermo-mechanical loading have been reported. Assuming exponential variation of material properties, Jin and Noda [7] investigated the steady thermal stress intensity factors in functionally graded semi-infinite space with an edge crack subjected to a thermal load. Using both experimental and numerical techniques, Kokini and Choules [8], and Kokini and Case [9] studied surface and interface cracking in FGM coatings subjected to thermal shocks. Jin and Paulino [10] studied transient thermal stresses in an FGM with an edge crack and having a constant Young's modulus and Poisson's ratio, but varying thermal properties along the thickness direction.

The above studies provide closed form solutions for stress intensity factors under thermo-mechanical loading, however, for extracting fracture parameters from experimental studies, asymptotic expansion of thermo-mechanical stress fields around the crack-tip is essential. Jain et al. [11] developed quasi-static stress and displacement fields for a crack in an infinite FGM medium under thermo-mechanical loading. Lee et al. [12] developed analytical expressions for dynamic crack-tip stress and displacement fields under thermo-mechanical loading in FGMs. Recently, Kidane et al. [13] developed the thermo-mechanical stress fields for a mixed mode propagating crack with a constant velocity along the gradation direction. Also, Chalivendra et al. [14] developed the elastic mechanical stress field solutions for an inclined propagating transient crack in FGMs. Even though the above mentioned studies of dynamic thermo-mechanical asymptotic field equations serve the purpose of obtaining fracture parameters from experimental data, these studies have not incorporated the crack path curvature associated with a propagating crack in these materials. It has been reported

in the experimental and numerical studies that the propagating cracks follow curved paths under various loading conditions due to the spatial variation of properties in graded materials [15-18]. In order to extract the fracture parameters accurately from the experimental data associated with curved cracks, it is essential to consider curvature terms in the field equations. Liu and Rosakis [19] developed the higher-order asymptotic expansion of a non-uniformly propagating dynamic crack along an arbitrary curved path for homogeneous materials and they emphasized the importance of the curvature terms when experimental data points are considered away from the singularity zone to extract fracture parameters. Recently, Chalivendra [20] developed crack-tip out of plane displacement field equations for transient curved cracks in FGMs. However, asymptotic expansion of near-tip field equations for a curving crack under transient thermo-mechanical loading conditions has not yet been reported.

Experimental studies have been conducted on Ti_2AlC and Hastelloy to understand the failure mechanisms and to predict their performance under a combination of extreme mechanical and thermal environments. Nanolaminated ternary carbides and nitrides, known as MAX phases, have attracted recent attention because of their potential for application in extreme environments. They have a general formula of $M_{n+1}AX_n$ ($n = 1, 2, 3$), where M is an early transition metal, A is a group-A element and X is either C or N. [21-23]. Titanium aluminum carbide, Ti_2AlC , one of the well characterized compounds with M_2AX chemistry, is lightweight (4.11 g/cm^3) material with high Young's modulus (278 GPa) [21], excellent electrical and thermal conductivity, high oxidation and corrosion resistance [24]. Like most MAX phases, Ti_2AlC is relatively soft (Vickers hardness of $\sim 4 \text{ GPa}$) and easily machinable

compared to binary transition metal carbides [25-26]. Because of their nanolaminated structure and kinking mechanism, Ti_2AlC is also exceedingly damage tolerant and thermal shock resistant and most likely creep and fatigue-resistant like some other MAX phases [27-29]. One of the interesting aspects of MAX phases in general, and Ti_2AlC in particular is unusual deformation behavior that can be traced back to their nanolaminated hexagonal crystal structure with high c/a ratio and presence of the relatively large number of movable dislocations. The dislocations, being confined to only parallel basal planes, give rise to extensive kinking and delamination in MAX phases upon deformation [30-31]. At room temperature, Ti_2AlC , similar to other MAX phases, shows nonlinear stress-strain behavior with fully reversible hysteresis loops and significant amount of energy dissipation under quasi-static cycling loading-unloading [30, 32-33]. Recently, a microscale model, based on nucleation, growth and annihilation of reversible nest of movable dislocations, so called incipient kink bands (IKBs), has been proposed to explain the, stress-strain hysteresis in MAX phases [30, 34-35]. At higher stresses or higher temperature, the IKBs transform into permanent kink bands (KBs). Formation of KB along with delamination has been argued in literature to be the primary reason for excellent damage tolerance of MAX phases [29]. At higher temperatures, i.e. above $1000^{\circ}C$, Ti_2AlC , undergoes a brittle-to-plastic (BTP) transition above and strains as large as 12% can be reach before failure during compressive loading [36].

Hastelloy X is a nickel based superalloy that possesses excellent high temperature strength and oxidation resistance. It is widely used in gas turbine operations, petrochemical and in aircraft parts [37]. Several researchers in the past

have investigated the behavior of Hastelloy X. Lai [38] investigated changes in the hardness and impact toughness at room temperature of Hastelloy X after aging up to 1000h. The author found that it exhibits age hardening at 540°C and 650°C. The author also observed a slight increase in hardness at 871°C followed by overaging after 4000h. Yasuo Kondo et al. [39] presented experimental results on the changes in the tensile mechanical properties of Hastelloy X after being used in the liner tube of a HENDEL hot gas duct under high temperature helium gas for about 6000h. They observed that the 0.2% proof stress and total elongation were slightly decreased when Hastelloy X was exposed to high temperature helium. Static tensile stress-strain curves of Hastelloy X were reported in Mil Handbook 5h [40]. Swindeman and Brinkman [41] reviewed high temperature mechanical properties for materials including Hastelloy X, used in a pressure vessel using stress-strain curves obtained experimentally. They studied the effect of cold work, chemistry, and heat treatment variations in Hastelloy X. Aghaie Khafri and Golarzi [42] characterized the hot deformation behavior of Hastelloy X using hot compression tests in the temperature range of 900°C-1150°C and at varying strain rates between 0.001 and 0.5s⁻¹. They showed that softening mechanisms, dynamic recovery and dynamic recrystallization occurred during hot working. Zhao et al. [43] studied the phase precipitation in Hastelloy X heat-treated at 750°C, 850°C and 900°C for 26 and 100 hours. They also provided a TTT (time-temperature-transformation) diagram by combining the new experimental results with the existing literature data. This TTT diagram depicted the presence of $M_{23}C_6$ and σ phases at temperatures < 900°C and μ phase between 800°C and 980°C. Rowley and Thornton [44] modeled visco plastic behavior of Hastelloy X

using the Bodner Partom unified constitutive model. Static compression experiments were conducted at different temperatures to get the parameters for the model. The model results of Hastelloy X for isothermal uniaxial tensile tests showed good agreement with the experimental stress-strain data. Although significant progress have been achieved in the recent years on understanding mechanical behavior of Hastelloy X and Ti_2AlC in quasi-static conditions, there is no literature available on the dynamic response of these materials under high strains rates and temperatures.

Also, there is a large volume of literature available on the response of monolithic plates and beams subjected to shock loading. Menkes and Opat [45] characterized the response of aluminum beams under shock loading. They identified three major damage modes, which respectively are inelastic deformation, tensile tearing and transverse shear. Later, (Teeling-Smith and Nurick), (Nurick et al.,) and (Nurick and Shave,) observed similar failure modes for circular, stiffened square and square plates, respectively [46-48]. Wierzbicki and Nurick investigated thin clamped plates for different loading radii and applied impulse [49]. They observed that the smaller loading radii led to a more localized damage towards the center of the plate, while the more distributed load produced tearing fracture at the clamped boundary. To date, there have been no studies reported on the damage behavior of aerospace materials under shock loading when exposed to extreme environments.

REFERENCES

[1] Suresh S, Mortensen A (1998) Fundamentals of functionally graded materials, processing and thermomechanical behavior of graded metals and metal-ceramic composites. IOM Communications Ltd., London.

- [2] Niino M, Hirai T, Watanabe R (1987) The functionally gradient materials. *J Jap Soc. Comp Mater*, 13(1), 257.
- [3] Kawasaki A, Wananabe R (1987) Finite element analysis of thermal stress of the metal/ceramics multilayer composites with controlled compositional gradients. *J Jpn Inst. Met*, 51:525-529.
- [4] Drake JT, Williamson RL, Rabin BH (1993) Finite element analysis of thermal residual stresses at graded ceramic-metal interfaces Part II: Interface optimization for residual stress reduction. *J Appl Phys*, 74:1321-1326.
- [5] Kuroda Y, Kusaka K, Moro A, Togawa M (1993) Evaluation Tests of ZrO₂ /Ni functionally gradient materials for regeneratively cooled thrust engine applications. *Functionally gradient materials (Ceramic Transactions)* (edited by Holt JB, Koisumi M, Hirai T, Munir ZA, American Ceramic Society, Westerville, OH, 34:289-296.
- [6] Takahashi H, Ishikawa T, Okugawa D, Hashida T (1993) Laser and plasma-ARC thermal shock/fatigue fracture evaluation procedure for functionally gradient materials. *Thermal Shock and Thermal Fatigue Behavior of Advanced Ceramics*, (edited by Scheneider, GA and Petzow G, Kluwer Academic, Dordrecht, 543-554.
- [7] Jin, ZH, Noda N (1994) Crack-tip singular fields in nonhomogeneous materials. *J Appl Mech*, 61:738-740.
- [8] Kokini K, Choules BD (1995) Surface thermal fracture of functionally graded ceramic coatings: Effect of architecture and materials. *Composites Eng*, 5:865-877.
- [9] Kokini K, Case M (1997) Initiation of surface and interface edge cracks in functionally graded ceramic thermal barrier coatings. *ASME J Eng Mater Technol*, 119:148-152.
- [10] Jin ZH, Paulino GH (2001) Transient thermal stress analysis of an edge crack in a functionally graded material. *Int J Fract*, 107:73-98.
- [11] Jain N, Shukla A, Chona R (2006) Asymptotic stress fields for thermo-mechanically loaded cracks in FGMs. *J of ASTM Int*, 3(7):78-90.

- [12] Lee KH, Chalivendra VB, Shukla A (2008) Dynamic crack-tip stress and displacement fields under thermomechanical loading in functionally graded materials. *J Appl Mech*, 75(5):1-7.
- [13] Kidane A, Chalivendra VB, Shukla A, Chona R (2010) Mixed-mode dynamic crack propagation in graded materials under thermo-mechanical loading. *Eng Fract Mech*, 77(14):2864-2880.
- [14] Chalivendra VB, Shukla A (2005) Transient elastodynamic crack growth in functionally gradient materials. *J Appl Mech*, 72:237-248.
- [15] Lambros J, Cheeseman BA, Santare MH (2000) Experimental investigation of the quasi-static fracture of functionally graded materials. *Int J Solids Struct*, 37:3715–3732.
- [16] Noda, N, Ishihara M, Yamamoto N, Fujimoto T (2003) Two-crack propagation in a functionally graded material plate under thermal loads. *Mater Sci Forum* 423–425, 607–612.
- [17] Tohgo K, Suzuki T, Araki H (2005) Evaluation of R-curve behavior of ceramic–metal functionally graded materials by stable crack growth. *Eng Fract Mech*, 72:2359–2372.
- [18] Tilbrook MT, Moon RJ, Hoffman M (2005) Curved crack propagation in homogeneous and graded materials. *Fatigue Fract Eng Mater Struct*, 28:939–950.
- [19] Liu C, Rosakis AJ (1994) On the higher order asymptotic analysis of a non-uniformly propagating dynamic crack along an arbitrary path. *J Elast*, 35:27–60.
- [20] Chalivendra VB (2007) Asymptotic analysis of transient curved crack in functionally graded materials. *Int J Solids Struct*, 44:465-479.
- [21] Barsoum, MW (2000) The $M_{n+1}AX_n$ Phases: A new class of solids; Thermodynamically stable nanolaminates. *Prog Solid State Chem*, 28: 201-281.

- [22] Wang J, Zhou Y (2009). Recent Progress in Theoretical Prediction, Preparation, and Characterization of Layered Ternary Transition-Metal Carbides Annual Review of Materials Research, 39:415-443.
- [23] Eklund P, Beckers M, Jansson U, Högberg H, Hultman L (2010) The $M_{n+1}AX_n$ phases: Materials science and thin-film processing. Thin Solid Films, 518: 1851-1878.
- [24] Barsoum MW (2001) Oxidation of $Ti_{n+1}AlX_n$ where $n = 1 \sim 3$ and X is C N. Part 1. J. Electrochem. Soc, 148(8): C544:C550.
- [25] Meng FL, Zhou YC, Wang JY (2005) Strengthening of Ti_2AlC by substituting Ti with V. Scr Mater, 53:1369-1372.
- [26] Barsoum MW, Brodtkin D, El-Raghy T (1997) Layered machinable ceramics for high temperature applications. Scr Mater, 36:535-541.
- [27] El-Raghy T, Zavaliangos A, Barsoum MW, and Kalidindi SR (1994) Damage mechanisms around hardness indentations in Ti_3SiC_2 . J Am Ceram Soc, 8:513-516.
- [28] Radovic M, Barsoum MW, El-Raghy T, Wiederhorn SM (2001) Tensile Creep of fine grained (3-5 μ m) Ti_3SiC_2 in the 1000-1200°C temperature Range. Acta Mater, 49:4103-4112.
- [29] Gilbert CJ, Bloyer DR, Barsoum MW, El-Raghy T, Tomasia AP, Ritchie RO (2000) Fatigue-crack growth and fracture properties of coarse and fine-grained Ti_3SiC_2 . Scr Mater, 238:761-767.
- [30] Barsoum MW, Radovic M (2011) The Elastic and Mechanical Properties of the MAX Phases. Annu Rev Mater Res, 41:195-227.
- [31] Barsoum MW, Farber L, El-Raghy T, Levin I (1999) , Dislocations, kink bands and room temperature plasticity of Ti_3SiC_2 . Met Mater Trans 30A:1727-1738.
- [32] Barsoum MW, Zhen T, Kalidindi SR, Radovic M, Murugahiah A (2003) Fully reversible, dislocation-based compressive deformation of Ti_3SiC_2 to 1 GPa. Nat Mater, 2:107-111.

- [33] Zhou AG, Barsoum MW, Basu S, Kalidindi SR, El-Raghy T (2006) , Incipient and regular kink bands in fully dense and 10 vol% porous Ti₂AlC. *Acta Mater*, 54:1631-1639.
- [34] Barsoum MW, Basu S (2010) in *Encyclopedia of Materials: Science and Technology*, edited by Buschow KHJ, Cahn RW, Flemings MC, Ilschner B, Kramer EJ, Mahajan S, Veyssiere P (Elsevier, 2010).
- [35] Zhou AG, Basu S, Friedman G, Finkel P, Yeheskel O, Barsoum MW (2010) Hysteresis in kinking nonlinear elastic solids and the Preisach-Mayergoyz model. *Phys Rev B*, 82:094105(1-10).
- [36] Zhou YC, Wang XH (2001) Deformation of polycrystalline Ti₂AlC under compression. *Mater Res. Innovat*, 5(2):87-93.
- [37] Haynes, International, Jan 2012. <http://www.haynesintl.com/pdf/h3009.pdf>
- [38] Lai GY (1978) An investigation of the thermal stability of a commercial Ni-Cr-Fe-Mo alloy (Hastelloy X). *Metall Mater Trans A*, 9:827-833.
- [39] Yasuo K, Kiyoshi F, Kazuhiko K, Yoshiaki M (1988) Tensile and impact properties changes of Hastelloy X after exposure in high temperature helium environment. *Metall Mater Trans A*, 19:1269-1275.
- [40] *Heat Resistant Alloys, Military Handbook-Mil-Handbook-5H* (1998). Metallic materials and elements for aerospace vehicle structures, Chapter 6, Knovel Interactive edition.
- [41] Swindeman RW, Brinkman CR (1981) Progress in understanding the mechanical behavior of pressure-vessel materials at elevated temperatures. Technical Report, ASME PVP Conference, Denver, Co, USA.
- [42] Aghaie-Khafri M, Golarzi N (2007) Forming behavior and workability of Hastelloy X superalloy during hot deformation. *Mater Sci Eng A*, 486:641-647.
- [43] Zhao JC, Larsen M, Ravikumar V (2000) Phase precipitation and time-temperature-transformations diagram of Hastelloy X. *Mater Sci Eng A*, 293:112-119.

- [44] Rowley MA, Thornton EA (1996) Constitutive modeling of the visco-plastic response of Hastelloy-X and Aluminium alloy 8009. *J Eng Mater Technol*, 118:19–27.
- [45] Menkes S, Opat H (1973) Broken beams. *Exp Mech*, 13: 480-486.
- [46] Teeling-Smith RG, Nurick GN (1991) The deformation and tearing of thin circular plates subjected to impulsive loads. *Int J Soilds Struct*, 11:77-91.
- [47] Nurick GN, Olson MD, Fagnan JR, Levin A (1995) Deformation and tearing of blast-loaded stiffened square plates. *Int J Impact Eng*, 16: 273-291.
- [48] Nurick GN, Shave GC (1996) The deformation and tearing of thin square plates subjected to impulsive loads -An experimental study. *Int J Impact Eng*, 18: 99-116.
- [48] Wierzbicki T, Nurick GN (1996) Large deformation of thin plates under localised impulsive loading. *Int J Impact Eng* 18: 899-918.

CHAPTER 2

DYNAMIC CURVING CRACKS IN FUNCTIONALLY GRADED MATERIALS UNDER THERMO-MECHANICAL LOADING

by

Sandeep Abotula, Addis Kidane, Vijaya B. Chalivendra and Arun Shukla

has been published in the International Journal of Solids and Structures

Corresponding Author: Arun Shukla

Dynamic Photo Mechanics Laboratory

Department of Mechanical, Industrial and Systems

Engineering

University of Rhode Island

206 Wales Hall, 92 Upper College Rd

Kingston, RI, 02881, USA

Phone: +1-401-874-2283

Email Address: shuklaa@egr.uri.edu

Abstract

Mixed-mode dynamic crack growth along an arbitrarily smoothly varying path in functionally graded materials (FGMs) under thermo-mechanical loading is studied. The property gradation in FGMs is considered by varying shear-modulus, mass density, thermal conductivity and coefficient of thermal expansion exponentially along the gradation direction. Asymptotic analysis in conjunction with displacement potentials is used to develop the stress fields around propagating cracks in FGMs. Asymptotic temperature fields are developed first for the exponential variation of thermal conductivity and later these temperature fields are used to derive thermo-mechanical stress fields for a curving crack in FGMs. Using these thermo-mechanical stress fields, various components of the stresses are developed and the effect of curvature parameters, temperature and gradation on these stresses are discussed. Finally, using the minimum strain energy density criterion, the effect of curvature parameters, crack-tip speeds, non-homogeneity values and temperature gradients on crack growth directions are determined and discussed.

Keywords: Thermo-mechanical stress fields, curving cracks, functionally graded materials, asymptotic analysis

1. Introduction

Functionally graded materials (FGMs) are essentially non-homogeneous composites which have characteristics of spatially varying microstructure and mechanical/thermal properties to meet a predetermined functional performance (e.g., Niino et al. 1987; Suresh and Mortensen, 1998). Although their performance in real-life engineering applications is still under investigation, FGMs have shown promising

results when they are subjected to thermo-mechanical loading (e.g., Suresh and Mortensen, 1998). There is an extensive amount of literature published on the fracture mechanics of FGMs under both quasi-static loading conditions (e.g., Delale and Erdogan, 1983; Schovance and Walton, 1988; Konda and Erdogan, 1994; Gu and Asaro, 1997; Wu and Erdogan, 1997; Jin et al. 2002; Kim and Paulino 2002; Parameswaran and Shukla, 2002; Chalivendra et al. 2003; Kubair et al. 2005; Chalivendra, 2008, 2009; Zhang and Kim, 2011) and dynamic loading conditions (e.g., Atkinson and List, 1978; Krishnaswamy et al. 1992; Parameswaran and Shukla, 1999; Rousseau and Tippur, 2001; Chalivendra et al. 2002; Shukla and Jain, 2004; Chalivendra and Shukla, 2005; Abanto-Bueno and Lambros, 2006; Kirugulige and Tippur, 2008).

The research output on the thermo-mechanical response of FGM's is limited. Hasselman and Youngblood (1978) were among the first to study thermal stresses in nonhomogeneous structures associated with thermo-mechanical loading. By introducing a thermal conductivity gradient, they demonstrated significant reductions in the magnitude of the tensile thermal stress in ceramic cylinders. In other studies, thermal residual stresses were relaxed in metal-ceramic layered materials by inserting a functionally graded interface layer between the metal and ceramic (e.g., Kawasaki and Wantanabe, 1987; Drake et al. 1993; Giannakopoulos et al. 1995). In their studies, Kuroda et al. (1993) and Takashashi et al. (1993) reported that when subjected to thermal shocks, FGM coatings suffer significantly less damage than conventional ceramic coatings.

In continuation of the above studies, several studies on the quasi-static fracture of FGMs under thermo-mechanical loading have been reported. Assuming exponential variation of material properties, Jin and Noda (1994) investigated the steady thermal stress intensity factors in functionally graded semi-infinite space with an edge crack subjected to thermal load. Later, Erdogan and Wu (1996) also determined the steady thermal stress intensity factor of a FGM layer with a surface crack perpendicular to the boundaries. By further assuming the exponential variation of thermal and mechanical properties of the materials, Jin and Batra (1996) investigated the stress intensity relaxation problem at the tip of an edge crack in a FGM subjected to a thermal shock. By employing a finite element method (FEM), Noda (1997) analyzed an edge crack problem in a zirconia/titanium FGM plate subjected to cyclic thermal loads. Jin and Paulino (2001) studied transient thermal stresses in a FGM with an edge crack having a constant Poisson's ratio and Young's Modulus but varying thermal properties along the thickness direction. Walters et al., (2004) developed general domain integral methods to obtain the stress intensity factors for the surface cracks in FGMs under mode-I thermo-mechanical loading conditions.

The above studies provide closed form solutions for stress intensity factors under thermo-mechanical loading, however for extracting fracture parameters from experimental studies, the asymptotic expansion of thermo-mechanical stress fields around the crack-tip are essential (e.g., Kirugulige and Tippur, 2008). Recently in this direction, Jain et al. (2006) developed quasi-static stress and displacement fields for a crack in an infinite FGM medium under thermo-mechanical loading. However, there were no studies until recently on the dynamic crack growth under thermo-mechanical

loads. Lee et al. (2008) developed analytical expressions for the dynamic crack-tip stress and displacement fields under thermo-mechanical loading in FGMs. Kidane et al. (2010a) developed the stress fields and strain energy associated with a propagating crack in a homogeneous material under thermo-mechanical loading using an asymptotic approach. Very recently, Kidane et al. (2010b) also developed stress field equations for dynamic crack propagation in FGMs under thermo-mechanical loading. Even though the above mentioned studies of dynamic thermo-mechanical asymptotic field equations serve the purpose of obtaining fracture parameters from experimental data, these studies have not incorporated the crack path curvature associated with a propagating crack in these materials. It has been reported in the experimental and numerical studies that the propagating cracks follow curved paths under various loading conditions due to the spatial variation of properties in graded materials (e.g., Lambros et al. 2000; Noda et al. 2003; Tohgo et al. 2005; Tilbrook et al. 2005). In order to extract the fracture parameters accurately from the experimental data associated with curved cracks, it is essential to consider curvature terms in the field equations. Liu and Rosakis (1994) developed the higher-order asymptotic expansion of a non-uniformly propagating dynamic crack along an arbitrary curved path for homogeneous materials and they emphasized the importance of the curvature terms when experimental data points are considered away from the singularity zone to extract fracture parameters. Recently, Chalivendra (2007) developed crack-tip out of plane displacement field equations for transient curved cracks in FGMs. To the authors' knowledge, there are no studies reported in the literature on the development

of crack-tip stress field equations for curving cracks in functionally graded materials under thermo-mechanical loading.

Hence in this paper, through asymptotic analysis, stress fields for a curving crack propagating at an arbitrary velocity in FGMs under steady state thermo-mechanical loading are developed. The property gradation is considered by varying the shear-modulus, mass density, thermal conductivity and coefficient of thermal expansion exponentially along the gradation direction. Asymptotic temperature field equations are first developed for a steady state temperature condition considering the heat flux singularity. These temperature fields are later used to develop the thermo-mechanical stress fields for curved crack analysis. Using these thermo-mechanical stress fields, the effect of curvature terms, temperature and material gradation on various stress components is discussed. The crack growth direction as a function of temperature, non-homogeneity parameters and crack-tip velocity are also evaluated using minimum strain energy density criterion. In addition, using the developed equations, the contours of maximum shear stress are plotted to show the effect of curvature terms and gradation around the crack-tip.

2. Theoretical Formulation

FGMs can be treated as isotropic non-homogeneous solids because, at a continuum level, the properties at any given point in an FGM can be assumed to be the same in all directions. Spatial variation of elastic properties, mass density, thermal properties and inclination of a curved crack with respect to the gradation direction make analytical solutions to the elastic-dynamic equations extremely difficult. Hence, an asymptotic analysis similar to that employed by Freund (1990) is used to expand

the stress field around a propagating curving crack under thermo-mechanical loading conditions.

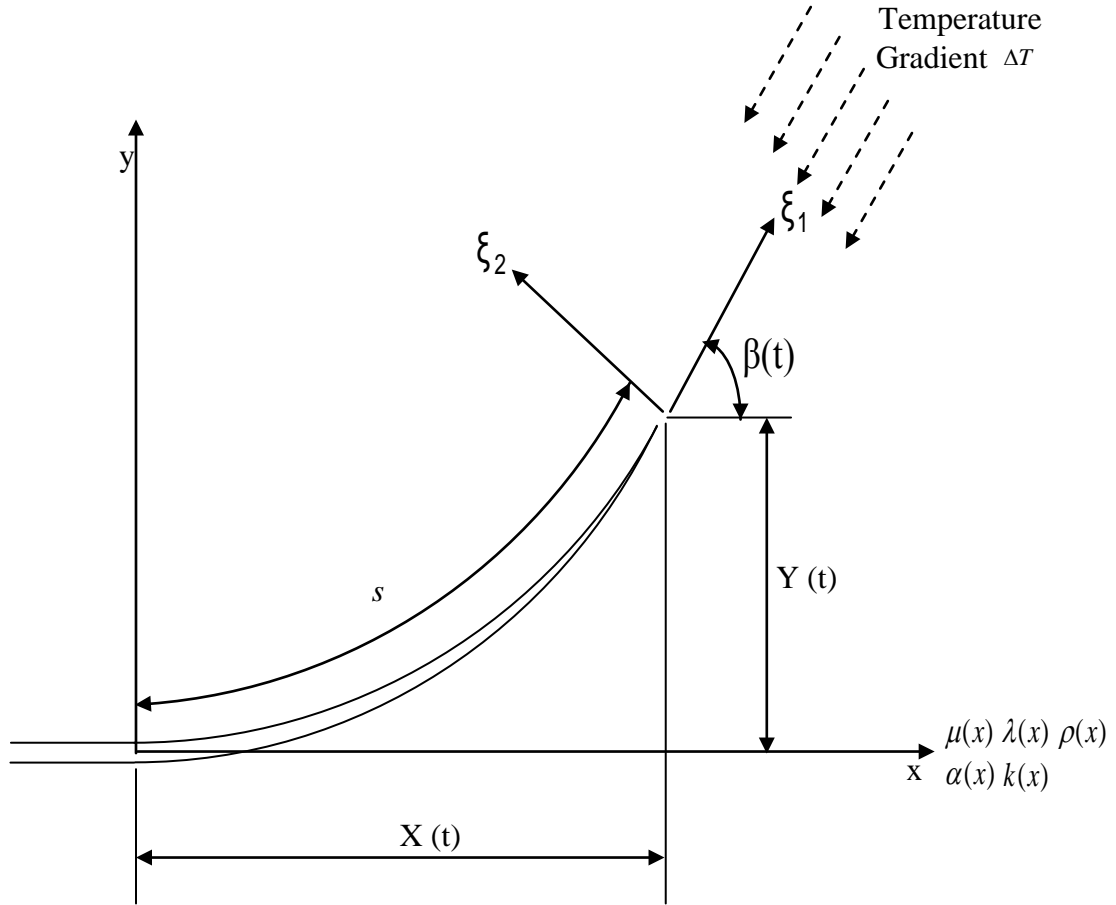


Fig. 1 Propagating curved crack orientation with respect to property gradation direction and temperature gradient.

An isotropic linear elastic FGM containing a propagating curving crack with temperature gradient in the x - y plane is shown in Fig. 1. At time $t = 0$, the crack-tip is at the origin of Cartesian coordinate system x - y . For any time $t > 0$, the position of the propagating crack-tip is given by $(X(t)$ and $Y(t))$ as shown in Fig. 1. Shear modulus(μ), Lamé's constant(λ), density(ρ), thermal expansion(α) and heat conductivity(k) of the FGM are assumed to vary in an exponential manner as given by

Eq. (1a) -1(e), whereas, Poisson's ratio (ν) is assumed to be a constant. Experimental studies (e.g., Shukla and Jain, 2004; Yao et al. 2007) reported in the literature support the exponential variation of modulus of elasticity and mass density.

$$\mu = \mu_0 \exp(\zeta x) \quad (1a)$$

$$\lambda = \lambda_0 \exp(\zeta x) \quad (1b)$$

$$\rho = \rho_0 \exp(\zeta x) \quad (1c)$$

$$\alpha = \alpha_0 \exp(\gamma_1 x) \quad (1d)$$

$$k = k_0 \exp(\gamma_2 x) \quad (1e)$$

The equations of motion for a plane problem are given by Eq. (2)

$$\frac{\partial \sigma_{xx}}{\partial x} + \frac{\partial \tau_{xy}}{\partial y} = \rho \frac{\partial^2 u}{\partial t^2} \quad (2a)$$

$$\frac{\partial \tau_{xy}}{\partial x} + \frac{\partial \sigma_{yy}}{\partial y} = \rho \frac{\partial^2 v}{\partial t^2} \quad (2b)$$

The relationship between stresses and strains for a plane strain thermo-mechanical problem can be written as

$$\sigma_{xx} = \exp(\zeta x) [\lambda_0 + 2\mu_0] \varepsilon_{xx} + \lambda_0 \varepsilon_{yy} - (3\lambda_0 + 2\mu_0) \alpha_0 \exp(\gamma_1 x) T] \quad (3a)$$

$$\sigma_{yy} = \exp(\zeta x) [\lambda_0 \varepsilon_{xx} + (\lambda_0 + 2\mu_0) \varepsilon_{yy} - (3\lambda_0 + 2\mu_0) \alpha_0 \exp(\gamma_1 x) T] \quad (3b)$$

$$\tau_{xy} = \exp(\zeta x) \mu_0 \gamma_{xy} \quad (3c)$$

where x and y are reference coordinates, σ_{ij} and ε_{ij} (where $i = x, y$ and $j = x, y$) are in-plane stress and strain components, and subscript “o” means at $x=0$ as shown in Fig.1. T represents the change in temperature in the infinite medium, ζ , γ_1 and γ_2 are non-homogeneity constants that have the dimension $(\text{length})^{-1}$. Each physical variable can have a different non-homogeneity parameter. However for mathematical

simplicity only three non-homogeneity parameters, one for mechanical properties and two for thermal properties, are considered. For a plane strain deformation, the displacements u and v are derived from dilatational and shear wave potentials Φ and Ψ . So, displacements can be expressed in terms of potentials as given below

$$u = \frac{\partial \phi}{\partial x} + \frac{\partial \psi}{\partial y}, \quad v = \frac{\partial \phi}{\partial y} - \frac{\partial \psi}{\partial x} \quad (4)$$

Substituting for the stresses and density from (3) and (1) respectively into Eq. (2) and after simplification, the equations of motion are written as

$$\begin{aligned} & (\lambda_0 + 2\mu_0) \nabla^2 \nabla^2 \phi + \zeta \left((\lambda_0 + 2\mu_0) \frac{\partial}{\partial x} \nabla^2 \phi + \mu_0 \frac{\partial}{\partial y} \nabla^2 \psi \right) \\ & - \alpha_c (3\lambda_0 + 2\mu_0) \left((\gamma_1 + \zeta) \gamma_1 T + (2\gamma_1 + \zeta) \frac{\partial T}{\partial x} \right) + \nabla^2 T = \rho_0 \frac{\partial^2}{\partial t^2} \nabla^2 \phi \end{aligned} \quad (5a)$$

$$\mu_0 \nabla^2 \nabla^2 \psi + \zeta \left(\mu_0 \frac{\partial}{\partial x} \nabla^2 \psi + \lambda_0 \frac{\partial}{\partial y} \nabla^2 \phi \right) - \alpha_c (3\lambda_0 + 2\mu_0) \zeta \frac{\partial T}{\partial y} = \rho_0 \frac{\partial^2}{\partial t^2} \nabla^2 \psi \quad (5b)$$

where α_c is the coefficient of thermal expansion in the vicinity of the instantaneous crack-tip and is assumed to be constant.

Equations (5a) and (5b) can be further written as

$$\begin{aligned} & (\delta + 2) \nabla^2 \phi + \zeta \left((\delta + 2) \frac{\partial}{\partial x} \phi + \frac{\partial}{\partial y} \psi \right) \\ & - \alpha_c (3\delta + 2) \left((\gamma_1 + \zeta) \gamma_1 \Delta^{-1} T + (2\gamma_1 + \zeta) \Delta^{-1} \frac{\partial T}{\partial x} \right) + T = \frac{\rho_0}{\mu_0} \frac{\partial^2 \phi}{\partial t^2} \end{aligned} \quad (6a)$$

$$\nabla^2 \psi + \xi \frac{\partial \psi}{\partial x} + \xi \delta \frac{\partial \phi}{\partial y} - \alpha_c (3\delta + 2) \zeta \Delta^{-1} \frac{\partial T}{\partial y} = \frac{\rho_0}{\mu_0} \frac{\partial^2 \psi}{\partial t^2} \quad (6b)$$

where $\Delta^{-1} = \frac{1}{\nabla^2}$, $\delta = \frac{\lambda_0}{\mu_0}$

Now, a new moving coordinate system (ξ_1, ξ_2) is introduced, so that the origin of the new system is at the moving crack-tip. The ξ_1 -axis is tangential to the crack trajectory at the crack-tip and coincides with the direction of the crack growth. The crack is propagating with constant velocity (c) as a function of time along the local ξ_1 -direction. The angle between ξ_1 -axis and the fixed x -axis are denoted by $\beta(t)$, as shown in Fig. 1. Therefore the relationship between the coordinates in these two Cartesian co-ordinate systems is

$$\begin{aligned}\xi_1 &= \{x - X(t)\}\cos \beta(t) + \{y - Y(t)\}\sin \beta(t) \\ \xi_2 &= -\{x - X(t)\}\sin \beta(t) + \{y - Y(t)\}\cos \beta(t)\end{aligned}\quad (7)$$

If the length of the trajectory that the crack-tip travels during the time interval, $[0, t]$, is denoted by $s(t)$, then the magnitude of the crack-tip speed $c(t)$ will be $\dot{s}(t)$, and the curvature of the crack trajectory at the crack-tip, $k(t)$, is given by

$$k(t) = \frac{d\beta(t)}{ds} = \frac{\dot{\beta}(t)}{c(t)} \quad (8)$$

where $c(t) = \sqrt{\dot{X}(t)^2 + \dot{Y}(t)^2}$

Using the transformations and the relations given below in Eqs. (9)-(11), and also neglecting the transient terms associated with acceleration and rate of curvature, the equations of motion (6a) and (6b) are further written in the crack-tip moving coordinate reference (ξ_1, ξ_2) as given in Eqs. (12a) and (12b).

$$\frac{\partial^2}{\partial x^2} + \frac{\partial^2}{\partial y^2} = \frac{\partial^2}{\partial \xi_1^2} + \frac{\partial^2}{\partial \xi_2^2} \quad (9)$$

$$\frac{\partial^2}{\partial t^2} = \frac{\partial^2}{\partial \xi_i \partial \xi_j} \dot{\xi}_i \dot{\xi}_j + \frac{\partial}{\partial \xi_i} \ddot{\xi}_i + 2 \frac{\partial^2}{\partial \xi_i \partial t} \dot{\xi}_i + \frac{\partial^2}{\partial t^2}, \quad \text{where } i = 1, 2 \text{ and } j = 1, 2 \quad (10)$$

where

$$\begin{aligned} \dot{\xi}_1 &= -c(t) + \beta(t)\xi_2 = -c(t) + c(t)k(t)\xi_2 \\ \dot{\xi}_2 &= -\dot{\beta}(t)\xi_1 = -c(t)k(t)\xi_1 \\ \ddot{\xi}_1 &= (k(t)\xi_2 - 1)\dot{c}(t) + c(t)\dot{k}(t)\xi_2 - c^2(t)k^2(t)\xi_1 \\ \ddot{\xi}_2 &= -\dot{c}(t)k(t)\xi_1 - c(t)\dot{k}(t)\xi_1 + c^2(t)k(t) - c^2(t)k^2(t)\xi_2 \end{aligned} \quad (11)$$

$$\begin{aligned} &\alpha_i^2 \frac{\partial^2 \phi}{\partial \xi_1^2} + \frac{\partial^2 \phi}{\partial \xi_2^2} + \zeta \left(\cos \beta(t) \frac{\partial \phi}{\partial \xi_1} - \sin \beta(t) \frac{\partial \phi}{\partial \xi_2} \right) + \frac{\zeta}{\delta + 2} \left(\sin \beta(t) \frac{\partial \psi}{\partial \xi_1} + \cos \beta(t) \frac{\partial \psi}{\partial \xi_2} \right) - \\ &\frac{\rho_0}{\mu_0(\delta + 2)} \left(\begin{aligned} &(c^2 k^2 \xi_2^2 - 2c^2 k \xi_2) \frac{\partial^2 \phi}{\partial \xi_1^2} + c^2 k^2 \xi_1^2 \frac{\partial^2 \phi}{\partial \xi_2^2} + (2c^2 k \xi_1 - 2c^2 k^2 \xi_1 \xi_2) \frac{\partial^2 \phi}{\partial \xi_1 \partial \xi_2} - \\ &c^2 k^2 \xi_1 \frac{\partial \phi}{\partial \xi_1} + (c^2 k - c^2 k^2 \xi_2) \frac{\partial \phi}{\partial \xi_2} \end{aligned} \right) \\ &- \alpha_c \frac{(3\delta + 2)}{\delta + 2} \left(T + \left\{ (2\gamma_1 + \zeta) \Delta^{-1} \left(\cos \beta(t) \frac{\partial T}{\partial \xi_1} - \sin \beta(t) \frac{\partial T}{\partial \xi_2} \right) + (\gamma_1 + \zeta) \gamma_1 \Delta^{-1} T \right\} \right) = 0 \end{aligned} \quad (12a)$$

$$\begin{aligned} &\alpha_s^2 \frac{\partial^2 \psi}{\partial \xi_1^2} + \frac{\partial^2 \psi}{\partial \xi_2^2} + \zeta \left(\cos \beta(t) \frac{\partial \psi}{\partial \xi_1} - \sin \beta(t) \frac{\partial \psi}{\partial \xi_2} \right) + \zeta \delta \left(\sin \beta(t) \frac{\partial \phi}{\partial \xi_1} + \cos \beta(t) \frac{\partial \phi}{\partial \xi_2} \right) - \\ &\frac{\rho_0}{\mu_0} \left(\begin{aligned} &(c^2 k^2 \xi_2^2 - 2c^2 k \xi_2) \frac{\partial^2 \psi}{\partial \xi_1^2} + c^2 k^2 \xi_1^2 \frac{\partial^2 \psi}{\partial \xi_2^2} + (2c^2 k \xi_1 - 2c^2 k^2 \xi_1 \xi_2) \frac{\partial^2 \psi}{\partial \xi_1 \partial \xi_2} - \\ &c^2 k^2 \xi_1 \frac{\partial \psi}{\partial \xi_1} + (c^2 k - c^2 k^2 \xi_2) \frac{\partial \psi}{\partial \xi_2} \end{aligned} \right) \\ &- \alpha_c (3\delta + 2) \zeta \Delta^{-1} \left(\sin \beta(t) \frac{\partial T}{\partial \xi_1} + \cos \beta(t) \frac{\partial T}{\partial \xi_2} \right) = 0 \end{aligned} \quad (12b)$$

$$\text{where, } \alpha_l = \sqrt{1 - \frac{\rho_0 c^2}{\mu_0 (\delta + 2)}}, \alpha_s = \sqrt{1 - \frac{\rho_0 c^2}{\mu_0}}$$

In the above formulation, we assume that the stress waves generated by the moving crack-tip are not influenced by the gradation. This assumption is acceptable as the property variation around the crack-tip is small in the zone of the interest.

2.1 Temperature Fields around the Crack-tip

In this analysis, it is assumed that the temperature field around the crack-tip also changes asymptotically. The transient effects, the thermo-elastic cooling effects, and the coupling effects $((3\lambda + 2\mu)\alpha T_0 \dot{\epsilon}_{ii})$ are neglected. It has been shown that for most materials under static loading conditions, this coupling term is small and can be neglected (Sadd, 2009). Several researchers studied the effect of coupling under dynamic loading conditions and found that the quantitative effect of coupling is less important for metals (Awrejcewicz and krys'ko, 2003). Few other authors observed that the difference between the couple and uncoupled solutions are about one percent (McQuillen and Brull, 1970; Shiari et al. 2003; Eslami et al. 1994). Brischetto and Carrera (2010) observed that when a mechanical load is applied, the differences between the coupled and uncoupled analysis are minimum, in terms of stresses. Nowinski (1978) in his book states ‘‘Practically speaking, it is generally possible to discount the coupling and to evaluate the temperature and deformation fields, in this order, separately’’. So, we establish the uncoupled conduction system and the temperature fields can be determined independent of the stress-field calculations. The developed field equations can be used for situations with small temperature gradient

thermal loading conditions. The heat conductivity is assumed to vary exponentially as given by Eq. (1e). The steady state heat conduction equation can be written as

$$\frac{\partial}{\partial x} \left(k \frac{\partial T}{\partial x} \right) + \frac{\partial}{\partial y} \left(k \frac{\partial T}{\partial y} \right) = 0 \quad (13)$$

Substituting the heat conductivity relation given by Eq. (1e) into Eq. (13) results in

$$\nabla^2 T + \gamma_2 \frac{\partial T}{\partial x} = 0 \quad (14)$$

where $\nabla^2 = \frac{\partial^2}{\partial x^2} + \frac{\partial^2}{\partial y^2}$

Transforming the above equation into the moving crack-tip coordinates, it can be written as

$$\nabla^2 T + \gamma_2 \left(\cos \beta(t) \frac{\partial T}{\partial \xi_1} - \sin \beta(t) \frac{\partial T}{\partial \xi_2} \right) = 0 \quad (15)$$

where $\nabla^2 = \frac{\partial^2}{\partial \xi_1^2} + \frac{\partial^2}{\partial \xi_2^2}$

At this stage, the asymptotic analysis is performed to solve the above Eq. (15). The advantages of this approach are: (i) it does not consider finite specimen geometry, and (ii) it does not need the information of external loading boundary conditions. It requires only crack-face and crack-line boundary conditions associated with the propagating crack to be satisfied. In this process, first a new set of scaled coordinates is defined as

$$\eta_1 = \xi_1 / \varepsilon, \quad \eta_2 = \xi_2 / \varepsilon \quad (16)$$

where ε is an arbitrary parameter and is assumed to be $0 < \varepsilon < 1$.

In the scaled coordinates, Eq. (15) can be written as

$$\nabla^2 T + \xi \gamma_2 \left(\cos \beta(t) \frac{\partial T}{\partial \eta_1} - \sin \beta(t) \frac{\partial T}{\partial \eta_2} \right) = 0 \quad (17)$$

For the asymptotic analysis, T is now represented as a power series expansion in ε .

$$T(\xi_1, \xi_2) = T(\varepsilon \eta_1, \varepsilon \eta_2) = \sum_{m=0}^{\infty} \varepsilon^{\frac{m+1}{2}} T_m(\eta_1, \eta_2) \quad (18)$$

Substituting Eq. (18) into Eq. (17) gives the following equation.

$$\sum_{m=0}^{\infty} \left\{ \varepsilon^{\frac{1+m}{2}} \left(\frac{\partial^2 T_m}{\partial \eta_1^2} + \frac{\partial^2 T_m}{\partial \eta_2^2} \right) + \varepsilon^{\frac{3+m}{2}} \gamma_2 \left(\cos \beta(t) \frac{\partial T_m}{\partial \eta_1} - \sin \beta(t) \frac{\partial T_m}{\partial \eta_2} \right) \right\} = 0 \quad (19)$$

For Eq. (19) to be valid, the partial differential equations corresponding to each power of ε ($\varepsilon^{1/2}, \varepsilon, \varepsilon^{3/2}, \dots$) should vanish independently. This leads to the following set of partial differential equations.

For $m=0$ and $m=1$

$$\frac{\partial^2 T_m}{\partial \eta_1^2} + \frac{\partial^2 T_m}{\partial \eta_2^2} = 0 \quad (20)$$

For $m=2$

$$\frac{\partial^2 T_2}{\partial \eta_1^2} + \frac{\partial^2 T_2}{\partial \eta_2^2} + \gamma_2 \left(\cos \beta(t) \frac{\partial T_0}{\partial \eta_1} - \sin \beta(t) \frac{\partial T_0}{\partial \eta_2} \right) = 0 \quad (21)$$

Equation (20) (i.e. for $m=0$ and $m=1$) is an ordinary Laplace's equation in the domain of $\rho = \eta_1 + i\eta_2$ and the solution is the same as for a homogenous material (e.g, Jain et al. 2006; Chalivendra, 2007). An asymmetric temperature field solution is developed to account for real-time thermal loading situations and the heat flux is assumed to be singular at the crack-tip (Jin and Noda, 1994). The singularity of heat

flux will not affect even if the transient effects are incorporated as the transient terms are of higher order.

For $m=0$

$$T_0 = q_0 \rho^{1/2} \cos \frac{\theta}{2} \quad (22)$$

For $m=1$

$$T_1 = q_1 \rho \sin \theta \quad (23)$$

where $\rho = (\eta_1^2 + \eta_2^2)^{1/2}$

The solution T_2 , for Eq. (21) corresponding to higher powers of ε ($m=2$) has two parts: a homogeneous and a particular solution. The particular solution can be obtained using a recursive approach (e.g., Parmeswaran and Shukla, 1999; Chalivendra et al. 2002; Chalivendra and Shukla, 2005) and the complete solution for Eq. (21) is given below.

$$T_2 = q_2 r^{3/2} \cos \frac{3\theta}{2} + \frac{1}{4} \gamma_2 q_0 r^{3/2} \left(\sin \beta(t) \sin \frac{\theta}{2} - \cos \beta(t) \cos \frac{\theta}{2} \right) \quad (24)$$

Transforming back to the crack-tip coordinates ξ_1 and ξ_2 , the full solution of the temperature field near the crack-tip is given as

$$T = q_0 r^{1/2} \cos \frac{\theta}{2} + q_1 r \sin \theta + q_2 r^{3/2} \cos \frac{3\theta}{2} + \frac{1}{4} \gamma_2 q_0 r^{3/2} \left(\sin \beta(t) \sin \frac{\theta}{2} - \cos \beta(t) \cos \frac{\theta}{2} \right) \quad (25)$$

Alternate temperature fields can be easily derived for the conditions such as singular temperature at the crack-tip.

2.2 Asymptotic Expansion of Crack-tip Stress Fields

Similar to the derivation of the temperature field, the asymptotic approach is again used in deriving the solutions for the displacement potentials for the equations of motion (12a) and (12b). The scaled coordinates, as discussed in Eq. (16), are now applied to equations (12a) and (12b) as given below

$$\begin{aligned}
& \alpha_i^2 \frac{\partial^2 \phi}{\partial \eta_1^2} + \frac{\partial^2 \phi}{\partial \eta_2^2} + \varepsilon \zeta \left(\cos \beta(t) \frac{\partial \phi}{\partial \eta_1} - \sin \beta(t) \frac{\partial \phi}{\partial \eta_2} \right) + \frac{\varepsilon \zeta}{\delta + 2} \left(\sin \beta(t) \frac{\partial \psi}{\partial \eta_1} + \cos \beta(t) \frac{\partial \psi}{\partial \eta_2} \right) - \\
& \frac{\rho_0}{\mu_0 (\delta + 2)} \left((c^2 k^2 \varepsilon^2 \eta_2^2 - 2c^2 k \varepsilon \eta_2) \frac{\partial^2 \phi}{\partial \eta_1^2} + c^2 k^2 \varepsilon^2 \eta_1^2 \frac{\partial^2 \phi}{\partial \eta_2^2} + (2c^2 k \varepsilon \eta_1 - 2c^2 k^2 \varepsilon^2 \eta_1 \eta_2) \frac{\partial^2 \phi}{\partial \eta_1 \partial \eta_2} - \right. \\
& \left. c^2 k^2 \varepsilon^2 \eta_1 \frac{\partial \phi}{\partial \eta_1} + (c^2 k \varepsilon - c^2 k^2 \varepsilon^2 \eta_2) \frac{\partial \phi}{\partial \eta_2} \right) \\
& - \alpha_c \frac{(3\delta + 2)}{\delta + 2} \left(\varepsilon^2 T + \left\{ \varepsilon^3 (2\gamma_1 + \zeta) \Delta^{-1} \left(\cos \beta(t) \frac{\partial T}{\partial \eta_1} - \sin \beta(t) \frac{\partial T}{\partial \eta_2} \right) + \varepsilon^4 (\gamma_1 + \zeta) \gamma_1 \Delta^{-1} T \right\} \right) = 0
\end{aligned} \tag{26a}$$

$$\begin{aligned}
& \alpha_s^2 \frac{\partial^2 \psi}{\partial \eta_1^2} + \frac{\partial^2 \psi}{\partial \eta_2^2} + \varepsilon \zeta \left(\cos \beta(t) \frac{\partial \psi}{\partial \eta_1} - \sin \beta(t) \frac{\partial \psi}{\partial \eta_2} \right) + \varepsilon \zeta \delta \left(\sin \beta(t) \frac{\partial \phi}{\partial \eta_1} + \cos \beta(t) \frac{\partial \phi}{\partial \eta_2} \right) - \\
& \frac{\rho_0}{\mu_0} \left((c^2 k^2 \varepsilon^2 \eta_2^2 - 2c^2 k \varepsilon \eta_2) \frac{\partial^2 \psi}{\partial \eta_1^2} + c^2 k^2 \varepsilon^2 \eta_1^2 \frac{\partial^2 \psi}{\partial \eta_2^2} + (2c^2 k \varepsilon \eta_1 - 2c^2 k^2 \varepsilon^2 \eta_1 \eta_2) \frac{\partial^2 \psi}{\partial \eta_1 \partial \eta_2} - \right. \\
& \left. c^2 k^2 \varepsilon^2 \eta_1 \frac{\partial \psi}{\partial \eta_1} + (c^2 k \varepsilon - c^2 k^2 \varepsilon^2 \eta_2) \frac{\partial \psi}{\partial \eta_2} \right) \\
& - \alpha_c (3\delta + 2) \varepsilon^3 \zeta \Delta^{-1} \left(\sin \beta(t) \frac{\partial T}{\partial \eta_1} + \cos \beta(t) \frac{\partial T}{\partial \eta_2} \right) = 0
\end{aligned} \tag{26b}$$

At this stage, it is assumed that Φ , ψ and T can be represented as a power series expansion in ε .

$$\begin{aligned}
\phi(\xi_1, \xi_2) &= \phi(\varepsilon\eta_1, \varepsilon\eta_2) = \sum_{m=0}^{\infty} \varepsilon^{\frac{m+3}{2}} \phi_m(\eta_1, \eta_2) \\
\psi(\xi_1, \xi_2) &= \psi(\varepsilon\eta_1, \varepsilon\eta_2) = \sum_{m=0}^{\infty} \varepsilon^{\frac{m+3}{2}} \psi_m(\eta_1, \eta_2) \\
T(\xi_1, \xi_2) &= T(\varepsilon\eta_1, \varepsilon\eta_2) = \sum_{m=0}^{\infty} \varepsilon^{\frac{m+1}{2}} q_m(\eta_1, \eta_2)
\end{aligned} \tag{27}$$

As discussed above, the temperature field is obtained by ensuring that the heat flux or the derivative of the temperature field near the crack-tip is singular. This means that the potentials for temperature are one power less than the displacement potentials. Substituting Eq. (27) into Eqs. (26a) and (26b) gives the following equations.

$$\left. \sum_{m=0}^{\infty} \left\{ \begin{aligned} &\varepsilon^{\frac{m+3}{2}} \left(\alpha_1^2 \frac{\partial^2 \phi_m}{\partial \eta_1^2} + \frac{\partial^2 \phi_m}{\partial \eta_2^2} \right) + \varepsilon^{\frac{m+5}{2}} \left[\zeta \left(\cos \beta(t) \frac{\partial \phi_m}{\partial \eta_1} - \sin \beta(t) \frac{\partial \phi_m}{\partial \eta_2} \right) + \right. \\ &\left. \frac{\zeta}{\delta + 2} \left(\sin \beta(t) \frac{\partial \psi_m}{\partial \eta_1} + \cos \beta(t) \frac{\partial \psi_m}{\partial \eta_2} \right) \right] - \\ &\varepsilon^{\frac{m+5}{2}} \left[\frac{\rho_0}{\mu_0(\delta + 2)} \left(-2c^2 k \eta_2 \frac{\partial^2 \phi_m}{\partial \eta_1^2} + 2c^2 k \eta_1 \frac{\partial^2 \phi_m}{\partial \eta_1 \partial \eta_2} + c^2 k \frac{\partial \phi_m}{\partial \eta_2} \right) - \alpha_c \frac{(3\delta + 2)}{\delta + 2} T_m \right] - \\ &\varepsilon^{\frac{m+7}{2}} \left[\frac{\rho_0}{\mu_0(\delta + 2)} \left(\begin{aligned} &c^2 k^2 \eta_2^2 \frac{\partial^2 \phi_m}{\partial \eta_1^2} + c^2 k^2 \eta_1^2 \frac{\partial^2 \phi_m}{\partial \eta_2^2} - 2c^2 k^2 \eta_1 \eta_2 \frac{\partial^2 \phi_m}{\partial \eta_1 \partial \eta_2} - \\ &c^2 k^2 \eta_1 \frac{\partial \phi_m}{\partial \eta_1} - c^2 k^2 \frac{\partial \phi_m}{\partial \eta_2} - \\ &\left(\alpha_c \frac{(3\delta + 2)}{\delta + 2} \right) (2\gamma_1 + \zeta) \Delta^{-1} \left(\cos \beta(t) \frac{\partial T_m}{\partial \eta_1} - \sin \beta(t) \frac{\partial T_m}{\partial \eta_2} \right) \right] \right] \\ &- \varepsilon^{\frac{m+9}{2}} \left[\alpha_c \frac{(3\delta + 2)}{\delta + 2} (\gamma_1 + \zeta) \gamma_1 \Delta^{-1} T_m \right] \end{aligned} \right\} = 0 \end{aligned} \tag{28a}$$

$$\sum_{m=0}^{\infty} \left\{ \begin{array}{l} \varepsilon^{\frac{m+3}{2}} \left(\alpha_s^2 \frac{\partial^2 \psi_m}{\partial \eta_1^2} + \frac{\partial^2 \psi_m}{\partial \eta_2^2} \right) + \varepsilon^{\frac{m+5}{2}} \left[\begin{array}{l} \zeta \left(\cos \beta(t) \frac{\partial \psi_m}{\partial \eta_1} - \sin \beta(t) \frac{\partial \psi_m}{\partial \eta_2} \right) + \\ \zeta \delta \left(\sin \beta(t) \frac{\partial \phi_m}{\partial \eta_1} + \cos \beta(t) \frac{\partial \phi_m}{\partial \eta_2} \right) \\ - \frac{\rho_0}{\mu_0} \left(-2c^2 k \eta_2 \frac{\partial^2 \psi_m}{\partial \eta_1^2} + 2c^2 k \eta_1 \frac{\partial^2 \psi_m}{\partial \eta_1 \partial \eta_2} + c^2 k \frac{\partial \psi_m}{\partial \eta_2} \right) \end{array} \right] \\ - \varepsilon^{\frac{m+7}{2}} \left[\begin{array}{l} \frac{\rho_0}{\mu_0} \left(c^2 k^2 \eta_2^2 \frac{\partial^2 \psi_m}{\partial \eta_1^2} + c^2 k^2 \eta_1^2 \frac{\partial^2 \psi_m}{\partial \eta_2^2} - 2c^2 k^2 \eta_1 \eta_2 \frac{\partial^2 \psi_m}{\partial \eta_1 \partial \eta_2} - c^2 k^2 \eta_1 \frac{\partial \psi_m}{\partial \eta_1} - \right. \\ \left. - c^2 k^2 \frac{\partial \psi_m}{\partial \eta_2} \right) \\ - \alpha_c (3\delta + 2) \zeta \Delta^{-1} \left(\sin \beta(t) \frac{\partial T}{\partial \eta_{1m}} + \cos \beta(t) \frac{\partial T_m}{\partial \eta_2} \right) \end{array} \right] \end{array} \right\} = 0 \quad (28b)$$

For Eqs. (28a) and (28b) to be valid, the partial differential equations corresponding to each power of ε ($\varepsilon^{3/2}$, ε^2 , $\varepsilon^{5/2}$, ...) should vanish independently. This leads to the following set of partial differential equations.

For $m = 0$ and $m = 1$,

$$\alpha_l^2 \frac{\partial^2 \phi_m}{\partial \eta_1^2} + \frac{\partial^2 \phi_m}{\partial \eta_2^2} = 0 \quad (29a)$$

$$\alpha_s^2 \frac{\partial^2 \psi_m}{\partial \eta_1^2} + \frac{\partial^2 \psi_m}{\partial \eta_2^2} = 0 \quad (29b)$$

For $m = 2$

$$\alpha_l^2 \frac{\partial^2 \phi_2}{\partial \eta_1^2} + \frac{\partial^2 \phi_2}{\partial \eta_2^2} = -\zeta \left(\cos \beta(t) \frac{\partial \phi_0}{\partial \eta_1} - \sin \beta(t) \frac{\partial \phi_0}{\partial \eta_2} \right) - \frac{\zeta}{\delta + 2} \left(\sin \beta(t) \frac{\partial \psi_0}{\partial \eta_1} + \cos \beta(t) \frac{\partial \psi_0}{\partial \eta_2} \right) + \quad (30a)$$

$$\frac{\rho_0}{\mu_0 (\delta + 2)} \left(-2c^2 k \eta_2 \frac{\partial^2 \phi_0}{\partial \eta_1^2} + 2c^2 k \eta_1 \frac{\partial^2 \phi_0}{\partial \eta_1 \partial \eta_2} + c^2 k \frac{\partial \phi_0}{\partial \eta_2} \right) + \alpha_c \frac{(3\delta + 2)}{\delta + 2} T_0$$

$$\alpha_s^2 \frac{\partial^2 \psi_2}{\partial \eta_1^2} + \frac{\partial^2 \psi_2}{\partial \eta_2^2} = -\zeta \left(\cos \beta(t) \frac{\partial \psi_0}{\partial \eta_1} - \sin \beta(t) \frac{\partial \psi_0}{\partial \eta_2} \right) - \zeta \delta \left(\sin \beta(t) \frac{\partial \phi_0}{\partial \eta_1} + \cos \beta(t) \frac{\partial \phi_0}{\partial \eta_2} \right) + \frac{\rho_0}{\mu_0} \left(-2c^2 k \eta_2 \frac{\partial^2 \psi_0}{\partial \eta_1^2} + 2c^2 k \eta_1 \frac{\partial^2 \psi_0}{\partial \eta_1 \partial \eta_2} + c^2 k \frac{\partial \psi_0}{\partial \eta_2} \right) \quad (30b)$$

Eqs. (29a) and (29b) are similar to those for a homogeneous material where the partial differential equations (30a) and (30b), associated with the higher powers of ε are coupled to the differentials of the lower order functions through the non-homogeneity parameters ζ and temperature term. Eqs. (29a) and (29b) (i.e. for $m=0$ and $m=1$) can be easily reduced to Laplace's equation in the respective complex domains $\zeta_l = \eta_1 + i\alpha_l \eta_2$, $\zeta_s = \eta_1 + i\alpha_s \eta_2$ $i = \sqrt{-1}$ and the solutions are the same as those for homogenous material (eg., Freund, 1990; Gu and Asaro, 1997; Irwin; Shukla and Jain, 2004), and can be written as

$$\begin{aligned} \phi_m(\rho_l, \theta_l, t) &= A_m \rho_l^{(m+3)/2} \cos \frac{1}{2}(m+3)\theta_l + C_m \rho_l^{(m+3)/2} \sin \frac{1}{2}(m+3)\theta_l \\ \psi_m(\rho_s, \theta_s, t) &= B_m \rho_s^{(m+3)/2} \sin \frac{1}{2}(m+3)\theta_s + D_m \rho_s^{(m+3)/2} \cos \frac{1}{2}(m+3)\theta_s \end{aligned} \quad (31)$$

where

$$\rho_l = \left[\eta_1^2 + \alpha_l^2 \eta_2^2 \right]^{1/2}, \tan \theta_l = \frac{\alpha_l \eta_2}{\eta_1}, \rho_s = \left[\eta_1^2 + \alpha_s^2 \eta_2^2 \right]^{1/2}, \tan \theta_s = \frac{\alpha_s \eta_2}{\eta_1},$$

and A_m , C_m , B_m and D_m are real constants.

Using the definition of the dynamic stress intensity factor K_{ID} and K_{IID} for the opening mode and shear mode (Chalivendra, 2007), the relation between A_o and K_{ID} and C_o and K_{IID} are obtained.

$$A_0 = \frac{4(1 + \alpha_s^2)}{3(4\alpha_l\alpha_s - (1 + \alpha_s^2)^2)} \frac{K_{ID}}{\mu_c \sqrt{2\pi}}, \quad (32)$$

$$C_0 = \frac{8\alpha_s}{3(4\alpha_l\alpha_s - (1 + \alpha_s^2)^2)} \frac{K_{IID}}{\mu_c \sqrt{2\pi}}, \quad (33)$$

where μ_c is the crack-tip shear modulus, K_{ID} and K_{IID} are the mode-I and mode-II dynamic stress intensity factors, respectively.

Now, considering the crack face boundary conditions, $\sigma_{22} = 0$ and $\sigma_{12} = 0$ we can also obtain the following relationship between A_o , B_o , C_o and D_o

$$B_o = \frac{-2\alpha_l}{1 + \alpha_s^2} A_o \quad (34)$$

$$D_o = \frac{1 + \alpha_s^2}{2\alpha_s} C_o \quad (35)$$

$$\begin{aligned} \phi_2 = & \rho_l^{5/2} \left(A_2 \cos \frac{5\theta_l}{2} + C_2 \sin \frac{5\theta_l}{2} \right) - \frac{1}{4} \frac{\zeta \cos \beta(t)}{\alpha_l^2} \rho_l^{5/2} \left(A_0 \cos \frac{\theta_l}{2} + C_0 \sin \frac{\theta_l}{2} \right) \\ & + \frac{1}{4} \frac{\zeta \sin \beta(t)}{\alpha_l} \rho_l^{5/2} \left(-A_0 \sin \frac{\theta_l}{2} + C_0 \cos \frac{\theta_l}{2} \right) - \frac{2}{5} \frac{\zeta}{\delta + 2} \frac{\sin \beta(t)}{\alpha_l^2 - \alpha_s^2} \rho_s^{5/2} \left(B_0 \sin \frac{5\theta_s}{2} + D_0 \cos \frac{5\theta_s}{2} \right) \\ & - \frac{2}{5} \frac{\zeta}{\delta + 2} \frac{\alpha_s \cos \beta(t)}{\alpha_l^2 - \alpha_s^2} \rho_s^{5/2} \left(B_0 \cos \frac{5\theta_s}{2} - D_0 \sin \frac{5\theta_s}{2} \right) + \frac{1}{4} \frac{\rho_0}{\mu_0} \frac{1}{\delta + 2} \frac{c^2 k}{\alpha_l} \rho_l^{5/2} \left(-A_0 \sin \frac{\theta_l}{2} + C_0 \cos \frac{\theta_l}{2} \right) \\ & - \frac{1}{16} \frac{\rho_0}{\mu_0} \frac{1}{\delta + 2} \frac{c^2 k}{\alpha_l^3} \rho_l^{5/2} \left(A_0 \left[3 \sin \frac{3\theta_l}{2} + 2 \sin \frac{\theta_l}{2} \right] - C_0 \left[2 \cos \frac{\theta_l}{2} - 3 \cos \frac{3\theta_l}{2} \right] \right) \\ & + \frac{1}{16} \frac{\rho_0}{\mu_0} \frac{1}{\delta + 2} \frac{c^2 k}{\alpha_l} \rho_l^{5/2} \left(A_0 \left[3 \sin \frac{3\theta_l}{2} - 2 \sin \frac{\theta_l}{2} \right] + C_0 \left[2 \cos \frac{\theta_l}{2} + 3 \cos \frac{3\theta_l}{2} \right] \right) \\ & + \frac{4}{15} \frac{3\delta + 2}{\delta + 2} \frac{\alpha_c}{\alpha_l^2 - 1} q_0 \rho^{5/2} \cos \left(\frac{5}{2} \theta \right) \end{aligned} \quad (36a)$$

In order to extract both mode-I and mode-II stress intensity factors accurately from the

experimental data when the crack-tip stress field is non-homogenous around the crack-tip due to imposed thermal fields and material non-homogeneity, higher-order stress-field equations are essential in addition to the leading terms and T-stress (non-singular stress). The solution for the equations (30a) and (30b), corresponding to higher powers of ε ($m = 2$), consists of two parts: a solution for the homogeneous equation and a particular solution due to non-homogeneity and temperature and these can be obtained recursively (eg., Parmeswaran and Shukla, 1999; Chalivendra et al. 2002; Chalivendra and Shukla, 2005). The solutions ϕ_2 and ψ_2 obtained are given below. The solutions for ϕ_0 , ψ_0 , ϕ_1 and ψ_1 automatically satisfy the compatibility equations because these solutions are the same as those for homogeneous materials. Since the non-homogeneous specific parts of ϕ_2 and ψ_2 are obtained from ϕ_0 and ψ_0 , they also automatically satisfy the compatibility equations

$$\begin{aligned}
\psi_2 = & \rho_s^{5/2} \left(B_2 \sin \frac{5\theta_s}{2} + D_2 \cos \frac{5\theta_s}{2} \right) - \frac{1}{4} \frac{\zeta \cos \beta(t)}{\alpha_s^2} \rho_s^{5/2} \left(B_0 \sin \frac{\theta_s}{2} + D_0 \cos \frac{\theta_s}{2} \right) \\
& + \frac{1}{4} \frac{\zeta \sin \beta(t)}{\alpha_s} \rho_s^{5/2} \left(B_0 \cos \frac{\theta_s}{2} - D_0 \sin \frac{\theta_s}{2} \right) + \frac{2}{5} \frac{\zeta \delta \sin \beta(t)}{\alpha_i^2 - \alpha_s^2} \rho_i^{5/2} \left(A_0 \cos \frac{5\theta_l}{2} + C_0 \sin \frac{5\theta_l}{2} \right) \\
& + \frac{2}{5} \zeta \delta \frac{\alpha_i \cos \beta(t)}{\alpha_i^2 - \alpha_s^2} \rho_i^{5/2} \left(-A_0 \sin \frac{5\theta_l}{2} + C_0 \cos \frac{5\theta_l}{2} \right) + \frac{1}{4} \frac{\rho_0 c^2 k}{\mu_0 \alpha_s} \rho_s^{5/2} \left(B_0 \cos \frac{\theta_s}{2} - D_0 \sin \frac{\theta_s}{2} \right) \\
& - \frac{1}{16} \frac{\rho_0 c^2 k}{\mu_0 \alpha_s^3} \rho_s^{5/2} \left(B_0 \left[3 \cos \frac{3\theta_s}{2} - 2 \cos \frac{\theta_s}{2} \right] + D_0 \left[3 \sin \frac{3\theta_s}{2} + 2 \sin \frac{\theta_s}{2} \right] \right) \\
& + \frac{1}{16} \frac{\rho_0 c^2 k}{\mu_0 \alpha_s} \rho_s^{5/2} \left(B_0 \left[2 \cos \frac{\theta_s}{2} + 3 \cos \frac{3\theta_s}{2} \right] + D_0 \left[3 \sin \frac{3\theta_s}{2} - 2 \sin \frac{\theta_s}{2} \right] \right)
\end{aligned}$$

(36b)

$$\begin{aligned}
\phi = & r_l^{3/2} \left(A_0 \cos \frac{3}{2} \theta_l + C_0 \sin \frac{3}{2} \theta_l \right) + r_l^2 (A_1 \cos 2\theta_l + C_1 \sin 2\theta_l) + r_l^{5/2} \left(A_2 \cos \frac{5\theta_l}{2} + C_2 \sin \frac{5\theta_l}{2} \right) \\
& - \frac{1}{4} \frac{\zeta \cos \beta(t)}{\alpha_l^2} r_l^{5/2} \left(A_0 \cos \frac{\theta_l}{2} + C_0 \sin \frac{\theta_l}{2} \right) + \frac{1}{4} \frac{\zeta \sin \beta(t)}{\alpha_l} r_l^{5/2} \left(-A_0 \sin \frac{\theta_l}{2} + C_0 \cos \frac{\theta_l}{2} \right) \\
& - \frac{2}{5} \frac{\zeta \sin \beta(t)}{\delta + 2} \frac{r_s^{5/2}}{\alpha_l^2 - \alpha_s^2} \left(B_0 \sin \frac{5\theta_s}{2} + D_0 \cos \frac{5\theta_s}{2} \right) - \frac{2}{5} \frac{\zeta \alpha_s \cos \beta(t)}{\delta + 2} \frac{r_s^{5/2}}{\alpha_l^2 - \alpha_s^2} \left(B_0 \cos \frac{5\theta_s}{2} - D_0 \sin \frac{5\theta_s}{2} \right) \\
& + \frac{1}{4} \frac{\rho_0}{\mu_0} \frac{1}{\delta + 2} \frac{c^2 k}{\alpha_l} r_l^{5/2} \left(-A_0 \sin \frac{\theta_l}{2} + C_0 \cos \frac{\theta_l}{2} \right) \\
& - \frac{1}{16} \frac{\rho_0}{\mu_0} \frac{1}{\delta + 2} \frac{c^2 k}{\alpha_l^3} r_l^{5/2} \left(A_0 \left[3 \sin \frac{3\theta_l}{2} + 2 \sin \frac{\theta_l}{2} \right] - C_0 \left[2 \cos \frac{\theta_l}{2} - 3 \cos \frac{3\theta_l}{2} \right] \right) \\
& + \frac{1}{16} \frac{\rho_0}{\mu_0} \frac{1}{\delta + 2} \frac{c^2 k}{\alpha_l} r_l^{5/2} \left(A_0 \left[3 \sin \frac{3\theta_l}{2} - 2 \sin \frac{\theta_l}{2} \right] + C_0 \left[2 \cos \frac{\theta_l}{2} + 3 \cos \frac{3\theta_l}{2} \right] \right) \\
& + \frac{4}{15} \frac{3\delta + 2}{\delta + 2} \frac{\alpha_c}{\alpha_l^2 - 1} q_0 r^{5/2} \cos \left(\frac{5}{2} \theta \right)
\end{aligned} \tag{37a}$$

By assembling together the above result for the first few terms and by transforming it back into the $\xi_1 - \xi_2$ plane, the combined solution can be written for ϕ and ψ as Eq. (37a and 37b),

$$\begin{aligned}
\psi = & r_s^{3/2} \left(B_0 \sin \frac{3}{2} \theta_s + D_0 \cos \frac{3}{2} \theta_s \right) + r_s^2 (B_1 \sin 2\theta_s + D_1 \cos 2\theta_s) + r_s^{5/2} \left(B_2 \sin \frac{5\theta_s}{2} + D_2 \cos \frac{5\theta_s}{2} \right) \\
& - \frac{1}{4} \frac{\zeta \cos \beta(t)}{\alpha_s^2} r_s^{5/2} \left(B_0 \sin \frac{\theta_s}{2} + D_0 \cos \frac{\theta_s}{2} \right) + \frac{1}{4} \frac{\zeta \sin \beta(t)}{\alpha_s} r_s^{5/2} \left(B_0 \cos \frac{\theta_s}{2} - D_0 \sin \frac{\theta_s}{2} \right) \\
& + \frac{2}{5} \frac{\zeta \delta \sin \beta(t)}{\alpha_l^2 - \alpha_s^2} r_l^{5/2} \left(A_0 \cos \frac{5\theta_l}{2} + C_0 \sin \frac{5\theta_l}{2} \right) + \frac{2}{5} \zeta \delta \frac{\alpha_l \cos \beta(t)}{\alpha_l^2 - \alpha_s^2} r_l^{5/2} \left(-A_0 \sin \frac{5\theta_l}{2} + C_0 \cos \frac{5\theta_l}{2} \right) \\
& + \frac{1}{4} \frac{\rho_0}{\mu_0} \frac{c^2 k}{\alpha_s} r_s^{5/2} \left(B_0 \cos \frac{\theta_s}{2} - D_0 \sin \frac{\theta_s}{2} \right) \tag{37b} \\
& - \frac{1}{16} \frac{\rho_0}{\mu_0} \frac{c^2 k}{\alpha_s^3} r_s^{5/2} \left(B_0 \left[3 \cos \frac{3\theta_s}{2} - 2 \cos \frac{\theta_s}{2} \right] + D_0 \left[3 \sin \frac{3\theta_s}{2} + 2 \sin \frac{\theta_s}{2} \right] \right) \\
& + \frac{1}{16} \frac{\rho_0}{\mu_0} \frac{c^2 k}{\alpha_s} r_s^{5/2} \left(B_0 \left[2 \cos \frac{\theta_s}{2} + 3 \cos \frac{3\theta_s}{2} \right] + D_0 \left[3 \sin \frac{3\theta_s}{2} - 2 \sin \frac{\theta_s}{2} \right] \right)
\end{aligned}$$

where $r_l = \left(\xi_1^2 + \alpha_l^2 \xi_2^3 \right)^{1/2}$, $\tan \theta_l = \frac{\alpha_l \xi_2}{\xi_1}$, $r_s = \left(\xi_1^2 + \alpha_s^2 \xi_1 \right)^{1/2}$, $\tan \theta_s = \frac{\alpha_s \xi_2}{\xi_1}$

The above definitions of the displacement potentials are now used in Eq. (4) to obtain the displacements fields. These displacement fields are then used to develop strain fields. These strain fields and Eq. (25) are substituted into Eq. (3) to obtain in-plane steady state stress fields around the crack-tip as given by Eq. (38).

$$\sigma_{ij} = \frac{(K_{I_d}, K_{II_d})}{(2\pi r)^{1/2}} F_{ij}(r, \theta, T, \xi, \gamma_1, \gamma_2, c, k, \beta, \dot{\beta}) \quad (38)$$

where σ_{ij} are stress components, T represents the change in temperature in the infinite medium ξ , γ_1 and γ_2 are non-homogeneity constants that have the dimension (length)⁻¹, c is the crack-tip speed, k is the curvature of the crack trajectory at crack-tip, β is the angle between ξ_1 -axis and the fixed x -axis as shown in Fig.1, $\dot{\beta}$ is the angular velocity as referred in Eq. (7).

3. Results and Discussion

The thermo-mechanical stress fields developed above are used to study the effect of temperature field, curvature of the crack path, crack-tip velocity, and the non-homogeneity on the variation of the maximum shear stress, the circumferential stress, maximum principal stress and the crack kinking angle at the crack-tip. The coefficient of thermal expansion (α_c) of ZrB_2 (which is of interest in our experimental research), $5.9 \times 10^{-6}/^\circ\text{C}$ is used in the analysis. It is assumed that the resulting temperature range generates elastic deformation around the crack-tip. Some of the terms associated with non-homogeneity and the stress field connected with temperature change impose normal and shear stresses on traction free crack faces. The presence of these normal and shear stresses on the crack face violates one of the boundary conditions and these

stresses need to be removed. The removal of these stresses from the crack face is accomplished by superimposing an equal and opposite stress field on the crack face. In particular each point on the crack face is subjected to a line load of specific magnitude such that the normal stresses from the crack face are removed. Jian et al. (1991) proposed a solution for a single line load to derive the stress field around the crack-tip and the solution is extended for multiple line loads applied on the crack face line. The revised in-plane stress-fields which have traction-free crack face conditions were then used in developing various results discussed in section 3.1. In the present analysis, since the stress fields are determined closer to the crack tip, the higher order temperature terms are neglected. The higher order temperature terms can be used when determining stress fields far away from the crack-tip in analyzing the experimental data. When the temperature coefficients and the non-homogeneity factors are set to zero, these equations fall down to the equations derived by Liu and Rosakis. The present analysis assumed constant velocity at the crack-tip. Even though the crack-tip acceleration is an important condition to consider, the stress fields may not significantly be affected by the acceleration terms as the acceleration terms will only appear in the higher order terms

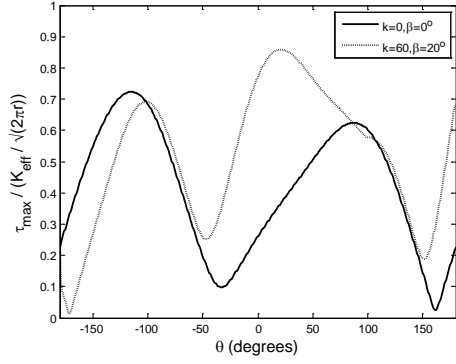
The material properties and fracture parameters of ZrB_2 are used in generating the plots and the properties can be found from Fahrenholtz et al. (2007). The properties are as follows: Poisson's ratio (ν) = 0.16, shear modulus at the crack-tip (μ_c) = 210GPa, density at the crack-tip (ρ_c) = 6119 kg/m^3 , crack-tip velocity c/c_s = 0.5, $K_{ID} = 5 \text{ MPa}\cdot\text{m}^{1/2}$, $K_{IID} = 0.2K_{ID}$, $K_{eff} = \sqrt{K_{ID}^2 + K_{IID}^2}$, $k = 20 \text{ rad/m}$, $\beta = 20^\circ$,

$q_o = 100 \text{ }^\circ\text{C}/\text{m}^{1/2}$, $\gamma_2 = 1$ and a typical value of radius, $r = 0.002\text{m}$. The choice of stress intensity factor is motivated by the fact that ceramics have low fracture toughness and they often form a part of FGM's. At this point, it is also important to mention that the relative dominance of the temperature or mechanical field will depend on the choice of K and q_o values.

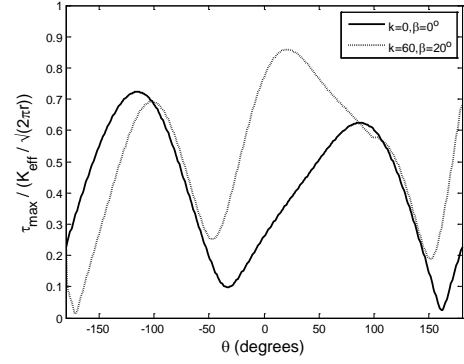
3.1 Variation of Stress Components near the Crack-tip

3.1.1 Effect of Curvature of the Crack path

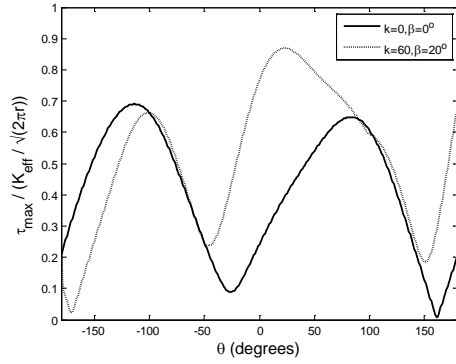
Three major stress components were considered to show the variation of stress fields under steady state thermo-mechanical loading: maximum shear stress, circumferential tensile stress and maximum principal stress. These stresses are normalized using $K_{eff} / \sqrt{2\pi r}$ and plotted as a function of θ (angle) around the crack-tip. The variation of normalized maximum shear stress as a function of curvature for both homogenous and FGM systems ($\zeta = 1$ and $\zeta = -1$) with and without the temperature field is shown in Fig. 2. The value of $\zeta = 1$ denotes the increasing shear and mass density ahead of the crack tip and $\zeta = -1$ denotes the reverse situation. The nature of the variation of the normalized shear stress changes significantly with the incorporation of curvature parameters but no significant variation was observed for different non-homogeneity values. For all the cases [(a) – (f)], when the curvature is introduced, the peak value of the maximum shear stress and the angle at which the maximum shear stress occurs changes significantly.



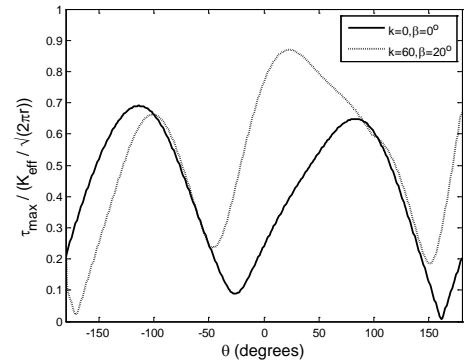
(a) Without temperature ($q_0 = 0, \zeta = 0$)



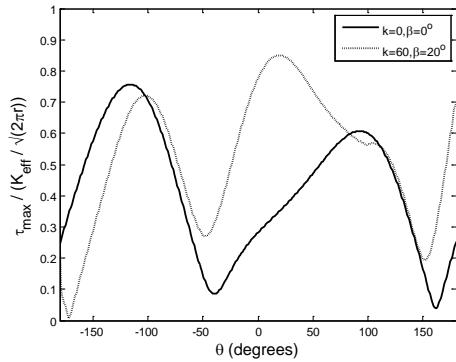
(b) With temperature ($q_0 = 100^0 C / m^{1/2}, \zeta = 0$)



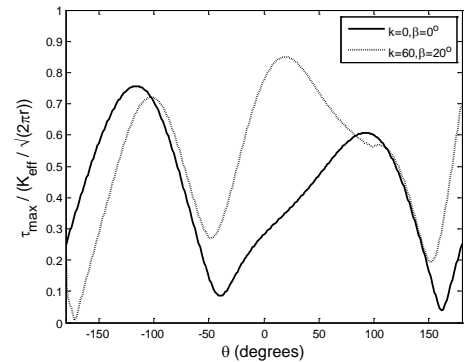
(c) Without temperature ($q_0 = 0, \zeta = 1$)



(d) With temperature ($q_0 = 100^0 C / m^{1/2}, \zeta = 1$)

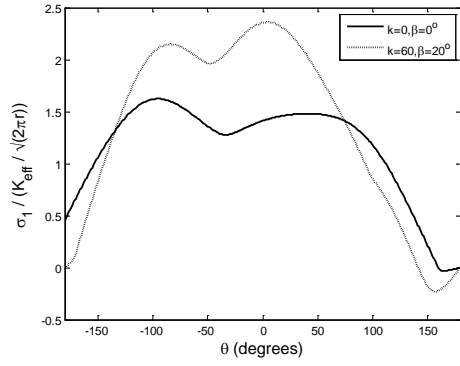


(e) Without temperature ($q_0 = 0, \zeta = -1$)

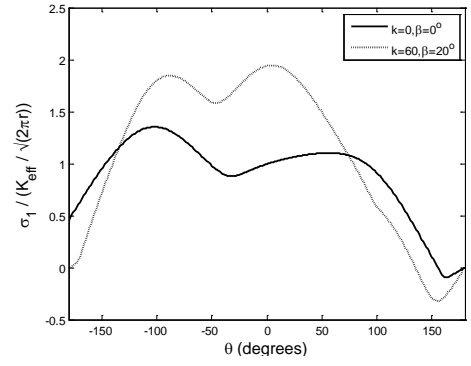


(f) With temperature ($q_0 = 100^0 C / m^{1/2}, \zeta = -1$)

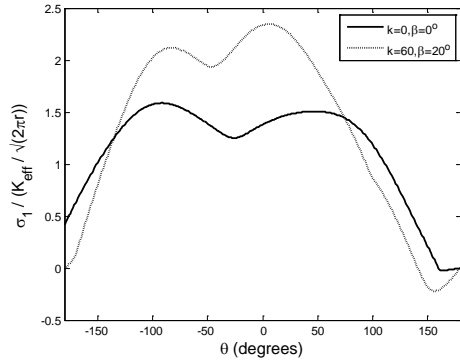
Fig. 2 Comparison of normalized maximum shear stress for a straight and curved crack around the crack-tip for a mixed-mode loading in an FGM with and without temperature field ($K_{II}/K_I = 0.2, c/c_s = 0.5, \gamma_2 = 1, r = 0.002m$).



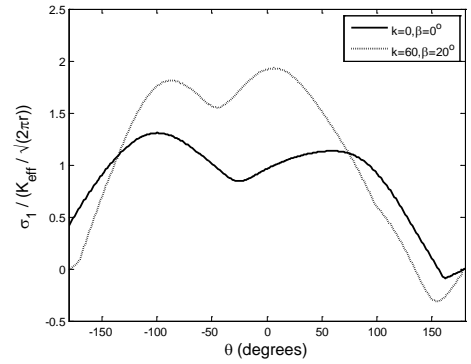
(a) Without temperature ($q_0 = 0, \zeta = 0$)



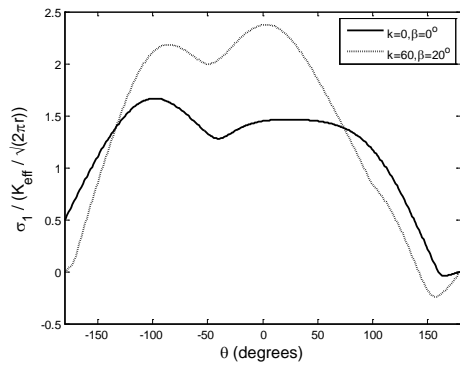
(b) With temperature ($q_0 = 100^0 C / m^{1/2}, \zeta = 0$)



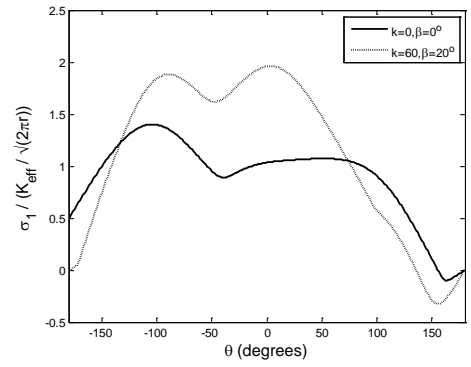
(c) Without temperature ($q_0 = 0, \zeta = 1$)



(d) With temperature ($q_0 = 100^0 C / m^{1/2}, \zeta = 1$)

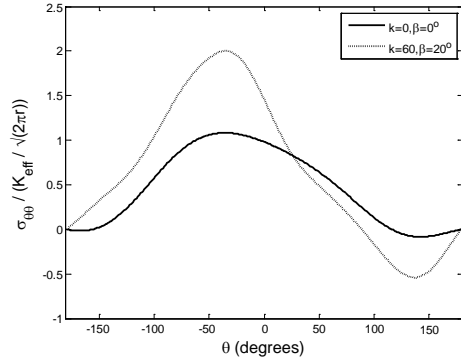


(e) Without temperature ($q_0 = 0, \zeta = -1$)

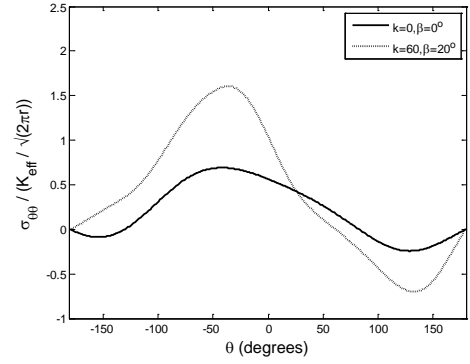


(f) With temperature ($q_0 = 100^0 C / m^{1/2}, \zeta = -1$)

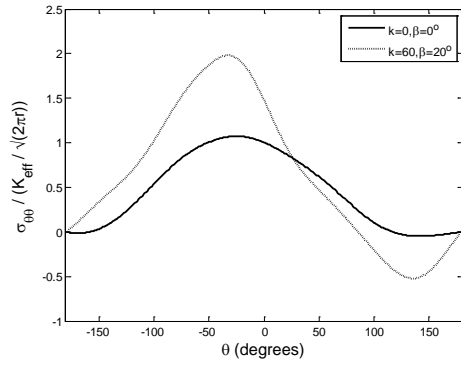
Fig. 3 Comparison of normalized maximum principal stress for a straight and curved crack around the crack-tip for a mixed-mode loading in an FGM with and without temperature field ($K_{IID}/K_{ID} = 0.2, c/c_s = 0.5, \gamma_2 = 1, r = 0.002m$).



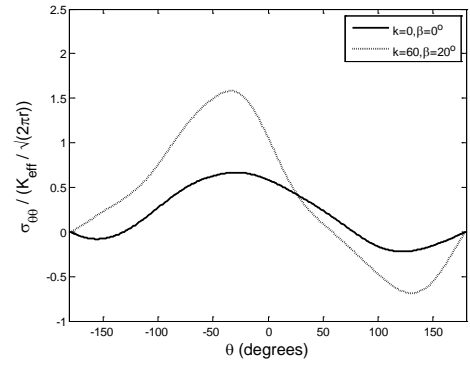
(a) Without temperature ($q_0 = 0, \zeta = 0$)



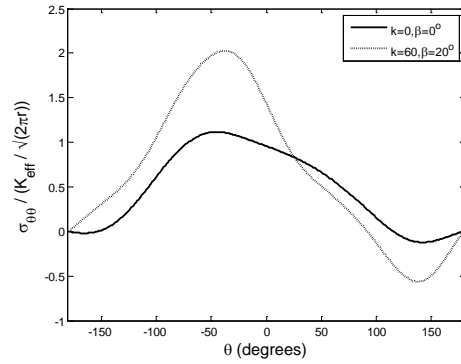
(b) With temperature ($q_0 = 100^0 C / m^{1/2}, \zeta = 0$)



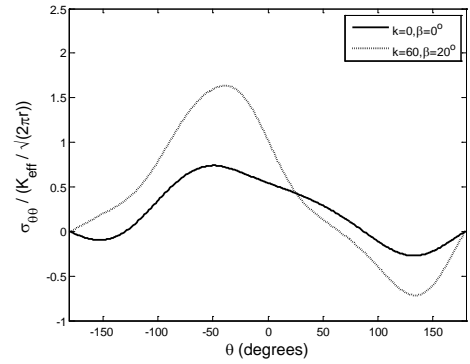
(c) Without temperature ($q_0 = 0, \zeta = 1$)



(d) With temperature ($q_0 = 100^0 C / m^{1/2}, \zeta = 1$)

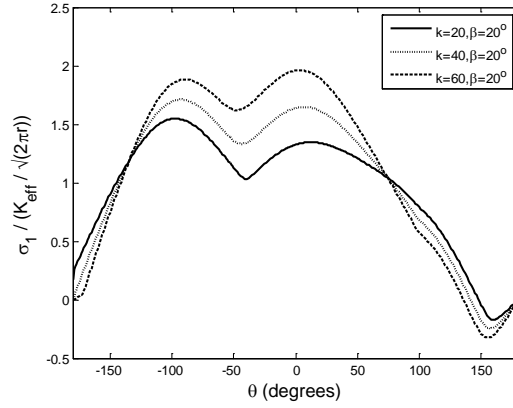


(e) Without temperature ($q_0 = 0, \zeta = -1$)

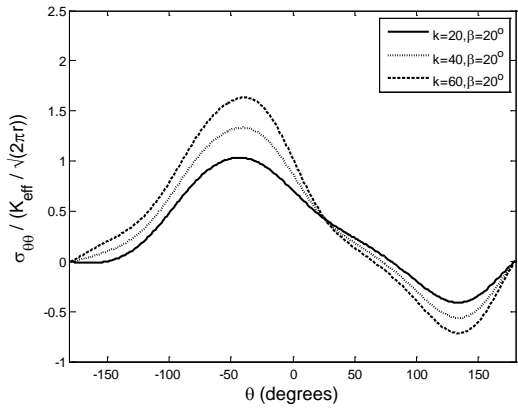


(f) With temperature ($q_0 = 100^0 C / m^{1/2}, \zeta = -1$)

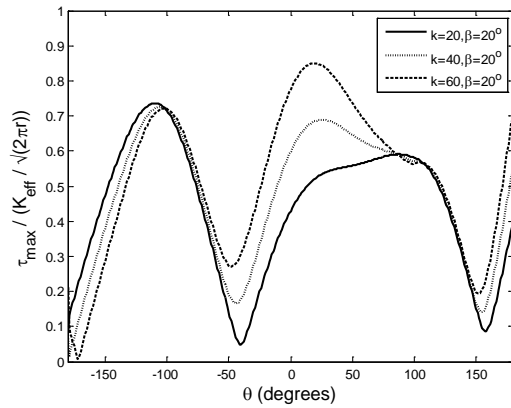
Fig. 4 Comparison of normalized maximum circumferential stress for a straight and curved crack around the crack-tip for a mixed-mode loading in an FGM with and without temperature field ($K_{II D} / K_{I D} = 0.2, c / c_s = 0.5, \gamma_2 = 1, r = 0.002m$).



(a) Maximum principal stress



(b) Circumferential tensile stress



(c) Maximum shear stress

Fig. 5 Effect of curvature on normalized (a) maximum principal stress, (b) the circumferential tensile stress, and (c) maximum shear stress around the crack–tip for a mixed-mode loading in an FGM with temperature field ($K_{II D}/K_{I D} = 0.2, c/c_s = 0.5, \gamma_2 = 1, \zeta = -1, q_0 = 100, r = 0.002\text{m}$).

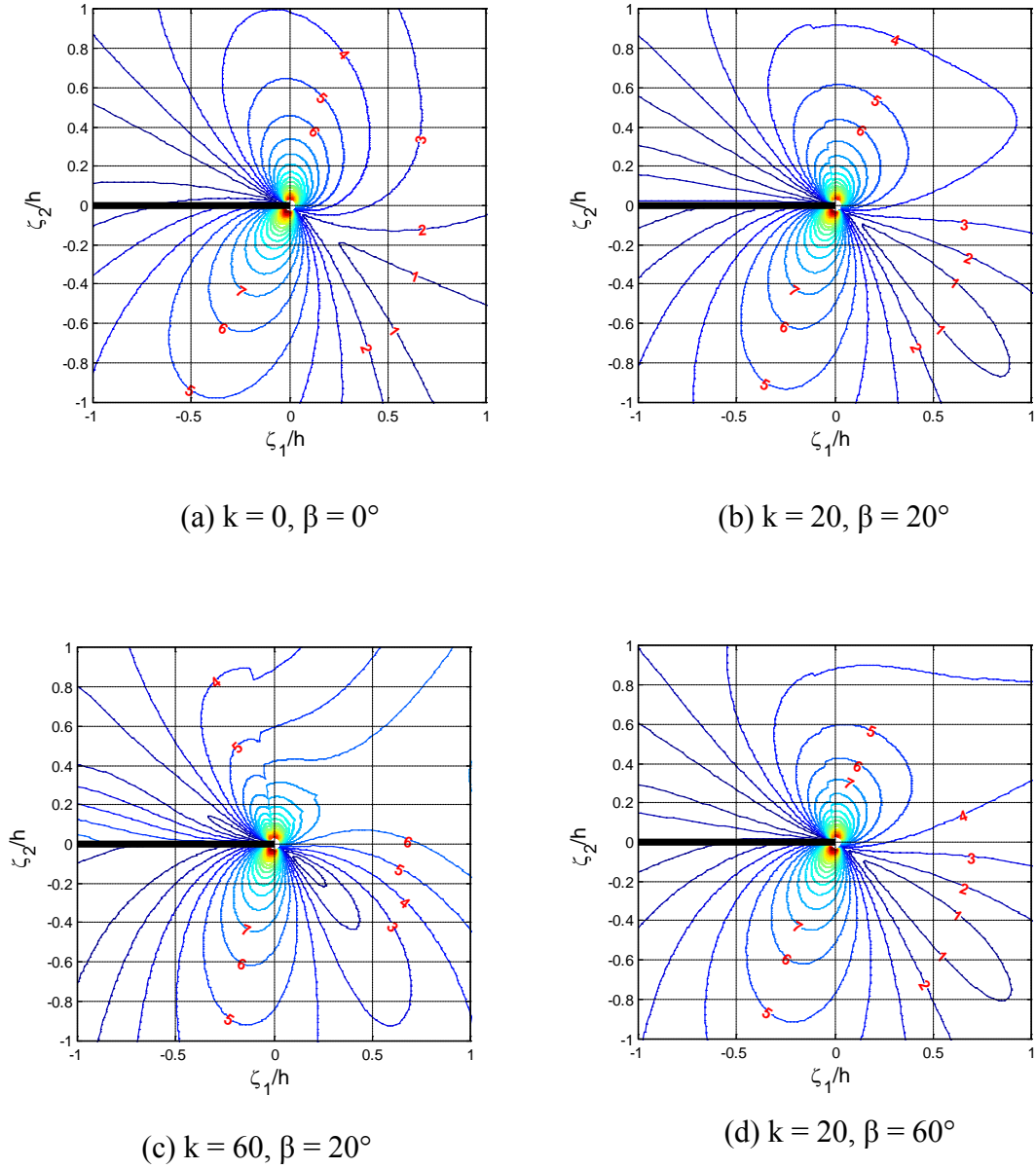


Fig. 6 Effect of curvature parameters on the contours of maximum shear stress around the crack–tip for a mixed-mode loading in an FGM with no temperature field ($K_{II}/K_I = 0.2$, $c/c_s = 0.5$, $\zeta = -1$).

Angular variation of the normalized maximum principal stress and circumferential tensile stress as a function of curvature with and without the temperature field is plotted in Fig. 3 and Fig. 4 respectively. The peak value of the principal and circumferential tensile stresses increase significantly when the curvature is introduced for both homogeneous and FGM systems and the increase in peak value of these stresses is approximately 50% higher for the case of a curved crack. Also the angle at which the peak values of these stresses occur changes slightly with the addition of the curvature parameters. As observed in the Fig. 2 and Fig. 3, the nature of variation of these normalized stresses changes significantly with the addition of curvature terms.

The angular variation of all three of the above normalized stress components for a fixed value of the non-homogeneity parameter, $\zeta = -1$, as a function of curvature with temperature field are shown in Fig.5. As the local curvature of the crack path (k) increases, the peak values of these stresses increase while the angle at which the peak value of these stresses occur changes slightly for all the cases.

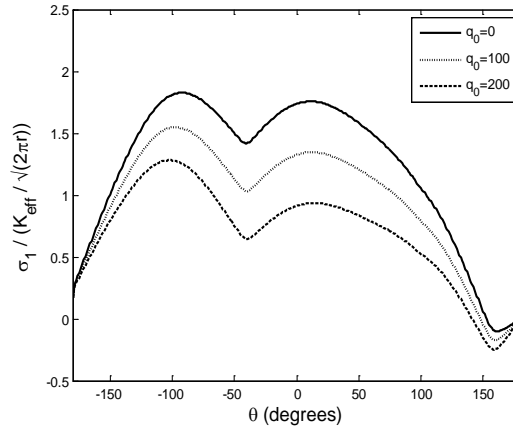
Fig. 6 shows the effect of the curvature on the contours of the maximum shear stress around the crack-tip with no temperature field for a mixed-mode loading in an FGM of $\zeta = -1$ for four different curvature conditions. In Fig. 6(a), when curvature parameters are set to zero, standard asymmetric contours of mixed-mode loading as reported in literature, are obtained. The effect of curvature under mixed-mode loading is brought into effect in Fig. 6(b) by considering $k = 20$, $\beta = 20^\circ$, and the figure shows that the number and size of the shear stress contours increases with the addition of curvature terms. If the angle between ξ_1 -axis and the fixed x -axis is kept

constant ($\beta = 20^\circ$) and the curvature is changed by three times as shown in Fig 6(c), the shear stress increases significantly and the stress contours tilt away from the crack direction. However, if we keep the curvature value constant at $k = 20$ and change the angle β to 60° , the shear stress contours tilt towards the crack direction, but there is no significant change in the size of shear stress contours. Hence, for cases discussed in the following sections, a typical value of $\beta = 20^\circ$ is used in further analysis.

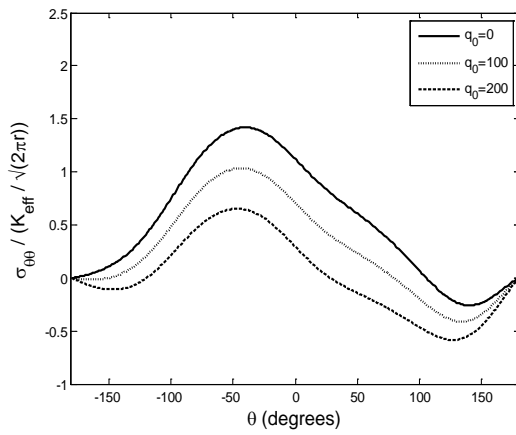
3.1.2 Effect of Temperature

Variation of the normalized maximum principal stress, circumferential stress and the maximum shear stress, is plotted around the crack-tip for different temperature gradients ($q_0 = 0$, $q_0 = 100$ and $q_0 = 200$) as shown in Fig. 7. As the temperature gradient increases, the peak value of both the normalized maximum principal stress and circumferential tensile stress decreases and the angles at which the peak value of these stresses occur change slightly for different temperature gradients. In the case of the maximum shear stress, there is no change in the stress values for different temperature gradients. This is due to the fact that the temperature field gets cancelled when σ_{yy} was subtracted from σ_{xx} as shown in below Eq. 39 and there are no temperature terms in τ_{xy} (Refer Eq. 3c).

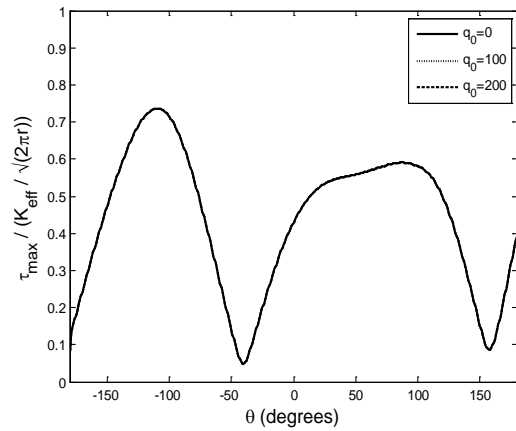
$$\tau_{\max} = \left(\left(\frac{\sigma_{xx} - \sigma_{yy}}{2} \right)^2 + \sigma_{xy}^2 \right)^{(1/2)} \quad (39)$$



(a) Maximum principal stress



(b) Circumferential tensile stress



(c) Maximum shear stress

Fig. 7 Variation of normalized (a) maximum principal stress, (b) the circumferential tensile stress, and (c) maximum shear stress around the crack-tip for a mixed-mode thermo-mechanical loading in an FGM for several values of temperature coefficients ($K_{II D}/K_{I D}=0.2$, $c/c_s=0.5$, $\gamma_2=1$, $\zeta=-1$, $k=20$, $\beta=20^\circ$, $r=0.002\text{m}$).

3.1.3 Effect of Non homogeneity

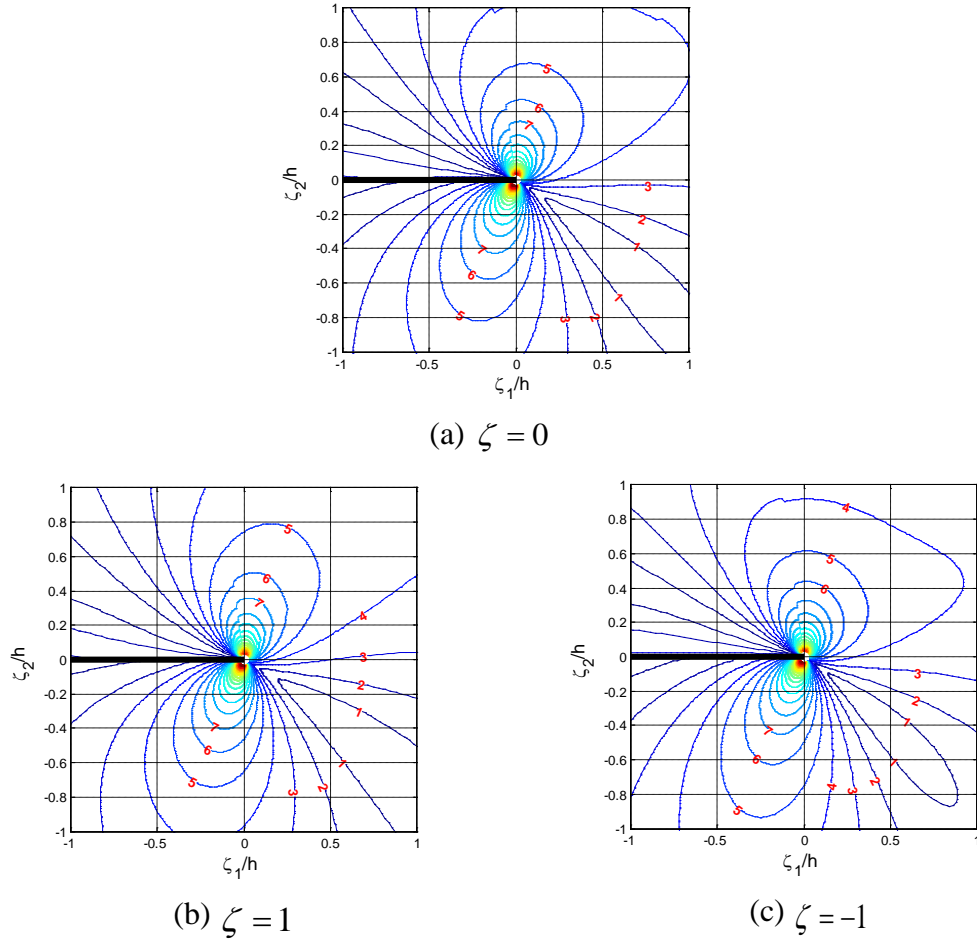


Fig. 8 Effect of property gradation for a curved crack on the contours of for maximum shear stress around the crack–tip for a mixed-mode loading in an FGM with no temperature field ($K_{II}/K_{ID} = 0.2$, $c/c_s = 0.5$, $k = 20$, $\beta = 20^\circ$).

The effect of property gradation for a curved crack on the contours of maximum shear stress around a propagating crack-tip for $k = 20$ and $\beta = 20^\circ$ with no temperature field is shown in Fig. 8. Fig. 8(a) shows the case of a homogeneous material, and Fig. 8(b) & 8(c) are plotted for $\zeta = 1$ and $\zeta = -1$ respectively. For $\zeta = 1$, the size of the contours increases above the crack-line and decreases below the crack-line. Moreover, these contours tilt towards the crack direction which is the increasing

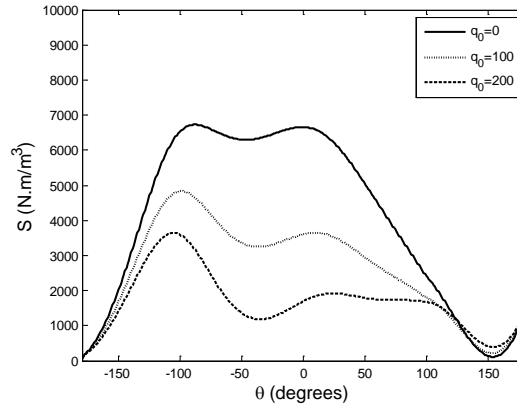
property gradation direction as shown in Fig 8(b). However, for $\zeta = -1$, the reverse happens with a decreased size above the crack-line and an increased size below the crack-line and the contours tilt away from the crack direction, which is again in the increasing property gradation direction.

A similar plot to that of Fig.8 is made by considering the thermal property gradation on the maximum principal stress with temperature gradient, $q_0 = 100$, there is no noticeable difference on the contours of maximum principal stress for different non-homogeneity values (γ_2). This is due to the dominance of first term (q_0) in the temperature field equation.

3.2 Crack Extension Angle

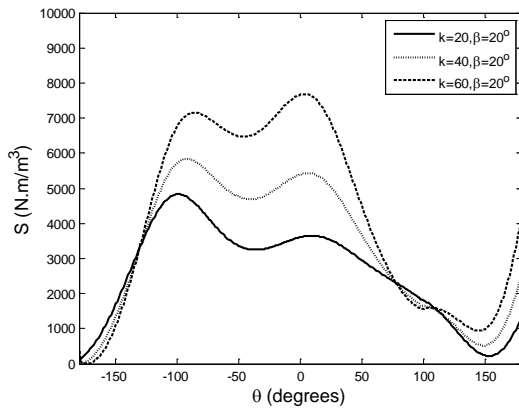
A dynamically moving crack tends to deviate from its path due to crack-tip instability conditions. The crack-tip instability becomes predominant when the cracks tend to propagate in non-homogeneous materials under thermo-mechanical loading. In the present study, using the derived thermo-mechanical stress field equations, the effects of curvature parameters, temperature, crack-tip velocity and material non-homogeneity on the crack-tip instability are presented. The theoretical prediction of the crack extension angle is investigated by using the well-known fracture criterion: minimum strain energy density (S-criterion). The strain energy density criterion was chosen because it provides a complete description of material damage by including both the distortional and dilatational effects (Gdoutos, 1990). Both distortional and dilatational vary in proportion, depending on the load history and location due to non-uniformity in stress or energy fields.

3.3 Minimum Strain-Energy Density (MSED) Criterion



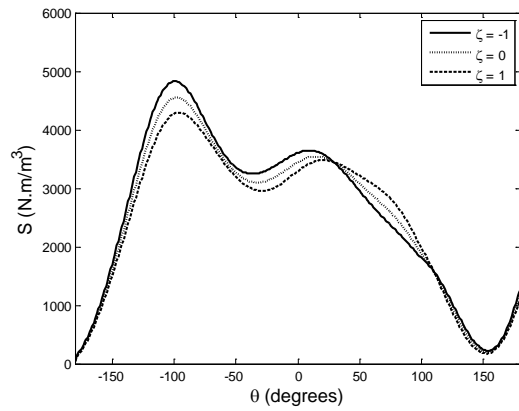
(a) Effect of temperature

$$(\zeta = -1, k = 20, \beta = 20^\circ)$$



(b) Effect of curvature

$$(\zeta = -1, q_0 = 100^0 C / m^{1/2})$$



(c) Effect of non-homogeneity

$$(k = 20, \beta = 20^\circ, q_0 = 100^0 C / m^{1/2})$$

Fig. 9 Effect of (a) temperature, (b) curvature and (c) non-homogeneity on strain energy density around the crack–tip for a mixed mode thermo-mechanical loading in an FGM ($K_{II D}/K_{I D} = 0.2$, $c/c_s = 0.5$, $\gamma_2 = 1$, $r = 0.002\text{m}$).

According to this criterion (Sih, 1974), the crack initiates when the strain energy density achieves a critical value and propagates in the direction of the

minimum strain-energy density value. The strain energy density dW/dV near the crack-tip for an FGM is given as

$$\frac{dW}{dV} = S = \frac{1}{4\mu e^{\epsilon_x}} \left\{ (1-\nu) \left\{ \sigma_{xx}^2 + \sigma_{yy}^2 \right\} - 2\nu \sigma_{xx} \sigma_{yy} + 2\sigma_{xy}^2 \right\} \quad (40)$$

Fracture takes place in the direction of minimum S , and the condition can be obtained by using Eq. (40)

$$\frac{\partial S}{\partial \theta} = 0 \quad ; \quad \frac{d^2 S}{d\theta^2} > 0 \quad \text{at } S = S_c \quad (41)$$

where S_c is the critical strain energy density.

Variation of strain energy density around the crack-tip for a thermo-mechanical loading in an FGM for different temperature gradients, curvatures and non-homogeneity is shown in Fig. 9. The angle at which the strain energy density reaches a minimum value changes with temperature, curvature and the non-homogeneity parameters as shown in Fig. 9.

3.3.1 Effect of Crack-tip Velocity

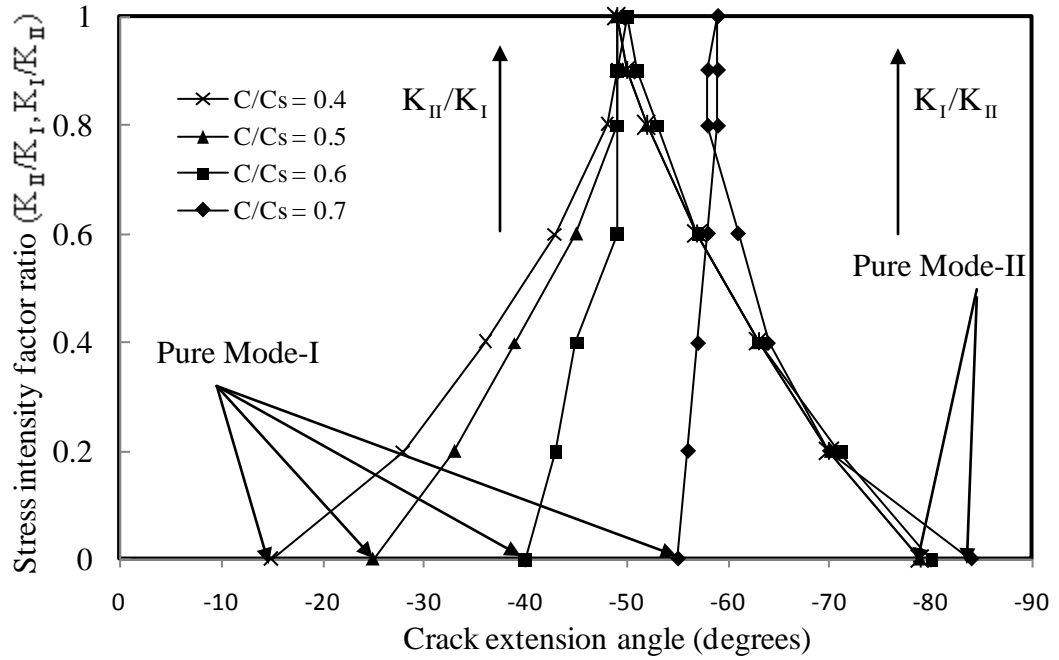


Fig. 10 Crack extension angle as a function of crack-tip velocity for a mixed-mode thermo-mechanical loading in homogeneous material using *MSED* criterion ($\zeta = 0$, $k = 20$, $\beta = 20^\circ$, $r = 0.002m$).

The crack extension angles as a function of crack-tip velocity for a typical curvature $k = 20$ and $\beta = 20^\circ$, temperature gradient, $q_0 = 100$ under thermo-mechanical loading as predicted by the *MSED* criterion is shown in Fig. 10. For pure mode-I loading ($K_{IID}/K_{ID}=0$), at a crack-tip velocity of $c/c_s=0.4$, the *MSED* criterion predicts a crack extension angle of about -15° . For all other crack-tip velocities shown in the figure, as the value of K_{IID}/K_{ID} and K_{ID}/K_{IID} increases from 0 to 1 the crack extension angle increases monotonically. Also as the crack-tip velocity increases, the crack kinks at a larger angle.

3.3.2 Effect of Non homogeneity

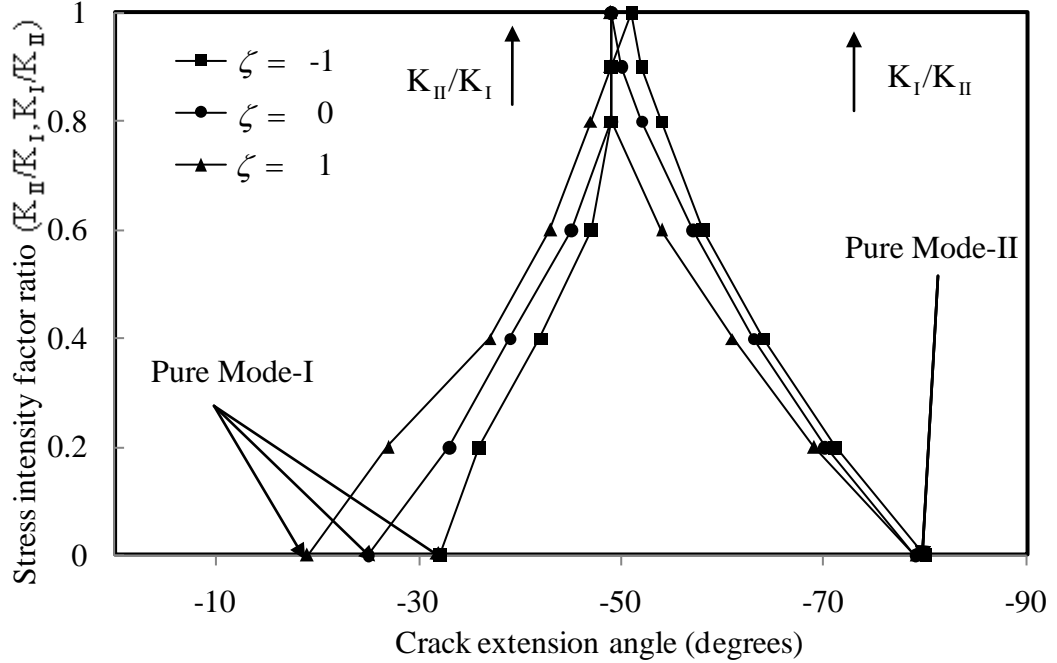


Fig. 11 Crack extension angle as a function of non-homogeneity parameter for a mixed- mode crack with temperature field ($c/c_s=0.5$, $k = 20$, $\beta = 20^\circ$, $r = 0.002m$).

The effect of the non-homogeneity parameter ($\zeta = 1$ and $\zeta = -1$) on the crack extension angle for a crack-tip velocity of $0.5c_s$ under thermo-mechanical loading ($q_0 = 100$) is shown in Fig. 11. Under pure mode-I loading, *MSED* criterion predicts crack extension angle of $\theta = -19^\circ$ for a FGM with $\zeta = 1$; $\theta = -25^\circ$ for a homogenous material (i.e. $\zeta = 0$) and $\theta = -32^\circ$ for a FGM with $\zeta = -1$. However under pure mode-II loading, *MSED* criterion predicted constant angle of $\theta = -49^\circ$ for both the homogeneous and FGMs with $\zeta = 1$ and an angle of $\theta = -51^\circ$ for FGM with $\zeta = -1$.

3.3.3 Effect of Temperature

The effect of the temperature on the crack extension angle for a mixed-mode thermo-mechanical loading is shown in Fig. 12 for different non-homogeneity values. Typical values of $k = 20$, $\beta = 20^\circ$, $\gamma_2 = 1$ are assumed for constructing Fig. 12. For a

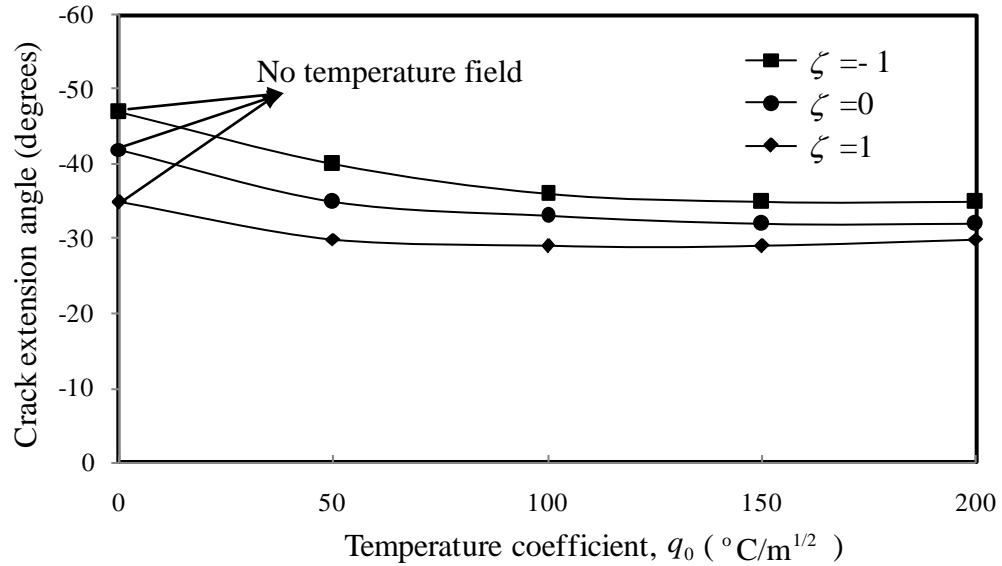
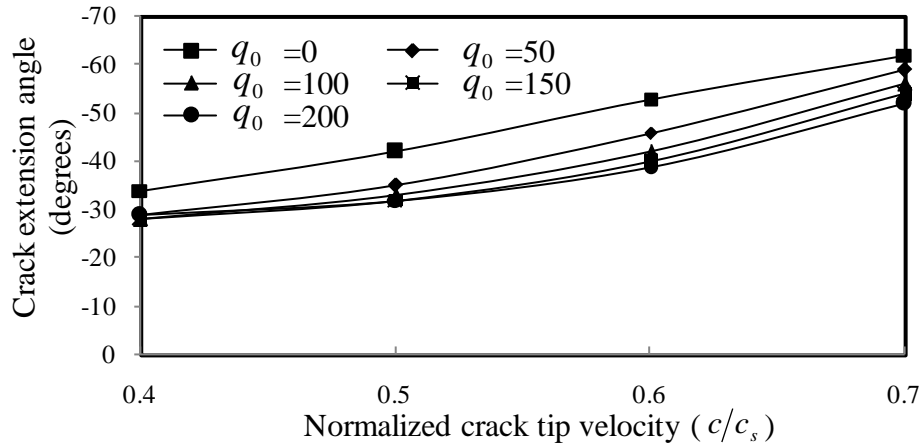
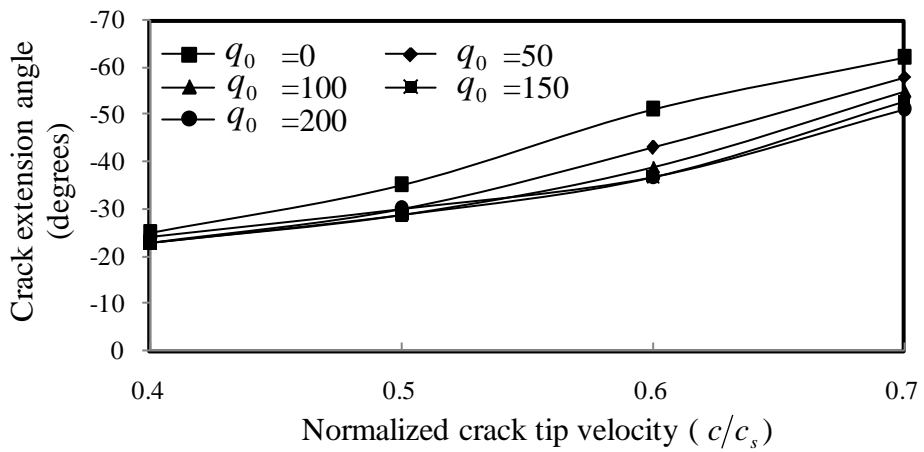


Fig. 12 Effect of temperature on the crack extension angle for a mixed-mode thermo-mechanical loading in FGM for different non-homogeneity values using *MSED* criterion ($K_{II}/K_I=0.2$, $c/c_s=0.5$, $k = 20$, $\beta = 20^\circ$, $\gamma_2 = 1$, $r = 0.002m$).

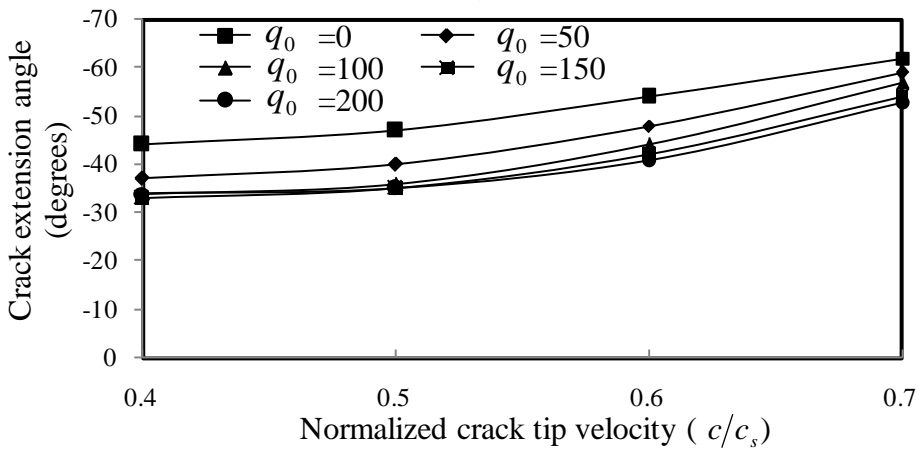
homogeneous material and FGMs with ($\zeta = 1$ and $\zeta = -1$), the crack extension angle decreases slowly with an increase in the temperature gradient. FGM with $\zeta = -1$ kinks at a larger angle compared to a homogeneous material and a FGM with increasing property gradation. This could be attributed to the presence of a compliant material ahead of the crack-tip in which the strain energy density reaches a minimum value at a higher angle.



(a) $\zeta = 0$



(b) $\zeta = 1$



(c) $\zeta = -1$

Fig. 13 Crack extension angle as a function of crack-tip velocity for a mixed-mode thermo-mechanical loading at different temperature fields using *MSED* criterion

$$(K_{IID}/K_{ID}=0.2, k=20, \beta=20^\circ, \gamma_2 = 1, r=0.002m).$$

The effects of temperature on the crack extension angle as a function of crack-tip velocity in a homogeneous material, a FGM with $\zeta = 1$ and a FGM with $\zeta = -1$ are plotted in Fig. 13 using *MSED* criterion. For all the three cases, the crack $\zeta = -1$ are plotted in Fig. 13 using *MSED* criterion. For all the three cases, the crack extension angle increases as the crack-tip velocity increases for various temperature gradients.

3.3.4 Effect of Curvature

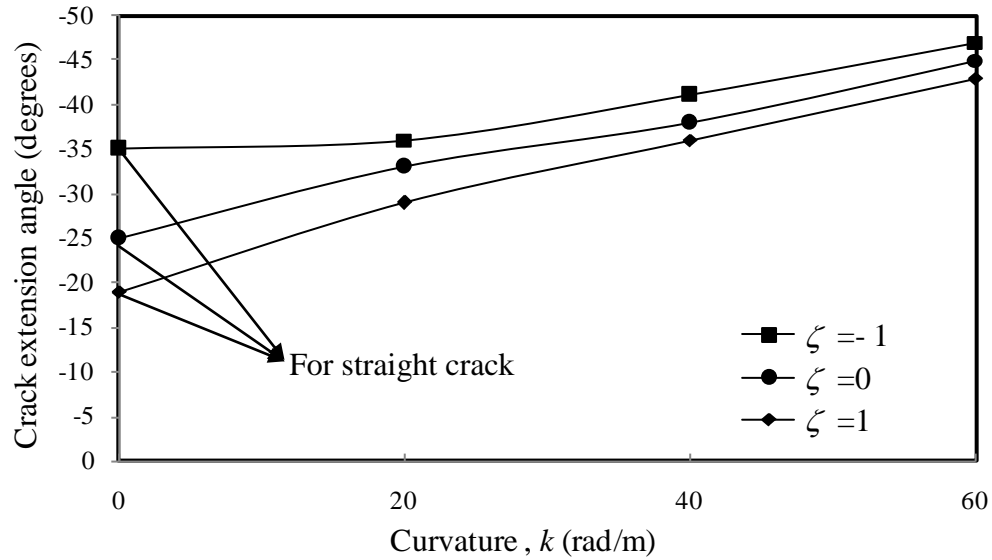
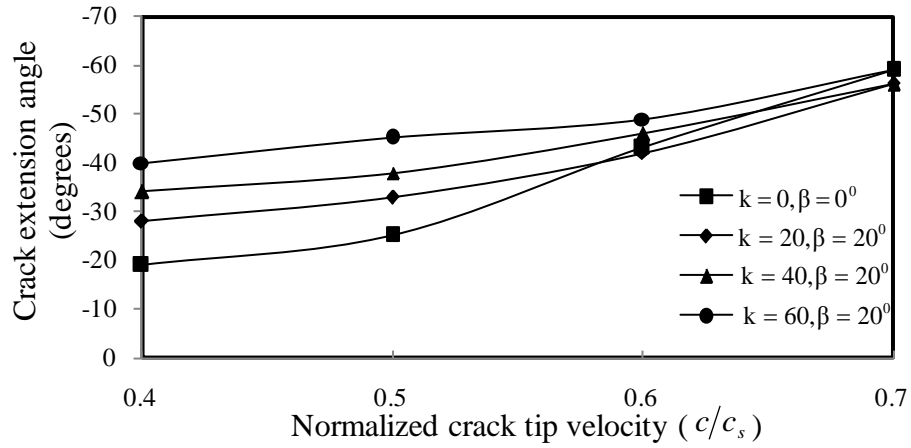
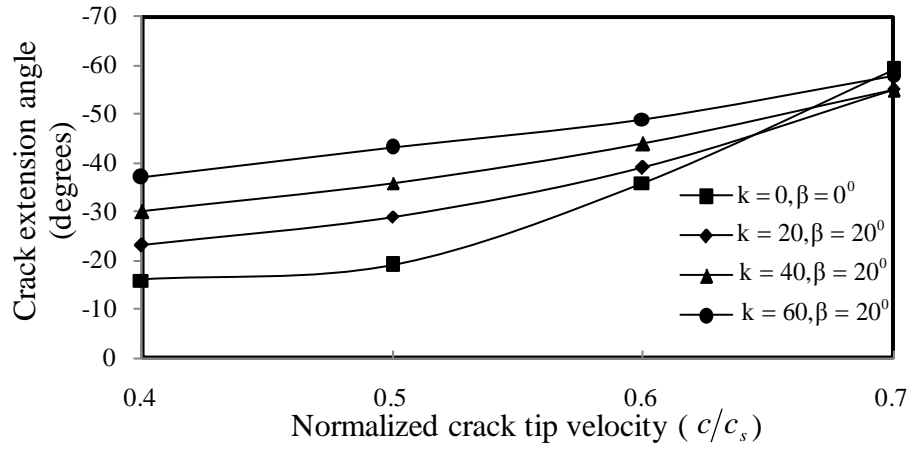


Fig. 14 Effect of curvature on the crack extension angle for a mixed-mode thermo-mechanical loading in FGM for different non-homogeneity factors using *MSED* criterion ($K_{IID}/K_{ID}=0.2$, $c/c_s=0.5$, $q_0 = 100$, $\beta = 20^\circ$, $\gamma_2 = 1$, $r=0.002m$).

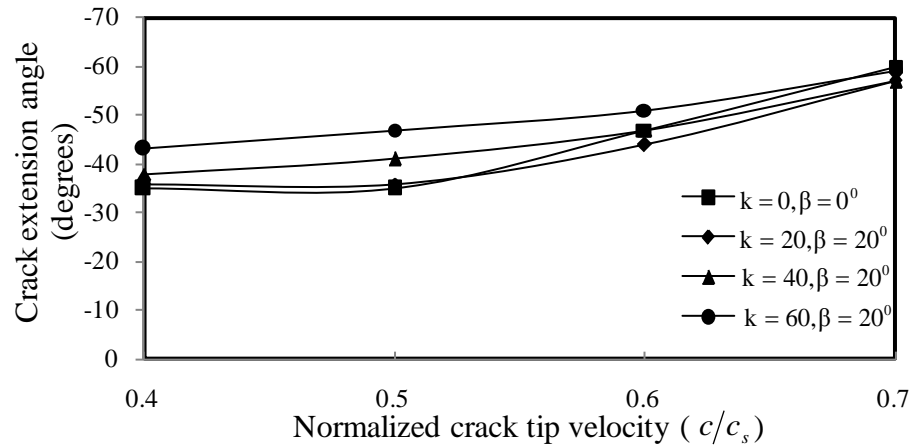
The effect of curvature on the crack extension angle for a crack-tip velocity of $0.5c_s$ for a mixed-mode thermo-mechanical loading is shown in Fig. 14 for different non homogeneity values using *MSED* criterion. A typical value of $q_0 = 100$ is assumed for plotting Fig. 14. Four different values of curvature (k) with fixed $\beta = 20^\circ$ are chosen at the crack-tip. For a homogeneous material, the crack extension angle increases as the value of (k) increases. A similar trend is observed for a FGM with



(a) $\zeta = 0$



(b) $\zeta = 1$



(c) $\zeta = -1$

Fig. 15 Crack extension angle as a function of crack-tip velocity for a mixed-mode thermo-mechanical loading for various curvature parameters using *MSED* criterion

$$(K_{II}/K_{ID}=0.2, q_0 = 100, \gamma_2 = 1, r=0.002m).$$

$\zeta = 1$ and $\zeta = -1$. Also at each value of the curvature at the crack-tip, the crack extension angle increases as the value of non-homogeneity decreases. Again, larger crack extension angles are noticed for the case of FGM with $\zeta = -1$.

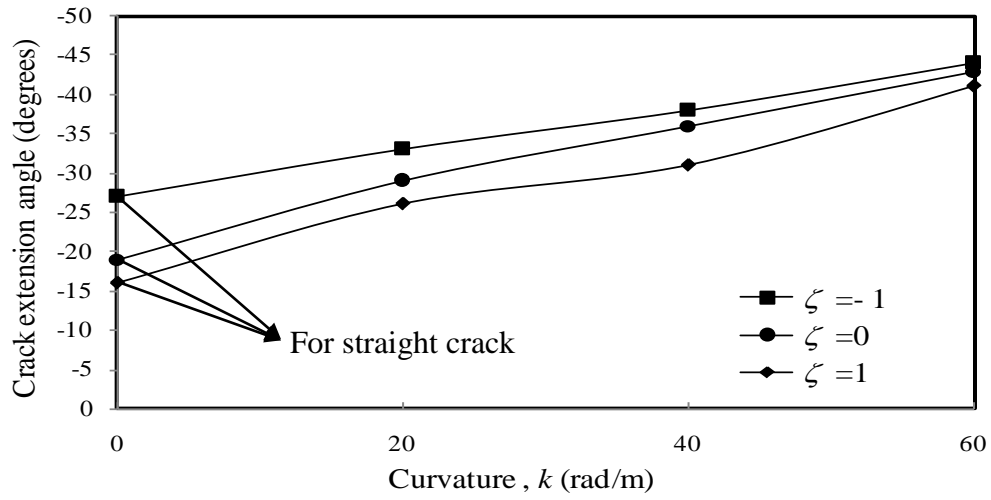
The effects of curvature on the crack extension angle as a function of crack-tip velocity in a homogeneous material, a FGM with $\zeta = 1$ and a FGM with $\zeta = -1$ is plotted in Fig. 15 using *MSED* criterion. For a homogeneous material, at each value of curvature at crack-tip, the crack extension angle increases as the crack-tip velocity increases. Similar behavior is observed for the case of FGMs with $\zeta = 1$ and $\zeta = -1$.

3.4 Effect of T-stress on Curvature and Temperature

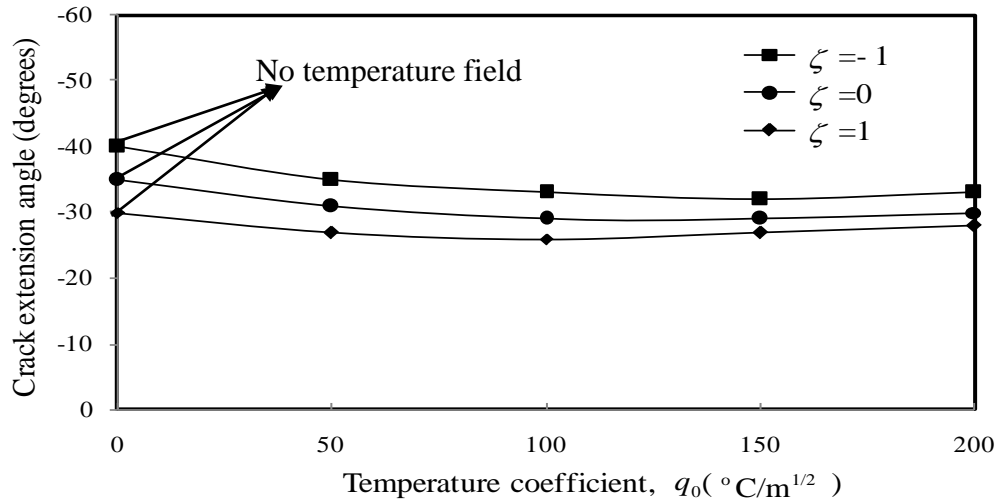
In the previous studies, it was reported in the literature that T-stress (σ_{ox} term) plays a vital role in crack kinking or crack branching for a homogeneous material (e.g., Cotterell and Rice, 1980; Shukla et al. 1990; Fang-Li and Roy-Xu, 2007). In this paper, the effect of T-stress is studied in FGMs under thermo-mechanical loading.

$$\sigma_{xx} = \frac{(K_{IId}, K_{IIId})}{(2\pi r)^{1/2}} F_{ij}(r, \theta, T, \xi, \gamma, c, k, \beta, \dot{\beta}) + T(\sigma_{ox}) \quad (42)$$

In the above Eq. 42, T is the non-singular stress term. The effect of T -stress (σ_{ox} term) on the crack extension angle for different curvature values and temperature gradients around a propagating crack under mixed-mode loading in an FGM is shown in Fig. 16 for different non homogeneity values using *MSED* criterion. A Typical value of $\sigma_{ox} = (-3/4 * K_{ID})m^{-1/2}$ was used for plotting. Fig. 16(a) shows the effect of T -stress on the crack extension angle as a function of curvature for a fixed temperature



(a) Effect of curvature



(b) Effect of temperature

Fig. 16 Effect of T-stress on the crack extension angle for different values of curvature and temperature for a mixed-mode thermo-mechanical loading in FGM for different non-homogeneity factors using *MSED* criterion ($\sigma_{ox} = (-3/4 * K_{ID})m^{-1/2}$,

$$K_{IID}/K_{ID}=0.2, c/c_s=0.5, \gamma_\gamma = 1, r=0.002m).$$

gradient ($q_0 = 100$) and fixed $\beta = 20^{\circ}$. The crack extension angle increases as the value of (k) increases for a homogeneous material and FGMs with $\zeta = 1$ and $\zeta = -1$.

For a FGM with $\zeta = -1$, the crack kinks at a larger angle. This could be again attributed to the presence of a compliant material ahead of the crack-tip in which the strain energy density reaches a minimum value at a higher angle.

Fig. 16(b) shows the effect of T -stress on the crack extension angle as a function of temperature gradient for a fixed value of curvature ($k = 20$, $\beta = 20^\circ$). For all the different non-homogeneity values, the crack extension angle decreases as the temperature gradient increases. The decrease in crack extension angle is more significant for less temperature gradient. Again, larger crack extension angles are observed for a FGM with $\zeta = -1$.

When the above results were compared with Fig. 12 and Fig. 14 (where $\sigma_{ox} = 0$), it is observed that the crack extension angle decreases when the T -stress (σ_{ox} term) is applied.

It can be concluded from above analysis (Fig. 2 to Fig. 16) that, the non-homogeneity parameters, curvature and temperature fields have significant effect on the contours of maximum shear stress, various stress components discussed and the crack extension angle. So, for curving cracks, non-homogeneity parameters, temperature field and curvature terms cannot be ignored in extracting fracture parameters from experimental data.

There are various experimental techniques such as photoelasticity, coherent gradient sensing (CGS), digital image correlation (DIC), interferometry etc. to obtain the full field experimental data around the crack-tip. Digital image correlation technique can be used to obtain the in plane and out of plane displacements around the

crack-tip (Abanto-Bueno and Lambros, 2006; Rousseau et al. 2010). Coherent gradient sensing technique can be used obtain the out of plane displacement gradients (using the reflection mode) or in plane stress gradients (using transmission mode) for opaque and transparent solids respectively (Rousseau et al. 2010; Tippur et al. 1991). The photoelasticity technique can be used for transparent materials. The high speed digital imaging along with dynamic photoelasticity can be employed to obtain real time, full field data around the crack-tip (Rousseau et al. 2010; Jain and Shukla, 2007). Combined experimental techniques of DIC and infrared photography have been recently used to study the displacement under dynamic thermo-mechanical loading (Silva and Ravichandran, 2011). The above mentioned techniques can be used to extract fracture parameters and thermal coefficients used in the stress field equations developed in this analysis (Rousseau et al. 2010; Krishnamoorthy and Tippur, 1998).

4. Conclusions

The stress-fields near the crack-tip for steady state mixed-mode thermo-mechanical loading in a graded material for a smoothly curving crack are developed using displacement potentials in conjunction with an asymptotic approach. First, asymptotic temperature fields near the crack-tip are developed and then by incorporating this developed temperature field into the mechanical field, the thermo-mechanical stress fields near the crack-tip are generated. Using these developed stress field equations, the effect of the non-homogeneity parameters, curvature, and temperature is studied on various stress components, on the contours of the maximum shear stress and the crack extension angle using minimum strain energy density criterion. The results are compared with the previous findings of static and dynamic

crack propagation in homogeneous and FGM systems under thermo-mechanical loadings (Kidane et al. (2010a) & (2010b)). When curvature terms are set to zero, the solutions match with the previous findings. This analytical study resulted in the following key findings:

- The thermo-mechanical stress fields around the crack-tip are significantly affected by the curvature, temperature and non-homogeneity parameters. As the curvature at the crack-tip increases, the peak value of the stress components also increases.
- For a given curvature conditions, as the temperature gradient increases, the peak value of the stress components decreases.
- The mechanical properties gradation affects the contours of the maximum shear stress considerably while the thermal properties gradations show no significant effect on the stresses.
- Crack-tip velocity plays a significant role in the crack extension angle. For a mixed-mode curving crack under thermo-mechanical loading, the crack extension angle increases with the increase in crack-tip velocity. Similar behavior was reported earlier for the case of homogeneous and FGMs without the curvature parameters (Kidane et al., 2010a and 2010b).
- Similar to previous findings (Kidane et al., 2010a and 2010b), the increase in the temperature gradient decreases the crack extension angle for different non-homogeneity values.
- The increase in the value of curvature (k) increases the crack extension angle for different non-homogeneity values.

- For a homogeneous material and FGMs with $\zeta = 1$ and $\zeta = -1$, the crack extension angle increases as the crack-tip velocity increases for different values of temperature coefficient (q_0) and curvature (k).
- For an applied T-stress, the increase in the value of curvature (k) increases the crack extension angle while the increase in the temperature gradient decreases the crack extension angle for different non-homogeneity values.
- There is a significant effect on the crack extension angle when the T-stress is applied. The crack extension angle decreases when the T-stress (σ_{ox} term) is applied when compared to the case of without the T-stress (where $\sigma_{ox} = 0$).

Acknowledgements

The financial support of the Air Force Office of Scientific Research under grant no FA9550-09-1-0639 is gratefully acknowledged.

References

- Abanto-Bueno, J., Lambros, J., 2006. An experimental study of mixed mode crack initiation and growth in functionally graded materials. *Exp Mech.* 46(2), 179–196.
- Atkinson, C., List, R.D., 1978. Steady state crack propagation into media with spatially varying elastic properties. *Int. J. Eng Sci.* 16, 717–730.
- Awrejcewicz, J., Krysko, V.A., 2003. Nonclassical thermoelastic problems in nonlinear dynamic of shells. Applications of the Bubnov-Galerkin and finite difference numerical methods. Springer, Germany.
- Brischetto, S., Carrera, E., 2010. Coupled thermo-mechanical analysis of one-layered and multilayered plates. *Compos. Struct.* 92, 1793-1812.

- Chalivendra, V.B., Shukla, A., Parameswaran, V., 2002. Dynamic out of plane displacement fields for an inclined crack in graded materials. *J. Elast.* 69, 99–119.
- Chalivendra, V.B., Shukla, A., Parameswaran, V., 2003. Quasi-static stress fields for a crack inclined to the property gradation in functionally graded materials. *Acta Mech.* 162, 167–184.
- Chalivendra, V.B., Shukla, A., 2005. Transient elastodynamic crack growth in functionally graded materials. *J. Appl. Mech.* 72, 237–248.
- Chalivendra, V.B., 2007. Asymptotic analysis of transient curved crack in functionally graded materials. *Int. J. Solids Struct.* 44, 465-479.
- Chalivendra, V. B., 2008. Mode-I crack-tip stress fields for inhomogeneous orthotropic medium. *Mech Mater.* 40, 293-301.
- Chalivendra, V. B., 2009. crack-tip stress fields for orthotropic functionally graded materials. *Acta Mech.* 204(1), 51-60.
- Cotterell, B., Rice, J.R., 1980. Slightly curved or kinked cracks. *Int. J. Fract.* 16, 155-169.
- Delale, F., Erdogan, F., 1983. The crack problem for a nonhomogeneous plane. *J. App. Mech.* 50, 67-80.
- Drake, J.T., Williamson, R.L., Rabin, B.H., 1993. Finite element analysis of thermal residual stresses at graded ceramic-metal interfaces. Part II: interface optimization for residual stress reduction. *J. App. Phys.* 74, 1321-1326.
- Erdogan, F., Sih, G.C., 1963. On the crack extension in plates under plane loading and transverse shear. *J. Basic. Eng.* 85, 519-527.

- Erdogan, F., Wu, B.H., 1996. Crack problems in FGM layers under thermal stresses. *J. Therm. Stresses*. 19, 237-265.
- Eslami, M.R., Shakeri, M., Sedaghati, R., 1994. Coupled thermoelasticity of axially symmetric cylindrical shells. *J. Therm. Stresses*. 10, 564-576.
- Fahrenholtz, W.G., Hilmas, G.E., Talmy, I.G., Zaykoski, J.A., 2007. Refractory Diborides of Zirconium and Hafnium. *J. Am. Ceram. Soc.* 90, 1347-1364.
- Fang, L, X., Roy, X, L., 2007. T-stresses across static crack kinking. *J. App. Mech.* 74, 181-190.
- Freund, L.B., 1990. *Dynamic Fracture Mechanics*. Cambridge University Press, Cambridge.
- Gdoutos, E.E., 1990. *Fracture mechanics criteria and applications*. Kluwer Academic Publishers.
- Giannakopoulos., A.E, Suresh, S., Finot, M., Olsson, M., 1995. Elastoplastic analysis of thermal cycling: layered materials with compositional gradient. *Acta Metall. Mater.* 43, 1335-1354.
- Gu, P., Asaro, R.J., 1997. Cracks in functionally graded materials. *Intl. J. Solids Struct.* 34 (1), 1–17.
- Hasselman, D.P.H., 1978. Youngblood G. E. Enhanced thermal stress resistance of structural ceramics with thermal conductivity gradient. *J. Am. Ceram. Soc.* 61, 49-52.
- Irwin, G.R., 1980. Series representation of the stress field around constant speed cracks. *University of Maryland Lecture Notes*, Maryland.

- Jain, N., Shukla, A., 2007. Asymptotic analysis and reflection photoelasticity for the study of transient crack propagation in graded materials. *J. Mech. Mater. Struct.* 2(4), 595-612.
- Jain, N., Shukla, A., Chona, R., 2006. Asymptotic stress fields for thermo-mechanically loaded cracks in FGMs. *J. ASTM Int.* 3(7), 78-90.
- Jiang, C.P., Zou, Z.Z., Wang, D., Liu, Y.W., 1991. A discussion about a class of stress intensity factors and its verification. *Int. J. Fract.* 49, 141-157.
- Jin, Z.H., Noda, N., 1994. Crack-tip singular fields in nonhomogeneous materials. *J. App. Mech.* 61, 738-740.
- Jin, Z.H., Batra, R.C., 1996. Stress intensity relaxation at the tip of an edge crack in a functionally graded materials subjected to a thermal shock. *J. Therm. Stresses.* 19, 317-339.
- Jin, Z.H., Paulino, G.H., 2001. Transient thermal stress analysis of an edge crack in a functionally graded materials. *Int. J. Frac.* 107, 73-98.
- Jin, G.H., Paulino, G.H., Dodds, R.H., 2002. Finite element investigation of quasi-static crack growth in functionally graded materials using a novel cohesive zone fracture model. *Jr. ASME. J. App. Mech.* 69, 370-379.
- Kawasaki, A., Wantanabe, R., 1987. Finite element analysis of thermal stress of the metal/ceramics multi-layer composites with controlled compositional gradients. *J. Jpn. Inst. Met.* 51, 525-529,.
- Kidane, A., Chalivendra, V.B., Shukla, A., 2010a. Thermo-mechanical stress fields and strain energy associated with a propagating crack. *Acta Mech.*

Kidane, A., Chalivendra, V.B., Shukla, A., Chona, R., 2010b. Dynamic crack propagation in graded materials under thermo-mechanical loading. *Eng. Fract. Mech.*

Kim, J.H., Paulino, G.H., 2002. Finite element evaluation of stress intensity factors in functionally graded materials. *Int. J. Numer. Meth. Eng.* 53, 1903-1935.

Kirugulige, M.S., Tippur, H.V., 2008. Mixed-mode dynamic crack growth in a functionally graded materials under mode-I thermomechanical loading. *Int. J. Soilds Struct.* 75(5), 1-14.

Konda, N., Erdogan, F., 1994. The mixed mode crack problem in a nonhomogeneous elastic plane. *Eng. Fract. Mech.* 47, 533-545.

Krishnamoorthy, H., Tippur, H.V., 1998. Extracting fracture parameters using local collocation of full-field displacement data. *Exp. Tech.* 22(1), 22-25.

Krishnaswamy, S., Tippur, H.V., Rosakis, A.J., 1992. Measurement of transient crack tip deformation fields using the method of coherent gradient sensing. *J. Mech. Phys. Solids.* 40, 339-372.

Kubair, D.V., Geubelle, P.H., Lambros, J., 2005. Analysis of a mode-3 stationary crack in a functionally graded material. *J. App. Mech. T ASME.* 72, 461-467.

Kuroda, Y., Kusaka, K., Moro, A., Togawa, M., 1993. Evaluation tests of ZrO₂/Ni functionally gradient materials for regeneratively cooled thrust engine applications, *Ceramic Transactions, Functionally Gradient Materials* (edited by J.B. Holt, M. Koisumi, T. Hirai and Z.A. Munir), Am. Ceram. Soc. Westerville, Ohio, 34, 289-296.

Lambros, J., Cheeseman, B.A., Santare, M.H., 2000. Experimental investigation of the quasi-static fracture of functionally graded materials. *Int. J. Soilds Struct.* 37, 3715–3732.

- Liu, C., Rosakis, A.J., 1994. On the higher order asymptotic analysis of a non-uniformly propagating dynamic crack along an arbitrary path. *J. Elast.* 35, 27–60.
- Lee, K.H., Chalivendra, V.B., Shukla, A., 2008. Dynamic crack-tip stress and displacement fields under thermomechanical loading in functionally graded materials. *J. Appl. Mech.* 75 (5), 1–7.
- McQuillen, E.J., Brull, M.A., 1970. Dynamic thermoelastic response of cylindrical shell. *Trans. ASME, J. Appl. Mech.* 37(3), 661-670.
- Nigam, H., Zervas, H., Shukla, A., 1990. Effect of Stress Field Parameters on Dynamic Crack Branching. *Eng. Fract. Mech.* 36(3), 429-438.
- Niino, M., Hirai, T., Watanabe, R., 1987. The Functionally Gradient Materials, *J. Jpn. Soc. Compos. Mater.* 13(1), 257,
- Noda, N., 1997. Thermal stress intensity for functionally graded plate with an edge crack, *J. Therm. Stresses.* 20, 373-387.
- Noda., N., Ishihara, M., Yamamoto, N., Fujimoto, T., 2003. Two-crack propagation in a functionally graded material plate under thermal loads. *Mater. Sci. Forum* 423–425, 607–612.
- Nowinski, J.L., 1978. *Theory of thermoelasticity with applications.* The Netherlands: Sijthoff & Noordhoff International publications.
- Parameswaran, V., Shukla, A., 1999. Crack-tip stress fields for dynamic fracture in functionally gradient materials. *Mech. Mater.* 31, 579–596.
- Parameswaran, V., Shukla, A., 2002. Asymptotic stress fields for stationary cracks along the gradient in functionally graded materials. *J. Appl. Mech.* 69, 240–243.

- Rousseau, C.E., Chalivendra, V.B., Tippur, H.V., Shukla, A., 2010. Experimental fracture mechanics of functionally graded materials: An overview of optical investigations. *Exp. Mech.* 50(7), 845-865.
- Rousseau, C.E., Tippur, H.V., 2001. Dynamic fracture of compositionally graded materials with cracks along the elastic gradient: Experiments and Analysis. *Mech. Mater.* 33, 403-421.
- Sadd, M.H., 2009. *Elasticity: Theory, Applications, and Numerics*. Academic Press Publications, Burlington, MA.
- Schovanec, L., Walton, J.R., 1988. On the order of stress singularity for an anti-plane shear crack at the interface of two bonded inhomogeneous elastic materials. *ASME J. App. Mech.* 55, 234-236.
- Shiari, B., Eslami, M.R., Shaker, M., 2003. Thermomechanical shocks in composite cylindrical shells: A coupled thermoelastic finite element analysis. *Scientia. Iranica.* 10(1), 13-22.
- Shukla, A., Jain, N., 2004. Dynamic damage growth in particle reinforced graded materials. *Int. J. Impact Eng.* 30, 777–803.
- Silva, M.L., Ravichandran, G., 2011. Combined thermoelastic stress analysis and digital image correlation with a single infrared camera. *J. Strain. Anal. Eng. Des.* 46, 783-793.
- Suresh, S., Mortensen, A., 1998. *Fundamentals of functionally graded materials, processing and thermomechanical behavior of graded metals and metal–ceramic composites*. IOM Communications Ltd., London.

- Sih, G.C., 1974. Strain-energy-density factor applied to mixed mode crack problems. *Int J. Fract.* 10(3), 305-321.
- Takahashi, H., Ishikawa, T., Okugawa, D., Hashida, T., 1993. Laser and plasma-ARC thermal shock/fatigue fracture evaluation procedure for functionally gradient materials. *Thermal Shock and Thermal Fatigue Behavior of Advanced Ceramics* (edited by G.A. Scheneider and G. Petzow), Kluwer Academic Publishers, Dordrecht. 543-554.
- Tilbrook, M.T., Moon, R.J., Hoffman, M., 2005. Curved crack propagation in homogeneous and graded materials. *Fatigue Fract. Eng. Mater. Struct.* 28, 939–950.
- Tippur, H.V., Krishnaswamy, S., Rosakis, A.J., 1991. Optical mapping of crack tip deformations using the methods of transmission and reflection coherent gradient sensing: a study of crack tip K-dominance. *Int. J. Fract.* 52, 91-117.
- Tohgo, K., Suzuki, T., Araki, H., 2005. Evaluation of R-curve behavior of ceramic–metal functionally graded materials by stable crack growth. *Engineering Eng. Fract. Mech.* 72, 2359–2372.
- Walters, M, C., Paulino, G.H., Dodds, Jr.R.H., 2004. Stress-intensity factors for surface cracks in functionally graded materials under mode-I thermomechanical loading. *Int. J. Soilds Struct.* 41, 1081-1118.
- Wu, B.H., Erdogan, F., 1997. The surface crack problem for a plate with functionally graded properties. *J. Appl. Mech.* 64 (3), 449–456.
- Yao, X, F., Xu, W., Yeh, H, Y., 2007. Investigation of crack tip evolution in functionally graded materials using optical caustics. *Polym. Test.* 26, 122-131.

Zhang, L., Kim, J.H., 2011. Higher-order terms for the mode-III stationary crack-tip fields in a functionally graded material. *J. Appl. Mech.* 78(1), 011005(1-10).

Appendix A

$$\begin{aligned}
& \frac{\sigma_{xx}}{\exp(\zeta x)\mu_0} = \\
& \frac{3}{4}A_0r_i^{-1/2}\cos\frac{\theta_l}{2}(\delta(1-\alpha_i^2)+2)-\frac{3}{4}C_0r_i^{-1/2}\sin\frac{\theta_l}{2}(\delta(1-\alpha_i^2)+2)+\frac{3}{2}B_0\alpha_s r_s^{-1/2}\cos\frac{\theta_s}{2}+\frac{3}{2}D_0\alpha_s r_s^{-1/2}\sin\frac{\theta_s}{2} \\
& +2A_1(\delta(1-\alpha_i^2)+2)+4B_1\alpha_s+\frac{15}{4}A_2r_i^{1/2}\cos\frac{\theta_l}{2}(\delta(1-\alpha_i^2)+2)+\frac{15}{4}C_2r_i^{1/2}\sin\frac{\theta_l}{2}(\delta(1-\alpha_i^2)+2) \\
& +\frac{15}{2}B_2\alpha_s r_s^{1/2}\cos\frac{\theta_s}{2}-\frac{15}{2}D_2\alpha_s r_s^{1/2}\sin\frac{\theta_s}{2}-\frac{\zeta\cos\beta(t)}{4}r_i^{1/2}\left(\frac{3}{4}A_0\cos\frac{3\theta_l}{2}-\frac{3}{4}C_0\sin\frac{3\theta_l}{2}\right)\left\{\delta\left(\frac{1}{\alpha_i^2}-1\right)+\frac{2}{\alpha_i^2}\right\} \\
& -\frac{\zeta\cos\beta(t)}{4}r_i^{1/2}\left(3A_0\cos\frac{\theta_l}{2}+3C_0\sin\frac{\theta_l}{2}\right)\left\{\delta\left(\frac{1}{\alpha_i^2}+1\right)+\frac{2}{\alpha_i^2}\right\} \\
& +\frac{\zeta\sin\beta(t)}{4}r_i^{1/2}\left(\frac{3}{4}A_0\sin\frac{3\theta_l}{2}+\frac{3}{4}C_0\cos\frac{3\theta_l}{2}\right)\left\{\delta\left(\frac{1}{\alpha_i}-\alpha_l\right)+\frac{2}{\alpha_l}\right\} \\
& +\frac{\zeta\sin\beta(t)}{4}r_i^{1/2}\left(-3A_0\sin\frac{\theta_l}{2}+3C_0\cos\frac{\theta_l}{2}\right)\left\{\delta\left(\frac{1}{\alpha_l}+\alpha_i\right)+\frac{2}{\alpha_l}\right\} \\
& -\frac{\zeta\cos\beta(t)}{2\alpha_s}r_s^{1/2}\left(\frac{3}{4}B_0\cos\frac{3\theta_s}{2}+\frac{3}{4}D_0\sin\frac{3\theta_s}{2}\right)+\frac{\zeta\sin\beta(t)}{2}r_s^{1/2}\left(\frac{3}{4}B_0\sin\frac{3\theta_s}{2}-\frac{3}{4}D_0\cos\frac{3\theta_s}{2}\right) \\
& -\frac{\zeta\sin\beta(t)}{\delta+2}\frac{r_s^{1/2}}{\alpha_l^2-\alpha_s^2}\left(\frac{3}{2}B_0\sin\frac{\theta_s}{2}+\frac{3}{2}D_0\cos\frac{\theta_s}{2}\right)(\delta(1-\alpha_s^2)+2) \\
& -\frac{\zeta\cos\beta(t)}{\delta+2}\frac{\alpha_s r_s^{1/2}}{\alpha_l^2-\alpha_s^2}\left(\frac{3}{2}B_0\cos\frac{\theta_s}{2}-\frac{3}{2}D_0\sin\frac{\theta_s}{2}\right)(\delta(1-\alpha_s^2)+2) \\
& +2\zeta\delta\sin\beta(t)\frac{\alpha_l r_i^{1/2}}{\alpha_l^2-\alpha_s^2}\left(-\frac{3}{2}A_0\sin\frac{\theta_l}{2}+\frac{3}{2}C_0\cos\frac{\theta_l}{2}\right) \\
& +2\zeta\delta\cos\beta(t)\frac{\alpha_l^2 r_i^{1/2}}{\alpha_l^2-\alpha_s^2}\left(-\frac{3}{2}A_0\cos\frac{\theta_l}{2}-\frac{3}{2}C_0\sin\frac{\theta_l}{2}\right) \\
& +\frac{1}{4}\frac{\rho_0}{\mu_0}\frac{1}{\delta+2}c^2kr_i^{1/2}\left(\frac{3}{4}A_0\sin\frac{3\theta_l}{2}+\frac{3}{4}C_0\cos\frac{3\theta_l}{2}\right)\left\{\delta\left(\frac{1}{\alpha_l}-\alpha_l\right)+\frac{2}{\alpha_l}\right\} \\
& +\frac{1}{4}\frac{\rho_0}{\mu_0}\frac{1}{\delta+2}c^2kr_i^{1/2}\left(-3A_0\sin\frac{\theta_l}{2}+3C_0\cos\frac{\theta_l}{2}\right)\left\{\delta\left(\frac{1}{\alpha_l}+\alpha_l\right)+\frac{2}{\alpha_l}\right\} \\
& +\frac{\rho_0}{\mu_0}\frac{c^2k}{2}r_s^{1/2}\left(\frac{3}{4}B_0\sin\frac{3\theta_s}{2}-\frac{3}{4}D_0\cos\frac{3\theta_s}{2}\right)
\end{aligned}$$

$$\begin{aligned}
& -\frac{1}{16} \frac{\rho_0}{\mu_0} \frac{1}{\delta+2} c^2 k r_l^{1/2} \left(-\frac{3}{4} A_0 \sin \frac{7\theta_l}{2} - \frac{3}{4} C_0 \cos \frac{7\theta_l}{2} \right) \left\{ \delta \left(\frac{1}{\alpha_l^3} + \alpha_l \right) + \frac{2}{\alpha_l^3} \right\} \\
& -\frac{1}{16} \frac{\rho_0}{\mu_0} \frac{1}{\delta+2} c^2 k r_l^{1/2} \left(\frac{9}{2} A_0 \sin \frac{3\theta_l}{2} + \frac{9}{2} C_0 \cos \frac{3\theta_l}{2} \right) \left\{ \delta \left(\frac{1}{\alpha_l^3} - \alpha_l \right) + \frac{2}{\alpha_l^3} \right\} \\
& + \frac{1}{16} \frac{\rho_0}{\mu_0} \frac{1}{\delta+2} \frac{c^2 k}{\alpha_l} r_l^{1/2} \left(-\frac{3}{4} A_0 \sin \frac{7\theta_l}{2} - \frac{3}{4} C_0 \cos \frac{7\theta_l}{2} + 12 C_0 \cos \frac{\theta_l}{2} - 12 A_0 \sin \frac{\theta_l}{2} \right) (2(\delta+1)) \\
& + \frac{1}{8} \frac{\rho_0}{\mu_0} \frac{1}{\delta+2} \frac{c^2 k}{\alpha_l} r_l^{1/2} \left(\frac{15}{2} A_0 \sin \frac{3\theta_l}{2} + \frac{15}{2} C_0 \cos \frac{3\theta_l}{2} \right) \\
& - \frac{1}{8} \frac{\rho_0}{\mu_0} \frac{c^2 k}{\alpha_s^2} r_s^{1/2} \left(-\frac{3}{4} B_0 \sin \frac{7\theta_s}{2} - \frac{3}{2} B_0 \sin \frac{3\theta_s}{2} + 6 B_0 \sin \frac{\theta_s}{2} + \frac{3}{4} D_0 \cos \frac{7\theta_s}{2} + \frac{3}{2} D_0 \cos \frac{3\theta_s}{2} + 6 D_0 \cos \frac{\theta_s}{2} \right) \\
& + \frac{1}{8} \frac{\rho_0}{\mu_0} c^2 k r_s^{1/2} \left(-\frac{3}{4} B_0 \sin \frac{7\theta_s}{2} + \frac{3}{2} B_0 \sin \frac{3\theta_s}{2} + 6 B_0 \sin \frac{\theta_s}{2} + \frac{3}{4} D_0 \cos \frac{7\theta_s}{2} - \frac{3}{2} D_0 \cos \frac{3\theta_s}{2} + 6 D_0 \cos \frac{\theta_s}{2} \right) \\
& + \frac{2\alpha_c}{\alpha_l^2 - 1} \frac{3\delta+2}{\delta+2} q_0 r^{1/2} \cos\left(\frac{\theta}{2}\right) \\
& - \alpha_c (3\delta+2) \left(q_0 r^{1/2} \cos \frac{\theta}{2} + q_1 r \sin \theta + q_2 r^{3/2} \cos \frac{3\theta}{2} + \frac{1}{4} \gamma_2 q_0 r^{3/2} \left(\sin \beta(t) \sin \frac{\theta}{2} - \cos \beta(t) \cos \frac{\theta}{2} \right) \right)
\end{aligned}$$

(A.1)

$$\begin{aligned}
\frac{\sigma_{yy}}{\exp(\zeta x)\mu_0} = & \frac{3}{4}A_0r_l^{-1/2}\cos\frac{\theta_l}{2}(\delta-\alpha_l^2(\delta+2))-\frac{3}{4}C_0r_l^{-1/2}\sin\frac{\theta_l}{2}(\delta-\alpha_l^2(\delta+2))-\frac{3}{2}B_0\alpha_s r_s^{-1/2}\cos\frac{\theta_s}{2}-\frac{3}{2}D_0\alpha_s r_s^{-1/2}\sin\frac{\theta_s}{2} \\
& +2A_1(\delta-\alpha_l^2(\delta+2))-4B_1\alpha_s+\frac{15}{4}A_2r_l^{1/2}\cos\frac{\theta_l}{2}(\delta-\alpha_l^2(\delta+2))+\frac{15}{4}C_2r_l^{1/2}\sin\frac{\theta_l}{2}(\delta-\alpha_l^2(\delta+2)) \\
& -\frac{15}{2}B_2\alpha_s r_s^{1/2}\cos\frac{\theta_s}{2}+\frac{15}{2}D_2\alpha_s r_s^{1/2}\sin\frac{\theta_s}{2}-\frac{\zeta\cos\beta(t)}{4}r_l^{1/2}\left(\frac{3}{4}A_0\cos\frac{3\theta_l}{2}-\frac{3}{4}C_0\sin\frac{3\theta_l}{2}\right)\left(\frac{\delta}{\alpha_l^2}-(\delta+2)\right) \\
& -\frac{\zeta\cos\beta(t)}{4}r_l^{1/2}\left(3A_0\cos\frac{\theta_l}{2}+3C_0\sin\frac{\theta_l}{2}\right)\left(\frac{\delta}{\alpha_l^2}+(\delta+2)\right) \\
& +\frac{\zeta\sin\beta(t)}{4}r_l^{1/2}\left(\frac{3}{4}A_0\sin\frac{3\theta_l}{2}+\frac{3}{4}C_0\cos\frac{3\theta_l}{2}\right)\left(\frac{\delta}{\alpha_l}-\alpha_l(\delta+2)\right) \\
& +\frac{\zeta\sin\beta(t)}{4}r_l^{1/2}\left(-3A_0\sin\frac{\theta_l}{2}+3C_0\cos\frac{\theta_l}{2}\right)\left(\frac{\delta}{\alpha_l}+\alpha_l(\delta+2)\right) \\
& +\frac{\zeta\cos\beta(t)}{2\alpha_s}r_s^{1/2}\left(\frac{3}{4}B_0\cos\frac{3\theta_s}{2}+\frac{3}{4}D_0\sin\frac{3\theta_s}{2}\right)-\frac{\zeta\sin\beta(t)}{2}r_s^{1/2}\left(\frac{3}{4}B_0\sin\frac{3\theta_s}{2}-\frac{3}{4}D_0\cos\frac{3\theta_s}{2}\right) \\
& -\frac{\zeta\sin\beta(t)}{\delta+2}\frac{r_s^{1/2}}{\alpha_l^2-\alpha_s^2}\left(\frac{3}{2}B_0\sin\frac{\theta_s}{2}+\frac{3}{2}D_0\cos\frac{\theta_s}{2}\right)(\delta-\alpha_s^2(\delta+2)) \\
& -\frac{\zeta\cos\beta(t)}{\delta+2}\frac{\alpha_s r_s^{1/2}}{\alpha_l^2-\alpha_s^2}\left(\frac{3}{2}B_0\cos\frac{\theta_s}{2}-\frac{3}{2}D_0\sin\frac{\theta_s}{2}\right)(\delta-\alpha_s^2(\delta+2)) \\
& -2\zeta\delta\sin\beta(t)\frac{\alpha_l r_l^{1/2}}{\alpha_l^2-\alpha_s^2}\left(-\frac{3}{2}A_0\sin\frac{\theta_l}{2}+\frac{3}{2}C_0\cos\frac{\theta_l}{2}\right) \\
& -2\zeta\delta\cos\beta(t)\frac{\alpha_l^2 r_l^{1/2}}{\alpha_l^2-\alpha_s^2}\left(-\frac{3}{2}A_0\cos\frac{\theta_l}{2}-\frac{3}{2}C_0\sin\frac{\theta_l}{2}\right) \\
& +\frac{1}{4}\frac{\rho_0}{\mu_0}\frac{1}{\delta+2}c^2kr_l^{1/2}\left(\frac{3}{4}A_0\sin\frac{3\theta_l}{2}+\frac{3}{4}C_0\cos\frac{3\theta_l}{2}\right)\left(\frac{\delta}{\alpha_l}-\alpha_l(\delta+2)\right) \\
& +\frac{1}{4}\frac{\rho_0}{\mu_0}\frac{1}{\delta+2}c^2kr_l^{1/2}\left(-3A_0\sin\frac{\theta_l}{2}+3C_0\cos\frac{\theta_l}{2}\right)\left(\frac{\delta}{\alpha_l}+\alpha_l(\delta+2)\right) \\
& -\frac{\rho_0}{\mu_0}\frac{c^2k}{2}r_s^{1/2}\left(\frac{3}{4}B_0\sin\frac{3\theta_s}{2}-\frac{3}{4}D_0\cos\frac{3\theta_s}{2}\right)
\end{aligned}$$

$$\begin{aligned}
& -\frac{1}{16} \frac{\rho_0}{\mu_0} \frac{1}{\delta+2} c^2 k r_l^{1/2} \left(-\frac{3}{4} A_0 \sin \frac{7\theta_l}{2} - \frac{3}{4} C_0 \cos \frac{7\theta_l}{2} \right) \left(\frac{\delta}{\alpha_l^3} + \alpha_l (\delta+2) \right) \\
& -\frac{1}{16} \frac{\rho_0}{\mu_0} \frac{1}{\delta+2} c^2 k r_l^{1/2} \left(\frac{9}{2} A_0 \sin \frac{3\theta_l}{2} + \frac{9}{2} C_0 \cos \frac{3\theta_l}{2} \right) \left(\frac{\delta}{\alpha_l^3} - \alpha_l (\delta+2) \right) \\
& + \frac{1}{16} \frac{\rho_0}{\mu_0} \frac{1}{\delta+2} \frac{c^2 k}{\alpha_l} r_l^{1/2} \left(-\frac{3}{4} A_0 \sin \frac{7\theta_l}{2} - \frac{3}{4} C_0 \cos \frac{7\theta_l}{2} + 12 C_0 \cos \frac{\theta_l}{2} - 12 A_0 \sin \frac{\theta_l}{2} \right) (2(\delta+1)) \\
& -\frac{1}{8} \frac{\rho_0}{\mu_0} \frac{1}{\delta+2} \frac{c^2 k}{\alpha_l} r_l^{1/2} \left(\frac{15}{2} A_0 \sin \frac{3\theta_l}{2} + \frac{15}{2} C_0 \cos \frac{3\theta_l}{2} \right) \\
& + \frac{1}{8} \frac{\rho_0}{\mu_0} \frac{c^2 k}{\alpha_s^2} r_s^{1/2} \left(-\frac{3}{4} B_0 \sin \frac{7\theta_s}{2} - \frac{3}{2} B_0 \sin \frac{3\theta_s}{2} + 6 B_0 \sin \frac{\theta_s}{2} + \frac{3}{4} D_0 \cos \frac{7\theta_s}{2} + \frac{3}{2} D_0 \cos \frac{3\theta_s}{2} + 6 D_0 \cos \frac{\theta_s}{2} \right) \\
& -\frac{1}{8} \frac{\rho_0}{\mu_0} c^2 k r_s^{1/2} \left(-\frac{3}{4} B_0 \sin \frac{7\theta_s}{2} + \frac{3}{2} B_0 \sin \frac{3\theta_s}{2} + 6 B_0 \sin \frac{\theta_s}{2} + \frac{3}{4} D_0 \cos \frac{7\theta_s}{2} - \frac{3}{2} D_0 \cos \frac{3\theta_s}{2} + 6 D_0 \cos \frac{\theta_s}{2} \right) \\
& -\frac{2\alpha_c}{\alpha_l^2 - 1} \frac{3\delta+2}{\delta+2} q_0 r^{1/2} \cos\left(\frac{\theta}{2}\right) \\
& -\alpha_c (3\delta+2) \left(q_0 r^{1/2} \cos \frac{\theta}{2} + q_1 r \sin \theta + q_2 r^{3/2} \cos \frac{3\theta}{2} + \frac{1}{4} \gamma_2 q_0 r^{3/2} \left(\sin \beta(t) \sin \frac{\theta}{2} - \cos \beta(t) \cos \frac{\theta}{2} \right) \right)
\end{aligned}$$

(A.2)

$$\begin{aligned}
& \frac{\tau_{yy}}{\exp(\zeta x)\mu_0} = \\
& \frac{3}{2}A_0\alpha_l r_l^{-1/2} \sin \frac{\theta_l}{2} + \frac{3}{2}C_0\alpha_l r_l^{-1/2} \cos \frac{\theta_l}{2} + \frac{3}{4}B_0 r_s^{-1/2} \sin \frac{\theta_s}{2}(1+\alpha_s^2) - \frac{3}{4}D_0 r_s^{-1/2} \cos \frac{\theta_s}{2}(1+\alpha_s^2) \\
& - 2A_1\alpha_l - 2B_1 + 2C_1\alpha_s - 2D_1\alpha_s^2 - \frac{15}{2}A_2\alpha_l r_l^{1/2} \sin \frac{\theta_l}{2} + \frac{15}{2}C_2\alpha_l r_l^{1/2} \cos \frac{\theta_l}{2} \\
& - \frac{15}{4}B_2 r_s^{1/2} \sin \frac{\theta_s}{2}(1+\alpha_s^2) - \frac{15}{4}D_2 r_s^{1/2} \cos \frac{\theta_s}{2}(1+\alpha_s^2) - \frac{\zeta \cos \beta(t)}{2\alpha_l} r_l^{1/2} \left(\frac{3}{4}A_0 \sin \frac{3\theta_l}{2} + \frac{3}{4}C_0 \cos \frac{3\theta_l}{2} \right) \\
& - \frac{\zeta \cos \beta(t)}{4} r_s^{1/2} \left(3B_0 \sin \frac{\theta_s}{2} + 3D_0 \cos \frac{\theta_s}{2} \right) \left(1 - \frac{1}{\alpha_s^2} \right) \\
& + \frac{\zeta \sin \beta(t)}{2} r_l^{1/2} \left(-\frac{3}{4}A_0 \cos \frac{3\theta_l}{2} + \frac{3}{4}C_0 \sin \frac{3\theta_l}{2} \right) \\
& - \frac{\zeta \sin \beta(t)}{4} r_s^{1/2} \left(\frac{3}{4}B_0 \cos \frac{3\theta_s}{2} + \frac{3}{4}D_0 \sin \frac{3\theta_s}{2} \right) \left(\alpha_s + \frac{1}{\alpha_s} \right) \\
& - \frac{\zeta \cos \beta(t)}{4} r_s^{1/2} \left(\frac{3}{4}B_0 \sin \frac{3\theta_s}{2} - \frac{3}{4}D_0 \cos \frac{3\theta_s}{2} \right) \left(1 + \frac{1}{\alpha_s^2} \right) - \frac{\zeta \sin \beta(t)}{4} r_s^{1/2} \left(3B_0 \cos \frac{\theta_s}{2} - 3D_0 \sin \frac{\theta_s}{2} \right) \left(-\alpha_s + \frac{1}{\alpha_s} \right) \\
& - \frac{\zeta \sin \beta(t)}{\delta + 2} \frac{\alpha_s r_s^{1/2}}{\alpha_l^2 - \alpha_s^2} \left(3B_0 \cos \frac{\theta_s}{2} - 3D_0 \sin \frac{\theta_s}{2} \right) \\
& + \frac{\zeta \cos \beta(t)}{\delta + 2} \frac{\alpha_s^2 r_s^{1/2}}{\alpha_l^2 - \alpha_s^2} \left(3B_0 \sin \frac{\theta_s}{2} + 3D_0 \cos \frac{\theta_s}{2} \right) \\
& + \zeta \delta \sin \beta(t) \frac{r_l^{1/2}}{\alpha_l^2 - \alpha_s^2} \left(-\frac{3}{2}A_0 \cos \frac{\theta_l}{2} - \frac{3}{2}C_0 \sin \frac{\theta_l}{2} \right) (1 + \alpha_l^2) \\
& - \zeta \delta \cos \beta(t) \frac{\alpha_l r_l^{1/2}}{\alpha_l^2 - \alpha_s^2} \left(-\frac{3}{2}A_0 \sin \frac{\theta_l}{2} + \frac{3}{2}C_0 \cos \frac{\theta_l}{2} \right) (1 + \alpha_l^2) \\
& + \frac{1}{4} \frac{\rho_0}{\mu_0} \frac{1}{\delta + 2} c^2 k r_l^{1/2} \left(-\frac{3}{2}A_0 \cos \frac{3\theta_l}{2} + \frac{3}{2}C_0 \sin \frac{3\theta_l}{2} \right) \\
& - \frac{1}{4} \frac{\rho_0}{\mu_0} c^2 k r_s^{1/2} \left(\frac{3}{4}B_0 \cos \frac{3\theta_s}{2} + \frac{3}{4}D_0 \sin \frac{3\theta_s}{2} \right) \left(\alpha_s + \frac{1}{\alpha_s} \right) \\
& - \frac{1}{4} \frac{\rho_0}{\mu_0} c^2 k r_s^{1/2} \left(3B_0 \cos \frac{\theta_s}{2} - 3D_0 \sin \frac{\theta_s}{2} \right) \left(-\alpha_s + \frac{1}{\alpha_s} \right)
\end{aligned}$$

$$\begin{aligned}
& -\frac{1}{8} \frac{\rho_0}{\mu_0} \frac{1}{\delta+2} \frac{c^2 k}{\alpha_i^2} r_i^{1/2} \left(\frac{3}{4} A_0 \cos \frac{7\theta_l}{2} + \frac{3}{2} A_0 \cos \frac{3\theta_l}{2} + 6A_0 \cos \frac{\theta_l}{2} - \frac{3}{4} C_0 \sin \frac{7\theta_l}{2} - \frac{3}{2} C_0 \sin \frac{3\theta_l}{2} + 6C_0 \sin \frac{\theta_l}{2} \right) \\
& + \frac{1}{8} \frac{\rho_0}{\mu_0} \frac{1}{\delta+2} c^2 k r_i^{1/2} \left(\frac{3}{4} A_0 \cos \frac{7\theta_l}{2} - \frac{3}{2} A_0 \cos \frac{3\theta_l}{2} + 6A_0 \cos \frac{\theta_l}{2} - \frac{3}{4} C_0 \sin \frac{7\theta_l}{2} + \frac{3}{2} C_0 \sin \frac{3\theta_l}{2} + 6C_0 \sin \frac{\theta_l}{2} \right) \\
& + \frac{1}{8} \frac{\rho_0}{\mu_0} \frac{c^2 k}{\alpha_s} r_s^{1/2} \left(-\frac{15}{2} B_0 \cos \frac{3\theta_s}{2} - \frac{15}{2} D_0 \sin \frac{3\theta_s}{2} \right) \\
& + \frac{1}{16} \frac{\rho_0}{\mu_0} c^2 k r_s^{1/2} \left(\frac{3}{4} B_0 \cos \frac{7\theta_s}{2} + \frac{3}{4} D_0 \sin \frac{7\theta_s}{2} \right) \left(-\frac{1}{\alpha_s^3} + \alpha_s \right) \\
& + \frac{1}{16} \frac{\rho_0}{\mu_0} c^2 k r_s^{1/2} \left(\frac{9}{2} B_0 \cos \frac{3\theta_s}{2} + \frac{9}{2} D_0 \sin \frac{3\theta_s}{2} \right) \left(\frac{1}{\alpha_s^3} + \alpha_s \right) \\
& - \frac{2\alpha_c}{\alpha_i^2 - 1} \frac{3\delta + 2}{\delta + 2} q_0 r^{1/2} \sin\left(\frac{\theta}{2}\right)
\end{aligned}$$

(A.3)

CHAPTER 3

TRANSIENT THERMO-MECHANICAL ANALYSIS OF DYNAMIC CURVING CRACKS IN FUNCTIONALLY GRADED MATERIALS

by

Sachin Gupta, Sandeep Abotula, Addis Kidane, Vijaya B. Chalivendra, Ravi Chona
and Arun Shukla

has been published in Acta Mechanica

Corresponding Author: Arun Shukla

Dynamic Photo Mechanics Laboratory

Department of Mechanical, Industrial and Systems

Engineering

University of Rhode Island

206 Wales Hall, 92 Upper College Rd

Kingston, RI, 02881, USA

Phone: +1-401-874-2283

Email Address: shuklaa@egr.uri.edu

Abstract

Mixed-mode dynamic crack growth behavior along an arbitrarily smoothly varying path in functionally graded materials (FGMs) under transient thermo-mechanical loading is studied. Asymptotic analysis in conjunction with displacement potentials is used to develop transient thermo-mechanical stress fields around the propagating crack-tip. Asymptotic temperature field equations are derived for exponentially varying thermal properties, and later these equations are used to derive transient thermo-mechanical stress fields for a curving crack in FGMs. The effect of transient parameters (loading rate, crack-tip acceleration, and temperature change) and temperature gradient on the maximum principal stress and circumferential stress associated with the propagating crack-tip is discussed. Finally, using the minimum strain energy density criterion, the effect of temperature gradient, crack-tip speeds and T-stress on crack growth directions are determined and discussed.

Keywords: Functionally graded materials, thermo-mechanical loading, transient crack growth, mixed-mode, curving cracks, exponential property gradation

1. Introduction

Functionally Graded Materials (FGMs) are non-homogeneous composites which have spatially varying microstructure and mechanical/thermal properties to meet desired functional performance [1, 2]. FGMs used in high temperature applications have metals and ceramics as their constituents and thus have both thermal and mechanical non-homogeneities. These materials can withstand high temperatures

effectively due to superior thermal properties of ceramics, and at the same time high strength can be achieved with the presence of metal. Several studies on the superior in-service advantages of FGMs over traditional duplex coatings under high temperature and high thermal cycling conditions have been reported. In their studies, Kawasaki and Wananabe [3], and Drake et al. [4] reported that the thermal residual stresses are relaxed in metal-ceramic layered materials by inserting a functionally graded interface layer between the metal and ceramic. Kudora et al. [5] and Takahashi et al. [6] reported that FGM coatings suffer significantly less damage than conventional ceramic coatings, under thermal shock condition.

Several studies on the quasi-static fracture behavior of FGMs under thermo-mechanical loading have been reported. Assuming exponential variation of material properties, Jin and Noda [7] investigated the steady thermal stress intensity factors in functionally graded semi-infinite space with an edge crack subjected to a thermal load. Later, Erdogan and Wu [8] also determined the steady thermal stress intensity factor of a FGM layer with a surface crack perpendicular to the boundaries. By further assuming the exponential variation of thermal and mechanical properties of the materials, Jin and Batra [9] investigated the stress intensity relaxation problem at the tip of an edge crack in a FGM subjected to a thermal shock. Using both experimental and numerical techniques, Kokini and Choules [10], and Kokini and Case [11] studied surface and interface cracking in FGM coatings subjected to thermal shocks. Jin and Paulino [12] studied transient thermal stresses in an FGM with an edge crack and having a constant Young's modulus and Poisson's ratio, but varying thermal properties along the thickness direction. Walters et al. [13] developed general domain

integral methods to obtain stress intensity factors for surface cracks in FGMs under mode-I thermo-mechanical loading conditions. Zhang and Kim [14] used a complex variable approach to characterize the higher order terms for stationary crack-tip fields in FGMs. Clements [15] analyzed the antiplane crack problem for inhomogeneous anisotropic elastic FGMs.

The above studies provide closed form solutions for stress intensity factors under thermo-mechanical loading, however, for extracting fracture parameters from experimental studies, asymptotic expansion of thermo-mechanical stress fields around the crack-tip is essential. Jain et al. [16] developed quasi-static stress and displacement fields for a crack in an infinite FGM medium under thermo-mechanical loading. Lee et al. [17] developed analytical expressions for dynamic crack-tip stress and displacement fields under thermo-mechanical loading in FGMs. Recently, Kidane et al. [18] developed the thermo-mechanical stress fields for a mixed mode propagating crack with a constant velocity along the gradation direction. Also, Chalivendra et al. [19] developed the elastic mechanical stress field solutions for an inclined propagating transient crack in FGMs. Even though the above mentioned studies of dynamic thermo-mechanical asymptotic field equations serve the purpose of obtaining fracture parameters from experimental data, these studies have not incorporated the crack path curvature associated with a propagating crack in these materials. It has been reported in the experimental and numerical studies that the propagating cracks follow curved paths under various loading conditions due to the spatial variation of properties in graded materials [20-23]. In order to extract the fracture parameters accurately from the experimental data associated with curved cracks, it is essential to consider

curvature terms in the field equations. Liu and Rosakis [24] developed the higher-order asymptotic expansion of a non-uniformly propagating dynamic crack along an arbitrary curved path for homogeneous materials and they emphasized the importance of the curvature terms when experimental data points are considered away from the singularity zone to extract fracture parameters. Recently, Chalivendra [25] developed crack-tip out of plane displacement field equations for transient curved cracks in FGMs. However, asymptotic expansion of near-tip field equations for a curving crack under transient thermo-mechanical loading conditions has not yet been reported.

In this paper, through an asymptotic analysis, the transient stress and displacement fields for a curving crack propagating at varying velocity in FGMs are developed. The thermal and mechanical properties are assumed to vary exponentially along the gradation direction. The mode-mixity due to the inclination of curved crack with respect to property gradient is accommodated in the analysis through the superposition of opening and shear modes. First, the three terms of stress fields are developed and then the effect of transient parameters on the maximum principal stress, circumferential stress and crack extension angle is discussed.

2. Theoretical Formulation

FGMs can be treated as isotropic non-homogeneous solids because, at a continuum level, the properties at any given point in an FGM can be assumed to be the same in all directions. Non-homogeneity at the grain-size level is not considered in the formulation of the problem. Spatial variation of elastic properties, mass density, thermal properties, inclination of the curved crack with respect to the gradation direction and transient conditions make analytical solutions to the elasto-dynamic

equations extremely difficult. Hence, an asymptotic analysis similar to that employed by Freund [26] is used to expand the stress field around a propagating crack under thermo-mechanical loading conditions.

Isotropic linear elastic FGM, containing a propagating curving crack with temperature gradient in the x - y two-dimensional plane is shown in Fig. 1. At time $t = 0$, the crack-tip happens to be at the origin of Cartesian coordinate system x - y . For any time $t > 0$, the position of the propagating crack-tip is supposed to be given by $(X(t)$ and $Y(t))$ as shown in Fig. 1. The crack is propagating with a varying velocity (c) as a function of time. It was identified in previous the experimental studies [27-28] that the variation of mechanical properties of laboratory-fabricated FGMs can be fitted by an exponential curve. Thus, the shear modulus (μ), Lamé's constant (λ), and density (ρ), are assumed to vary in an exponential manner as given by Eq. (1a)-(1c). The thermal properties, namely thermal expansion (α), heat conductivity (k) and heat capacity(C) are assumed to vary exponential as given by Eq. (1d)-(1f). Two different non-homogeneity parameters were used for the thermal properties, where γ_1 was used for thermal expansion, and γ_2 was used for both heat conductivity and heat capacity.

$$\mu = \mu_0 \exp(\zeta x) \quad (1a)$$

$$\lambda = \lambda_0 \exp(\zeta x) \quad (1b)$$

$$\rho = \rho_0 \exp(\zeta x) \quad (1c)$$

$$\alpha = \alpha_0 \exp(\gamma_1 x) \quad (1d)$$

$$k = k_0 \exp(\gamma_2 x) \quad (1e)$$

$$C = C_0 \exp(\gamma_2 x) \quad (1f)$$

where ζ , γ_1 and γ_2 are non-homogeneity constants that have the dimension $(\text{length})^{-1}$.

Each physical variable can have a different non-homogeneity parameter. However for mathematical simplicity only three non-homogeneity parameters, one for mechanical properties and two for thermal properties, are considered. Let u and v , functions of x , y and t , represent the displacement field in x and y directions, respectively, with t representing the time. The Hooke's law for a plane strain thermo-mechanical problem can be written as

$$\sigma_{xx} = \exp(\zeta x) [\lambda_0 + 2\mu_0) \varepsilon_{xx} + \lambda_0 \varepsilon_{yy} - (3\lambda_0 + 2\mu_0) \alpha_0 \exp(\gamma_1 x) T] \quad (2a)$$

$$\sigma_{yy} = \exp(\zeta x) [\lambda_0 \varepsilon_{xx} + (\lambda_0 + 2\mu_0) \varepsilon_{yy} - (3\lambda_0 + 2\mu_0) \alpha_0 \exp(\gamma_1 x) T] \quad (2b)$$

$$\tau_{xy} = \exp(\zeta x) \mu_0 \gamma_{xy} \quad (2c)$$

where x and y are reference coordinates, σ_{ij} and ε_{ij} (where $i = x, y$ and $j = x, y$) are

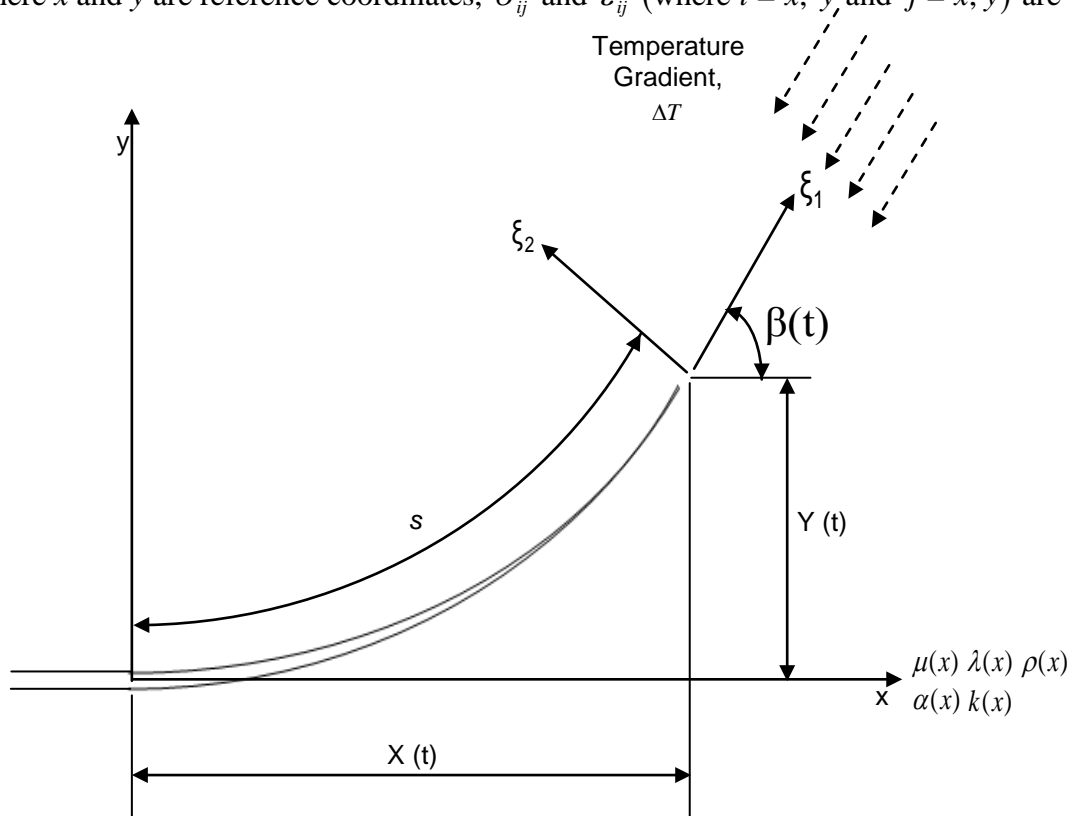


Fig. 1 Propagating curved crack orientation with respect to property gradation direction and temperature gradient.

in-plane stress and strain components, and subscript “o” denotes at $x=0$ as shown in Fig.1. T represents the change in temperature in the infinite medium.

The equations of motion of a plane problem can be written as

$$\frac{\partial \sigma_{xx}}{\partial x} + \frac{\partial \tau_{xy}}{\partial y} = \rho \frac{\partial^2 u}{\partial t^2} \quad (3a)$$

$$\frac{\partial \tau_{xy}}{\partial x} + \frac{\partial \sigma_{yy}}{\partial y} = \rho \frac{\partial^2 v}{\partial t^2} \quad (3b)$$

For a plane strain deformation, the displacements u and v are derived from the dilatational and shear wave potentials ϕ and ψ . These potentials can be expressed as

$$u = \frac{\partial \phi}{\partial x} + \frac{\partial \psi}{\partial y}, \quad v = \frac{\partial \phi}{\partial y} - \frac{\partial \psi}{\partial x} \quad (4)$$

Substituting the displacement relations into the stress expressions in Eq. (2), and then substituting these stresses into the equations of motion (Eq. 3), after simplification, we get

$$\begin{aligned} & (\delta + 2)\nabla^2 \phi + \zeta \left((\delta + 2) \frac{\partial}{\partial x} \phi + \frac{\partial}{\partial y} \psi \right) \\ & - \alpha_0 (3\delta + 2) \left(\left\{ \gamma_1 \zeta \Delta^{-1} T + (2\gamma_1 + \zeta + \gamma_1 \zeta x) \Delta^{-1} \frac{\partial T}{\partial x} \right\} + (1 + \gamma_1 x) T \right) = \frac{\rho_0}{\mu_0} \frac{\partial^2 \phi}{\partial t^2} \end{aligned} \quad (5a)$$

$$\nabla^2 \psi + \xi \frac{\partial \psi}{\partial x} + \xi \delta \frac{\partial \phi}{\partial y} - \alpha_0 (3\delta + 2) (\zeta + \zeta \gamma_1 x) \Delta^{-1} \frac{\partial T}{\partial y} = \frac{\rho_0}{\mu_0} \frac{\partial^2 \psi}{\partial t^2} \quad (5b)$$

where $\Delta^{-1} = \frac{1}{\nabla^2}$, $\delta = \frac{\lambda_0}{\mu_0}$ and $\nabla^2 = \frac{\partial^2}{\partial x^2} + \frac{\partial^2}{\partial y^2}$

Now, a new moving coordinate system (ξ_1, ξ_2) is introduced, so that the origin of the new system is at the moving crack-tip. The ξ_1 -axis is tangential to the crack

trajectory at the crack-tip and coincides with the direction of the crack growth. The crack is propagating with varying velocity (c) as a function of time along the local ξ_1 -direction. The angle between ξ_1 -axis and the fixed x -axis are denoted by $\beta(t)$, as shown in Fig. 1. Therefore the relationship between the coordinates in these two Cartesian co-ordinate systems is

$$\begin{aligned}\xi_1 &= \{x - X(t)\}\cos\beta(t) + \{y - Y(t)\}\sin\beta(t) \\ \xi_2 &= -\{x - X(t)\}\sin\beta(t) + \{y - Y(t)\}\cos\beta(t)\end{aligned}\quad (6)$$

If the length of the trajectory that the crack-tip travels during the time interval, $[0, t]$, is denoted by $s(t)$, then the magnitude of the crack-tip speed $c(t)$ will be $\dot{s}(t)$, and the curvature of the crack trajectory at the crack-tip, $k(t)$, is given by

$$k(t) = \frac{d\beta(t)}{ds} = \frac{\dot{\beta}(t)}{c(t)} \quad (7)$$

where $c(t) = \sqrt{\dot{X}(t)^2 + \dot{Y}(t)^2}$

Using the transformations and the relations given below in Eqs. (8)-(10), the equations of motion (5a) and (5b) are further written in the crack-tip moving coordinate reference (ξ_1, ξ_2) as given in Eqs. (11a) and (11b).

$$\frac{\partial^2}{\partial x^2} + \frac{\partial^2}{\partial y^2} = \frac{\partial^2}{\partial \xi_1^2} + \frac{\partial^2}{\partial \xi_2^2} \quad (8)$$

$$\frac{\partial^2}{\partial t^2} = \frac{\partial^2}{\partial \xi_i \partial \xi_j} \dot{\xi}_i \dot{\xi}_j + \frac{\partial}{\partial \xi_i} \ddot{\xi}_i + 2 \frac{\partial^2}{\partial \xi_i \partial t} \dot{\xi}_i + \frac{\partial^2}{\partial t^2}, \quad \text{where } i = 1, 2 \text{ and } j = 1, 2 \quad (9)$$

where

$$\begin{aligned}
\dot{\xi}_1 &= -c(t) + \dot{\beta}(t)\xi_2 = -c(t) + c(t)k(t)\xi_2 \\
\dot{\xi}_2 &= -\dot{\beta}(t)\xi_1 = -c(t)k(t)\xi_1 \\
\ddot{\xi}_1 &= (k(t)\xi_2 - 1)\dot{c}(t) + c(t)\dot{k}(t)\xi_2 - c^2(t)k^2(t)\xi_1 \\
\ddot{\xi}_2 &= -\dot{c}(t)k(t)\xi_1 - c(t)\dot{k}(t)\xi_1 + c^2(t)k(t) - c^2(t)k^2(t)\xi_2
\end{aligned} \tag{10}$$

$$\begin{aligned}
&\alpha_l^2 \frac{\partial^2 \phi}{\partial \xi_1^2} + \frac{\partial^2 \phi}{\partial \xi_2^2} + \zeta \left(\cos \beta(t) \frac{\partial \phi}{\partial \xi_1} - \sin \beta(t) \frac{\partial \phi}{\partial \xi_2} \right) + \frac{\zeta}{\delta + 2} \left(\sin \beta(t) \frac{\partial \psi}{\partial \xi_1} + \cos \beta(t) \frac{\partial \psi}{\partial \xi_2} \right) - \\
&\frac{\rho_0}{\mu_0(\delta + 2)} \left[(c^2 k^2 \xi_2^2 - 2c^2 k \xi_2) \frac{\partial^2 \phi}{\partial \xi_1^2} + c^2 k^2 \xi_1^2 \frac{\partial^2 \phi}{\partial \xi_2^2} + (2c^2 k \xi_1 - 2c^2 k^2 \xi_1 \xi_2) \frac{\partial^2 \phi}{\partial \xi_1 \partial \xi_2} + \right. \\
&\left. [(K \xi_2 - 1)\dot{c} + c \dot{k} \xi_2 - c^2 k^2 \xi_1] \frac{\partial \phi}{\partial \xi_1} + (-\dot{c} k \xi_1 - c \dot{k} \xi_1 + c^2 k - c^2 k^2 \xi_2) \frac{\partial \phi}{\partial \xi_2} \right. \\
&\left. + 2(-c + c k \xi_2) \frac{\partial^2 \phi}{\partial \xi_1 \partial t} - 2c k \xi_1 \frac{\partial^2 \phi}{\partial \xi_2 \partial t} + \frac{\partial^2 \phi}{\partial t^2} \right] \\
&- \alpha_0 \frac{(3\delta + 2)}{\delta + 2} \left((1 + \gamma_1 x) T + \left\{ \gamma_1 \zeta \Delta^1 T + (2\gamma_1 + \zeta + \gamma_1 \zeta x) \Delta^1 \left(\cos \beta(t) \frac{\partial T}{\partial \xi_1} - \sin \beta(t) \frac{\partial T}{\partial \xi_2} \right) \right\} \right) = 0
\end{aligned} \tag{11a}$$

$$\begin{aligned}
&\alpha_s^2 \frac{\partial^2 \psi}{\partial \xi_1^2} + \frac{\partial^2 \psi}{\partial \xi_2^2} + \zeta \left(\cos \beta(t) \frac{\partial \psi}{\partial \xi_1} - \sin \beta(t) \frac{\partial \psi}{\partial \xi_2} \right) + \zeta \delta \left(\sin \beta(t) \frac{\partial \phi}{\partial \xi_1} + \cos \beta(t) \frac{\partial \phi}{\partial \xi_2} \right) - \\
&\frac{\rho_0}{\mu_0} \left[(c^2 k^2 \xi_2^2 - 2c^2 k \xi_2) \frac{\partial^2 \psi}{\partial \xi_1^2} + c^2 k^2 \xi_1^2 \frac{\partial^2 \psi}{\partial \xi_2^2} + (2c^2 k \xi_1 - 2c^2 k^2 \xi_1 \xi_2) \frac{\partial^2 \psi}{\partial \xi_1 \partial \xi_2} + \right. \\
&\left. [(K \xi_2 - 1)\dot{c} + c \dot{k} \xi_2 - c^2 k^2 \xi_1] \frac{\partial \psi}{\partial \xi_1} + (-\dot{c} k \xi_1 - c \dot{k} \xi_1 + c^2 k - c^2 k^2 \xi_2) \frac{\partial \psi}{\partial \xi_2} \right. \\
&\left. + 2(-c + c k \xi_2) \frac{\partial^2 \psi}{\partial \xi_1 \partial t} - 2c k \xi_1 \frac{\partial^2 \psi}{\partial \xi_2 \partial t} + \frac{\partial^2 \psi}{\partial t^2} \right] \\
&- \alpha_0 (3\delta + 2) (\zeta + \zeta \gamma_1 x) \Delta^1 \left(\sin \beta(t) \frac{\partial T}{\partial \xi_1} + \cos \beta(t) \frac{\partial T}{\partial \xi_2} \right) = 0
\end{aligned} \tag{11b}$$

$$\text{where } \alpha_l = \sqrt{1 - \frac{\rho_0 c^2}{\mu_0(\delta + 2)}}, \alpha_s = \sqrt{1 - \frac{\rho_0 c^2}{\mu_0}}, x = X(t) + \xi_1 \cos \beta(t) - \xi_2 \sin \beta(t) \tag{12}$$

It is assumed that the crack velocity c is a function of time for transient crack growth, and the potentials ϕ and ψ explicitly depend on the time in the moving coordinate reference.

2.1 Temperature Field around the Crack-tip

In this analysis, it is assumed that the temperature field around the crack-tip changes asymptotically. The general heat conduction equation for isotropic materials can be written as

$$\frac{\partial}{\partial x} \left(k \frac{\partial T}{\partial x} \right) + \frac{\partial}{\partial y} \left(k \frac{\partial T}{\partial y} \right) = \rho C \frac{\partial T}{\partial t} \quad (13)$$

Density (ρ), heat conductivity (k), and heat capacity (C) are assumed to vary exponentially as given by Eqs. (1c), (1e) and (1f). The simplified equation can be expressed as

$$\alpha_{to} \left(\nabla^2 T + \gamma_2 \frac{\partial T}{\partial x} \right) = \exp(\zeta x) \frac{\partial T}{\partial t} \quad (14)$$

where $\frac{k_0}{\rho_0 C_0} = \alpha_{to}$, $\nabla^2 = \frac{\partial^2}{\partial x^2} + \frac{\partial^2}{\partial y^2}$

For the simplification of Eq. (14), the exponential term on the right-hand side is expanded using Taylor series.

$$\exp(\zeta x) = 1 + \zeta x + \frac{(\zeta x)^2}{2!} + \dots \quad (15)$$

In the vicinity of the crack-tip, higher order terms having exponential 2 or more can be neglected, which leads to the equation

$$\nabla^2 T + \gamma_2 \frac{\partial T}{\partial x} = \frac{1}{\alpha_{to}} \left(\frac{\partial T}{\partial t} + \zeta x \frac{\partial T}{\partial t} \right) \quad (16)$$

Transforming the above equation into the moving crack-tip coordinates, it can be written as

$$\nabla^2 T + \gamma_2 \left(\cos \beta(t) \frac{\partial T}{\partial \xi_1} - \sin \beta(t) \frac{\partial T}{\partial \xi_2} \right) = \frac{(1 + \zeta x)}{\alpha_{to}} \left(\frac{\partial T}{\partial \xi_1} (-c + ck\xi_2) - ck\xi_1 \frac{\partial T}{\partial \xi_2} + \frac{\partial T}{\partial t} \right) \quad (17)$$

where $\nabla^2 = \frac{\partial^2}{\partial \xi_1^2} + \frac{\partial^2}{\partial \xi_2^2}$, $x = X(t) + \xi_1 \cos \beta(t) - \xi_2 \sin \beta(t)$

At this stage, the asymptotic analysis is performed to solve the above Eq. (17). The advantages of this approach are: (i) it does not consider finite specimen geometry, and (ii) it does not need the information of the external loading boundary conditions. It requires only crack-face and crack-line boundary conditions associated with the propagating crack to be satisfied. In this process, first a new set of scaled coordinates is defined as

$$\eta_1 = \xi_1 / \varepsilon, \quad \eta_2 = \xi_2 / \varepsilon \quad (18)$$

where ε is an arbitrary parameter and is assumed to be $0 < \varepsilon < 1$.

In the scaled coordinates, Eq. (17) can be written as

$$\begin{aligned}
\nabla^2 T + \gamma_2 \varepsilon \left(\cos \beta(t) \frac{\partial T}{\partial \eta_1} - \sin \beta(t) \frac{\partial T}{\partial \eta_2} \right) &= \left(\frac{1}{\alpha_{\iota_0}} \right) \left(\begin{array}{l} -c\varepsilon \frac{\partial T}{\partial \eta_1} + ck\eta_2 \varepsilon^2 \frac{\partial T}{\partial \eta_1} \\ -ck\eta_1 \varepsilon^2 \frac{\partial T}{\partial \eta_2} + \varepsilon^2 \frac{\partial T}{\partial t} \end{array} \right) + \\
\left(\frac{\zeta}{\alpha_{\iota_0}} \right) &\left(\begin{array}{l} -c\varepsilon X(t) \frac{\partial T}{\partial \eta_1} + ck\eta_2 \varepsilon^2 X(t) \frac{\partial T}{\partial \eta_1} - ck\eta_1 \varepsilon^2 X(t) \frac{\partial T}{\partial \eta_2} + \varepsilon^2 X(t) \frac{\partial T}{\partial t} \\ -c\eta_1 \varepsilon^2 \cos \beta(t) \frac{\partial T}{\partial \eta_1} + ck\eta_1 \eta_2 \cos \beta(t) \varepsilon^3 \frac{\partial T}{\partial \eta_1} - ck\eta_1^2 \varepsilon^3 \cos \beta(t) \frac{\partial T}{\partial \eta_2} \\ + \eta_1 \varepsilon^3 \cos \beta(t) \frac{\partial T}{\partial t} + c\eta_2 \varepsilon^2 \sin \beta(t) \frac{\partial T}{\partial \eta_1} - ck\eta_2^2 \sin \beta(t) \varepsilon^3 \frac{\partial T}{\partial \eta_1} \\ + ck\eta_1 \eta_2 \varepsilon^3 \sin \beta(t) \varepsilon^3 \frac{\partial T}{\partial \eta_2} - \eta_2 \varepsilon^3 \sin \beta(t) \frac{\partial T}{\partial t} \end{array} \right)
\end{aligned} \tag{19}$$

For the asymptotic analysis, T is now represented as a power series expansion in ε .

$$T(\xi_1, \xi_2) = T(\varepsilon\eta_1, \varepsilon\eta_2) = \sum_{m=0}^{\infty} \varepsilon^{\frac{m+1}{2}} T_m(\eta_1, \eta_2) \tag{20}$$

Substituting the above infinite series expansion in Eq. (19) results in

$$\left. \begin{aligned}
& \varepsilon^{\frac{m+1}{2}} \left(\frac{\partial^2 T_m}{\partial \eta_1^2} + \frac{\partial^2 T_m}{\partial \eta_2^2} \right) + \varepsilon^{\frac{m+3}{2}} \gamma_2 \left[\left(\cos \beta(t) \frac{\partial T_m}{\partial \eta_1} - \sin \beta(t) \frac{\partial T_m}{\partial \eta_2} \right) + \right. \\
& \left. \left(\frac{1}{\alpha_{\iota_0}} \right) \left(c \frac{\partial T_m}{\partial \eta_1} + \zeta c X(t) \frac{\partial T_m}{\partial \eta_1} \right) \right] \\
& + \varepsilon^{\frac{m+5}{2}} \left(\frac{1}{\alpha_{\iota_0}} \right) \left[\begin{aligned}
& ck\eta_1 \frac{\partial T_m}{\partial \eta_2} - ck\eta_2 \frac{\partial T_m}{\partial \eta_1} - \frac{\partial T_m}{\partial t} - \zeta X(t) ck\eta_2 \frac{\partial T_m}{\partial \eta_1} \\
& + \zeta X(t) ck\eta_1 \frac{\partial T_m}{\partial \eta_2} - \zeta X(t) \frac{\partial T_m}{\partial t} + \zeta X(t) c\eta_1 \cos \beta(t) \frac{\partial T_m}{\partial \eta_1} \\
& - \zeta X(t) c\eta_2 \sin \beta(t) \frac{\partial T_m}{\partial \eta_1}
\end{aligned} \right] \\
& + \varepsilon^{\frac{m+7}{2}} \left(\frac{\zeta}{\alpha_{\iota_0}} \right) \left[\begin{aligned}
& - ck\eta_1 \eta_2 \cos \beta(t) \frac{\partial T_m}{\partial \eta_1} + ck\eta_1^2 \cos \beta(t) \frac{\partial T_m}{\partial \eta_2} \\
& - \eta_1 \cos \beta(t) \frac{\partial T_m}{\partial t} + ck\eta_2^2 \sin \beta(t) \frac{\partial T_m}{\partial \eta_1} \\
& - ck\eta_1 \eta_2 \sin \beta(t) \frac{\partial T_m}{\partial \eta_2} + \eta_2 \sin \beta(t) \frac{\partial T_m}{\partial t}
\end{aligned} \right]
\end{aligned} \right\} = 0$$

(21)

For Eq. (21) to be valid, the partial differential equations corresponding to each power of ε ($\varepsilon^{1/2}$, ε , $\varepsilon^{3/2}$, ...) should vanish independently. This leads to a set of partial differential equations.

For $m = 0$ and 1

$$\frac{\partial^2 T_m}{\partial \eta_1^2} + \frac{\partial^2 T_m}{\partial \eta_2^2} = 0$$

(22)

For $m = 2$ and 3

$$\frac{\partial^2 T_m}{\partial \eta_1^2} + \frac{\partial^2 T_m}{\partial \eta_2^2} + \gamma_2 \left(\cos \beta(t) \frac{\partial T_{m-2}}{\partial \eta_1} - \sin \beta(t) \frac{\partial T_{m-2}}{\partial \eta_2} \right) + \left(\frac{1 + \zeta X(t)}{\alpha_{\iota_0}} \right) \left(c \frac{\partial T_{m-2}}{\partial \eta_1} \right) = 0$$

(23)

For $m = 4$ and 5

$$\begin{aligned}
& \frac{\partial^2 T_m}{\partial \eta_1^2} + \frac{\partial^2 T_m}{\partial \eta_2^2} + \gamma_2 \left(\cos \beta(t) \frac{\partial T_{m-2}}{\partial \eta_1} - \sin \beta(t) \frac{\partial T_{m-2}}{\partial \eta_2} \right) + \left(\frac{1 + \zeta X(t)}{\alpha_{io}} \right) \left(c \frac{\partial T_{m-2}}{\partial \eta_1} \right) \\
& + \left(\frac{1}{\alpha_{io}} \right) \left(\begin{aligned}
& ck\eta_1 \frac{\partial T_{m-4}}{\partial \eta_2} - ck\eta_2 \frac{\partial T_{m-4}}{\partial \eta_1} - \frac{\partial T_{m-4}}{\partial t} - \zeta X(t) ck\eta_2 \frac{\partial T_{m-4}}{\partial \eta_1} \\
& + \zeta X(t) ck\eta_1 \frac{\partial T_{m-4}}{\partial \eta_2} - \zeta X(t) \frac{\partial T_{m-4}}{\partial t} + \zeta X(t) c\eta_1 \cos \beta(t) \frac{\partial T_{m-4}}{\partial \eta_1} \\
& - \zeta X(t) c\eta_2 \sin \beta(t) \frac{\partial T_{m-4}}{\partial \eta_1}
\end{aligned} \right) = 0
\end{aligned} \tag{24}$$

The homogeneous solutions for the temperature field can be written in the form of $\rho^i \cos j\theta$ or $\rho^i \sin j\theta$, where i and j are arbitrary real numbers. The solutions for Eqs. (23) and (24) corresponding to the higher powers of ε (12) consist of two parts: the classical solution and the solution due to non-homogeneity, and the latter can be obtained recursively. The details of the procedure are given in Kidane et al. [18]. The temperature field solution (first 3 terms) including the non-homogeneity parameters and the transient term ($\dot{q}_0(t)$) can be written as

$$\begin{aligned}
T = & q_0(t)r^{1/2} \cos \frac{\theta}{2} + q_1(t)r \sin \theta + q_2 r^{3/2} \cos \frac{3\theta}{2} + \frac{1}{4} \gamma_2 q_0(t)r^{3/2} \\
& \left(\sin \beta(t) \sin \frac{\theta}{2} - \cos \beta(t) \cos \frac{\theta}{2} \right) - \left(\frac{1 + \zeta X(t)}{4\alpha_{io}} \right) c q_0(t)r^{3/2} \cos \frac{\theta}{2} + \left(\frac{1 + \zeta X(t)}{6\alpha_{io}} \right) \dot{q}_0(t)r^{5/2} \cos \frac{\theta}{2}
\end{aligned} \tag{25}$$

where $\rho = \left(\eta_1^2 + \eta_2^2 \right)^{1/2}$ and $\theta = \tan^{-1} \frac{\eta_2}{\eta_1}$

The full solution of the temperature field is attached in the Appendix (A1).

2.2 Asymptotic Expansion of Crack-tip Stress Fields

A process similar to the asymptotic approach used for deriving the temperature field around the crack-tip is used for deriving solutions of the displacement potentials of the equations of motion. The scaled coordinates discussed in Eq. (18) are now applied to Eqs. (11a) and (11b) as given below

$$\begin{aligned}
& \alpha_i^2 \frac{\partial^2 \phi}{\partial \eta_1^2} + \frac{\partial^2 \phi}{\partial \eta_2^2} + \varepsilon \zeta \left(\cos \beta(t) \frac{\partial \phi}{\partial \eta_1} - \sin \beta(t) \frac{\partial \phi}{\partial \eta_2} \right) + \frac{\varepsilon \zeta}{\delta + 2} \left(\sin \beta(t) \frac{\partial \psi}{\partial \eta_1} + \cos \beta(t) \frac{\partial \psi}{\partial \eta_2} \right) - \\
& \left. \begin{aligned}
& \left((c^2 k^2 \varepsilon^2 \eta_2^2 - 2c^2 k \varepsilon \eta_2) \frac{\partial^2 \phi}{\partial \eta_1^2} + c^2 k^2 \varepsilon^2 \eta_1^2 \frac{\partial^2 \phi}{\partial \eta_2^2} + (2c^2 k \eta_1 \varepsilon - 2c^2 k^2 \eta_1 \eta_2 \varepsilon^2) \right. \\
& \frac{\rho_0}{\mu_0 (\delta + 2)} \left. \frac{\partial^2 \phi}{\partial \eta_1 \partial \eta_2} + [(K \eta_2 \varepsilon^2 - \varepsilon) \dot{c}] + c \dot{k} \eta_2 \varepsilon^2 - c^2 k^2 \eta_1 \varepsilon^2 \right] \frac{\partial \phi}{\partial \eta_1} + (-\dot{c} k \eta_1 \varepsilon^2 - c \dot{k} \eta_1 \varepsilon^2 \\
& + c^2 k \varepsilon - c^2 k^2 \eta_2 \varepsilon^2) \frac{\partial \phi}{\partial \eta_2} + 2(-c \varepsilon + c k \eta_2 \varepsilon^2) \frac{\partial^2 \phi}{\partial \eta_1 \partial t} - 2c k \eta_1 \varepsilon^2 \frac{\partial^2 \phi}{\partial \eta_2 \partial t} \\
& \left. + \varepsilon^2 \frac{\partial^2 \phi}{\partial t^2} \right) \\
& - \alpha_0 \frac{(3\delta + 2)}{\delta + 2} \left(\begin{aligned}
& (1 + \gamma_1 X(t)) \varepsilon^2 T + \varepsilon^3 \left[(2\gamma_1 + \zeta + \gamma_1 \zeta X(t)) \Delta^{-1} \left(\cos \beta(t) \frac{\partial T}{\partial \eta_1} - \sin \beta(t) \frac{\partial T}{\partial \eta_2} \right) + \right. \\
& \left. \gamma_1 T (\eta_1 \cos \beta(t) - \eta_2 \sin \beta(t)) \right] \\
& \left. + \varepsilon^4 \left\{ \gamma_1 \zeta \Delta^{-1} T + \left[\gamma_1 \zeta \Delta^{-1} \eta_1 \cos \beta(t) - \gamma_1 \zeta \Delta^{-1} \eta_2 \sin \beta(t) \right] \left(\begin{aligned}
& \cos \beta(t) \frac{\partial T}{\partial \eta_1} - \\
& \sin \beta(t) \frac{\partial T}{\partial \eta_2}
\end{aligned} \right) \right\} \right) = 0
\end{aligned} \right)
\end{aligned}
\tag{26a}$$

$$\begin{aligned}
& \alpha_s^2 \frac{\partial^2 \psi}{\partial \eta_1^2} + \frac{\partial^2 \psi}{\partial \eta_2^2} + \varepsilon \zeta \left(\cos \beta(t) \frac{\partial \psi}{\partial \eta_1} - \sin \beta(t) \frac{\partial \psi}{\partial \eta_2} \right) + \varepsilon \zeta \delta \left(\sin \beta(t) \frac{\partial \phi}{\partial \eta_1} + \cos \beta(t) \frac{\partial \phi}{\partial \eta_2} \right) - \\
& \left((c^2 k^2 \eta_2^2 \varepsilon^2 - 2c^2 k \eta_2 \varepsilon) \frac{\partial^2 \psi}{\partial \eta_1^2} + c^2 k^2 \eta_1^2 \varepsilon^2 \frac{\partial^2 \psi}{\partial \eta_2^2} + (2c^2 k \eta_1 \varepsilon - 2c^2 k^2 \eta_1 \eta_2 \varepsilon^2) \frac{\partial^2 \psi}{\partial \eta_1 \partial \eta_2} \right. \\
& \left. \frac{\rho_0}{\mu_0} + [(K \eta_2 \varepsilon^2 - \varepsilon) \dot{c}] + c k \eta_2 \varepsilon^2 - c^2 k^2 \eta_1 \varepsilon^2 \right] \frac{\partial \psi}{\partial \eta_1} + (-c k \eta_1 \varepsilon^2 - c k \eta_1 \varepsilon^2 \\
& \left. + c^2 k \varepsilon - c^2 k^2 \eta_2 \varepsilon^2) \frac{\partial \psi}{\partial \eta_2} + 2(-c \varepsilon + c k \eta_2 \varepsilon^2) \frac{\partial^2 \psi}{\partial \eta_1 \partial t} - 2c k \eta_1 \varepsilon^2 \frac{\partial^2 \psi}{\partial \eta_2 \partial t} + \varepsilon^2 \frac{\partial^2 \psi}{\partial t^2} \right) \\
& - \alpha_0 (3\delta + 2) \left\{ \varepsilon^3 \left[(\zeta + \zeta \gamma_1 X(t)) \Delta^{-1} \left(\sin \beta(t) \frac{\partial T}{\partial \eta_1} + \cos \beta(t) \frac{\partial T}{\partial \eta_2} \right) + \right. \right. \\
& \left. \left. \varepsilon^4 \left[(\zeta \gamma_1 \eta_1 \cos \beta(t) - \zeta \gamma_1 \eta_2 \sin \beta(t)) \Delta^{-1} \left(\sin \beta(t) \frac{\partial T}{\partial \eta_1} + \cos \beta(t) \frac{\partial T}{\partial \eta_2} \right) \right] \right\} = 0
\end{aligned} \tag{26b}$$

At this point, it is assumed that ϕ , ψ and T can be represented in the power series of ε .

$$\begin{aligned}
\phi(\xi_1, \xi_2) &= \phi(\varepsilon \eta_1, \varepsilon \eta_2) = \sum_{m=0}^{\infty} \varepsilon^{\frac{m+3}{2}} \phi_m(\eta_1, \eta_2) \\
\psi(\xi_1, \xi_2) &= \psi(\varepsilon \eta_1, \varepsilon \eta_2) = \sum_{m=0}^{\infty} \varepsilon^{\frac{m+3}{2}} \psi_m(\eta_1, \eta_2) \\
T(\xi_1, \xi_2) &= T(\varepsilon \eta_1, \varepsilon \eta_2) = \sum_{m=0}^{\infty} \varepsilon^{\frac{m+1}{2}} q_m(\eta_1, \eta_2)
\end{aligned} \tag{27}$$

Substituting the series expansions from Eq. (27) into Eq. (26) results in

$$\sum_{m=0}^{\infty} \left\{ \begin{aligned} & \varepsilon^{\frac{m+3}{2}} \left(\alpha_1^2 \frac{\partial^2 \phi_m}{\partial \eta_1^2} + \frac{\partial^2 \phi_m}{\partial \eta_2^2} \right) + \varepsilon^{\frac{m+5}{2}} \left[\zeta \left(\cos \beta(t) \frac{\partial \phi_m}{\partial \eta_1} - \sin \beta(t) \frac{\partial \phi_m}{\partial \eta_2} \right) + \right. \\ & \left. \frac{\zeta}{\delta+2} \left(\sin \beta(t) \frac{\partial \psi_m}{\partial \eta_1} + \cos \beta(t) \frac{\partial \psi_m}{\partial \eta_2} \right) \right] - \\ & \varepsilon^{\frac{m+5}{2}} \left[\frac{\rho_0}{\mu_0(\delta+2)} \left(-2c^2 k \eta_2 \frac{\partial^2 \phi_m}{\partial \eta_1^2} + 2c^2 k \eta_1 \frac{\partial^2 \phi_m}{\partial \eta_1 \partial \eta_2} - \dot{c} \frac{\partial \phi_m}{\partial \eta_1} + c^2 k \frac{\partial \phi_m}{\partial \eta_2} - 2c \frac{\partial^2 \phi_m}{\partial \eta_1 \partial t} \right) \right. \\ & \left. - \alpha_0 \frac{(3\delta+2)}{\delta+2} (1 + \gamma_1 X(t)) T_m \right] - \\ & \varepsilon^{\frac{m+7}{2}} \frac{\rho_0}{\mu_0(\delta+2)} \left[\begin{aligned} & c^2 k^2 \eta_2^2 \frac{\partial^2 \phi_m}{\partial \eta_1^2} + c^2 k^2 \eta_1^2 \frac{\partial^2 \phi_m}{\partial \eta_2^2} - 2c^2 k^2 \eta_1 \eta_2 \frac{\partial^2 \phi_m}{\partial \eta_1 \partial \eta_2} + k \dot{c} \eta_2 \frac{\partial \phi_m}{\partial \eta_1} + \\ & c k \eta_2 \frac{\partial \phi_m}{\partial \eta_1} - c^2 k^2 \eta_1 \frac{\partial \phi_m}{\partial \eta_1} - \dot{c} k \eta_1 \frac{\partial \phi_m}{\partial \eta_2} - c k \eta_1 \frac{\partial \phi_m}{\partial \eta_2} - c^2 k^2 \eta_2 \frac{\partial \phi_m}{\partial \eta_2} \\ & + 2c k \eta_2 \frac{\partial^2 \phi_m}{\partial \eta_1 \partial t} - 2c k \eta_1 \frac{\partial^2 \phi_m}{\partial \eta_2 \partial t} + \frac{\partial^2 \phi_m}{\partial t^2} - \\ & \left(\alpha_0 \frac{(3\delta+2)}{\delta+2} \right) (2\gamma_1 + \zeta + \zeta \gamma_1 X(t)) \Delta^{-1} \\ & \left(\cos \beta(t) \frac{\partial T_m}{\partial \eta_1} - \sin \beta(t) \frac{\partial T_m}{\partial \eta_2} \right) + \gamma_1 T(\eta_1 \cos \beta(t) - \eta_2 \sin \beta(t)) \end{aligned} \right] - \\ & - \varepsilon^{\frac{m+9}{2}} \left[\alpha_0 \frac{(3\delta+2)}{\delta+2} \left\{ \gamma_1 \zeta \Delta^{-1} T_m + \left[\left(\gamma_1 \zeta \Delta^{-1} \eta_1 \cos \beta(t) - \gamma_1 \zeta \Delta^{-1} \eta_2 \sin \beta(t) \right) \right] \right\} \right] \end{aligned} \right\} = 0$$

(28a)

$$\left. \begin{aligned}
& \left[\begin{aligned}
& \zeta \left(\cos \beta(t) \frac{\partial \psi_m}{\partial \eta_1} - \sin \beta(t) \frac{\partial \psi_m}{\partial \eta_2} \right) + \zeta \delta \begin{pmatrix} \sin \beta(t) \frac{\partial \phi_m}{\partial \eta_1} \\ + \cos \beta(t) \frac{\partial \phi_m}{\partial \eta_2} \end{pmatrix} \\
& - \frac{\rho_0}{\mu_0} \begin{pmatrix} -2c^2 k \eta_2 \frac{\partial^2 \psi_m}{\partial \eta_1^2} + 2c^2 k \eta_1 \frac{\partial^2 \psi_m}{\partial \eta_1 \partial \eta_2} - \dot{c} \frac{\partial \psi_m}{\partial \eta_1} + c^2 k \frac{\partial \psi_m}{\partial \eta_2} \\ -2c \frac{\partial^2 \psi_m}{\partial \eta_1 \partial t} \end{pmatrix} \end{aligned} \right] \\
\sum_{m=0}^{\infty} \left\{ \begin{aligned}
& \left[\begin{aligned}
& c^2 k^2 \eta_2^2 \frac{\partial^2 \psi_m}{\partial \eta_1^2} + c^2 k^2 \eta_1^2 \frac{\partial^2 \psi_m}{\partial \eta_2^2} - 2c^2 k^2 \eta_1 \eta_2 \frac{\partial^2 \psi_m}{\partial \eta_1 \partial \eta_2} + k \eta_2 \dot{c} \frac{\partial \psi_m}{\partial \eta_1} \\
& + \dot{c} k \eta_2 \frac{\partial \psi_m}{\partial \eta_1} - c^2 k^2 \eta_1 \frac{\partial \psi_m}{\partial \eta_1} - \dot{c} k \eta_1 \frac{\partial \psi_m}{\partial \eta_2} - \dot{c} k \eta_1 \frac{\partial \psi_m}{\partial \eta_2} - c^2 k^2 \eta_2 \frac{\partial \psi_m}{\partial \eta_2} + 2c k \eta_2 \frac{\partial^2 \psi_m}{\partial \eta_1 \partial t} \\
& - 2c k \eta_1 \frac{\partial^2 \psi_m}{\partial \eta_2 \partial t} + \frac{\partial^2 \psi_m}{\partial t^2} \end{aligned} \right] \\
& - \alpha_0 (3\delta + 2) \left[(\zeta + \zeta \gamma_1 X(t)) \Delta^{-1} \left(\sin \beta(t) \frac{\partial T_m}{\partial \eta_1} + \cos \beta(t) \frac{\partial T_m}{\partial \eta_2} \right) \right] \\
& - \alpha_0 (3\delta + 2) \left[(\zeta \gamma_1 \eta_1 \cos \beta(t) - \zeta \gamma_1 \eta_2 \sin \beta(t)) \Delta^{-1} \left(\sin \beta(t) \frac{\partial T_m}{\partial \eta_1} + \cos \beta(t) \frac{\partial T_m}{\partial \eta_2} \right) \right] \end{aligned} \right\} = 0
\end{aligned} \right. \tag{28b}$$

For Eqs. (28a) and (28b) to be valid, the partial differential equations corresponding to each power of ε ($\varepsilon^{1/2}$, ε , $\varepsilon^{3/2}$, ...) should vanish independently. This leads to the following set of partial differential equations.

For $m = 0$ and 1 ,

$$\alpha_l^2 \frac{\partial^2 \phi_m}{\partial \eta_1^2} + \frac{\partial^2 \phi_m}{\partial \eta_2^2} = 0 \tag{29a}$$

$$\alpha_s^2 \frac{\partial^2 \psi_m}{\partial \eta_1^2} + \frac{\partial^2 \psi_m}{\partial \eta_2^2} = 0 \tag{29b}$$

For $m = 2$ and 3 ,

$$\begin{aligned}
\alpha_l^2 \frac{\partial^2 \phi_m}{\partial \eta_1^2} + \frac{\partial^2 \phi_m}{\partial \eta_2^2} = & -\zeta \left(\cos \beta(t) \frac{\partial \phi_{m-2}}{\partial \eta_1} - \sin \beta(t) \frac{\partial \phi_{m-2}}{\partial \eta_2} \right) - \frac{\zeta}{\delta + 2} \left(\begin{aligned} & \sin \beta(t) \frac{\partial \psi_{m-2}}{\partial \eta_1} \\ & + \cos \beta(t) \frac{\partial \psi_{m-2}}{\partial \eta_2} \end{aligned} \right) + \\
\frac{\rho_0}{\mu_0(\delta + 2)} \left(-2c^2 k \eta_2 \frac{\partial^2 \phi_{m-2}}{\partial \eta_1^2} + 2c^2 k \eta_1 \frac{\partial^2 \phi_{m-2}}{\partial \eta_1 \partial \eta_2} - \dot{c} \frac{\partial \phi_{m-2}}{\partial \eta_1} + c^2 k \frac{\partial \phi_{m-2}}{\partial \eta_2} - 2c \frac{\partial^2 \phi_{m-2}}{\partial \eta_1 \partial t} \right) \\
+ \alpha_0 \frac{(3\delta + 2)}{\delta + 2} (1 + \gamma_1 X(t)) T_{m-2}
\end{aligned} \tag{30a}$$

$$\begin{aligned}
\alpha_s^2 \frac{\partial^2 \psi_m}{\partial \eta_1^2} + \frac{\partial^2 \psi_m}{\partial \eta_2^2} = & -\zeta \left(\cos \beta(t) \frac{\partial \psi_{m-2}}{\partial \eta_1} - \sin \beta(t) \frac{\partial \psi_{m-2}}{\partial \eta_2} \right) - \zeta \delta \left(\begin{aligned} & \sin \beta(t) \frac{\partial \phi_{m-2}}{\partial \eta_1} \\ & + \cos \beta(t) \frac{\partial \phi_{m-2}}{\partial \eta_2} \end{aligned} \right) + \\
\frac{\rho_0}{\mu_0} \left(-2c^2 k \eta_2 \frac{\partial^2 \psi_{m-2}}{\partial \eta_1^2} + 2c^2 k \eta_1 \frac{\partial^2 \psi_{m-2}}{\partial \eta_1 \partial \eta_2} - \dot{c} \frac{\partial \psi_{m-2}}{\partial \eta_1} + c^2 k \frac{\partial \psi_{m-2}}{\partial \eta_2} - 2c \frac{\partial^2 \psi_{m-2}}{\partial \eta_1 \partial t} \right)
\end{aligned} \tag{30b}$$

Equations (29a) and (29b) are similar to those for homogeneous material where as the partial differential equations (30a) and (30b), associated with higher powers of ε are coupled to the differentials of the lower order functions through the non-homogeneity parameter ζ , and the temperature term. Equations (29a) and (29b) (i.e. for $m = 0$ and $m = 1$) can be easily reduced to Laplace's equation in the respective complex domains $z_1 = \eta_1 + i\alpha_l \eta_2, z_2 = \eta_1 + i\alpha_s \eta_2, t = \sqrt{-1}$, and the solutions are same as those for homogenous materials [26, 29-33], and can be written as

$$\begin{aligned}
\phi_m(\rho_l, \theta_l, t) = & A_m \rho_l^{(m+3)/2} \cos \frac{1}{2}(m+3)\theta_l + C_m \rho_l^{(m+3)/2} \sin \frac{1}{2}(m+3)\theta_l \\
\psi_m(\rho_s, \theta_s, t) = & B_m \rho_s^{(m+3)/2} \sin \frac{1}{2}(m+3)\theta_s + D_m \rho_s^{(m+3)/2} \cos \frac{1}{2}(m+3)\theta_s
\end{aligned} \tag{31}$$

where $\rho_l = \left[\eta_l^2 + \alpha_l^2 \eta_2^2 \right]^{1/2}$, $\tan \theta_l = \frac{\alpha_l \eta_2}{\eta_1}$, $\rho_s = \left[\eta_s^2 + \alpha_s^2 \eta_2^2 \right]^{1/2}$, $\tan \theta_s = \frac{\alpha_s \eta_2}{\eta_1}$ and

A_m , C_m , B_m and D_m are real constants.

Using the definitions of dynamic stress intensity factors K_{ID} and K_{IID} for the opening mode and shear mode [26] as given in Eq. (32), the relation between $A_o(t)$ and $K_{ID}(t)$, $C_o(t)$ and $K_{IID}(t)$ are obtained.

$$K_{ID} = \lim_{x \rightarrow 0, y=0} \sqrt{2\pi x} \sigma_{yy} \quad , \quad K_{IID} = \lim_{x \rightarrow 0, y=0} \sqrt{2\pi x} \sigma_{xy} \quad (32)$$

$$A_o(t) = \frac{4(1 + \alpha_s^2)}{3(4\alpha_l\alpha_s - (1 + \alpha_s^2)^2)} \frac{K_{ID}(t)}{\mu_c \sqrt{2\pi}}, \quad B_o(t) = \frac{-2\alpha_l}{1 + \alpha_s^2} A_o(t) \quad (33a)$$

$$C_o(t) = \frac{8\alpha_s}{3(4\alpha_l\alpha_s - (1 + \alpha_s^2)^2)} \frac{K_{IID}(t)}{\mu_c \sqrt{2\pi}}, \quad D_o(t) = \frac{1 + \alpha_s^2}{2\alpha_s} C_o(t) \quad (33b)$$

where μ_c is the crack-tip shear modulus, $K_{ID}(t)$ and $K_{IID}(t)$ are the mode-I and mode-II dynamic stress intensity factors, respectively.

In order to extract both mode-I and mode-II stress intensity factors accurately from the experimental data when the crack-tip stress field is non-homogenous due to imposed transient thermo-mechanical fields and material non-homogeneity, higher-order stress-field equations are essential in addition to leading terms and thermal stress. The solution for Eq. (30a) and Eq. (30b) corresponding to higher powers of ε ($m = 2$) consists of two parts: the solution for the homogeneous equation and a particular solution due to non-homogeneity and temperature, and these can be obtained recursively [29-31]. The solutions for ϕ_0 , ψ_0 , ϕ_1 and ψ_1 automatically satisfy the compatibility equations because these solutions are same as those for homogeneous materials.

To include the effect of the transient temperature term ($\dot{q}_0(t)$), the particular solution for ϕ_6 is derived. The differential equation is as follows

$$\alpha_i^2 \frac{\partial^2 \phi_6}{\partial \eta_1^2} + \frac{\partial^2 \phi_6}{\partial \eta_2^2} = \left(\frac{(1 + \zeta X(t))(1 + \gamma_2 X(t))}{6\alpha_{i0}} \right) \left(\frac{3\delta + 2}{\delta + 2} \right) \dot{q}_0(t) r^{5/2} \cos \frac{\theta}{2} \quad (34)$$

The ratio $(1/\alpha_i^2)$ can be calculated for different crack speeds c/c_s from the knowledge of elastic coefficients. The variation is represented by the approximation given by the following equation,

$$\frac{1}{\alpha_i^2} = 1 + \omega \left(\frac{c}{c_s} \right)^2 \quad (35)$$

$$\alpha_i^2 (1 + \xi) = 1 \quad , \quad \xi = \omega \left(\frac{c}{c_s} \right)^2 \quad (36)$$

The constant ω can be obtained by curve fitting. Using the relation

$$\rho = \sqrt{\eta_1^2 + \alpha_i^2 (1 + \xi) \eta_2^2} \quad \text{and} \quad \tan \theta = \sqrt{1 + \xi} \alpha_i \frac{\eta_2}{\eta_1},$$

the right hand side, in terms of ρ and θ ,

is expanded using Taylor series in terms of ρ_i and θ_i [34]. Parmeswaran and Shukla [34] provided a remedial solution to solve this type of equations. When they compared their analytical solutions obtained using this approach with the finite element simulations, they observed a maximum error of 5% [34]. Using the same approach, the equation can be written as

$$\alpha_i^2 \frac{\partial^2 \phi_6}{\partial \eta_1^2} + \frac{\partial^2 \phi_6}{\partial \eta_2^2} = \left(\alpha_0 \frac{(1 + \zeta X(t))(1 + \gamma_2 X(t))}{6\alpha_{i0}} \right) \left(\frac{3\delta + 2}{\delta + 2} \right) \dot{q}_0(t) r^{5/2} \left[\begin{array}{c} \cos \frac{\theta_i}{2} \\ \left(\frac{5}{8} \cos \frac{\theta_i}{2} \right) \\ + \xi \left[\begin{array}{c} -\frac{3}{8} \cos \frac{3\theta_i}{2} \\ -\frac{1}{4} \cos \frac{5\theta_i}{2} \end{array} \right] \end{array} \right] \quad (37)$$

The solution for ϕ_6 can be written as

$$\phi_6 = \left(\alpha_0 \frac{(1 + \zeta X(t))(1 + \gamma_2 X(t))}{6\alpha_{io}} \right) \left(\frac{3\delta + 2}{\delta + 2} \right) \frac{\dot{q}_0}{\alpha_i^2} (t) r^{9/2} \begin{bmatrix} \frac{1}{20} \cos \frac{\theta_l}{2} + \frac{1}{32} \left(\frac{1}{\alpha_i^2} - 1 \right) \cos \frac{\theta_l}{2} \\ - \frac{3}{144} \left(\frac{1}{\alpha_i^2} - 1 \right) \cos \frac{3\theta_l}{2} \\ - \frac{1}{56} \left(\frac{1}{\alpha_i^2} - 1 \right) \cos \frac{5\theta_l}{2} \end{bmatrix} \quad (38)$$

By collecting all the above terms of ϕ and ψ , and then transforming back to the $\xi_1 - \xi_2$ plane, the solutions for ϕ and ψ can be written as,

$$\begin{aligned} \phi = & r_i^{3/2} \left(A_0(t) \cos \frac{3\theta_l}{2} + C_0(t) \sin \frac{3\theta_l}{2} \right) + r_i^2 (A_1(t) \cos 2\theta_l + C_1(t) \sin 2\theta_l) + r_i^{5/2} \begin{pmatrix} A_2(t) \cos \frac{5\theta_l}{2} \\ + C_2(t) \sin \frac{5\theta_l}{2} \end{pmatrix} \\ & + Q_1(t) r_i^{5/2} \cos \frac{\theta_l}{2} + Q_2(t) r_i^{5/2} \sin \frac{\theta_l}{2} + Q_3(t) r_s^{5/2} \sin \frac{5\theta_s}{2} + Q_4(t) r_s^{5/2} \cos \frac{5\theta_s}{2} + Q_5(t) r_i^{5/2} \sin \frac{3\theta_l}{2} \\ & + Q_6(t) r_i^{5/2} \cos \frac{3\theta_l}{2} + \frac{4}{15} \frac{3\delta + 2}{\delta + 2} \frac{\alpha_o (1 + \gamma_1 X(t))}{\alpha_i^2 - 1} q_0(t) r^{5/2} \cos \frac{5\theta}{2} \\ & + \alpha_o (1 + \gamma_1 X(t)) \frac{3\delta + 2}{\delta + 2} \frac{(1 + \zeta X(t)) \dot{q}_0(t)}{6\alpha_{io} \alpha_i^2} r_i^{9/2} \begin{bmatrix} \frac{1}{20} \cos \frac{\theta_l}{2} + \frac{1}{32} \left(\frac{1}{\alpha_i^2} - 1 \right) \cos \frac{\theta_l}{2} \\ - \frac{3}{144} \left(\frac{1}{\alpha_i^2} - 1 \right) \cos \frac{3\theta_l}{2} \\ - \frac{1}{56} \left(\frac{1}{\alpha_i^2} - 1 \right) \cos \frac{5\theta_l}{2} \end{bmatrix} \end{aligned} \quad (39)$$

$$\begin{aligned} \psi = & r_s^{3/2} \left(B_0(t) \sin \frac{3\theta_s}{2} + D_0(t) \cos \frac{3\theta_s}{2} \right) + r_s^2 (B_1(t) \sin 2\theta_s + D_1(t) \cos 2\theta_s) \\ & + r_s^{5/2} \left(B_2(t) \sin \frac{5\theta_s}{2} + D_2(t) \cos \frac{5\theta_s}{2} \right) + R_1(t) r_s^{5/2} \cos \frac{\theta_s}{2} + R_2(t) r_s^{5/2} \sin \frac{\theta_s}{2} \\ & + R_3(t) r_i^{5/2} \sin \frac{5\theta_l}{2} + R_4(t) r_i^{5/2} \cos \frac{5\theta_l}{2} + R_5(t) r_s^{5/2} \sin \frac{3\theta_s}{2} + R_6(t) r_s^{5/2} \cos \frac{3\theta_s}{2} \end{aligned} \quad (40)$$

where $r_l = (\xi_1^2 + \alpha_l^2 \xi_2^2)^{1/2}$, $\tan \theta_l = \frac{\alpha_l \xi_2}{\xi_1}$, $r_s = (\xi_1^2 + \alpha_s^2 \xi_2^2)^{1/2}$, $\tan \theta_s = \frac{\alpha_s \xi_2}{\xi_1}$

$$Q_1(t) = -\frac{1}{4} \frac{\zeta \cos \beta(t)}{\alpha_l^2} A_0(t) + \frac{1}{4} \frac{\zeta \sin \beta(t)}{\alpha_l} C_0(t) - \frac{\rho_0}{\mu_0} \frac{1}{\delta + 2} \left[\begin{array}{l} -\frac{1}{8\alpha_l^3} c^2 k C_0(t) - \frac{1}{8\alpha_l} c^2 k C_0(t) \\ -\frac{1}{4\alpha_l} c^2 k C_0(t) + \frac{1}{4\alpha_l^2} \dot{C}_0(t) \end{array} \right]$$

$$+ \frac{D_l^1[A_0(t)]}{6\alpha_l^2} + \frac{B_l[A_0(t)]}{12\alpha_l^2}$$

$$Q_2(t) = -\frac{1}{4} \frac{\zeta \cos \beta(t)}{\alpha_l^2} C_0(t) - \frac{1}{4} \frac{\zeta \sin \beta(t)}{\alpha_l} A_0(t) - \frac{\rho_0}{\mu_0} \frac{1}{\delta + 2} \left[\begin{array}{l} \frac{1}{8\alpha_l^3} c^2 k A_0(t) + \frac{1}{8\alpha_l} c^2 k A_0(t) \\ + \frac{1}{4\alpha_l} c^2 k A_0(t) + \frac{1}{4\alpha_l^2} \dot{C}_0(t) \end{array} \right]$$

$$+ \frac{D_l^1[C_0(t)]}{6\alpha_l^2} + \frac{B_l[C_0(t)]}{12\alpha_l^2}$$

$$Q_3(t) = -\frac{2}{5} \frac{\zeta}{\delta + 2} \frac{1}{\alpha_l^2 - \alpha_s^2} [B_0(t) \sin \beta(t) - D_0(t) \cos \beta(t) \alpha_s]$$

$$Q_4(t) = -\frac{2}{5} \frac{\zeta}{\delta + 2} \frac{1}{\alpha_l^2 - \alpha_s^2} [B_0(t) \cos \beta(t) \alpha_s + D_0(t) \sin \beta(t)]$$

$$Q_5(t) = \frac{\rho_0}{\mu_0} \frac{1}{\delta + 2} \left[-\frac{3}{16\alpha_l^3} c^2 k A_0(t) + \frac{3}{16\alpha_l} c^2 k A_0(t) \right] + \frac{B_l[C_0(t)]}{8\alpha_l^2}$$

$$Q_6(t) = \frac{\rho_0}{\mu_0} \frac{1}{\delta + 2} \left[-\frac{3}{16\alpha_l^3} c^2 k C_0(t) + \frac{3}{16\alpha_l} c^2 k C_0(t) \right] - \frac{B_l[A_0(t)]}{8\alpha_l^2}$$

$$R_1(t) = -\frac{1}{4} \frac{\zeta \cos \beta(t)}{\alpha_s^2} D_0(t) + \frac{1}{4} \frac{\zeta \sin \beta(t)}{\alpha_s} B_0(t) + \frac{\rho_0}{\mu_0} \left[\begin{array}{l} \frac{1}{8\alpha_s^3} c^2 k B_0(t) + \frac{1}{8\alpha_s} c^2 k B_0(t) \\ + \frac{1}{4\alpha_s} c^2 k B_0(t) - \frac{1}{4\alpha_s^2} \dot{D}_0(t) \end{array} \right]$$

$$+ \frac{D_s^1[D_0(t)]}{6\alpha_s^2} + \frac{B_s[D_0(t)]}{12\alpha_s^2}$$

$$R_2(t) = -\frac{1}{4} \frac{\zeta \cos \beta(t)}{\alpha_s^2} B_0(t) - \frac{1}{4} \frac{\zeta \sin \beta(t)}{\alpha_s} D_0(t) - \frac{\rho_0}{\mu_0} \left[\frac{1}{8\alpha_s^3} c^2 k D_0(t) + \frac{1}{8\alpha_s} c^2 k D_0(t) \right. \\ \left. + \frac{1}{4\alpha_s} c^2 k D_0(t) + \frac{1}{4\alpha_s^2} \dot{c} B_0(t) \right] \\ + \frac{D_s^1[B_0(t)]}{6\alpha_s^2} + \frac{B_s[B_0(t)]}{12\alpha_s^2}$$

$$R_3(t) = \frac{2}{5} \frac{\zeta \delta}{\alpha_l^2 - \alpha_s^2} [C_0(t) \sin \beta(t) - A_0(t) \cos \beta(t) \alpha_l]$$

$$R_3(t) = \frac{2}{5} \frac{\zeta \delta}{\alpha_l^2 - \alpha_s^2} [A_0(t) \sin \beta(t) + C_0(t) \cos \beta(t) \alpha_l]$$

$$R_5(t) = \frac{\rho_0}{\mu_0} \left[-\frac{3}{16\alpha_s^3} c^2 k D_0(t) + \frac{3}{16\alpha_s} c^2 k D_0(t) \right] + \frac{B_s[B_0(t)]}{8\alpha_s^2}$$

$$R_6(t) = \frac{\rho_0}{\mu_0} \left[-\frac{3}{16\alpha_s^3} c^2 k B_0(t) + \frac{3}{16\alpha_s} c^2 k B_0(t) \right] - \frac{B_s[D_0(t)]}{8\alpha_s^2}$$

$$D_l^1[A_0(t)] = \frac{-3\rho_0 \sqrt{c(t)}}{\mu_0(\delta+2)} \frac{d}{dt} (\sqrt{c(t)} A_0(t)) \quad D_l^1[C_0(t)] = \frac{-3\rho_0 \sqrt{c(t)}}{\mu_0(\delta+2)} \frac{d}{dt} (\sqrt{c(t)} C_0(t))$$

$$B_l[A_0(t)] = \frac{3}{2} \left(\frac{\rho_0}{\mu_0(\delta+2)} \right)^2 \frac{c^2(t)}{\alpha_l^2} A_0(t) \frac{dc(t)}{dt} \quad B_l[C_0(t)] = \frac{3}{2} \left(\frac{\rho_0}{\mu_0(\delta+2)} \right)^2 \frac{c^2(t)}{\alpha_l^2} C_0(t) \frac{dc(t)}{dt}$$

$$D_s^1[B_0(t)] = \frac{-3\rho_0 c(t)}{\mu_0} \frac{d}{dt} (B_0(t))$$

$$D_s^1[D_0(t)] = \frac{-3\rho_0 c(t)}{\mu_0} \frac{d}{dt} (D_0(t))$$

$$B_s[B_0(t)] = \frac{3}{2} \left(\frac{\rho_0}{\mu_0} \right)^2 \frac{c^2(t)}{\alpha_s^2} B_0(t) \frac{dc(t)}{dt}$$

$$B_s[D_0(t)] = \frac{3}{2} \left(\frac{\rho_0}{\mu_0} \right)^2 \frac{c^2(t)}{\alpha_s^2} D_0(t) \frac{dc(t)}{dt}$$

The above definitions of the displacement potentials are now used in Eq. (4) to obtain the displacement fields. These displacement fields are then used to develop the strain fields. These strain fields and Eq. (25) are substituted into Eq. (2) to obtain in-plane stress fields around the crack-tip as given in Appendix (A2-A4).

3. Results and Discussion

To study the effects of the transient terms in both mechanical and thermal loading on crack propagation, the contours of the maximum principal stress and circumferential stress are generated for mixed-mode loading conditions. The asymptotic expansion of the crack-tip stress and displacement fields contain the coefficients of $A_n(t)$, $B_n(t)$, $C_n(t)$ and $D_n(t)$, which can be related to the fracture parameters such as the dynamic stress intensity factor and the nonsingular stress components around the crack-tip. The constants $A_0(t)$, $B_0(t)$, $C_0(t)$ and $D_0(t)$, are related to the mode-I and II stress intensity factors [$K_{ID}(t)$ and $K_{IID}(t)$ respectively] as given in Eq. (32) and (33). The higher order coefficients $A_I(t)$, $B_I(t)$, $C_I(t)$ and $D_I(t)$ are assumed to be zero. The material properties and fracture parameters of ZrB_2 are used in generating the plots [35]. Since the cracks are more likely to propagate from the ceramic side, we used the properties of ceramics and varied the properties exponentially along the gradation direction. The properties are as follows: Poisson's ratio (ν) = 0.16, shear modulus at the crack-tip (μ_0) = 210 GPa, density at the crack-tip (ρ_0) = 6000 kg/m³, coefficient of thermal expansion at crack-tip (α_0) = 5.9x10⁻⁶ /°C, thermal diffusivity at crack-tip (α_{t0}) = 1x10⁻⁵ m²/s, non-homogeneity parameters, $\zeta = -2$, $\gamma_1 = 0.2$, $\gamma_2 = 0.5$, crack-tip velocity (c/c_s) = 0.5, $k(t) = 20$ rad/m, $\beta(t) = 20^\circ$,

$$K_{ID} = 5 \text{ MPa}\cdot\text{m}^{1/2}, K_{IID} = 1 \text{ MPa}\cdot\text{m}^{1/2}, K_{eff} = \sqrt{K_{ID}^2 + K_{IID}^2}.$$

It is assumed that the applied thermal field generates elastic deformation around the crack-tip. Some of the terms associated with non-homogeneity and with the thermal stress field impose normal and shear stresses on the traction free crack faces. The removal of these stresses from the crack face is accomplished by superimposing an equal and opposite stress field on the crack face. In particular, each point on the crack face is subjected to a line load of specific magnitude such that the normal and shear stresses from the crack face are removed. Jiang et al. [36] proposed a solution for a single line load to derive the stress field around the crack-tip and the solution is extended for multiple line loads applied on the crack face line. The revised in-plane stress fields with traction free crack face conditions are used in analyzing the effect of various parameters.

3.1 Effect of Transient Terms on the Maximum Principal Stress

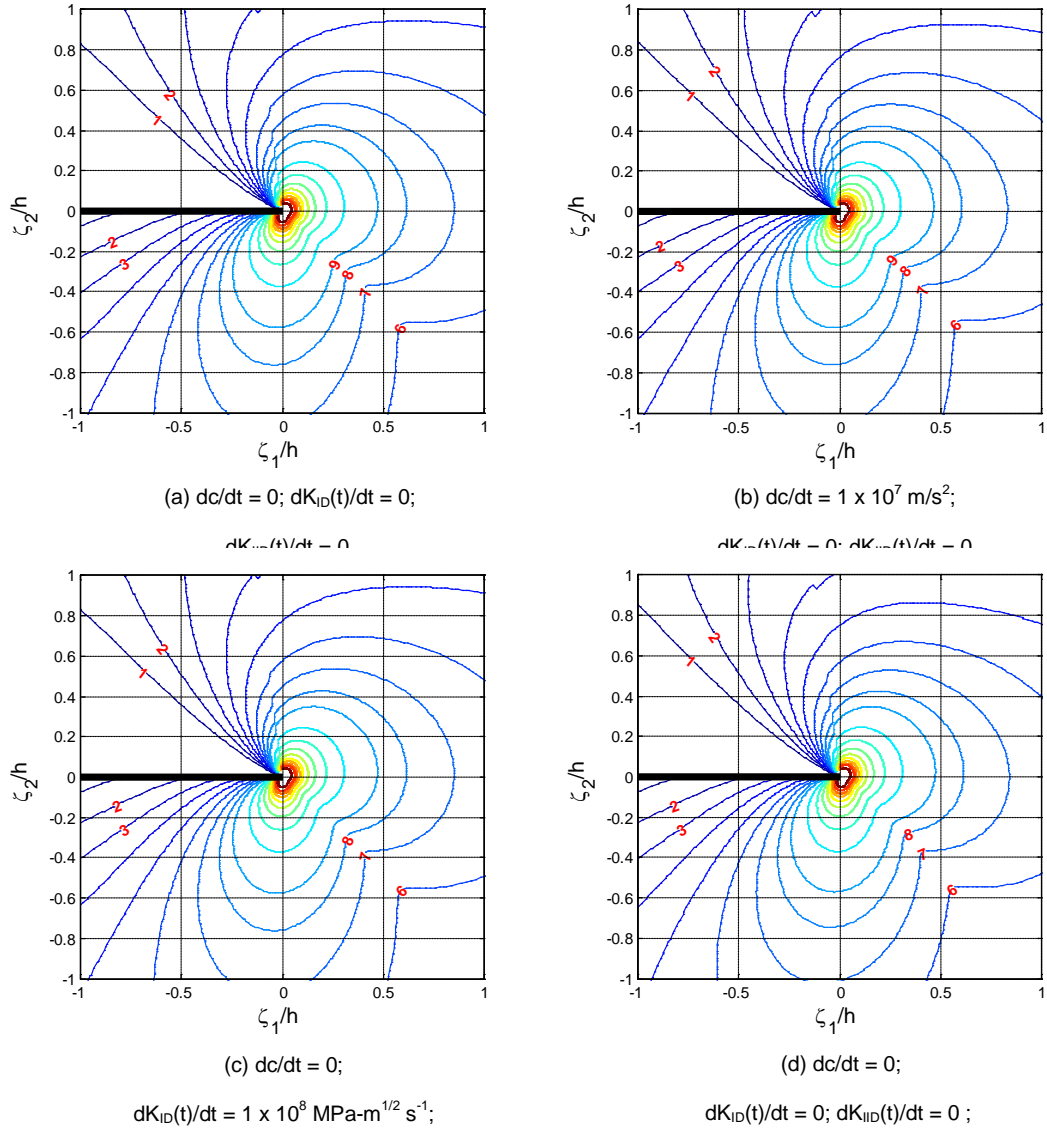


Fig. 2 Effect of transient terms on the contours of maximum principal stress around the crack-tip for mixed mode loading in an FGM ($\zeta = -2$, $\gamma_1 = 0.2$, $\gamma_2 = 0.5$, $c/c_s = 0.5$, $k(t) = 20 \text{ rad/m}$, $\beta(t) = 20^\circ$, $K_{ID} = 5 \text{ MPa}\cdot\text{m}^{1/2}$, $K_{IID} = 1 \text{ MPa}\cdot\text{m}^{1/2}$).

The effect of transient terms on the contours of the maximum principal stress around the crack-tip with no temperature field for a mixed mode loading in a FGM is

shown in Fig. 2. In Fig. 2(a), by setting the coefficients associated with transient terms to zero, the contours of maximum principal stress with no transient effects are obtained for relative comparison. Fig. 2(b) shows the effect of the crack-tip acceleration on the contours of maximum principal stress. To study the effect of crack-tip acceleration, the value of dc/dt was varied over seven orders of magnitude. Dally and Shukla [37] have shown that the rate of change of velocity at crack initiation could be of the order of 10^7 m/s². As the acceleration is increased, the contours ahead of the crack-tip are compressed. Also, the contour size reduces in the direction perpendicular to the crack surface. The effect of loading-rate on the contours of maximum principal stress is demonstrated by Fig. 2(c). To study this effect, $dK_{ID}(t)/dt$ and $dK_{IID}(t)/dt$ are varied over eight orders of magnitude. The stress contours show slight compression (almost negligible) in front of the crack-tip for $dK_{ID}(t)/dt$ and $dK_{IID}(t)/dt$ of 1×10^8 MPa-m^{1/2}-s⁻¹ and 2×10^7 MPa-m^{1/2}-s⁻¹, respectively. To study the effect of thermal shock, $\dot{q}_0(t) = 100^\circ\text{C}\cdot\text{m}^{-1/2}\cdot\text{s}^{-1}$ was chosen as a reference value. It is clearly visible in Fig. 2(d) that the stress contours are significantly affected as $\dot{q}_0(t)$ is introduced. The size of the stress contours decreases significantly away from the crack-tip, due to the higher order dependence of the stress field on $\dot{q}_0(t)$.

3.2 Effect of Transient Terms on the Circumferential Tensile Stress

The effect of transient terms on the contours of circumferential stress around the crack-tip with no temperature field for a mixed mode loading in a FGM is discussed in Fig. 3. The contours of the circumferential stress without transient

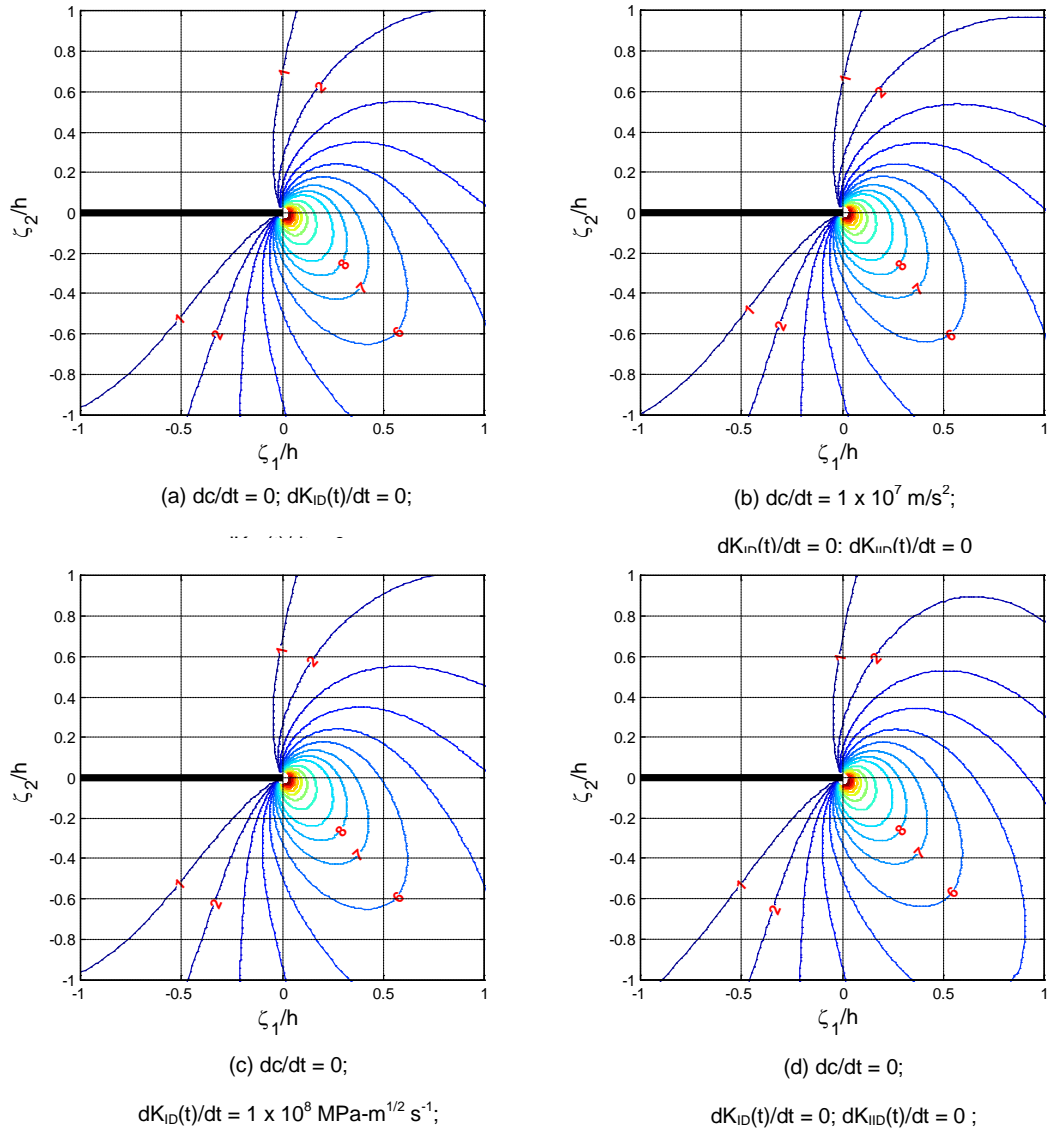


Fig. 3 Effect of transient terms on the contours of circumferential stress around the crack-tip for mixed mode loading in an FGM ($\zeta = -2$, $\gamma_1 = 0.2$, $\gamma_2 = 0.5$, $c/c_s = 0.5$, $k(t) = 20$ rad/m, $\beta(t) = 20^\circ$, $K_{ID} = 5$ MPa·m^{1/2}, $K_{IID} = 1$ MPa·m^{1/2}).

Parameters are shown in Fig. 3(a). The transient effect due to crack-tip acceleration as shown in Fig. 3(b), decreased the size of the contours of circumferential stress ahead of the crack-tip as the acceleration is increased. Also, Fig. 3(c) shows that the effect of $dK_{ID}(t)/dt$ and $dK_{IID}(t)/dt$ on the contour size in front of the crack-tip is negligible.

For $\dot{q}_0(t) = 100^\circ\text{C}\cdot\text{m}^{-1/2}\cdot\text{s}^{-1}$, the size of the contours decreases significantly and the shape changes considerably as shown in Fig. 3(d).

3.3 Effects of Temperature

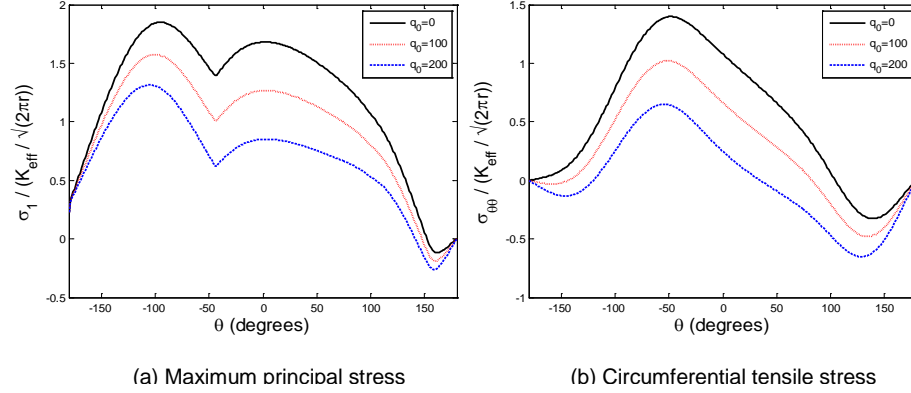


Fig. 4 Variation of normalized (a) maximum principal stress, and (b) the circumferential tensile stress, around the crack–tip for a mixed-mode thermo-mechanical loading in an FGM for several values of temperature coefficients. ($\zeta = -2$, $\gamma_1 = 0.2$, $\gamma_2 = 0.5$, $c/c_s = 0.5$, $k(t) = 20$ rad/m, $\beta(t) = 20^\circ$, $K_{ID} = 5$ MPa-m^{1/2}, $K_{IID} = 1$ MPa-m^{1/2}, $\dot{K}_{ID} = 1 \times 10^8$ MPa-m^{1/2}-s⁻¹, $\dot{K}_{IID} = 2 \times 10^7$ MPa-m^{1/2}-s⁻¹, $\dot{c} = 1 \times 10^7$ m/s, $q_1(t) = q_2(t) = 50^\circ\text{C}\cdot\text{m}^{-1/2}$, $\dot{q}_0(t) = 100^\circ\text{C}\cdot\text{m}^{-1/2}\cdot\text{s}^{-1}$ and a typical value for radius, $r = 0.002\text{m}$).

Variation of normalized maximum principal stress and circumferential stress, is plotted around the crack-tip for different temperature gradients ($q_0 = 0$, $q_0 = 100$ and $q_0 = 200$) as shown in Fig. 4. Typical values of $dc/dt = 10^7$ m/s², $dK_{ID}(t)/dt = 1 \times 10^8$ MPa-m^{1/2}-s⁻¹, $dK_{IID}(t)/dt$ of 2×10^7 MPa-m^{1/2}-s⁻¹, $\dot{q}_0(t) = 100^\circ\text{C}\cdot\text{m}^{-1/2}\cdot\text{s}^{-1}$, and a typical value for radius, $r = 0.002\text{m}$ are assumed for plotting Fig. 4. As the temperature gradient increases, the peak value of both the normalized maximum principal stress and circumferential tensile stress decreases while the angles at which

the peak value of these stresses occur change slightly for different temperature gradients.

3.4 Effect of Temperature gradient and Crack-tip Velocity on the Crack Extension Angle

The value of the crack extension angle has been calculated using the minimum strain energy density criterion (S-criterion). The strain energy density criterion is used in order to provide a complete description of material damage by including both the distortional and dilatational effects [38]. The strain energy density dW/dV near the crack-tip for an FGM is given as

$$\frac{dW}{dV} = S = \frac{1}{4\mu e^{\epsilon x}} \left\{ (1-\nu) \left\{ \sigma_{xx}^2 + \sigma_{yy}^2 \right\} - 2\nu\sigma_{xx}\sigma_{yy} + 2\sigma_{xy}^2 \right\} \quad (41)$$

Fracture takes place in the direction of minimum S , and the condition can be obtained by using Eq. (41)

$$\frac{\partial S}{\partial \theta} = 0 \quad ; \quad \frac{d^2 S}{d\theta^2} > 0 \quad \text{at } S = S_c \quad (42)$$

where S_c is the critical strain energy density.

The dependence of crack extension angle on the temperature gradient (q_0) is shown in Fig. 5. Typical values of $dc/dt = 10^7$ m/s², $dK_{ID}(t)/dt = 1 \times 10^8$ MPa-m^{1/2}-s⁻¹, $dK_{IID}(t)/dt = 2 \times 10^7$ MPa-m^{1/2}-s⁻¹, $q_1(t) = q_2(t) = 50^\circ\text{C-m}^{-1/2}$ and $\dot{q}_0(t) = 100^\circ\text{C-m}^{-1/2}\text{s}^{-1}$ are assumed for plotting Fig. 5 and Fig. 6. The crack extension angle decreases slowly with an increase in the temperature gradient as shown in Fig. 5. The crack extension angle is decreased from -51° to -37° as the value of q_0 is increased from 0 to $200^\circ\text{C-m}^{-1/2}$.

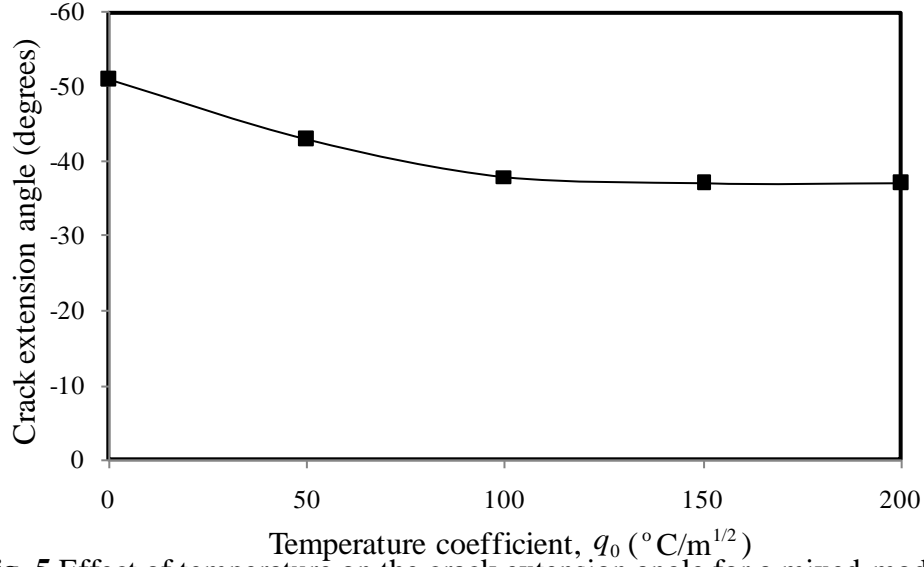


Fig. 5 Effect of temperature on the crack extension angle for a mixed-mode thermo-mechanical loading in. ($\zeta = -2$, $\gamma_1 = 0.2$, $\gamma_2 = 0.5$, $c/c_s = 0.5$, $k(t) = 20$ rad/m, $\beta(t) = 20^{\circ}$, $K_{ID} = 5$ MPa-m $^{1/2}$, $K_{IID} = 1$ MPa-m $^{1/2}$, $\dot{K}_{ID} = 1 \times 10^8$ MPa-m $^{1/2}$ -s $^{-1}$, $\dot{K}_{IID} = 2 \times 10^7$ MPa-m $^{1/2}$ -s $^{-1}$, $\dot{c} = 1 \times 10^7$ m/s, $q_1(t) = q_2(t) = 50^{\circ}\text{C}\cdot\text{m}^{-1/2}$ and $\dot{q}_0(t) = 100^{\circ}\text{C}\cdot\text{m}^{-1/2}\text{s}^{-1}$).

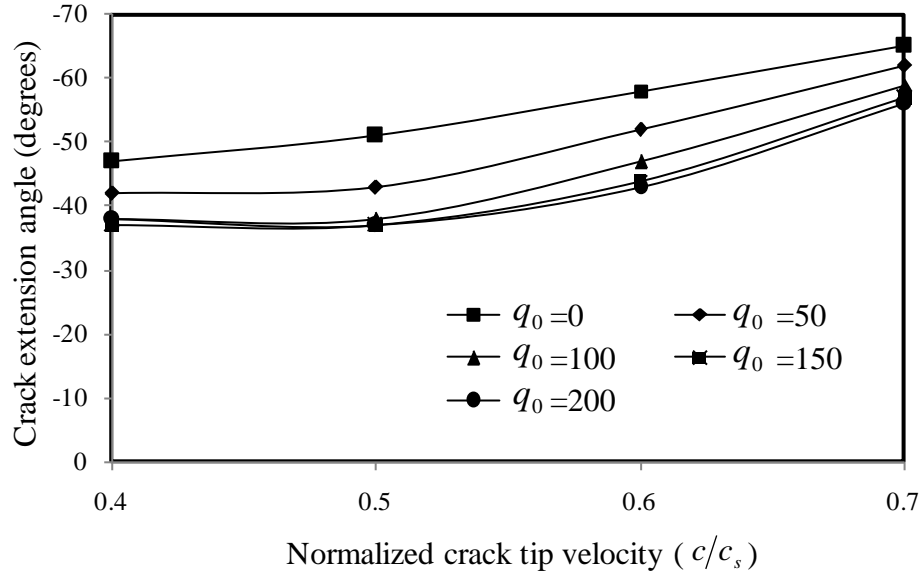


Fig. 6 Crack extension angle as a function of crack-tip velocity for different values of temperature gradient for a mixed-mode thermo-mechanical loading in FGM. ($\zeta = -2$, $\gamma_1 = 0.2$, $\gamma_2 = 0.5$, $k(t) = 20$ rad/m, $\beta(t) = 20^{\circ}$, $K_{ID} = 5$ MPa-m $^{1/2}$, $K_{IID} = 1$ MPa-m $^{1/2}$, $\dot{K}_{ID} = 1 \times 10^8$ MPa-m $^{1/2}$ -s $^{-1}$, $\dot{K}_{IID} = 2 \times 10^7$ MPa-m $^{1/2}$ -s $^{-1}$, $\dot{c} = 1 \times 10^7$ m/s, $q_1(t) = q_2(t) = 50^{\circ}\text{C}\cdot\text{m}^{-1/2}$ and $\dot{q}_0(t) = 100^{\circ}\text{C}\cdot\text{m}^{-1/2}\text{s}^{-1}$).

The effects of temperature on the crack extension angle as a function of crack-tip velocity in a FGM with $\zeta = -2$ is plotted in Fig. 6 using the minimum strain energy density criterion. The crack extension angle increases as the crack-tip velocity increases for various temperature gradients.

3.5 Effects of T-stress on the Crack Extension Angle

Previous studies have shown that the T -stress (σ_{ox} term) plays an important role in crack branching and crack kinking for a homogenous material [39, 40]. The effect of T -stress on the stress fields in FGMs has been accounted using the following equation:

$$\sigma_{xx} = \frac{(K_{I_d}, K_{II_d})}{(2\pi r)^{1/2}} F_{ij}(r, \theta, T, \xi, \gamma_1, \gamma_2, c, \dot{c}, k, \beta, \dot{\beta}, \dot{K}_{I_d}, \dot{K}_{II_d}) + T(\sigma_{ox}) \quad (43)$$

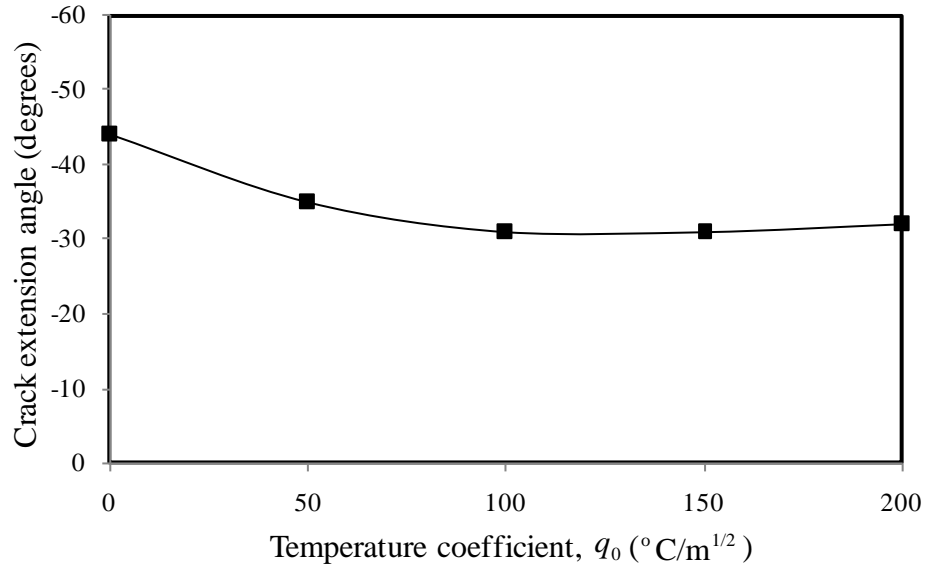


Fig. 7 Effect of T-stress on the crack extension angle for different values of temperature gradient for a mixed-mode thermo-mechanical loading in FGM. ($\zeta = -2$, $\gamma_1 = 0.2$, $\gamma_2 = 0.5$, $c/c_s = 0.5$, $k(t) = 20$ rad/m, $\beta(t) = 20^{\circ}$, $K_{I_d} = 5$ MPa-m $^{1/2}$, $K_{II_d} = 1$ MPa-m $^{1/2}$, $\dot{K}_{I_d} = 1 \times 10^8$ MPa-m $^{1/2}$ -s $^{-1}$, $\dot{K}_{II_d} = 2 \times 10^7$ MPa-m $^{1/2}$ -s $^{-1}$, $\dot{c} = 1 \times 10^7$ m/s, $q_1(t) = q_2(t) = 50^{\circ}\text{C}\cdot\text{m}^{-1/2}$ and $\dot{q}_0(t) = 100^{\circ}\text{C}\cdot\text{m}^{-1/2}\text{s}^{-1}$).

In the above Eq. (43), $T(\sigma_{ox})$ is the non-singular stress term. The effect of T-stress on the crack extension angle for different temperature gradients around a propagating crack under mixed-mode thermo-mechanical loading in an FGM is shown in Fig. 7 using minimum strain energy criterion. Typical values of $\sigma_{ox}/K_{ID} = - (3/4) m^{-1/2}$, $dc/dt = 10^7 m/s^2$, $dK_{ID}(t)/dt = 1 \times 10^8 MPa \cdot m^{1/2} \cdot s^{-1}$, $dK_{IID}(t)/dt = 2 \times 10^7 MPa \cdot m^{1/2} \cdot s^{-1}$, $q_1(t) = q_2(t) = 50^\circ C \cdot m^{-1/2}$ and $\dot{q}_0(t) = 100^\circ C \cdot m^{-1/2} \cdot s^{-1}$ are assumed for constructing Fig. 7. The value of the crack extension angle decreases as the temperature gradient is increased as shown in Fig. 7. The decrease in the crack extension angle is more significant for less temperature gradient. The crack extension angle decreases from -44° to -32° as the value of q_0 is increased from 0 to $200^\circ C/m^{-1/2}$. Therefore, it can be concluded that the application of thermal loading decreases the crack extension angle even in the presence of non-singular stresses. Also, for the same temperature field, the value of the crack extension angle is found to be lower under T-stress when compared to that of the zero T-stress case.

4. Concluding Remarks

Thermo-mechanical stress and displacement fields for a smoothly curving crack in FGMs are obtained using displacement potentials and an asymptotic analysis. In addition to the mechanical fields, temperature fields are also developed for exponentially varying thermal properties along the gradation direction. The effect of the rate of change of stress intensity factors, acceleration, temperature gradient and transient thermal loading on the contours of the maximum principal stress and the

circumferential stress under mixed-mode loading conditions are discussed. The key findings are as follows:

- The thermo-mechanical stress fields are significantly affected by transient parameters. As the crack-tip acceleration increases, the size of stress contours ahead of the crack-tip decreases.
- The transient thermal loading term influences the higher-order terms in asymptotic crack-tip fields: the displacement in the order of $O(r^{7/2})$ and the stress in $O(r^{5/2})$.
- Crack-tip velocity plays a significant role in the crack extension angle under transient loading conditions. For a mixed-mode curving crack under transient thermo-mechanical loading, the crack extension angle increases with the increase in crack-tip velocity.
- The increase in temperature gradient decreases the crack extension angle for different crack-tip velocities with and without the T-stress.
- There is a significant effect on the crack extension angle when the T-stress is applied. The value of crack extension angle decreases when the T-stress (σ_{ox} term) is applied when compared to the case without the T-stress (where $\sigma_{ox} = 0$).

Acknowledgement

The financial support of the Air Force Office of Scientific Research under Grant No. FA9550-09-1-0639 is greatly acknowledged.

References

- [1] Suresh, S., Mortensen, A.: Fundamentals of Functionally Graded Materials, Processing and Thermomechanical Behavior of Graded Metals and Metal-Ceramic Composites. IOM Communications Ltd., London (1998)
- [2] Niino, M., Hirai, T., Watanabe, R.: The Functionally Gradient Materials. J. Jap. Soc. Comp. Mater. 13(1), 257(1987)
- [3] Kawasaki, A., Wananabe, R.: Finite Element Analysis of Thermal Stress of the Metal/Ceramics Multilayer Composites with Controlled Compositional Gradients. J. Jpn. Inst. Met. 51, 525-529 (1987)
- [4] Drake, J.T., Williamson, R.L., Rabin, B.H.: Finite Element Analysis of Thermal Residual Stresses at Graded Ceramic-Metal Interfaces Part II: Interface Optimization for Residual Stress Reduction. J. Appl. Phys. 74, 1321-1326 (1993)
- [5] Kuroda, Y., Kusaka, K., Moro, A., Togawa, M. Evaluation Tests of ZrO₂ /Ni Functionally Gradient Materials for Regeneratively Cooled Thrust Engine Applications. Functionally Gradient Materials (Ceramic Transactions), J. B. Holt, M. Koisumi, T. Hirai, and Z. A. Munir, eds., American Ceramic Society, Westerville, OH, 34, 289-296 (1993)
- [6] Takahashi, H., Ishikawa, T., Okugawa, D., Hashida, T.: Laser and Plasma-ARC Thermal Shock/Fatigue Fracture Evaluation Procedure for Functionally Gradient Materials. Thermal Shock and Thermal Fatigue Behavior of Advanced Ceramics, G. A. Schneider and G. Petzow, eds., Kluwer Academic, Dordrecht, 543-554 (1993)
- [7] Jin, Z.H., Noda, N.: Crack-Tip Singular Fields in Nonhomogeneous Materials. J. Appl. Mech. 61, 738-740 (1994)

- [8] Erdogan, F., Wu, B.: Crack Problems in FGM Layers under Thermal Stresses. *J. Therm. Stresses* 19, 237-265 (1996)
- [9] Jin, Z.H., Batra, R.C.: Stress Intensity Relaxation at the Tip of an Edge Crack in a Functionally Graded Materials Subjected to a Thermal Shock. *J. Therm. Stresses* 19, 317-339, (1996)
- [10] Kokini, K., Choules, B.D.: Surface Thermal Fracture of Functionally Graded Ceramic Coatings: Effect of Architecture and Materials. *Composites Eng.* 5, 865-877 (1995)
- [11] Kokini, K., Case, M.: Initiation of Surface and Interface Edge Cracks in Functionally Graded Ceramic Thermal Barrier Coatings. *ASME J. Eng. Mater. Technol.* 119, 148-152 (1997)
- [12] Jin, Z.H., Paulino, G.H.: Transient Thermal Stress Analysis of an Edge Crack in a Functionally Graded Material. *Int. J. Fract.* 107, 73-98 (2001)
- [13] Walters, M.C., Paulino, G.C., Dodds, R.H., Jr.: Stress-Intensity Factors for Surface Cracks in Functionally Graded Materials under Mode-I Thermomechanical Loading. *Int. J. Solids Struct.* 41, 1081-1118 (2004)
- [14] Zhang, L., Kim, J.H.: Higher-order Terms for the Mode-III Stationary Crack-tip Fields in a Functionally Graded Material. *J. Appl. Mech.* 78(1), 011005(1-10) (2011)
- [15] Clements, D.L.: On a Displacement Based Solution to an Antiplane Crack Problem for Inhomogeneous Anisotropic Elastic Materials. *J. Elast.* (2011) doi: 10.1007/s10659-010-9274-5
- [16] Jain, N., Shukla, A., Chona, R.: Asymptotic Stress Fields for Thermo-Mechanically Loaded Cracks in FGMs. *J. of ASTM International* 3(7), 78-90 (2006)

- [17] Lee, K.H., Chalivendra, V.B., Shukla, A.: Dynamic Crack-tip Stress and Displacement Fields under Thermomechanical Loading in Functionally Graded Materials. *J. Appl. Mech.* 75 (5), 1-7 (2008)
- [18] Kidane, A., Chalivendra, V.B., Shukla, A., Chona, R.: Mixed-mode Dynamic Crack Propagation in Graded Materials under Thermo-mechanical Loading. *Eng. Fract. Mech.* 77(14), 2864-2880 (2010)
- [19] Chalivendra, V.B., Shukla, A.: Transient Elastodynamic Crack Growth in Functionally Gradient Materials. *J. Appl. Mech.* 72, 237-248 (2005)
- [20] Lambros, J., Cheeseman, B.A., Santare, M.H.: Experimental investigation of the quasi-static fracture of functionally graded materials. *Int. J. Solids Struct.* 37, 3715–3732 (2000)
- [21] Noda, N., Ishihara, M., Yamamoto, N., Fujimoto, T.: Two-crack propagation in a functionally graded material plate under thermal loads. *Mater. Sci. Forum* 423–425, 607–612 (2003)
- [22] Tohgo, K., Suzuki, T., Araki, H.: Evaluation of R-curve behavior of ceramic–metal functionally graded materials by stable crack growth. *Eng. Fract. Mech.* 72, 2359–2372 (2005)
- [23] Tilbrook, M.T., Moon, R.J., Hoffman, M.: Curved crack propagation in homogeneous and graded materials. *Fatigue Fract. Eng. Mater. Struct.* 28, 939–950 (2005)
- [24] Liu, C., Rosakis, A.J.: On the higher order asymptotic analysis of a non-uniformly propagating dynamic crack along an arbitrary path. *J. Elast.* 35, 27–60 (1994)

- [25] Chalivendra, V.B.: Asymptotic analysis of transient curved crack in functionally graded materials. *Int. J. Solids Struct.* 44, 465-479 (2007)
- [26] Freund L. B.: *Dynamic Fracture Mechanics*. Cambridge University Press. (1990)
- [27] Yao, X.F., Xu, W., Yeh, H.Y.: Investigation of crack tip evolution in functionally graded materials using optical caustics. *Polym. Test.* 26, 122-131 (2007)
- [28] Jain, N., Shukla, A.: Mixed mode dynamic fracture in particulate reinforced functionally graded materials. *Exp. Mech.* 46(2), 137–154 (2006)
- [29] Shukla, A., Jain, N.: Dynamic Damage Growth in Particle Reinforced Graded Materials. *Int. J. Impa. Engg* 30, 777-803 (2004)
- [30] Chalivendra, V.B., Shukla, A., Parameswaran, V.: Dynamic Out of Plane Displacement Fields for an Inclined Crack in Graded Materials. *J. Elast.* 69, 99-119 (2002)
- [31] Parameswaran, V., Shukla, A.: Crack-Tip Stress Fields for Dynamic Fracture in Functionally Gradient Materials. *Mech. Mater.* 31, 579-596 (1999)
- [32] Gu, P., Asaro, R.J., 1997. Cracks in functionally graded materials. *Intl. J. Solids Struct.* 34 (1), 1–17.
- [33] Irwin, G.R., 1980. Series representation of the stress field around constant speed cracks. University of Maryland Lecture Notes, Maryland.
- [34] Parameswaran, V., Shukla, A.: Near-Tip Out of Plane Displacement Fields for Dynamic Crack Propagation in Functionally Graded Materials. *Mech. Res. Commun.* 29, 397–406 (2002)
- [35] Fahrenholtz, W.G., Hilmas, G.E., Talmy, I.G., Zaykoski, J.A.: Refractory Diborides of Zirconium and Hafnium. *J. Am. Ceram. Soc.* 90, 1347-1364 (2007)

- [36] Jiang, C.P., Zou, Z.Z., Wang, D., Liu, Y.W.: A Discussion about a Class of Stress Intensity Factors and its Verification. *Int. J. Fract.* 49, 141-157 (1991)
- [37] Dally, J.W., Shukla, A.: Dynamic Crack Behavior at Initiation. *Mech. Res. Commun.* 6 (4), 239-244 (1979)
- [38] Gdoutos, E.E.: *Fracture mechanics criteria and applications*. Kluwer Academic Publishers. (1990)
- [39] Cotterell, B., Rice, J.R.: Slightly curved or kinked cracks. *Int. J. Fract.* 16, 155-169 (1980)
- [40] Shukla, A., Nigam, H., Zervas, H.: Effect of Stress Field Parameters on Dynamic Crack Branching. *Eng. Fract. Mech.* 36(3), 429-438 (1990)

CHAPTER 4

EFFECT OF STRAIN-RATE AND TEMPERATURE ON DYNAMIC DEFORMATION OF NANOLAMINATED Ti₂AlC

by

Sandeep Abotula, Sandip Basu, Miladin Radovic and Arun Shukla

Under preparation for submission to the Acta Materialia letter

Corresponding Author: Miladin Radovic

Department of Mechanical Engineering

Texas A&M University

Office 424, Mechanical Engineering Building

College Station, TX, 77843, USA

Phone: +1-979-845-5114

Email Address: mradovic@tamu.edu

Abstract

Nanolaminated ternary carbide, Ti_2AlC , was characterized under dynamic loading using Split Hopkinson Pressure Bar (SHPB) compression apparatus. The dynamic loading experiments were performed in the strain-rate range of 1500-4200/s and at temperatures ranging from room temperature (RT) to 1150 °C. At room temperature, the failure stress and strain show little dependence on strain rate, whereas the failure stress drops considerably at temperatures above 900°C. At all strain rates and temperatures, Ti_2AlC exhibits softening after failure initiation and a more graceful failure due to delamination and kink band (KB) formation. At temperatures higher than 900 °C, grain boundary decohesion is suggested to contribute towards the decrease in the failure stress.

1. Introduction

Nanolaminated ternary carbides and nitrides, known as MAX phases, have attracted recent attention because of their potential for application in extreme environments. They have a general formula of $M_{n+1}AX_n$ ($n = 1, 2, 3$), where M is an early transition metal, A is a group-A element and X is either C or N.¹⁻³ Titanium aluminum carbide, Ti_2AlC , one of the well characterized compounds with M_2AX chemistry, is lightweight (4.11 g/cm^3)¹ material with high Young's modulus (278 GPa),¹ excellent electrical and thermal conductivity,⁴ high oxidation and corrosion resistance.⁵⁻⁹ Like most MAX phases, Ti_2AlC is relatively soft (Vickers hardness of $\sim 4 \text{ GPa}$)¹⁰ and easily machinable¹¹ compared to binary transition metal carbides. Because of their nanolaminated structure and kinking mechanism, Ti_2AlC is also

exceedingly damage tolerant and thermal shock resistant,¹² and most likely creep-,¹³⁻¹⁵ and fatigue-resistant¹⁶⁻¹⁸ like some other MAX phases.

One of the interesting aspects of MAX phases in general, and Ti_2AlC in particular is unusual deformation behavior that can be traced back to their nanolaminated hexagonal crystal structure with high c/a ratio and presence of the relatively large number of movable dislocations. The dislocations, being confined to only parallel basal planes, give rise to extensive kinking and delamination in MAX phases upon deformation.^{15,19} At room temperature, Ti_2AlC , similar to other MAX phases, shows nonlinear stress-strain behavior with fully reversible hysteresis loops and significant amount of energy dissipation under quasi-static cycling loading-unloading.^{15,20-23} Recently, a microscale model, based on nucleation, growth and annihilation of reversible nest of movable dislocations, so called incipient kink bands (IKBs), has been proposed to explain the stress-strain hysteresis in MAX phases.^{15,24-25} At higher stresses or higher temperature, the IKBs transform into permanent kink bands (KBs). Formation of KB along with delamination has been argued in literature to be the primary reason for excellent damage tolerance of MAX phases.^{16-17,19} At higher temperatures, i.e. above 1000 °C, Ti_2AlC , undergoes a brittle-to-plastic (BTP) transition and strains as large as 12% can be reached before failure during compressive loading.²⁶ Although significant progress has been made in the recent years on understanding mechanical behavior of Ti_2AlC and other MAX phases under quasi-static conditions, we are unaware of any studies published in the open literature on the effect of high strain rate deformation behavior of Ti_2AlC at room or elevated temperatures.

In this letter we demonstrate that Ti_2AlC exhibits strain rate independent deformation behavior below BTP transition temperature up to very high strain rates under dynamic conditions. The maximum stress in the dynamic true stress-strain curves, corresponding to the failure initialization, is comparable with that measured in quasi-static experiments. Above BTP transition temperature, maximum stress measured in dynamic conditions was found to decrease significantly, in the similar way as in quasi-static testing.

2. Experimental Details

Dense Ti_2AlC , with a grain size of $\sim 100 \mu\text{m}$, was processed by hot pressing Ti_2AlC powders (3-ONE-2, Voorhees, NJ) in graphite die at 1500°C and 20 MPa for 4 hour in the vacuum of 10^{-2} torr. Dynamic compression experiments were carried out on cylindrical specimens having 10.16 mm in diameter and 5.33 mm thick for room temperature (RT) measurements, and 6.35 mm in diameter and 3.175 mm thick for measurements at elevated temperatures.

A Split Hopkinson Pressure Bar (SHPB) apparatus – with incident and transmission bars, made of Maraging steel, having a diameter and length of 12.7 mm and 1220 mm , respectively, was used to study the dynamic behavior of Ti_2AlC . A clay pulse shaper of thickness of 2 mm was placed at the impact end of the incident bar to improve force equilibrium conditions at the specimen-bar interface. The theoretical and experimental details of SHPB are given elsewhere.²⁷⁻²⁹ By varying the velocities of the striker bar, room temperature experiments were carried out at strain rates ranging from $1500\text{-}4200/\text{s}$. Using one-dimensional wave theory, the engineering stress

and strain in the specimen can be determined from the transmitted and reflected strain pulses respectively as given in Eqs. 1 and 2.

$$\sigma_s = E_b \frac{A_b}{A_s} \varepsilon_t(t) \quad (1)$$

$$\varepsilon_s = \frac{-2c_b}{L_s} \int_0^t \varepsilon_r(t) dt \quad (2)$$

where, ε_r and ε_t represent reflected and transmitted strains respectively, c_b , E_b and A_b represent wave speed, Young's modulus and cross sectional area of the bar respectively, σ_s , ε_s , and A_s , L_s , represent stress, strain and cross sectional area of the specimen respectively, and t represents the time. Equations (1) and (2) were suitably modified to obtain the true stress and true strain in the material.

For experiments at elevated temperatures, the SHPB apparatus in conjunction with the induction coil heating system was utilized. A special fixture was designed and fabricated to load the specimen. The details of our high temperature SHPB setup can be found in (28, 29). High temperature experiments were carried out from RT to 1150°C under identical strain rate of about 3500/s.

3. Results and Discussion

The dynamic true stress-true strain curves for Ti₂AlC at room temperature for different strain rates ranging from 1500/s to 4200/s are plotted in Fig 1. For all strain rates, the maximum dynamic compressive stress of 480 – 600 MPa is attained around 2% true strain, followed by a stress relaxation up to maximum true strain of 9-16%. Unlike most ceramics, and similar to quasi-static experiments,³⁰ Ti₂AlC exhibits a more graceful failure rather than brittle failure under dynamic loading (insert in Figure

1). More interestingly, the maximum stress during the deformation of Ti_2AlC does not depend significantly on the strain rate during dynamic experiments. The slight variation observed in the maximum stress may be due to the difference in pre-existing defect concentration in the samples. The adiabatic nature of dynamic tests may also affect dislocation nucleation and propagation, which in turn can result in decrease in

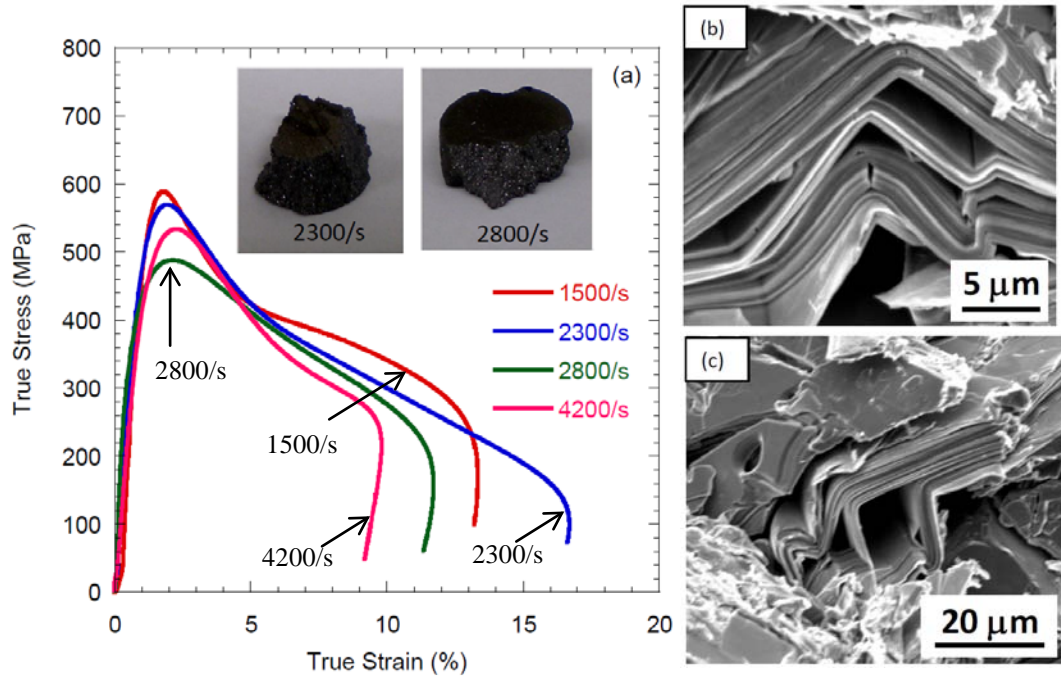


Fig. 1 (a) Dynamic stress-strain response of bulk Ti_2AlC at room temperature for different strain rates. Inserts show the samples tested at strain rates of 2300/s and 2800/s. Results of Scanning Electron Microscopy, SEM, show extensive kink band formation and delamination for the samples tested at strain-rates of (b) 2300/s and (c) 2800/s.

maximum stress with increase in strain rates. There is some evidence that the energy absorbed by the material decreases marginally with increasing strain-rates. This is indicated by the decrease in area under stress-strain curve. However, the material still exhibits graceful failure. These comments notwithstanding, more work is needed to

understand the small variations in true stress-true strain curves with increasing strain rates.

Scanning Electron Microscopy, SEM, images of the fracture surfaces in Figures 1(b) and 1(c) show extensive delamination and KB formation along the fracture surface after testing of Ti_2AlC at strain rates of 2800/s and 5000/s, respectively. The high density of KBs found in the fracture surfaces imply significant amount of plastic deformation during crack propagation, which in turn is evident from the graceful failure shown in Figure 1(a). As the strain-rate increases, the intensity of KB formation decreases slightly and resulting in the decrease of the dissipation energy. It is interesting to note here that, similar to quasi-static deformation, no evidence of KB has been observed in the polished cross-sections of the interior of the samples (not shown here). This suggests that if IKBs – which are reversible in nature – form inside the favorably oriented grains during high strain rate deformation, they do not develop in full KB and disappear upon unloading. However, these IKBs transform to fully developed KBs along the fracture surfaces. Since formation of KBs (Figures 1(b) and 1(c)) and delamination dissipate significant amount of energy, it hinders the crack propagation and results in graceful failure of Ti_2AlC even at strain rates as high as 4200/s.

The dynamic true stress-strain curves for Ti_2AlC tested at a strain rate of 3500/s and different temperatures are shown in Figure 2(a) Initially, as the temperature increases from room temperature to 900°C, there is no significant change in the maximum compressive strength (about 520-540 MPa). However, at 1150°C, the material shows a significant decrease in the maximum true compressive strength to

around 400 MPa. For all the temperatures, the failure initiates at a true strain of ~4% and reaches a maximum true strain of 45-50%. Since the diameter of the specimen for

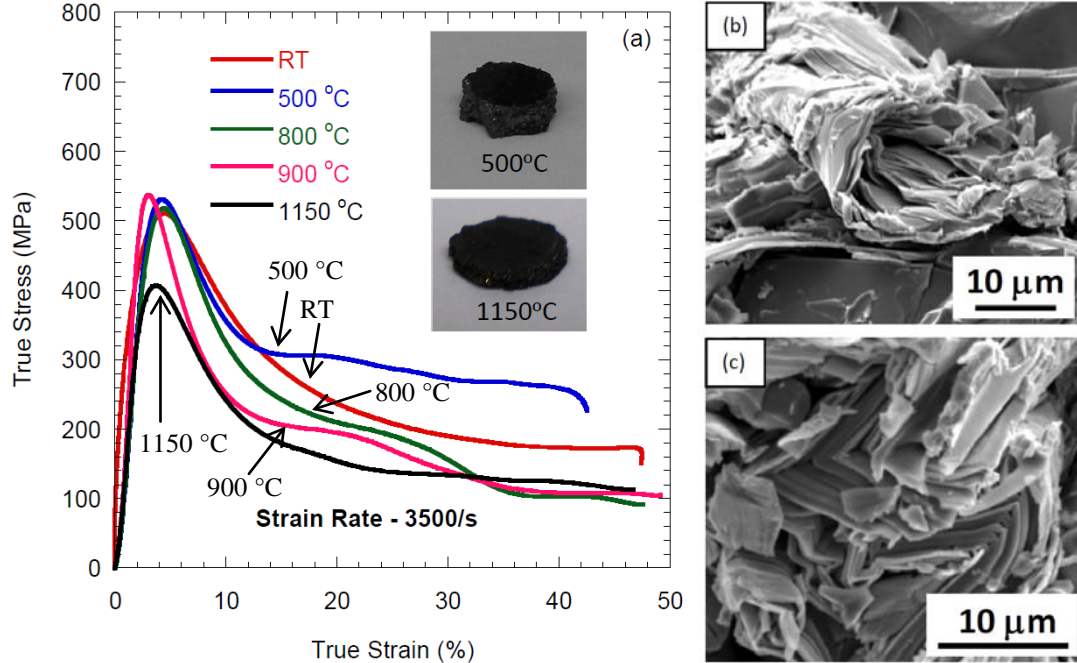


Fig. 2 (a) Dynamic stress-strain response of bulk Ti_2AlC at different temperatures at a strain-rate of 3500/s. Inserts show the samples tested at 500 and 1150 °C. Results of Scanning Electron Microscopy, SEM, show deformation kinking along the fracture surfaces of samples tested at (b) 500 °C and (c) 1150 °C, respectively.

high temperature testing is smaller in comparison to the room temperature testing the resulting stress on the sample for a given loading is higher and this results in larger strains²⁹. Even at high temperatures, the material exhibits graceful failure (inset in Figure 2a). Here again, SEM micrographs from the fracture surfaces after dynamic deformation at elevated temperatures, as illustrated in Figures 2(b) and 2(c) for samples tested at 500 °C and 1150 °C respectively, reveal large amount of kinking. It is important to note here that it is difficult to infer from the fracture surfaces whether

the amount of plastic deformation by kinking depends on the testing temperature,. However, the drop in maximum stress clearly indicates that the material softens, i.e. undergoes brittle-to-plastic transition at temperatures above 900 °C even at deformation rates of 3500/s.

The later is even more obvious when the change in maximum stress with temperature for the dynamic experiments is plotted, Figure 3. For comparison, the change in maximum stress from quasi-static tests¹⁰ at 10⁻⁴/s is also plotted in the same graph. The similar nature of change in maximum stress for both strain rates again confirms our conclusion that deformation in Ti₂AlC is quite strain-rate insensitive

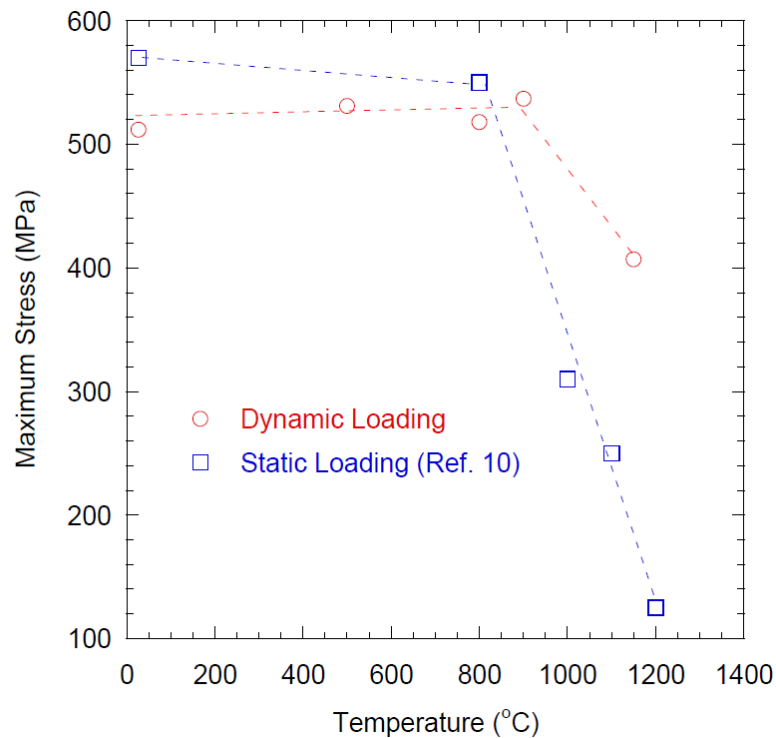


Fig. 3 Effect of temperature on the maximum stress during the dynamic deformation of Ti₂AlC. The quasi-static compressive strengths at different temperatures, from Ref. 10, are also plotted for comparison.

below BTP transition temperature even when strain rates are as high as 3500/s. More importantly, Figure 3 suggests that the material goes through the same BTP transition at strain rates that are orders of magnitude different from each other.

As far as we are aware this is the first report on dynamic stress-strain behavior of Ti_2AlC at different strain rates and temperatures, and thus more work is needed to fully understand observed trends. However, taking into account structural and mechanical similarities between the Ti_2AlC and Ti_3SiC_2 , for which effect of strain rate (of the order of $10^{-7} - 10^{-4}/\text{s}$) has been extensively studied,³¹ it is not unreasonable to assume that both of them would behave in a qualitatively similar way. Below the BTP transition temperature, Ti_3SiC_2 exhibits brittle deformation with fully reversible hysteresis at low strains, and maximum stresses that are almost independent on the deformation rate.³¹ The hysteretic behavior is shown to be due to reversible motion of dislocations in parallel slip planes, and has been discussed in more details elsewhere.^{15,20} Above the BTP transition temperature, the deformation in Ti_3SiC_2 depends on the strain rate. For example, maximum stress in Ti_3SiC_2 shows strain rate dependency in the 1100 – 1200 °C temperature range for strain rates below $10^{-6}/\text{s}$. However, above a strain rate of $10^{-5}/\text{s}$, there is little effect of strain rate on maximum stress, and Ti_3SiC_2 behaves as a brittle solid.³¹ Hence, like in quasi-static experiments,¹⁵ the primary reason for decrease in stress above BTP can be argued to be grain boundary decohesion and/or extensive delamination. Thus, further work on understanding the role of grain boundaries on the dynamic stress-strain behavior of MAX phases in general, and Ti_2AlC in particular, will shed more light on the nature of maximum stress decrease above BTP transition temperature.

4. Conclusions

In conclusion, stress-strain analysis along with microscopic investigation of the fracture surfaces in nanolaminated Ti_2AlC under dynamic loading reveal that, like quasi-static conditions, the underlying failure mechanism is independent of strain rate at temperatures below $900^\circ C$ and that it is predominantly controlled by delamination of the nanolaminated structure and KB formation. At temperatures higher than $900^\circ C$, grain boundary decohesion plays an important role in crack propagation, and subsequently in decrease of failure stress.

Acknowledgements

This work was supported in part by the Air Force Office of Scientific Research under the MURI Award No. FA9550-09-1-0686 at the Texas A&M University, and by the Grant No. FA9550-09-1-0639 at the University of Rhode Island.

References

- ¹ M. W. Barsoum, Prog. Solid State Chem **28**, 201 (2000).
- ² J. Wang and Y. Zhou, Annual Review of Materials Research **39**, 415 (2009).
- ³ P. Eklund, M. Beckers, U. Jansson, H. Högberg, and L. Hultman, Thin Solid Films **518**, 1851 (2010).
- ⁴ J. D. Hettinger, S. E. Lofland, P. Finkel, T. Meehan, J. Palma, K. Harrell, S. Gupta, A. Ganguly, T. El-Raghy, and M. W. Barsoum, Phys. Rev. B **72**, 115120 (2005).
- ⁵ M. W. Barsoum, J. Electrochem. Soc. **148**, C544 (2001).
- ⁶ M. W. Barsoum, N. Tzenov, A. Procopio, T. El-Raghy, and M. Ali, J. Electrochem. Soc., **148**, C551 (2001).

- 7 X. H. Wang and Y. C. Zhou, *Oxidation of Metals* **59**, 303 (2003).
- 8 M. Sonestedt, J. Frodelius, M. Sundberg, L. Hultman, and K. Stiller, *Corrosion Science* **52**, 3955 (2010).
- 9 J. Byeon, J. Liu, M. Hopkins, W. Fischer, N. Garimella, K. Park, M. Brady, M. Radovic, T. El-Raghy, and Y. Sohn, *Oxidation of Metals* **68**, 97 (2007).
- 10 F. L. Meng, Y. C. Zhou, and J. Y. Wang, *Scripta Materialia* **53**, 1369 (2005).
- 11 M. W. Barsoum, D. Brodtkin, and T. El-Raghy, *Scrip. Met. et. Mater.* **36**, 535 (1997).
- 12 T. El-Raghy, A. Zavaliangos, M. W. Barsoum, and S. R. Kalidindi, *J. Amer. Cer. Soc.* **80**, 513 (1997).
- 13 M. Radovic, M. W. Barsoum, T. El-Raghy, and S. M. Wiederhorn, *Acta Mater.* **49**, 4103 (2001).
- 14 M. Radovic, M. W. Barsoum, T. El-Raghy, and S. M. Wiederhorn, *J. Alloys and Compds.* **361**, 299 (2003).
- 15 M. W. Barsoum and M. Radovic, *Annual Review of Materials Research* **41**, 195 (2011).
- 16 C. J. Gilbert, D. R. Bloyer, M. W. Barsoum, T. El-Raghy, A. P. Tomasia, and R. O. Ritchie, *Scripta Materialia* **238**, 761 (2000).
- 17 D. Chen, K. Shirato, M. W. Barsoum, T. El-Raghy, and R. O. Ritchie, *J. Amer. Cer. Soc.* **84**, 2914 (2001).
- 18 H. Zhang, Z. G. Wang, Q. S. Zang, Z. F. Zhang, and Z. M. Sun, *Scripta Mater.* **49**, 87 (2003).

- 19 M. W. Barsoum, L. Farber, T. El-Raghy, and I. Levin, *Met. Mater. Trans.* **30A**,
1727 (1999).
- 20 M. W. Barsoum, T. Zhen, S. R. Kalidindi, M. Radovic, and A. Murugahiah,
Nature Materials **2**, 107 (2003).
- 21 A. G. Zhou, M. W. Barsoum, S. Basu, S. R. Kalidindi, and T. El-Raghy, *Acta*
Mater. **54**, 1631 (2006).
- 22 A. G. Zhou and M. W. Barsoum, *Journal of Alloys and Compounds* **498**, 62
(2010).
- 23 M. W. Barsoum, T. Zhen, A. Zhou, S. Basu, and S. R. Kalidindi, *Phys. Rev. B.*
71, 134101 (2005).
- 24 M. W. Barsoum and S. Basu, in *Encyclopedia of Materials: Science and*
Technology, edited by K. H. J. Buschow, R. W. Cahn, M. C. Flemings, B.
Ilshner, E. J. Kramer, S. Mahajan, and P. Veysiere (Elsevier, 2010).
- 25 A. G. Zhou, S. Basu, G. Friedman, P. Finkel, O. Yeheskel, and M. W.
Barsoum, *Physical Review B* **82**, 094105 (2010).
- 26 Y. C. Zhou and X. H. Wang, *Materials Research Innovations* **5**, 87 (2001).
- 27 H. Kolsky, *Proceedings of the Physical Society. Section B* **62**, 676 (1949).
- 28 A. Kidane and A. Shukla, *Journal of Materials Science* **43**, 2771 (2008).
- 29 S. Abotula, A. Shukla, and R. Chona, *Journal of Materials Science* **46**, 4971
(2011).
- 30 M. W. Barsoum, M. Ali, and T. El-Raghy, *Met Mater Trans* **31A**, 1857 (2000).
- 31 M. Radovic, M. W. Barsoum, T. El-Raghy, S. M. Wiederhorn, and W. E.
Luecke, *Acta Materialia* **50**, 1297 (2002).

CHAPTER 5

DYNAMIC CONSTITUTIVE BEHAVIOR OF HASTELLOY X UNDER THERMO-MECHANICAL LOADS

by

Sandeep Abotula, Arun Shukla and Ravi Chona

has been published in Journal of Materials Science

Corresponding Author: Arun Shukla

Dynamic Photo Mechanics Laboratory

Department of Mechanical, Industrial and Systems

Engineering

University of Rhode Island

206 Wales Hall, 92 Upper College Rd

Kingston, RI, 02881, USA

Phone: +1-401-874-2283

Email Address: shuklaa@egr.uri.edu

Abstract

An experimental investigation has been conducted to study the dynamic constitutive behavior of Hastelloy X (AMS 5754) at room and elevated temperatures under varying rates of loading. A split Hopkinson pressure bar (SHPB) apparatus was used in conjunction with an induction coil heating system for applying dynamic loads at elevated temperatures. Experiments were carried out at different temperatures ranging from room temperature (25°C) to 1100°C at an average strain rate of 5000/s. Room temperature experiments were carried out at varying strain rates from 1000/s to 4000/s. The results show that as the strain rate increases from quasi-static to 4000/s, the yield strength increases by approximately 50%. Also, under dynamic loading, the yield stress decreases with temperature up to 700°C, after which it shows a peak at 900°C before beginning to decrease again as the temperature is further increased. The Johnson-Cook model was used to predict the dynamic plastic response under varying rates of loading and at different temperatures.

Keywords: Hastelloy X, thermo-mechanical loading, constitutive behavior, high temperatures, SHPB, Johnson-Cook model.

1. Introduction

Hastelloy X is a nickel based superalloy that possesses excellent high temperature strength and oxidation resistance. It is widely used in gas turbine operations, petrochemical and in aircraft parts. Due to its high oxidation resistance, it

is also used for structural components in industrial furnace applications [1]. Thus, it is important to understand the constitutive behavior of this material.

Several researchers in the past have investigated the behavior of Hastelloy X. Lai [2] investigated changes in the hardness and impact toughness at room temperature of Hastelloy X after aging up to 1000h. The author found that it exhibits age hardening at 540°C and 650°C. The author also observed a slight increase in hardness at 871°C followed by overaging after 4000h. Yasuo Kondo et al. [3] presented experimental results on the changes in the tensile mechanical properties of Hastelloy X after being used in the liner tube of a HENDEL hot gas duct under high temperature helium gas for about 6000h. They observed that the 0.2% proof stress and total elongation were slightly decreased when Hastelloy X was exposed to high temperature helium. Static tensile stress-strain curves of Hastelloy X were reported in Mil Handbook 5h [4]. Swindeman and Brinkman [5] reviewed high temperature mechanical properties for materials including Hastelloy X, used in a pressure vessel using stress-strain curves obtained experimentally. They studied the effect of cold work, chemistry, and heat treatment variations in Hastelloy X. Aghaie Khafri and Golarzi [6] characterized the hot deformation behavior of Hastelloy X using hot compression tests in the temperature range of 900°C-1150°C and at varying strain rates between 0.001 and 0.5/s. They showed that softening mechanisms, dynamic recovery and dynamic recrystallization occurred during hot working. Zhao et al. [7] studied the phase precipitation in Hastelloy X heat-treated at 750°C, 850°C and 900°C for 26 and 100 hours. They also provided a TTT (time-temperature-transformation) diagram by combining the new experimental results with the existing literature data.

This TTT diagram depicted the presence of $M_{23}C_6$ and σ phases at temperatures $< 900^\circ\text{C}$ and μ phase between 800°C and 980°C . Hong et al. [8] performed low cycle fatigue tests of Hastelloy X in the temperature range of 650°C - 870°C under various strain rates. They found that the Coffin-Manson (C-M) plot was different from those at other temperatures and also the fatigue life significantly decreased at the total strain range less than 0.6%. Krompholz and Ullrich [9] determined J-integral R curves for Hastelloy X upto 660°C using potential drop technique and showed that there is a decrease in J-integral value at 660°C . Rowley and Thornton [10] modeled visco plastic behavior of Hastelloy X using the Bodner Partom unified constitutive model. Static compression experiments were conducted at different temperatures to get the parameters for the model. The model results of Hastelloy X for isothermal uniaxial tensile tests showed good agreement with the experimental stress-strain data.

Based upon the careful literature search, it was determined that there is no detailed study of the dynamic characterization of Hastelloy X under thermo-mechanical loading. Hence this study focuses mainly on the dynamic constitutive behavior of Hastelloy X at room and elevated temperatures.

2. Material and Specimen Geometry

% wt	C	Si	Mn	P	S	Ni	Cr	Mo	Co	W	Fe	B
Min	0.05	--	--	--	--	--	20.50	8.00	0.5	0.2	17.00	--
Max	0.15	1.00	1.00	0.040	0.030	Residual	23.00	10.00	2.50	1.00	20.00	0.01

Table 1. Chemical composition of Hastelloy X [1].

The material used in this experimental study is Hastelloy X, supplied by Haynes International. The chemical composition of the material is listed in Table 1

[1]. It can be observed from the table that Hastelloy X has high content of Ni, Cr, Fe and Mo. Three different types of specimens were machined as per the requirement of the experiments. According to ASTM E9, cylindrical specimens with a diameter of 12.7mm and thickness of 25.4mm were machined for quasi-static experiments. Specimens, having a diameter of 7.62mm and thickness of 3.81mm were used for dynamic characterization at room temperature and specimens with a diameter of 6.35mm and thickness of 3.175mm were used at elevated temperatures.

3. Experimental Details

3.1 Quasi-Static Characterization

The quasi-static compression tests were performed using Instron Materials Testing System-5585. ASTM standard E9-89a was followed for the specimen dimensions and testing procedure. Experiments were performed at a compression-extension rate of 1mm/min and the tests were continued up to a strain of 25%. Molybdenum disulphide was used as a lubricant between the specimen and loading head.

3.2 Dynamic Characterization

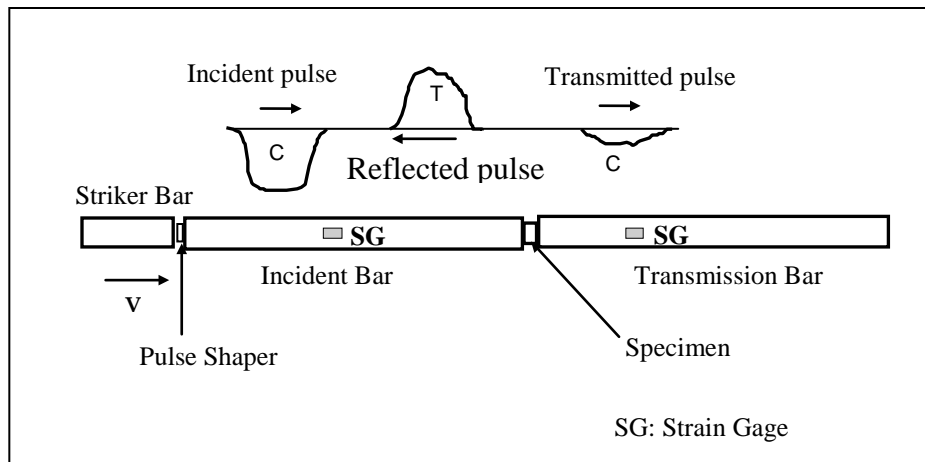


Fig. 1 Experimental setup of SPHB.

A Split Hopkinson Pressure Bar (SHPB) apparatus was used to study the dynamic behavior of Hastelloy X. The SHPB consists of a striker bar, a solid incident bar and a solid transmission bar, all made out of Maraging steel. Incident and transmission bars have a diameter of 12.5mm and a length of 1220mm. The striker bar is propelled using an air-operated gun. A clay pulse shaper of thickness 2mm was placed at the impact end of the incident bar as shown in Fig. 1 to improve force equilibrium conditions at the specimen-bar interface. The theoretical details of SHPB can be obtained from Kolsky [11]. The specimen was sandwiched between the incident bar and the transmission bar. Molybdenum disulfide was used as a lubricant between the specimen and the contacting surfaces of the bars to minimize friction.

When the striker bar impacts the incident bar, an elastic compressive stress pulse, referred to as the incident pulse, is generated. The generated pulse deforms the pulse shaper at the impact end and creates a ramp in the incident pulse which further propagates along the incident bar. When the incident pulse reaches the specimen, part of it reflects back into the incident bar (reflected pulse) in the form of tensile pulse due to the impedance mismatch at the bar-specimen interface and the remaining pulse is transmitted (transmission pulse) to the transmission bar. Axial strain gages mounted on the surfaces of the incident and transmission bar provide time-resolved measures of the elastic strain pulses in the bars.

Room temperature experiments were carried out at strain rates ranging from 1000-4000/s. Different strain rates are obtained by varying the velocities of the striker bar. Using one-dimensional wave theory, the true strain and true stress in the specimen

can be determined from the reflected and transmitted strain pulses respectively as given in Eqs. 1 and 2.

$$\sigma_s = E_b \frac{A_b}{A_s} \varepsilon_t(t) \quad (1)$$

$$\varepsilon_s = \frac{-2c_b}{L_s} \int_0^t \varepsilon_r(t) dt \quad (2)$$

The expressions for the forces at the specimen incident bar interface and at the specimen transmission bar interface are given in equations Eqs. 3 and 4 respectively.

$$F_i = A_b E_b (\varepsilon_i + \varepsilon_r) \quad (3)$$

$$F_t = A_b E_b \varepsilon_t \quad (4)$$

Where $\varepsilon_i, \varepsilon_r, \varepsilon_t$ are the time-resolved strain values of the incident, reflected and transmitted pulses respectively, $c_b = \sqrt{E_b / \rho_b}$ is the longitudinal bar wave speed, E_b is the Young's modulus of the bar material, ρ_b is the density of the bar material, L_s is the thickness of the specimen, A_b the is cross-sectional area of the bar and A_s is the cross-sectional area of the specimen.

Force equilibrium within the specimen during the wave loading is attained when the forces on each face of the specimen are equal. The ratio of these two forces (as given in Eq. 5) provides a measure for force equilibrium. For ideal equilibrium conditions, the ratio should be 1.0.

$$\text{ForceRatio, } \frac{F_i}{F_t} = \frac{(\varepsilon_i + \varepsilon_r)}{\varepsilon_t} \quad (5)$$

For experiments at elevated temperatures, the SHPB apparatus in conjunction with the induction coil heating system was utilized as shown in Fig. 2. A special

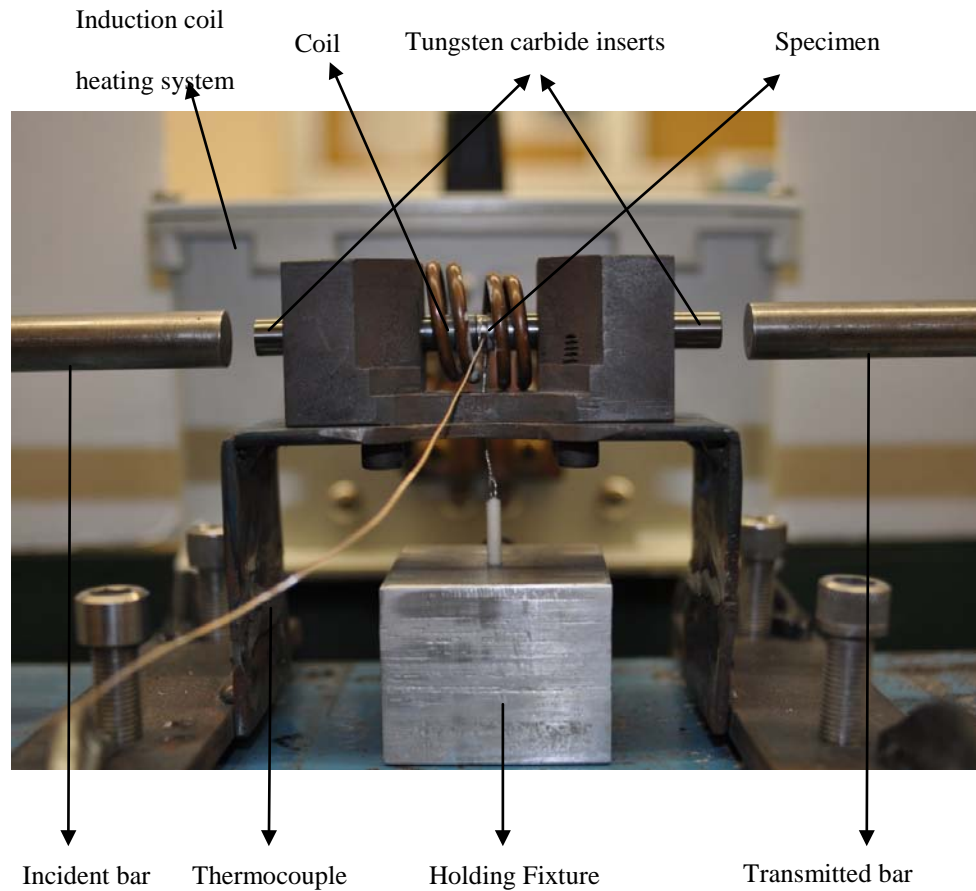


Fig. 2 Experimental setup of SHPB apparatus with induction coil heating system.

fixture was designed and fabricated to load the specimen. Two tungsten carbide inserts were placed between the two pressure bars and the specimen was sandwiched between the tungsten carbide inserts as shown in Fig. 2. The inserts were used to eliminate the temperature gradient in the bars and thus protect the strain gages mounted on them. The impedance of the inserts was matched with the bars; hence they do not disturb the stress wave profiles in the bar. The impedance matching requires the diameter of these tungsten carbide inserts to be smaller than the main pressure bars. This is the reason

for the specimen diameter for high temperature testing being smaller than that for room temperature testing. The bars were kept apart initially, later the specimen and carbide inserts were heated in isolation to the desired temperature (usually about 20-50°C higher than the test temperature) and soon after the bars were brought manually into contact with the specimen. The temperature of the specimen was monitored using a 0.127mm chromel-alumel thermocouple, which was spot welded onto the specimen. In most of the experiments, it takes less than two minutes to heat the specimen to the required temperature and it takes less than 10 seconds to bring the pressure bars into contact with the tungsten inserts and fire the gun.

High temperature experiments were carried out from room temperature to 1100°C under identical strain rate of about 5000/s. Molybdenum disulphide was used as lubricant in the initial experiments and subsequently this was replaced with Boron Nitride. Molybdenum disulphide works well till about 300°C and Boron nitride is supposed to work till about 1200°C. Both the lubricants show about same amount of barreling (1 to 2% differences in the center diameter to outside diameter).

3.3 Johnson Cook Constitutive Model

3.3.1 Model Description

Johnson and Cook proposed an empirical constitutive model [12, 13] to predict the plastic behavior of metals that are subjected to large strains, high strain rates and high temperatures. It is one of the most widely used models due to its simplicity and yet effective form. According to the model, the flow stress can be written as

$$\sigma = (A + B\varepsilon_p^n) \left(1 + C \ln \left(\frac{\dot{\varepsilon}_p}{\dot{\varepsilon}_o} \right) \right) \left(1 - (T^*)^m \right) \quad (6)$$

where σ is the flow stress, A and B are the strain hardening parameters and typically A is referred as the yield stress at reference strain rate and reference temperature, C is a dimensionless strain hardening coefficient, ε_p is the plastic strain, $\dot{\varepsilon}_p/\dot{\varepsilon}_o$ is the dimensionless strain rate with $\dot{\varepsilon}_p$ being the plastic strain rate and $\dot{\varepsilon}_o$, the reference strain rate. Parameters n and m are power exponents of the strain hardening and thermal softening terms. T^* represents normalized temperature as given below in Eq. 7,

$$T^* = \frac{T - T_{reference}}{T_{melt} - T_{reference}} \quad (7)$$

where T_{melt} is the melting temperature, $T_{reference}$ is the reference temperature and T is the test temperature. The expression in the first set of parentheses in Eq. 6 represents stress as a function of strain, the expression in the second set of parentheses represents the effect of strain rate and the expression in the third set represents the effect of temperature.

3.3.2 Determination of Parameters of Model

As shown in Eq. 6, there is a set of five model parameters that need to be identified (A , B , C , n and m). A , B and n are obtained from a quasi-static test at room temperature. The parameter A is often defined as the yield stress of the reference strain rate [12]. Here, the quasi-static strain rate is considered as the reference strain rate. Parameter A (yield stress) is determined by considering 0.2% strain offset from the quasi-static test. Once A is determined, parameters B and n are obtained by fitting the quasi-static test data to the model as given in Eq. 8.

$$\ln(\sigma - A) = (\ln B + n \ln \varepsilon_p) \quad (8)$$

Having identified A , B and n , the next step is to determine the value of C . Dynamic SHPB experiments at reference temperature and different strain rates are used to estimate the value of C . The initial yield point and strain rate ($\dot{\varepsilon}_p$) from each dynamic test was used to determine C . In doing so, it was ensured that the heat generated from plastic work was not taken into account, thus ignoring the temperature effect. The parameter C for a given dynamic test can be calculated as given in Eq. 9,

$$C = \frac{\left(\frac{\sigma}{A + B \varepsilon_p^n} - 1 \right)}{\ln \left(\frac{\dot{\varepsilon}_p}{\dot{\varepsilon}_o} \right)} \quad (9)$$

The calculated value of C at different strain rates may not be the same due to variations in the experimental data so an average value of C is obtained.

Now the final task is to identify the value of m . A set of experiments at different temperatures but identical strain rate are used to determine the value of m . A similar procedure is followed to that of parameter C , but the effect of temperature is included. As each of the parameters is identified from separate experiments, the final set of parameters may or may not predict the material behavior when all the terms vary at the same time. Therefore, the identified parameters may predict few experiments very well but not other experiments. So it is important to optimize the identified parameters, which can be done by minimizing the average relative error (Δ) between the experimental data and the predicted flow stress [14].

$$\Delta = \frac{1}{N} \sum_{i=1}^N \left| \frac{\sigma_{\text{exp}}^i - \sigma_p^i}{\sigma_{\text{exp}}^i} \right| \times 100\% \quad (10)$$

where σ_{exp} is the experimental flow stress, σ_p is the predicted flow stress and N is the total number of data. The Johnson-Cook material parameters of Hastelloy X are given in Table 2.

Parameters	A (MPa)	B (MPa)	C	n	m
Value	380	1200	0.012	0.55	2.5

Table 2. Johnson-Cook material parameters of Hastelloy X.

4. Experimental Results

4.1 Quasi-Static Response

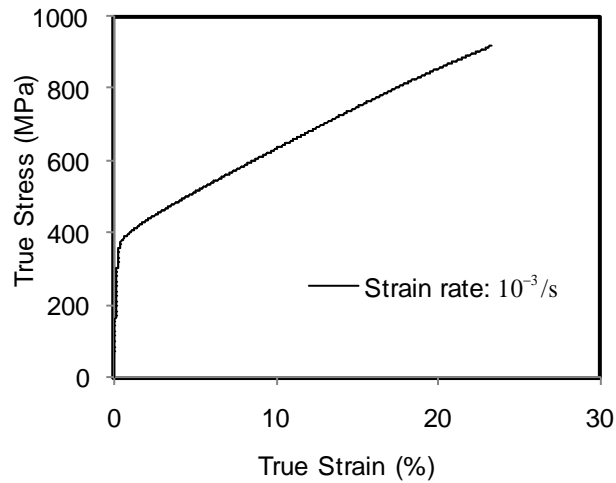


Fig. 3 True compressive stress-strain curve of Hastelloy X under quasi-static loading.

The true stress versus true strain curve for Hastelloy X under quasi-static conditions is shown in Fig. 3. It has two regions: the initial linear portion and the non-linear portion. The material exhibited yield strength of 380 MPa and Young's

Modulus of 190GPa. The flow stress (strain hardening) of the material increases as the true strain increases.

4.2 Dynamic Constitutive Response at Room Temperature

The real time strain-pulses obtained for Hastelloy X at an average strain rate of 2500/s are shown in Fig 4. It can be observed from the figure that the clay pulse shaper used in all these experiments helped to reduce high frequency oscillations in the incident stress wave. It is important for the specimen to be in equilibrium under dynamic loading conditions for valid analysis of data. Fig. 5 shows the typical force

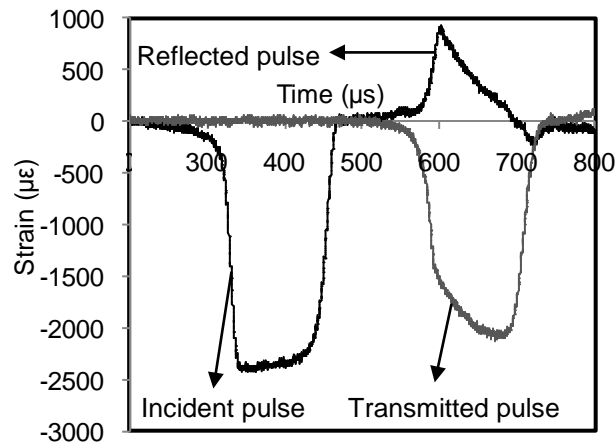


Fig. 4 Typical real-time strain pulses obtained from strain gages mounted on the bars for an average strain rate of 2500/s.

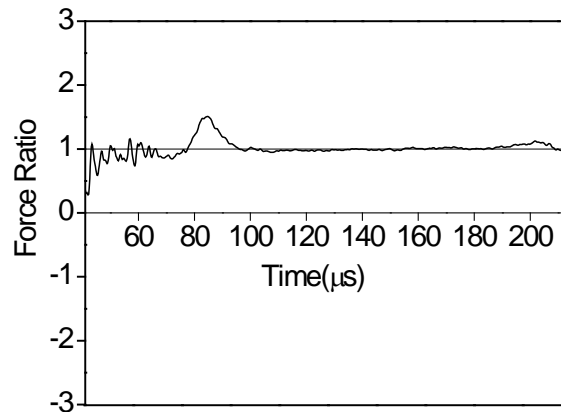


Fig. 5 Typical force equilibrium conditions at the specimen-bar interface at an average strain rate of 2500/s.

equilibrium conditions at an average strain rate of 2500/s. The solid line in the figure indicates the ideal force ratio of 1.0. The pulse shaper used improved the force equilibrium conditions at the specimen-bar interface. The force equilibrium was attained at around 50 μ s and was maintained during the entire loading duration.

The dynamic true stress-true strain curve for different strain rates ranging from 1000/s to 4000/s are plotted along with the quasi-static true stress-true strain curve for Hastelloy X at room temperature in Fig 6. Hastelloy X shows rate dependency from

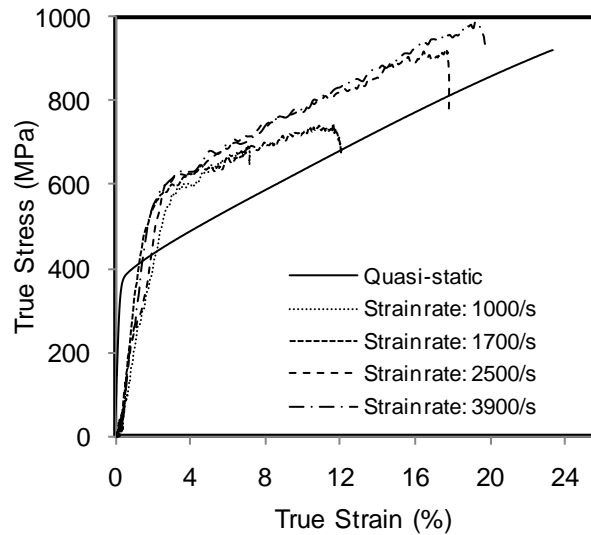


Fig. 6 True compressive stress-strain curve of Hastelloy X under dynamic loading at room temperature.

quasi-static loading to dynamic loading. The dynamic yield strength is about 50% higher than the quasi-static yield strength, while the dynamic flow stress is about 200MPa higher than the quasi-static flow stress. The constituent elements in the material are responsible for the rate sensitivity of Hastelloy X. Under dynamic loading conditions, the material showed small increase in yield strength and flow stress as the strain rate is increased from 1000/s to 4000/s.

4.3 Dynamic Constitutive Response at Elevated Temperatures

A series of experiments were conducted to investigate the dynamic constitutive behavior of Hastelloy X at different temperatures under identical strain rate of about 5000/s. Fig. 7 shows the dynamic true stress-strain curves for Hastelloy X at different

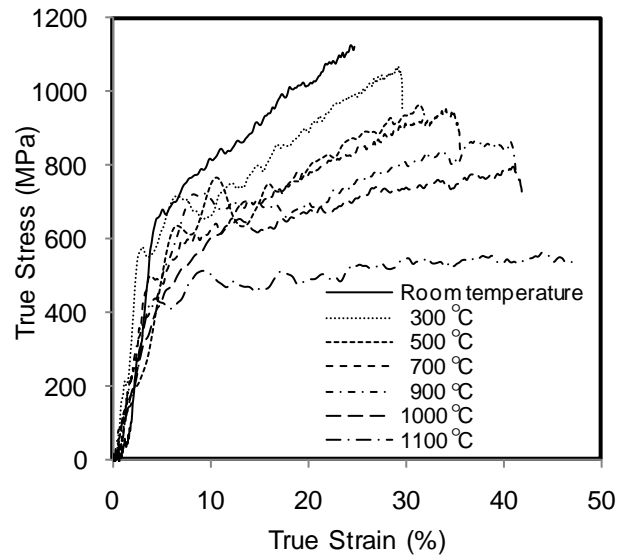


Fig. 7 True compressive stress-strain curve of Hastelloy X under dynamic loading at elevated temperatures and a strain rate of about 5000/s.

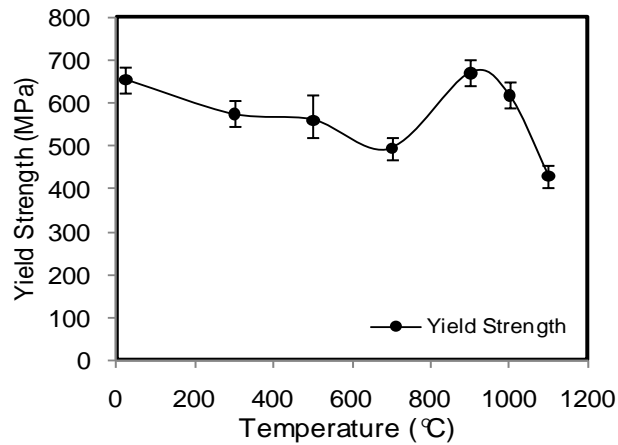


Fig. 8 Effect of temperature on the yield strength under dynamic loading at an average strain rate of 5000/s.

temperatures. All experiments were carried out with the same striker bar and at the same pressure. Fig. 7 clearly shows that as the temperature increases, the yield strength of the material decreases except at temperatures of 900°C and 1000°C. The true strain in the specimen increases and the flow stress decreases as the temperature increases. As the temperature increases, the material shows more ductile behavior and this result in a decrease in its yield strength and increase in the strain for a given applied stress.

Fig. 8 shows the effect of temperature on the yield strength under dynamic loading and the error bars indicate the range of values obtained from three different experiments. As temperature increases, the yield strength decreases initially up to 700°C, then increases and shows a peak at 900°C and then again monotonically decreases as the temperature is further increased. The trend reported in this paper is in good agreement with the previous findings for Ni base superalloys [15-20] under quasi-static loadings. Bettge et al. [15] studied the temperature dependence of yield strength of Ni-base superalloy IN 738LC and concluded that the yield strength of the material decreases up to 450°C, then increases up to 750°C and finally decreases sharply. Sajjadi et al. [19] observed that the yield strength of GTD-111 under tensile loading decreases with increasing temperature and reaches a minimum value of 750MPa at 600°C. With a further increase in temperature to 750°C, the yield strength increased up to 1090MPa and then suddenly decreases. Three important factors were proposed [16, 17, 19] for the behavior of Ni base superalloys. These are (i) Grain boundary embrittlement, (ii) deformation mechanisms and (iii) γ' coarsening. Grain boundary embrittlement by carbide particles and deformation mechanisms has almost

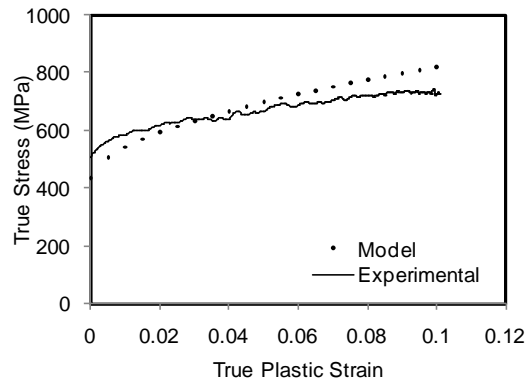
the same influence on the ductility of these alloys with temperature. The presence of transgranular cracks are more noticeable at higher temperatures but more intergranular cracks can be seen between 750°C to 950°C leading to increase in the yield strength of the material. Also the ratio of intergranular cracks to transgranular cracks decreases above 950°C. The transition of crack initiation on the surface from transgranular to intergranular is also noticed in other experiments of Hastelloy X [2, 7, 8, 21]. It was also found that in the tensile properties of Hastelloy X above 950°C, there is a change in the fracture mode from transgranular dimple rupture to intergranular [3]. For Hastelloy X-280, the presence of M_6C , M_6C' and $M_{23}C$ phases in the 650°C to 930°C temperature range creates a ductility minimum at those temperatures [22].

4.4 Johnson Cook Constitutive Model Response

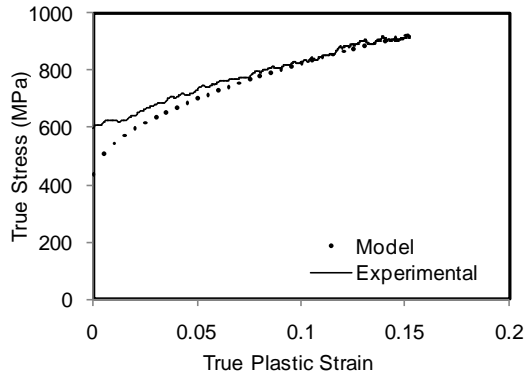
As the Johnson Cook model could only predict the stress in the plastic region, the elastic region was not considered for plotting. The comparison between the experimental data and the predicted data at various strain rates is shown in Fig. 9. A small deviation between the experimental data and the predicted data was observed at all three strain rates and the deviation was more at lower strain rates compared to higher strain rates. The predictability of the Johnson-Cook model for the dynamic plastic response of Hastelloy X was also quantified by calculating average relative error (A) and correlation coefficient (R). Average relative error was calculated using Eq. 10 and correlation coefficient (R) can be mathematically expressed as given in Eq. 11 [14].

$$R = \frac{\sum_{i=1}^N (\sigma_{\text{exp}}^i - \bar{\sigma}_{\text{exp}})(\sigma_p^i - \bar{\sigma}_p)}{\sqrt{\sum_{i=1}^N (\sigma_{\text{exp}}^i - \bar{\sigma}_{\text{exp}})^2 \sum_{i=1}^N (\sigma_p^i - \bar{\sigma}_p)^2}} \quad (11)$$

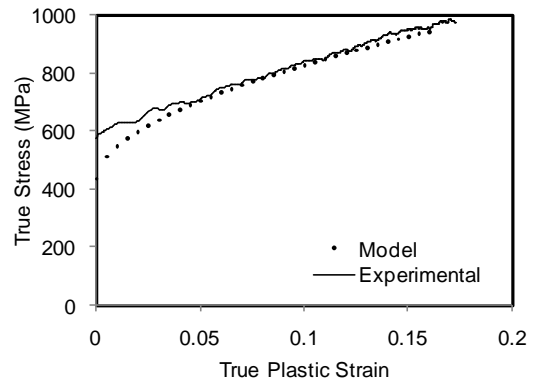
where $\bar{\sigma}_{\text{exp}}$ and $\bar{\sigma}_p$ are the mean values of σ_{exp} and σ_p respectively and N denotes the number of data points. The correlation coefficient provides information on the strength of linear relationship between the experimental data and the predicted data. The



(a) 1700/s



(b) 2500/s



(c) 3900/s

Fig. 9 Experimental data and model prediction of Hastelloy X under dynamic loading at different strain rates.

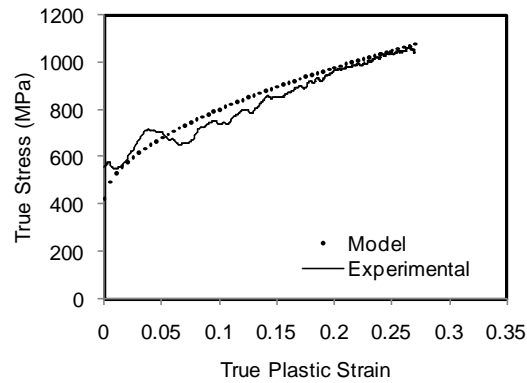
Strain rate (s^{-1})	Correlation coefficient (R^2)	Average relative error (Δ), %
1700	0.983	7.24
2500	0.985	2.80
3900	0.987	2.58

Table 3. Predictability of the model for the dynamic plastic response of Hastelloy X at room temperature under various strain rates.

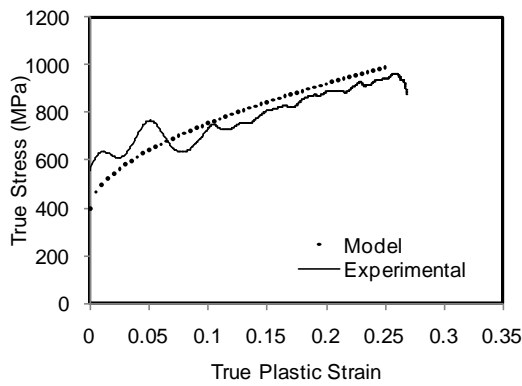
predictability of the model for the dynamic plastic response of Hastelloy X at room temperature under various strain rates is shown in Table 3. There is good correlation between the experimental data and the predicted data for all the three strain rates and the average relative error was low at higher strain rates compared to lower strain rates. Higher value of R^2 (0.985) was observed for strain rate of 2500/s. Even though the value of R^2 (0.983) is high for a strain rate of 1700/s, it has a high relative error (7.24%) which indicates larger deviation between the experimental data and the predicted data. It should be noted that higher value of R^2 may not necessarily indicate better performance [23]. The model has the tendency to be biased towards higher or lower values, whereas Δ is calculated through a term by term comparison of relative error between the experimental data and the predicted data, therefore it produces unbiased statistics. Better correlation can be achieved if the value of Δ is low and this can noticed for a strain rate of 3900/s.

Temperature (°C)	Correlation coefficient (R^2)	Average relative error (Δ), %
300	0.955	4.24
500	0.895	6.90
700	0.989	2.21

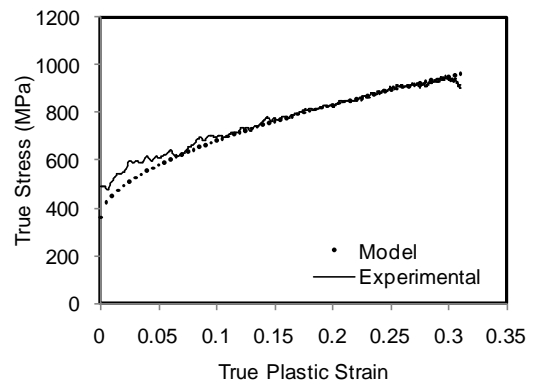
Table 4. Predictability of the model for the dynamic plastic response of Hastelloy X at different temperatures.



(a) 300°C



(b) 500°C



(c) 700°C

Fig. 10 Experimental data and model prediction of Hastelloy X under dynamic loading at different temperatures.

The comparison between the experimental data and the predicted data at different temperatures is shown in Fig. 10. Model predictions for the dynamic plastic response of Hastelloy X at different temperatures are shown in Table 4. The model was not used to predict the dynamic plastic response of Hastelloy X above 700°C as the material showed different behavior after 700°C as discussed in the previous section. The model predicted very well for all the three temperatures chosen, with Δ ranging between 2.21% and 6.90%. Excellent correlation between the experimental data and the predicted data was achieved for the temperature of 700°C and this can be observed in Table 4 showing a low value of Δ (2.21%). Relatively high value of Δ (6.90%) was observed for a temperature of 500°C.

5. Conclusions

A series of experiments were conducted to investigate the dynamic constitutive behavior of Hastelloy X at room and elevated temperatures. Clay was used as a pulse shaper in all the experiments to improve force equilibrium conditions at the bar-specimen interfaces. A Johnson-Cook model was used to predict the dynamic plastic response of Hastelloy X under varying strain rates and at different temperatures. Following are the major conclusions of this study:

- Quasi-static experiments showed yield strength of 380MPa and a Young's Modulus of 190GPa for Hastelloy X.
- The material showed rate dependency from quasi-static to dynamic loading. An increase of 50% in yield stress and 200MPa in flow stress was observed from the quasi-static to dynamic loading. Under dynamic loading, the flow stress of the material decreases as the temperature increases.

- The yield strength of the specimen monotonically decreases as the temperature increases up to about 700°C. Between 700°C and 1000°C the yield stress increases before again decreasing as the temperature is further increased.
- The Johnson-Cook model predicted very well for all the experiments and the best correlation was observed for a strain rate of 3900/s ($\Delta=2.58\%$) in case of room temperatures experiments and for a temperature of 700°C ($\Delta=2.21\%$) in case of high temperature experiments.

Acknowledgements

The first two authors kindly acknowledge the financial support provided by the Air Force Office of Scientific Research under Grant No. FA9550-09-1-0639. Also the authors would like to thank professor John Lambros for his valuable discussions.

References

- [1] Haynes, International, Jan 2012. <http://www.haynesintl.com/pdf/h3009.pdf>
- [2] Lai GY (1978) An investigation of the thermal stability of a commercial Ni-Cr-Fe-Mo alloy (Hastelloy X). Metall Mater Trans A 9:827-833
- [3] Yasuo K, Kiyoshi F, Kazuhiko K, Yoshiaki M (1988) Tensile and impact properties changes of Hastelloy X after exposure in high temperature helium environment. Metall Mater Trans A 19: 1269-1275
- [4] Heat Resistant Alloys, Military Handbook-Mil-Handbook-5H (1998). Metallic materials and elements for aerospace vehicle structures, Chapter 6, Knovel Interactive edition.

- [5] Swindeman RW, Brinkman CR (1981) Progress in understanding the mechanical behavior of pressure-vessel materials at elevated temperatures. Technical Report, ASME PVP Conference, Denver, Co, USA
- [6] Aghaie-Khafri, M, Golarzi N (2007) Forming behavior and workability of Hastelloy X superalloy during hot deformation. *Mater Sci Eng A* 486:641-647
- [7] Zhao JC, Larsen M, Ravikumar V (2000) Phase precipitation and time-temperature-transformations diagram of Hastelloy X. *Mater Sci Eng A* 293:112-119
- [8] Hong HU, Kim IS, Choi BG, Jeong C Y Jo (2008) Effects of temperature and strain range on Fatigue Cracking Behavior in Hastelloy X. *Mater Lett* 62:4351-4353
- [9] Krompholz K, Grosser ED, Ewert K (2004) Determination of J-Integral R-Curves for Hastelloy X and Inconel 617 up to 1223K using the potential drop technique. *Materialwiss. Werkstofftech* 13:236-244
- [10] Rowley MA, Thornton EA (1996) Constitutive modeling of the visco-plastic reponse of Hastelloy-X and Aluminium alloy 8009. *J Eng Mater Technol* 118:19-27
- [11] Kolsky, H (1949) An investigation of the mechanical properties of materials at very high strain rates of loading. *Proc Phys Soc* 62:676-700
- [12] Milani AS, Dabboussi W, Nemes JA, Abeyaratne RC (2009) An improved multi-objective identification of Johnson-Cook material parameters. *Int J Impact Eng* 36:294-302
- [13] Johnson GR, Cook WH (1983) A constitutive model and data for metals subjected to large strains, high strain rates and high temperatures. Proceedings of seventh international symposium on ballistics, The Hague, The Netherlands:541-547

- [14] Hou QY, Wang JT (2010) A modified Johnson-Cook constitutive model for Mg-Gd-Y alloy extended to a wide range of temperatures. *Comput Mater Sci*. DOI:10.1016/j.commatsci.2010.07.018
- [15] Bettge D, Osterle W, Ziebs J (1995) Temperature dependence of additional cyclic hardening of a nickel-base superalloy during out-of-phase multiaxial deformation. *Scr Metall Mater* 32:1601-1606
- [16] Sajjadi SA, Zebarjad SM (2006) Study of fracture mechanisms of a Ni-base superalloy at different temperatures. *J Achieve Mater Manuf Eng* 18:227-230
- [17] Sajjadi SA, Zebarjad SM (2006) Effect of temperature on tensile fracture mechanisms of a Ni-base superalloy. *J Achieve Mater Manuf Eng* 28:34-40
- [18] Sieborger D, Knake H, Glatzel G (2001) Temperature dependence of the elastic moduli of the nickel-base superalloy CMSX-4 and its isolated phases. *Mater Sci Eng A* 298:26-33
- [19] Sajjadi SA, Nategh S, Isac M, Zebarjad SM (2004) Tensile deformation mechanisms at different temperatures in the Ni-base superalloy GTD-111. *J Mater Process Technol* 155-156:1900-1904
- [20] Matthews SJ, Greentown, Klein HJ, Hodge FG (1978) High yield strength Ni-Cr-Mo alloys and methods of producing the same. United States Patent 4129464
- [21] Petronic S, Milosavljevic A (2007) Heat treatment effect on multicomponent nickel alloys structure. *FME transactions* 35:189-193
- [22] Claudson TT, Westerman RE (1965) An evaluation of the corrosion resistance of several high temperature alloys for nuclear applications. Metallurgy Research Section, Reactor and Materials Technology Department

[23] Samantaray D, Mandal S, Bhaduri AK (2009) A comparative study on Johnson Cook, modified Zerilli-Armstrong and Arrhenius type constitutive model to predict elevated temperature flow behaviour in modified 9Cr-1Mo steel. *Comput Mater Sci* 47:568-576

CHAPTER 6

DYNAMIC THERMO-MECHANICAL RESPONSE OF HASTELLOY X UNDER SHOCK WAVE LOADING

by

Sandeep Abotula, Nicholas Heeder, Ravi Chona and Arun Shukla

Under preparation for submission to the Mechanics of Materials

Corresponding Author: Arun Shukla

Dynamic Photo Mechanics Laboratory

Department of Mechanical, Industrial and Systems

Engineering

University of Rhode Island

206 Wales Hall, 92 Upper College Rd

Kingston, RI, 02881, USA

Phone: +1-401-874-2283

Email Address: shuklaa@egr.uri.edu

Abstract

A comprehensive series of experiments were conducted to study the dynamic response of rectangular Hastelloy X plates at room and elevated temperatures when subjected to shock wave loading. A shock tube apparatus, capable of testing materials at temperatures up to 900 °C, was developed. Propane gas was used as the heating source to effectively provide an extreme heating environment that is both robust and capable of providing uniform heating during shock loading. A cooling system was also implemented to prevent the shock tube from reaching high temperatures. High-speed photography coupled with the optical technique of Digital Image Correlation (DIC) was used to obtain the real-time 3D deformation of the specimen under shock wave loading. To eliminate the influence of thermal radiations at high temperatures, the DIC technique was used in conjunction with band pass optical filters and a high intensity light source to obtain the full-field deformation. In addition, a high speed camera was utilized to record the side-view deformation images and this information was used to validate the data obtained from the high temperature 3D DIC technique. The results showed that uniform heating of the specimen was consistently achieved with the designed heating system. For the same applied incident pressure, the highest impulse was imparted on the specimen at room temperature. As a consequence of temperature dependent material properties, the specimen demonstrated an increasing trend in back face (nozzles side) deflection, in-plane strain and out-of-plane velocity with increasing temperature.

Keywords: Hastelloy X, thermo-mechanical loading, extreme environments, shock tube, high temperature DIC.

1. Introduction

The objective of this study was to investigate the performance of Hastelloy X under a combination of extreme mechanical and thermal environments. For this purpose, a unique experimental set up was established to evaluate the performance of Hastelloy X at high temperatures when subjected to a controlled shock wave loading. The present shock tube apparatus was modified for testing Hastelloy X at high temperatures (up to 900 °C). Propane gas was used as the heating source to effectively provide an extreme heating environment that is both robust and capable of providing uniform heating during shock loading. A 3D digital image correlation (DIC) system was utilized to record the transient deformation data of the specimen during the blast loading. A side-view high speed camera was also used to record the real-time deformation images. For experiments at elevated temperatures, a blue color optical band pass filter and a high intensity light source was utilized in conjunction with the 3D DIC system. The transient mid-point deflections obtained from the 3D DIC system were compared with the deflections from the side-view camera. The DIC analysis was implemented to investigate the transient deflection, in-plane strain and out-of-plane velocity of the back face of the specimen. The shock pressure profiles and the real-time deformation images were later used to calculate the deformation energy. Post-mortem analysis was carried out to evaluate the performance of Hastelloy X at different temperatures under shock loading.

Hastelloy X is a nickel based superalloy that possesses excellent high temperature strength and oxidation resistance. It is widely used in gas turbine operations, petrochemical applications and in aircraft parts. Due to its high oxidation resistance, it is also used for structural components in industrial furnace applications (Haynes, 2012). Several researchers have previously investigated the behavior of Hastelloy X. (Lai, 1978) investigated changes in the hardness and room temperature impact toughness of Hastelloy X after aging at 538 °C, 649 °C, 760 °C and 871 °C up to 10000 h. The author found that it exhibits age hardening at 649 °C and 760 °C. The results also indicated a slight increase in hardness at 871 °C followed by over aging after 4000 h. (Kondo et al., 1988) presented experimental results on the changes in the tensile mechanical properties of Hastelloy X after being used in the liner tube of a HENDEL hot gas duct under high temperature helium gas for about 6000 h. They observed that the 0.2 % proof stress and total elongation were slightly decreased when Hastelloy X was exposed to high temperature helium. (Aghaie-Khafri and Golarzi, 2008) characterized the hot deformation behavior of Hastelloy X using hot compression tests in the temperature range of 900 °C - 1150 °C and at varying strain rates between 0.001 and 0.5 s⁻¹. They showed that softening mechanisms, dynamic recovery and dynamic recrystallization occurred during hot working. (Zhao et al., 2000) studied the phase precipitation in Hastelloy X heat-treated at 750 °C, 850 °C and 900 °C for 26 and 100 hours. They also provided a TTT (time-temperature-transformation) diagram by combining the new experimental results with the existing literature data. This TTT diagram depicted the presence of $M_{23}C_6$ and σ phases at temperatures < 900 °C and the μ phase between 800 °C and 980 °C. (Hong et al.,

2008) performed low cycle fatigue tests of Hastelloy X in the temperature range of 650 °C - 870 °C under various strain rates. They found that the Coffin-Manson (C-M) plot was different from those at other temperatures and also the fatigue life significantly decreased at the total strain range less than 0.6 %. Recently, (Abotula et al., 2011) studied the dynamic constitutive behavior of Hastelloy X at different temperatures ranging from 25 °C to 1100 °C and observed that the yield stress under dynamic loading decreases up to 700 °C, after which it shows a peak at 900 °C before beginning to decrease again as the temperature is further increased. They also observed that the amount of strain hardening and flow stress of Hastelloy X decreases with increase in temperature.

Also, there is a large volume of literature available on the response of monolithic plates and beams subjected to shock loading. (Menkes and Opat, 1973) characterized the response of aluminum beams under shock loading. They identified three major damage modes, which respectively are inelastic deformation, tensile tearing and transverse shear. Later, (Teeling-Smith and Nurick, 1991), (Nurick et al., 1995) and (Nurick and Shave, 1996) observed similar failure modes for circular, stiffened square and square plates, respectively. (Wierzbicki and Nurick, 1996) investigated thin clamped plates for different loading radii and applied impulse. They observed that the smaller loading radii led to a more localized damage towards the center of the plate, while the more distributed load produced tearing fracture at the clamped boundary. To date, there have been no studies reported on the damage behavior of aerospace materials under shock loading when exposed to extreme environments. Thus, the present study focuses on the dynamic response of Hastelloy X

when subjected to controlled shock loading under extreme environments. The results showed that uniform heating of the specimen was consistently achieved with the designed heating system. The high temperature flame proof paint used in the experiments withstood the temperatures and the intensive shock wave loading. For the same applied incident pressure, the highest impulse was imparted on the specimen at room temperature. However, due to the temperature dependent material properties, the specimen showed an increasing trend in back face deflection, in-plane strain and out-of-plane velocity with increasing temperature.

2. Material and Specimen Geometry

The material used in this experimental study was Hastelloy X, supplied by Haynes International. The chemical composition of the material is listed in Table 1.

%wt	C	Si	Mn	P	S	Ni	Cr	Mo	Co	W	Fe	B
Min	0.05	--	--	--	--	--	20.50	8.00	0.5	0.2	17.00	--
Max	0.15	1.00	1.00	0.040	0.030	Residual (~40%)	23.00	10.00	2.50	1.00	20.00	0.01

Table 1. Chemical composition of Hastelloy X.

The table shows that Hastelloy X has a high content of Ni, Cr, Fe and Mo. The density of the material is 8220 kg/m^3 and the melting temperature ranges between $1260 \text{ }^\circ\text{C}$ and $1355 \text{ }^\circ\text{C}$ (Haynes, 2012). The dynamic true compressive stress-strain curves of Hastelloy X for different temperatures at an average strain rate of about 5000 s^{-1} were obtained using a split Hopkinson pressure bar setup and are plotted in Fig.1. The material exhibited yield strength of 380 MPa and a Young's Modulus of 190 GPa under quasi-static loading. The flow stress (strain hardening) of the material increases as the true strain increases. Hastelloy X showed rate dependency from quasi-static

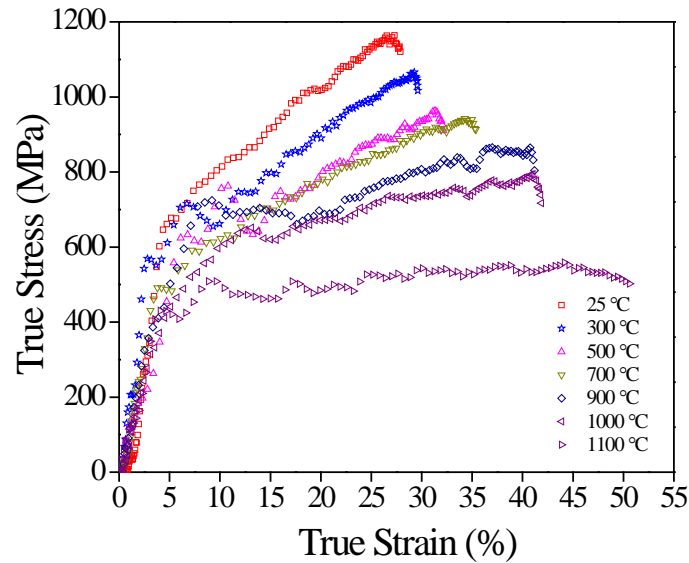


Fig. 1 True compressive stress-strain curve of Hastelloy X under dynamic loading at elevated temperatures along with the quasi-static true compressive stress-strain curve.

loading to dynamic loading. The dynamic yield strength was about 50 % higher than the quasi-static yield strength, while the dynamic flow stress was approximately 200 MPa higher than the quasi-static flow stress. At elevated temperatures, the yield strength of the material decreases as the temperature increases with an exception at 900 °C and 1000 °C. The true strain in the specimen increases and the flow stress decreases as the temperature increases (Abotula et al., 2011). This behavior is due to an increase in material ductility at elevated temperatures. The Johnson-Cook parameters were determined for Hastelloy X from the experimental data. In the present study, rectangular plates 203 mm long, 51 mm wide and 3 mm thick were used in the experiments.

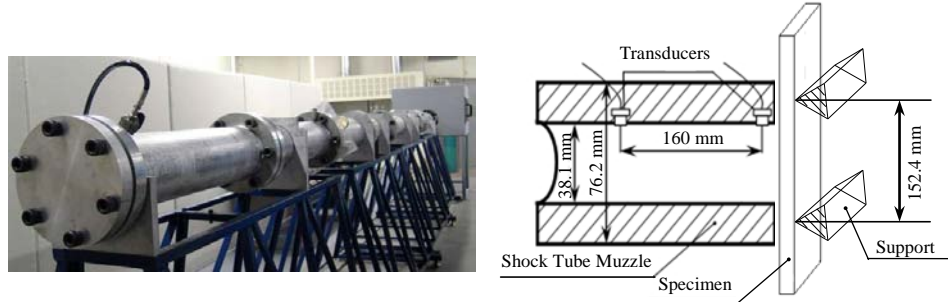
3. Experimental Procedures

For the present study, three experiments were conducted for each temperature in order to ensure repeatability as well as to better evaluate specimen performance and

behavior under shock loading. Experiments were carried out for 25 °C, 360 °C, 700 °C and 900 °C temperatures.

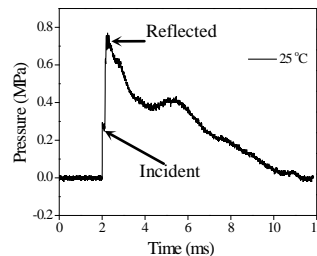
3.1 Shock Tube

The shock tube apparatus was utilized to generate controlled blast loadings as shown in Fig. 2(a) (Gardner et al., 2011; Gupta and Shukla, 2012; Tekalu et al., 2009; Wang et al., 2009). The shock tube has an overall length of 8 m, consisting of a driver, driven and muzzle section. The high-pressure driver section and the low pressure driven section are separated by a diaphragm. By pressurizing the high-pressure section, a pressure difference across the diaphragm is created. When this difference reaches a critical value, the diaphragm ruptures. This rapid release of gas creates a shock wave, which travels down the tube to impart dynamic loading on the specimen.



(a) Shock tube

(a) Detail Dimensions of the Muzzle



(c) Typical Pressure Profile

Fig. 2 Shock tube apparatus.

Fig. 2(b) shows the shock tube apparatus with a detailed image of the muzzle. The final muzzle diameter is 38.1 mm. Two pressure transducers (PCB102A) are mounted at the end of the muzzle section to measure the incident and reflected pressure profiles during the experiment. The distance between the two sensors is 160.0 mm and the distance between the second transducer and the end of the muzzle is 20.0 mm. The specimen was placed in the supports and positioned 5 mm away from the end of the muzzle. The support fixtures ensured simply supported boundary conditions with a span of 152.4 mm.

A typical pressure profile obtained from the transducer closest to the specimen at room temperature is shown in Fig. 2(c). In the present study, a simply stacked diaphragm of 2 plies of 2.5 mil mylar sheets with a total thickness of 0.5 mm was utilized to generate a shock wave loading that impinged on the specimen with an incident peak pressure of approximately 0.25 MPa, a reflected peak pressure of approximately 0.72 MPa, an incident shock wave speed of 665 ms^{-1} and a reflected shock wave speed of 235 ms^{-1} . The shock wave generated had a short rise time ($\sim 80 \text{ }\mu\text{s}$) and showed an exponential decay period of approximately $4500 \text{ }\mu\text{s}$.

3.2 High Temperature Shock Tube Setup

The shock tube set up was modified for testing Hastelloy X at high temperatures. Initial efforts of using quartz lamps as the heating source were given up due to the fragile nature of the heaters. It was determined that the quartz lamps would not be suitable to withstand the intense and violent loads developed during shock loading since the quartz lamps would have to be placed very close to the specimen in order to direct most of the heat onto the specimen. Later, it was decided to use propane

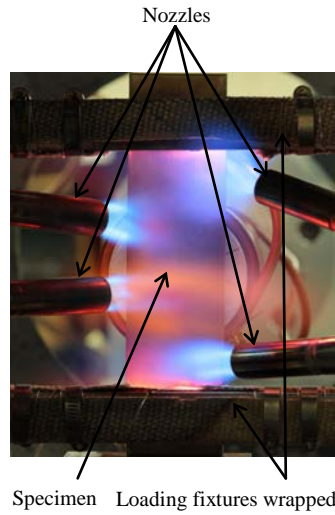


Fig. 3 Front-view of the modified shock tube set up.

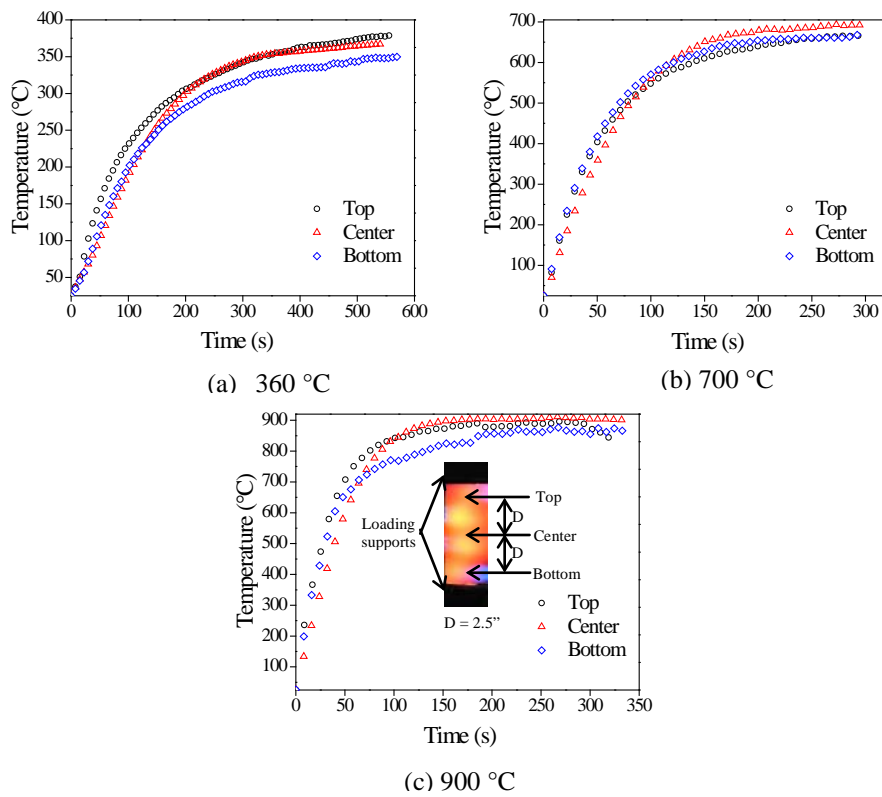


Fig. 4 Calibration curves for 360 °C, 700 °C and 900 °C temperatures.

gas as the heating source and it was directed onto the specimen via four nozzles as shown in Fig. 3. Two nozzles were located on each side of the specimen. The nozzles on the left side were directed at the center of the specimen, while the nozzles on the right side were directed towards the top and bottom of the specimen, respectively. Different temperatures were obtained by adjusting the distance between the specimen and nozzles. For each temperature, the angle and intensity of all four flames were adjusted to obtain uniform heating of the specimen between the supports. The temperature on the front face (blast side) of the specimen was monitored at three different locations (between the supports) using chromel-alumel thermocouples to ensure uniform temperature distribution on the specimen. The temperatures recorded at these locations for 360 °C, 700 °C, and 900 °C are shown in Fig. 4. It can be seen that a uniform temperature was achieved between the supports for all the temperatures with a maximum gradient of ± 15 °C. Later, temperatures were also recorded on the front face (blast side) and back face (nozzles side) of the specimen using chromel-alumel thermocouples and infrared thermometer respectively to ensure uniform temperature on both sides of the specimen. To protect the supports from the high

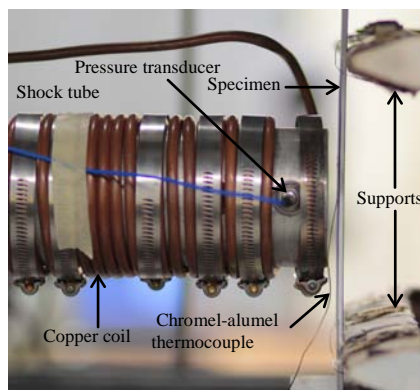


Fig. 5 Side-view of the modified shock tube set up with cooling set up.

temperatures, a high temperature flame resistant paint was applied and then wrapped with a heat shield. A cooling system was also implemented to prevent the muzzle section of the shock tube from reaching high temperatures. This was crucial in protecting the highly sensitive pressure sensors located towards the end of the muzzle. The cooling system, as shown in Fig. 5, consists of a copper coil tightly wound around the muzzle end in which tap water is circulated. In addition, a distance of 5 mm was maintained between the specimen and the muzzle to protect the shock tube from reaching high temperatures. For a distance of 5 mm away from the specimen, a maximum temperature of 70 °C was observed at the location where the closest pressure sensor was mounted. Both heating and cooling systems together permit the specimen to be heated to temperatures up to 900 °C while protecting the surrounding equipment, thus allowing for precise pressure measurements during each experiment.

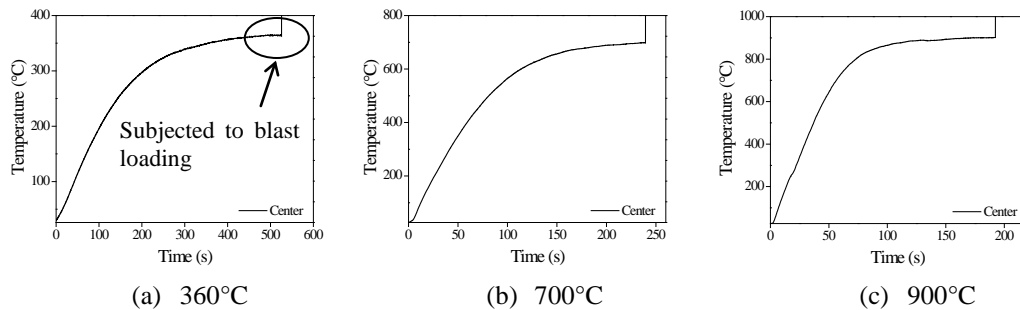


Fig. 6 Temperature vs. time plot for 360 °C, 700 °C and 900 °C experiments.

For each experiment, the temperature at the center of the specimen was monitored during the shock loading. Fig. 6 shows the temperature vs. time curves for 360 °C, 700 °C and 900 °C experiments. Fig. 6 clearly shows that the steady temperature was achieved in the specimen before the shock wave loading occurs. At

the instant the shock wave impinges on the specimen, the thermocouple disengages from the specimen and the recorded data shows a peak in the temperature-time curve.

3.3 High Speed Photography Systems

Two high-speed photography systems were utilized to capture the real-time 3D deformation data of the specimen during the blast experiment. The experimental setup, shown in Fig. 7, consisted of a back-view 3D Digital Image Correlation (DIC) system with two cameras facing the back side of the specimen to obtain the real-time full field data. Another high speed camera was placed perpendicular to the side surface

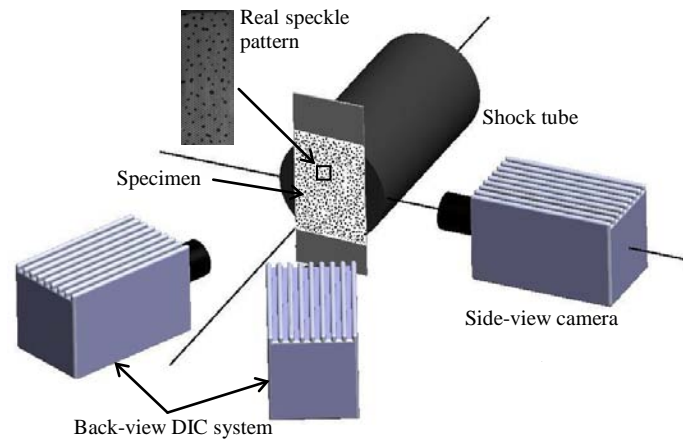


Fig. 7 High-speed photography systems.

of the specimen to capture the side-view deformation images. All cameras were Photron SA1 high-speed digital cameras and were used at a frame-rate of 30,000 fps with an image resolution of 256×512 pixels for a one second time duration. These cameras were synchronized to ensure that the images and data can be correlated and compared.

3.3.1 High Temperature DIC System under Dynamic Loading

The 3D DIC technique is one of the most recent non-contact methods for analyzing full-field shape, motion and deformation (Gardner et al., 2012; Luo et al., 1993; Sutton et al., 2009). Two cameras capture two images from different angles simultaneously. By correlating these two images, one can obtain the three dimensional shape of the surface. Correlating this deformed shape to a reference (zero-load) shape gives full-field in-plane and out-of-plane deformations. However, there were limitations in using DIC for high temperature applications. It was observed that when a material exceeds a certain temperature, the self radiation of the heated material leads to decorrelation effects in the images. This phenomenon occurs because the radiated light of the heated material will dramatically intensify the brightness while decreasing the contrast of the captured image (Pan et al., 2010). Therefore, most of the high temperature DIC applications were limited to 600 °C (Bing et al., 2009; De Strycker et al., 2010; Li et al., 2008). Recently, (Grant et al., 2009) proposed an effective countermeasure to measure the Young's modulus and coefficient of thermal expansion (CTE) of a nickel-base superalloy through the use of filters and blue illumination to obtain images up to 800 °C. The recorded images were further analyzed by using a Fourier transform cross-correlation algorithm and by frequently updating the reference image. This technique requires the specimen to be abraded by a silicon carbide paper to form a random pattern without the use of an artificial speckle pattern. However, the maximum temperature reported in their work was 800 °C. Very recently, (Pan et al., 2011) proposed a simple, easy to implement and yet high performance DIC method that could be used to obtain full-field deformation measurements of objects up to 1200

°C. They used the commonly employed iterative spatial-domain cross-correlation algorithm and optical bandpass filters. Since the optical bandpass filter only allows the light of certain wavelengths to pass, it effectively reduces the image intensity increment caused by the thermal radiation of heated objects. The authors also proposed a simple and effective speckle pattern fabrication as a carrier of deformation information.

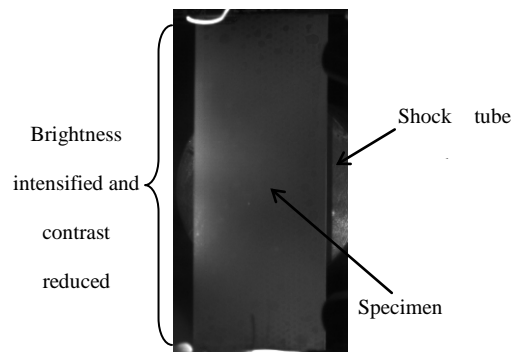


Fig. 8 Captured image of the specimen (Hastelloy X) at 900 °C using an ordinary DIC system.

When an object is heated, it emits electromagnetic waves of all wavelengths ranging from infrared to ultraviolet depending on the temperature of the object. As the temperature increases, the peak (primary) wavelength slowly shifts towards the shorter wavelength and the amount of thermal radiation increases very fast. Fig. 8 shows the captured image using an ordinary DIC technique for a temperature of 900 °C. Since the amount of radiation increases at high temperatures, the brightness of the image was significantly intensified while reducing the contrast of the image as shown in Fig. 8. This captured image can no longer be correlated with the reference image to obtain the full field deformation data. Using a bandpass optical filter of shorter wavelength eliminates the light of other wavelengths and remains insensitive to the intensity

changes induced by thermal radiation. For this purpose, an optical bandpass filter of shorter wavelength (blue color) was used in this study. The center peak wavelength of the filter is 450 nm with a full-width at half-maximum (FWHM) value of 40 ± 8 nm and transmission efficiency at peak wavelength is 45 %. Since the bandpass filter allows the light between 410-490 nm wavelengths, only very limited light will pass through the filter. As a result, even though the filter eliminates the intensity changes, the captured images will be of low intensity and contrast. To ensure sufficient contrast in the image, the object can be illuminated with halogen lamps or LED lights of wavelengths closer to the filter. Since the exposure times are very long under the static loading and no loading case, these light sources will provide sufficient contrast in the specimen. However, under dynamic loadings and short exposure times, ensuring that sufficient light passes through the filter to enhance the intensity of the image becomes very challenging. Therefore, a high energy flash lamp (Cordin, Model 659) was used as a light source which can provide controlled and relatively consistent illumination throughout the entire duration of the event. It has a maximum capacity of 1100 joules regardless of the single flash duration. The light source can be illuminated for a duration of 0.5 ms to 11 ms in 1 ms increments. In our experiments, the flash lamp was illuminated for 5 ms, which gives a power of 220 KW.

To extract accurate and reliable information using DIC, the specimen is required to have either a natural or artificial speckle pattern with random variations of gray scale intensity which serves as a carrier of deformation information. For high temperature experiments, commercially available flame proof paint (VHT) which can sustain temperatures up to 1200 °C was used to speckle the specimen. Fig. 9 shows the

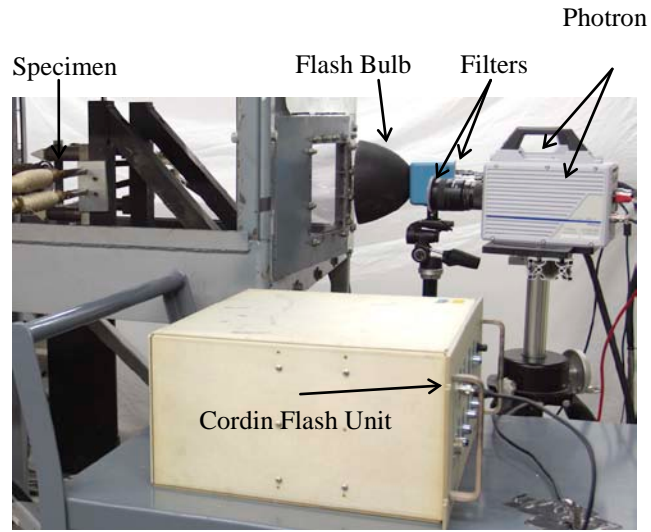


Fig. 9 Complete experimental set up with bandpass filters, high speed cameras and the high energy flash unit.

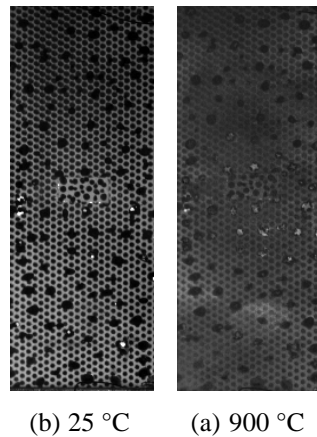


Fig. 10 Images captured at 25 °C and 900 °C using the proposed DIC system in conjunction with the optical band pass filters and high intensity light source energy flash unit.

proposed experimental set up with bandpass filters, high speed cameras and the high energy flash unit. The image recorded using this proposed set up for Hastelloy X at 900 °C without any loading is shown in Fig. 10. When the image at 900 °C (Fig. 10b) is compared to the reference image (Fig. 10a), there was no significant change in the

intensities of these images. This indicates that the bandpass filters eliminated the blackbody radiation and helped acquire high quality image. Also, Fig. 10b ensures that the flash unit provided sufficient light for the specimen. The captured images using the proposed set up can be used to generate the full field deformation data.

4. Experimental Results & Discussion

4.1 Pressure profile & Impulse

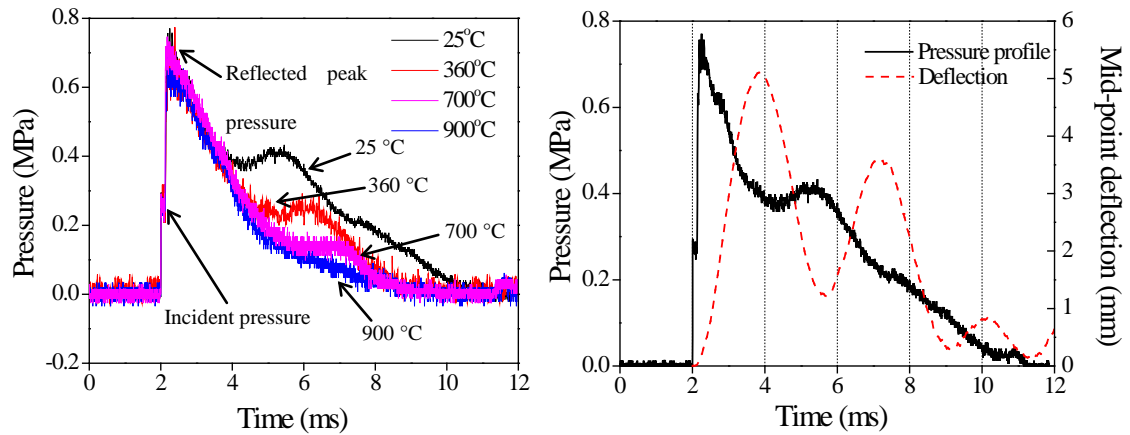


Fig. 11 (a) Pressure profiles measured for different temperatures (b) Pressure profile and deflection curve for 25 °C experiment.

The pressure profiles measured for Hastelloy X at different temperatures under shock loading are shown in Fig. 11a. Three important observations can be made from these pressure profiles. (i) The incident and reflected peak pressures are the same for different temperatures. This is consistent with the previous findings (Wang et al., 2011) which showed that the reflected peak pressure for different materials only depends on the incident peak pressure. (ii) The overall time period of the load acting on the specimen (reflected pressure) changes with temperature. The positive time

period of the reflected pressure decreased from 9 ms at 25 °C to 6.5 ms at 900 °C. Due to thermal softening at higher temperatures, higher deflections were observed in the specimens which caused the pressure to drop relatively faster than at room temperature. Thus, the rigid plate will experience reflected pressure for a longer duration and obtain more impulse from the blast loading. (iii) Humps are observed during the decay of the reflected pressure profile for different temperatures. These humps are an artifact of the specimen reverberating after reaching its peak deflection as shown in Fig. 11b. As the temperature increases, the specimen takes a longer time to reach its maximum deflection and therefore the humps for high temperature experiments are observed at later times.

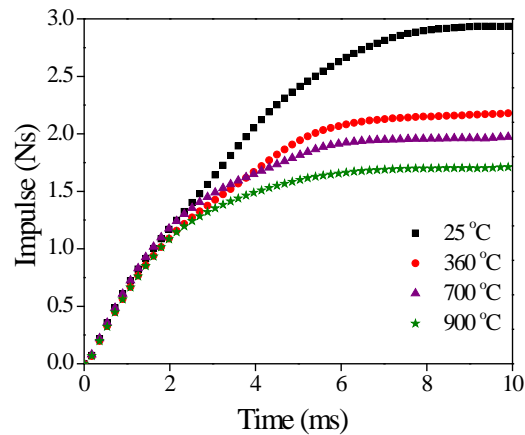


Fig. 12 Impulse imparted on the specimen for different temperatures.

Fig. 12 shows the impulse imparted on the specimen for 25 °C, 360 °C, 700 °C and 900 °C temperatures. The impulse imparted on the specimen is calculated by integrating the force-time data of the reflected pressure profile. As discussed above, at higher temperatures, the time period of the reflected pressure profile decreased which reduced the impulse imparted on the specimen. Since the overall time period of the reflected pressure profile was longer at room temperature and the reflected peak

pressure was the same for different temperatures, the specimen at room temperature obtained a maximum impulse of 2.9 Ns from the blast loading. When the temperature was increased from 25 °C to 900 °C, the maximum impulse achieved in the specimen decreased by approximately 41% (2.9 Ns to 1.7 Ns).

4.2 Real-time Deformation Images

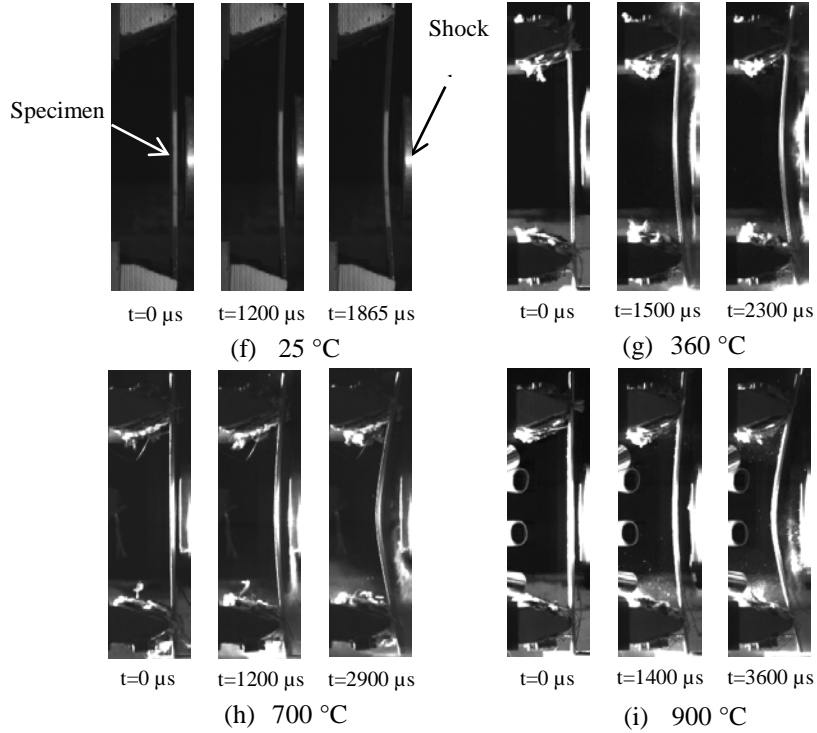


Fig. 13 Real-time side-view deformation images of the specimen for different temperatures.

The real-time observations of the transient behavior of Hastelloy X under shock loading for different temperatures are shown in Fig. 13. The shock wave is propagating from the right side of the image to the left side causing deformation in the specimens. Time $t=0 \mu\text{s}$ represents the beginning of the event where the shock wave impinged on the specimen. The side-view images were shown at different times during the event. The final image for each temperature represents the maximum deflection of

the specimen. These images were later used to calculate the mid-point deflections in the specimens. Since the distance between the nozzles and the specimen is significantly less for 900 °C, the nozzles are observed in the images.

At room temperature, when the shock wave impinges on the specimen, mode-I failure was observed with large plastic deformation at the center of the specimen and resulted in global bending of the specimen. Compressive stresses in the front face and tensile stresses in the back face of the specimen are generated during the global bending deformation under blast loading. The mid-point deflections increase monotonically with time. By $t=400 \mu\text{s}$, the specimen had deflected 0.5 mm on the back face. After $t=400 \mu\text{s}$, the specimen showed significant deflection and reached a maximum deflection of 5.2 mm at $t=1865 \mu\text{s}$.

Similar to room temperature, mode-I failure was observed for 360 °C, 700 °C and 900 °C experiments and the specimens compressed monotonically with time. As the temperature increases, the value of the flow stress for Hastelloy X decreased (as shown in Fig. 1) due to thermal softening which caused higher deflections in the specimens and deformed for a longer time. The specimens at 360 °C, 700 °C and 900 °C reached its maximum deflections at 2300 μs , 2900 μs and 3600 μs respectively.

4.3 Digital Image Correlation Analysis

The deflection, in-plane strain (ϵ_{yy}) and velocity of the back face for each temperature were obtained using the 3D Digital Image Correlation (DIC) technique. For higher temperatures, as discussed in section 3.3.1, the DIC technique was used in conjunction with an optical blue pass filter and high intensity light source. Since the thermal radiation greatly influences the image quality above 600 °C, the results

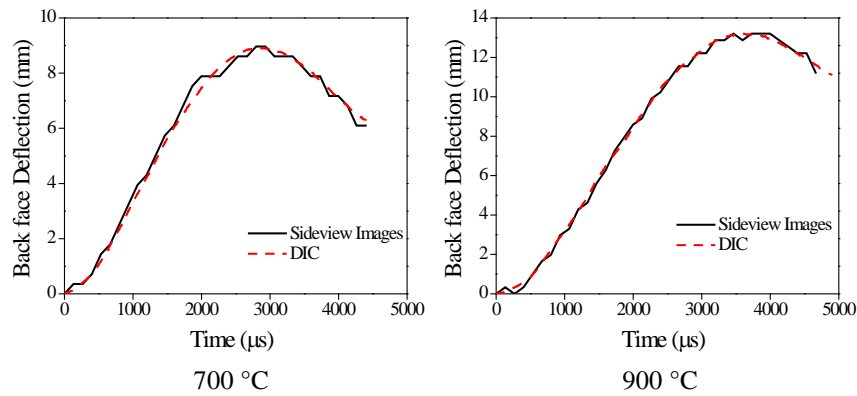


Fig. 14 Comparison of mid-point deflections obtained from the DIC technique with the side-view high speed images.

obtained using the proposed DIC method for 700 °C and 900 °C need to be validated. To verify the performance of the proposed DIC method, the back face mid-point deflections obtained using the proposed DIC technique were compared with the deflections measured from the high speed side-view images (Fig. 13). Fig. 14 shows the comparison of the deflections obtained from the DIC and the side-view images for 700 °C and 900 °C experiments. For both experiments, the deflections obtained from the DIC match very well with the deflections measured from the high speed images (maximum error at their peak deflections is less than 3%). For any time frame, the maximum difference in the deflections observed was 0.55 mm for 700 °C and 0.31 mm for 900 °C. The small variations could be attributed to the different methods used to measure the deflections. The results ensure the accuracy of the proposed DIC technique and therefore this technique can be used for the measurement of full field deformation data at elevated temperatures under dynamic loading.

The structural response of monolithic plates subjected to a blast loading is divided into two sequential stages. Stage I is the one-dimensional fluid-structure

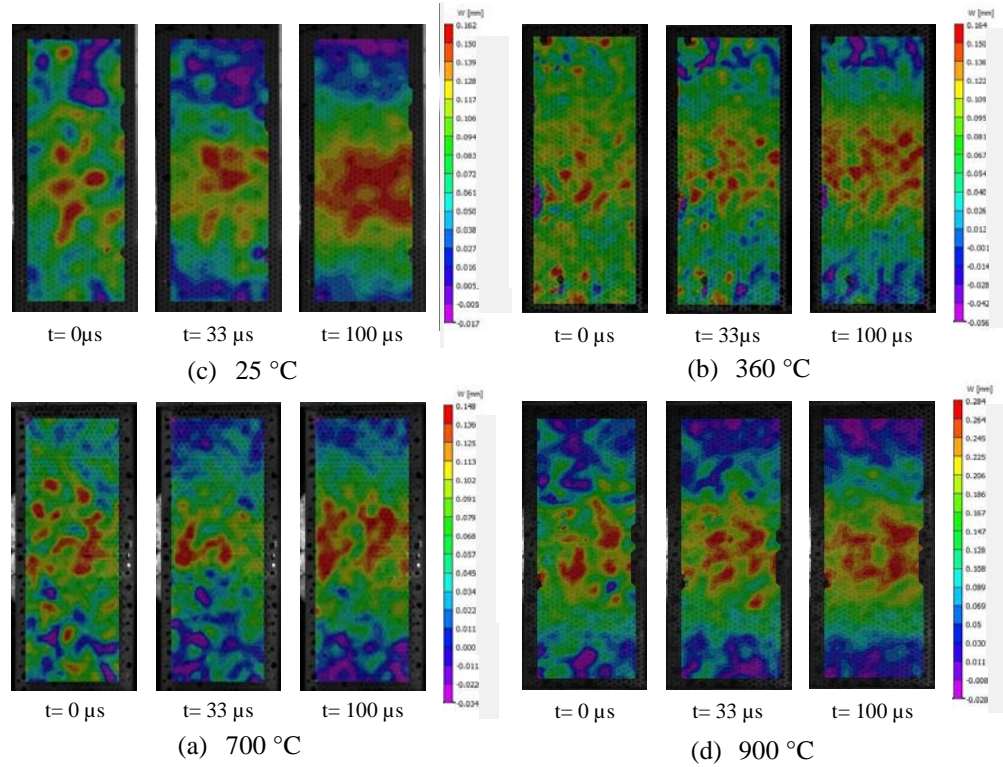


Fig. 15 Deflection of the back face during fluid structure interaction time for different temperatures.

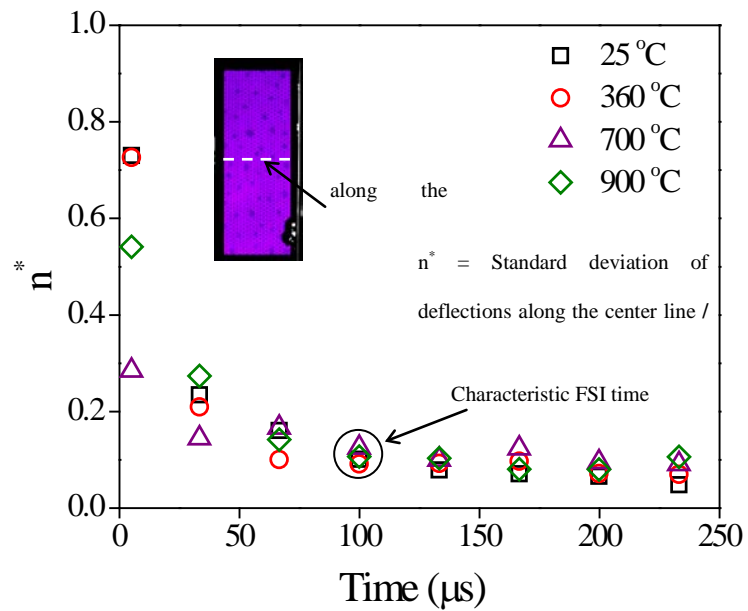


Fig. 16 Normalized standard deviation of the back face deflections along the center line as a function of time

interaction during the blast loading event, in which the front face of the plate is accelerated to a velocity by the incoming shock wave, while the back face of the plate remain stationary. Stage II is the retardation phase where the plate is brought to rest by plastic bending and stretching (Qiu et al., 2011). The deflection contours on the back face of the specimen for different temperatures during the fluid structure interaction phase between the gas and the specimen are shown in Fig. 15. The shock impinged on the specimen at $t=0 \mu\text{s}$. The localized deflection contours were observed during the early stages of the event. The transient deflection contours on the back face evolve with time. After a critical time ($\sim 100 \mu\text{s}$), the non-uniform loading disappears and a uniform loading is achieved, where the stress wave became stabilized. This time interval can be related to the characteristic fluid structure interaction time. The characteristic fluid structure interaction (FSI) time was approximately $100 \mu\text{s}$ for all temperatures. To better understand FSI, the standard deviation of the deflections was calculated along the center line of the specimen for each time frame. The standard deviation was normalized by its mean and plotted as shown in Fig. 16. This normalized standard deviation, represented as n^* in Fig. 16 estimates the non-uniformities in the loading. When the value of n^* is zero, it represents the ideal case of uniform loading. For all experiments, the value of n^* stabilized at around $100 \mu\text{s}$, which is defined as characteristic fluid structure interaction time.

The mid-point back face deflections obtained using DIC for different temperatures is shown in Fig. 17. These deflections were also in agreement with the deflections measured using the high speed images (as shown in Fig. 13). All of the curves exhibit a maximum plastic deformation in its first peak, followed by elastic

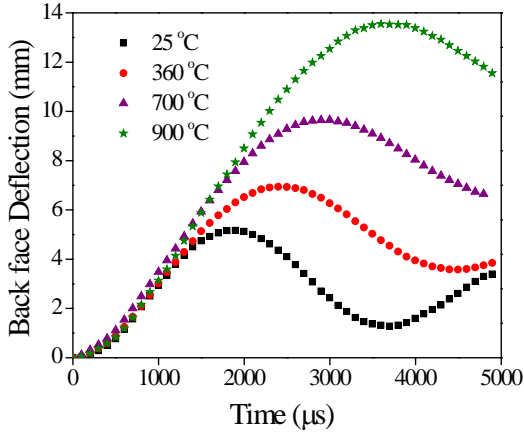


Fig. 17 Back face deflections of the specimen for different temperatures.

deformation. For all temperatures, the specimens deflect in the same manner up to approximately 4 mm at $t=1300 \mu\text{s}$. The specimen at room temperature showed a maximum deflection of 5.2 mm at $t=1865 \mu\text{s}$ and then began to reverberate. For the same incident pressure loading, the specimens at higher temperatures continued to deform for longer time due to thermal softening and lower values of flow stress. At 900 °C, the specimen deformed for almost twice the duration than the room temperature specimen. The specimens at 360 °C, 700 °C and 900 °C showed maximum back face deflections of 7.0 mm, 9.6 mm and 13.5 mm at 2300 μs , 2900 μs and 3600 μs respectively.

The average in-plane strain-rate observed in these experiments was 10 s^{-1} . Using the Johnson-Cook parameters as listed in Table 2, the stress-strain curves of Hastelloy X were obtained for 25 °C, 360 °C, 700 °C, 900 °C and 1100 °C temperatures at a strain-rate of 10 s^{-1} . From the stress-strain curves of Hastelloy X, it was determined that the flow stress at 360 °C had decreased by 3.25% when compared to room temperature and as a result, the back face deflection was increased by 35%. In comparison to room temperature, the value of flow stress at 700 °C and 900 °C had

decreased by 18.5 % and 35% respectively. Due to a significant decrease in flow stress values at these temperatures, the back face deflections at 700 °C and 900 °C had shown an increase of 85 % and 160 % respectively.

A polynomial fit was made between the percentage increase in peak deflections and the percentage decrease in flow stress values for different temperatures to predict the deflection of Hastelloy X at 1100 °C (~90% of melting temperature). For a temperature of 1100 °C, the value of flow stress had decreased by 60% and this would result in a back face deflection of approximately 21.0 mm.

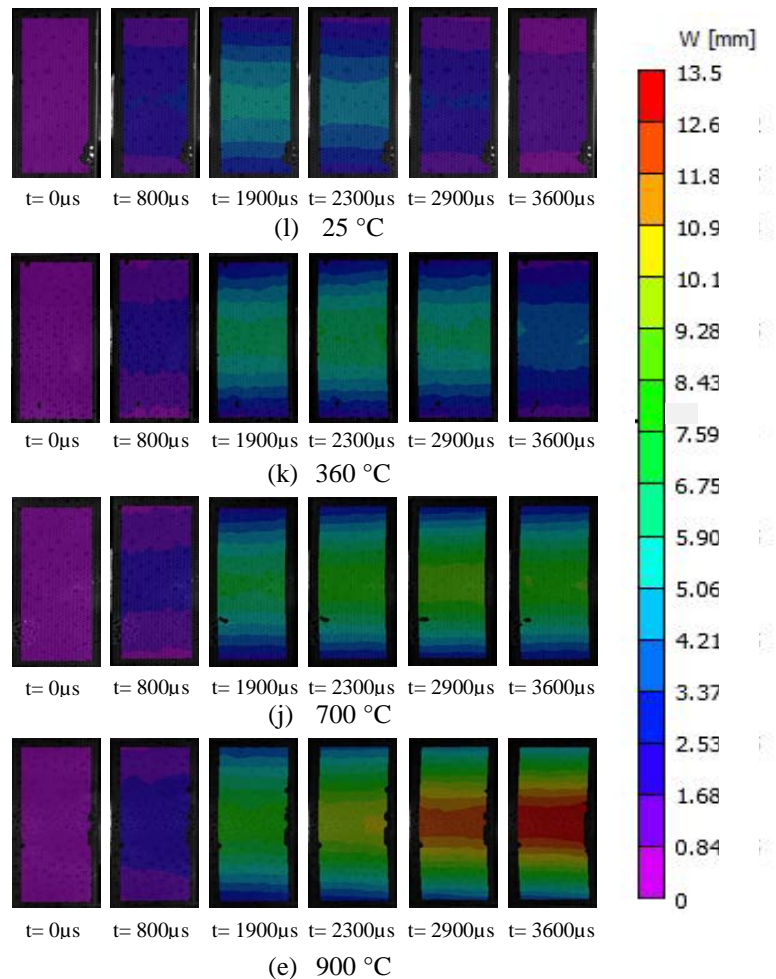


Fig. 18 Full-field out-of-plane deflection images for 25 °C, 360 °C, 700 °C and 900 °C experiments.

The full field out-of-plane deflection (W) images for different temperatures, with a scale of 0 mm to 13.5 mm, are shown in Fig. 18. For a better comparison, the time scales were kept constant for all temperatures. These images ensure that the full-field deformation data can be obtained from the modified DIC technique under shock wave loading at high temperatures. At time $t=0 \mu\text{s}$, the shock wave impinges on the specimen. For all temperatures, local deflection contours were observed during the early time of the event and the specimens exhibited very minimal out-of-plane deflections up to $t=300 \mu\text{s}$. For the specimen at room temperature, between $t=300 \mu\text{s}$ and $t=1900 \mu\text{s}$, a significant amount of deflection was observed. At this time ($t=1900 \mu\text{s}$), the specimens at 360°C , 700°C and 900°C had shown significant deflections of 6.6 mm, 7.6 mm and 8 mm respectively. After $t=1900 \mu\text{s}$, as the specimen at room temperature began to reverberate, the specimens at higher temperatures continued to deform. The specimen at 360°C deformed further for $400 \mu\text{s}$ before reaching its maximum deflection of 7.0 mm at $2300 \mu\text{s}$. In comparison to the room temperature experiment, the specimens at 700°C and 900°C continued to deform further for $1000 \mu\text{s}$ and $1600 \mu\text{s}$ respectively before reaching their maximum deflections. The specimen at 900°C deformed for a longer time of $3600 \mu\text{s}$.

The in-plane strain (ϵ_{yy}) on the back face of the specimen is plotted in Fig. 19. It can be observed from the figure that all the specimens exhibit very minimal in-plane strain of 0.05 % up to $t=400 \mu\text{s}$. After $t=400 \mu\text{s}$, the specimens showed significant bending and resulted in higher in-plane strain values. At room temperature, a maximum in-plane strain of 0.4 % was observed at $t=1865 \mu\text{s}$. As the temperature increases, the specimens exhibited higher deflections (more bending) causing an

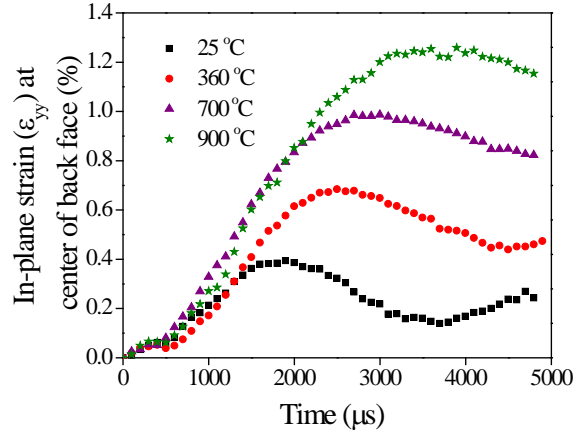


Fig. 19 Back face in-plane strains at the center of the specimen for different temperatures.

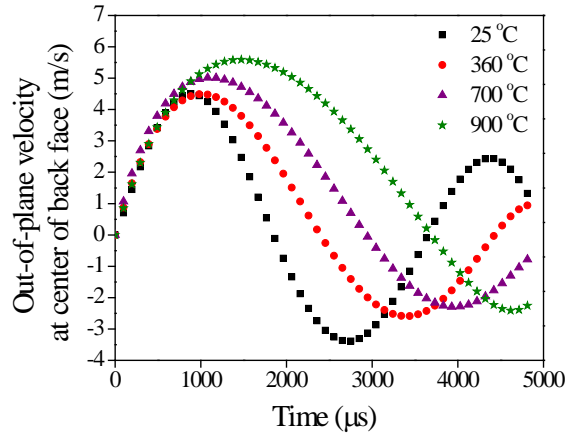


Fig. 20 Back face out-of-plane velocities at the center of the specimen for different temperatures.

increase in the in-plane strain values. For 360 °C experiment, a maximum in-plane strain of 0.7 % was observed at 2300 μs . For 700 °C and 900 °C experiments, the specimens showed maximum in-plane strain of 0.97 % and 1.25 % at 2900 μs and 3600 μs respectively. In comparison to the room temperature experiment, the specimens at 360 °C, 700 °C and 900 °C had shown an increase in ϵ_{yy} by 75 %, 142 % and 212 % respectively. Since the strains exceeded the elastic limit, the increase in

yield stress at 900 °C (as explained in section 2) had no effect on the performance of Hastelloy X under shock loading.

The out-of-plane velocity on the back face of the specimen is shown in Fig. 20. All experiments at different temperatures showed similar velocity profiles up to $t=750 \mu\text{s}$. At $t=750 \mu\text{s}$, all the specimens showed an approximate velocity of 4.25 ms^{-1} . The specimen at room temperature reached a maximum out-of-plane velocity of 4.5 ms^{-1} at $t=875 \mu\text{s}$ and began to decelerate after that. In comparison to room temperature, the specimen at 360 °C reached same maximum velocity of 4.5 ms^{-1} (at $t=975 \mu\text{s}$) but was delayed by approximately 105 μs . A maximum out-of-plane velocity of 5.0 ms^{-1} and 5.6 ms^{-1} was observed at $t=1100 \mu\text{s}$ and $1400 \mu\text{s}$ for the specimens at 700 °C and 900 °C respectively. As observed at room temperature, the specimen at higher temperatures also begins to decelerate at a later time.

4.4 Deformation Energy Evaluation

After the incident shock wave impinges upon the specimen, a reflected shock wave is generated and the reflected pressure is applied on the panel to deform the specimen. The total work done by the gas to deform the specimen is defined as the deformation energy. The deformation energy is calculated by evaluating the deflection-time data from the high speed images (Fig. 13) and the force-time data from the reflected pressure profile. Since the force was applied on the front face of the specimen, the deflection of the front face of the specimen was determined. By using curve fitting method, such as cubic spline curve fitting, the shape of the deformed front face was matched and the deflection of every point inside the shock loading area was calculated along the front face. Combining the deflection-time data and the force-

time data will result in force-deflection data. Now the deformation energy can be obtained by integrating the force-deflection data (Wang and Shukla, 2010).

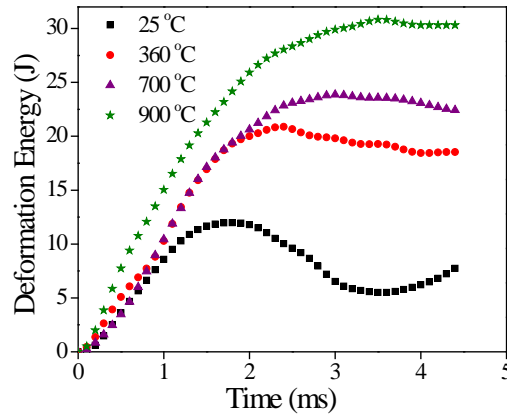


Fig. 21 Deformation energy of the specimens for different temperatures.

The deformation energy for 25 °C, 360 °C, 700 °C and 900 °C experiments is plotted in Fig. 21. The maximum deformation energy of 31 joules was observed for 900 °C. The experiments at 25 °C, 360 °C and 700 °C showed maximum deformation energy of 12 joules, 21 joules and 24 joules respectively. The deformation energy for the specimen at 900 °C was approximately 160 % higher than that at room temperature. This indicates that the specimens at higher temperatures consume more energy during the shock loading process.

4.5 Post-mortem Analysis

The post-mortem images of the specimens tested at 25 °C, 360 °C, 700 °C and 900 °C are shown in Fig. 20. Post-mortem images show that the high temperature flame proof paint used to speckle the specimens withstood these temperatures under dynamic loading. The specimens at 25 °C, 360 °C, 700 °C and 900 °C had recovered their deflection by approximately 70 %, 50 %, 20 % and 18% respectively.



Fig. 22 Post-mortem images of the specimens tested at 25 °C, 360 °C, 700 °C and 900 °C under blast loading.

5. Conclusions

A series of experiments were conducted to investigate the dynamic behavior of Hastelloy X at room and elevated temperatures under shock wave loading. A 3D DIC technique was used in conjunction with an optical blue pass filter and high intensity light source to record the transient behavior of Hastelloy X at elevated temperatures. Following are the major conclusions of this study:

- A unique experimental set up was built for studying materials at high temperatures (up to 900 °C) under shock loading.
- The DIC system has been modified and validated for obtaining the full-field data at elevated temperatures under dynamic loading. The mid-point deflections obtained from the DIC technique for 700 °C and 900 °C match very well with the deflections obtained using the high speed side-view images.
- The characteristic fluid structure time is determined to be $\sim 100 \mu\text{s}$ for all the temperatures studied.
- The impulse imparted on the specimen decreased as the temperature increased from 25 °C to 900 °C.

- The maximum back face deflection of the specimen at 900 °C is approximately 160 % higher than the specimen at room temperature.
- The maximum in-plane strain showed an increase of 212 % as the temperature increased from room temperature (0.4 %) to 900 °C (1.25 %).

Acknowledgements

The first three authors kindly acknowledge the financial support provided by the Air Force Office of Scientific Research under Grant No. FA9550-09-1-0639.

References

- Abotula, S., Shukla, A., Chona, R., 2011. Dynamic constitutive behavior of Hastelloy X under thermo-mechanical loads. *Journal of Materials Science* 46, 4971-4979.
- Aghaie-Khafri, M., Golarzi, N., 2008. Forming behavior and workability of Hastelloy X superalloy during hot deformation. *Materials Science and Engineering: A* 486, 641-647.
- Bing, P., Dafang, W., Zhaoyang, W., 2012. Internal displacement and strain measurement using digital volume correlation: a least-squares framework. *Measurement Science and Technology* 23, 045002.
- Bing, P., Hui-min, X., Tao, H., Asundi, A., 2009. Measurement of coefficient of thermal expansion of films using digital image correlation method. *Polymer Testing* 28, 75-83.
- De Strycker, M., Schueremans, L., Van Paepegem, W., Debruyne, D., 2010. Measuring the thermal expansion coefficient of tubular steel specimens with digital image correlation techniques. *Optics and Lasers in Engineering* 48, 978-986.

Gardner, N., Wang, E., Kumar, P., Shukla, A., 2012. Blast Mitigation in a Sandwich Composite Using Graded Core and Polyurea Interlayer. *Experimental Mechanics* 52, 119-133.

Grant, B.M.B., Stone, H.J., Withers, P.J., Preuss, M., 2009. High-temperature strain field measurement using digital image correlation. *The Journal of Strain Analysis for Engineering Design* 44, 263-271.

Gupta, S., Shukla, A., 2012. Blast Performance of Marine Foam Core Sandwich Composites at Extreme Temperatures. *Experimental Mechanics* 52, 1521-1534.

Haynes, I., 2012. <http://www.haynesintl.com/pdf/h3009.pdf>

Hong, H.U., Kim, I.S., Choi, B.G., Jeong, H.W., Jo, C.Y., 2008. Effects of temperature and strain range on fatigue cracking behavior in Hastelloy X. *Materials Letters* 62, 4351-4353.

Kondo, Y., Fukaya, K., Kunitomi, K., Miyamoto, Y., 1988. Tensile and impact properties changes of HASTELLOY X after exposure in high-temperature helium environment. *Metallurgical and Materials Transactions A* 19, 1269-1275.

Lai, G., 1978. An investigation of the thermal stability of a commercial Ni-Cr-Fe-Mo alloy (hastelloy alloy X). *Metallurgical and Materials Transactions A* 9, 827-833.

Li, N., Sutton, M., Li, X., Schreier, H., 2008. Full-field Thermal Deformation Measurements in a Scanning Electron Microscope by 2D Digital Image Correlation. *Experimental Mechanics* 48, 635-646.

Luo, P.F., Chao, Y.J., Sutton, M.A., Peters, W.H., III, 1993. Accurate measurement of three-dimensional deformations in deformable and rigid bodies using computer vision. *Experimental Mechanics* 33, 123-132.

- Lyons, J., Liu, J., Sutton, M., 1996. High-temperature deformation measurements using digital-image correlation. *Experimental Mechanics* 36, 64-70.
- Menkes, S., Opat, H., 1973. Broken beams. *Experimental Mechanics* 13, 480-486.
- Nurick, G.N., Olson, M.D., Fagnan, J.R., Levin, A., 1995. Deformation and tearing of blast-loaded stiffened square plates. *International Journal of Impact Engineering* 16, 273-291.
- Nurick, G.N., Shave, G.C., 1996. The deformation and tearing of thin square plates subjected to impulsive loads-An experimental study. *International Journal of Impact Engineering* 18, 99-116.
- Pan, B., Wu, D., Wang, Z., Xia, Y., 2011. High-temperature digital image correlation method for full-field deformation measurement at 1200 °C. *Measurement Science and Technology* 22, 11.
- Pan, B., Wu, D., Xia, Y., 2010. High-temperature deformation field measurement by combining transient aerodynamic heating simulation system and reliability-guided digital image correlation. *Optics and Lasers in Engineering* 48, 841-848.
- Qiu, X., Deshpande, V.S., Fleck, N.A., 2011. Dynamic Response of a Clamped Circular Sandwich Plate Subject to Shock Loading. *Journal of Applied Mechanics* 71, 637-645.
- Sutton, M.A., Orteu, J.-J., Schreier, H., 2009. *Image correlation for shape, motion and deformation measurements*. Springer.
- Teeling-Smith, R.G., Nurick, G.N., 1991. The deformation and tearing of thin circular plates subjected to impulsive loads. *International Journal of Impact Engineering* 11, 77-91.

- Tekalur, S.A., Bogdanovich, A.E., Shukla, A., 2009. Shock loading response of sandwich panels with 3-D woven E-glass composite skins and stitched foam core. *Compos Sci Tech* 69, 736-753.
- Wang, E., Gardner, N., Shukla, A., 2009. The blast resistance of sandwich composites with stepwise graded cores. *International Journal of Solids and Structures* 46, 3492-3502.
- Wang, E., Shukla, A., 2010. Analytical and experimental evaluation of energies during shock wave loading. *International Journal of Impact Engineering* 37, 1188-1196.
- Wang, E., Wright, J., Shukla, A., 2011. Analytical and experimental study on the fluid structure interaction during air blast loading. *Journal of Applied Physics* 110, 114901-114901-114912.
- Wierzbicki, T., Nurick, G.N., 1996. Large deformation of thin plates under localised impulsive loading. *International Journal of Impact Engineering* 18, 899-918.
- Zhao, J.C., Larsen, M., Ravikumar, V., 2000. Phase precipitation and time-temperature-transformation diagram of Hastelloy X. *Materials Science and Engineering: A* 293, 112-119.

CHAPTER 7

CONCLUSIONS AND FUTURE WORKS

1. Conclusions

The main objective of this investigation is to advance the development of aerospace materials that eliminate high-maintenance, parasitic, external thermal protection systems and integrate the thermal-load carrying function within the structure. The properties of different high temperature materials that are of interest to the Air Force for integrated hot/light-weight thermal structures have been exploited for this purpose. A unique high temperature/extreme environment experimental test set up also has been developed and validated. 3D- Digital Image Correlation (3D DIC) technique coupled with high speed imaging, band pass optical filters and high energy flash unit was used to obtain the back face out-of-plane deflections and velocities, as well as the in-plane strains during the high temperature experiments. The necessary fundamental understanding of failure mechanisms and failure modes of the high temperature capable aerospace materials have been evaluated, to predict their performance and structural integrity under a combination of extreme mechanical and thermal environments. Materials that are investigated include Hastelloy X, max phase material (Ti_2AlC), and functionally graded materials. The evolution of damage in these materials under shock conditions when simultaneously subjected to high pressures and high temperatures have been studied. Using the experimental data, dynamic failure criteria for these materials was established. The specific deliverables of the project can be summarized as follows:

- (1) The thermo-mechanical stress fields around the crack-tip are significantly affected by the curvature, temperature and non-homogeneity parameters. As the curvature at the crack-tip increases, the peak value of the stress components also increases.
- (2) Crack-tip velocity plays a significant role in the crack extension angle. For a mixed-mode curving crack under thermo-mechanical loading, the crack extension angle increases with the increase in crack-tip velocity. Similar behavior was reported earlier for the case of homogeneous and FGMs without the curvature parameters.
- (3) There is a significant effect on the crack extension angle when the T-stress is applied. The crack extension angle decreases when the T-stress (σ_{ox} term) is applied when compared to the case of without the T-stress (where $\sigma_{ox} = 0$).
- (4) The thermo-mechanical stress fields are not significantly affected by transient parameters. As the crack-tip acceleration increases, the size of stress contours ahead of the crack-tip decreases slightly. There is not much significant effect on the rate of change of stress intensity factor.
- (5) The transient thermal loading term influences the higher-order terms in asymptotic crack-tip fields: the displacement in the order of $O(r^{7/2})$ and the stress in $O(r^{5/2})$.
- (6) Ti_2AlC exhibited graceful failure under dynamic loading. The amount of kinking decreases as the strain rate or temperature increases. The energy absorbed by the material decreases marginally as the strain-rate increases. The material did not show any rate sensitivity below brittle to plastic transition

(BTP) temperature even for strain rates as high as 3500/s. however, after BTP temperature, the maximum stress dropped significantly.

- (7) Hastelloy X showed rate dependency from quasi-static to dynamic loading. The yield stress of the material increased by 50% and the flow stress by 200 MPa as the strain rate increases from 10^{-3} /s to 4000/s. As the temperature increases, the flow stress of the material decreases but the yield stress decreases initially up to 700°C, then increases and shows a peak at 900°C and then again monotonically decreases as the temperature is further increased. The Johnson-Cook parameters were determined for Hastelloy X and they could be used to model the behavior of the material under different dynamic loading conditions.
- (8) A unique experimental set up has been developed and validated for testing materials under shock wave loading. DIC system has been modified for obtaining full-field deformation data under dynamic loading at extreme temperatures. The modified shock wave and DIC systems together can be used to study the response of different materials under extreme environments.
- (9) Under shock wave loading, Hastelloy X showed 150 % increase in the back face deflection as the temperature increased from 25°C to 900°C.
- (10) The methods used to evaluate the energy as described by Wang *et al.* (2010) were implemented and the results analyzed. The energy needed to deform the specimen increased from 10J to 30J as the temperature increased from 25°C to 900°C.

2. Future Work

The current research is a step forward in understanding the dynamic response of aerospace materials under extreme environments. It elucidates a more comprehensive understanding on the dynamic behavior and mechanisms of failure of materials subjected to high-intensity loadings. Different materials, ranging from functionally graded materials, Hastelloy X and Ti_2AlC were studied. The proposed future projects are as follows,

- (1) The thermo-mechanical stress fields were developed for mixed mode curving cracks under steady-state and transient loading conditions. These equations were developed for elastic deformations at the crack-tip. There is a need to determine the thermo-mechanical stress fields by accounting the plastic deformation at crack-tip. This study can be started for a simple case by assuming bilinear model for the plastic deformation of the material. The stress fields for elastic, plastic and thermal loadings can be determined individually and later these fields can be super imposed to obtain elasto-plastic thermo-mechanical stress fields.
- (2) Later, the stress fields can be determined for curving cracks under transient loading.
- (3) The response of Ti_2AlC (a max phase material) was investigated under dynamic compressive loading for different strain rates and temperatures. More work is needed to fully understand the deformation mechanisms of this material under dynamic loading conditions. Experiments have to be carried out to study its response under dynamic tensile loading conditions. Also the

dynamic fracture toughness of this material is needed to determine under thermo-mechanical loadings for deeper understanding of the mechanical properties in these novel class of materials, enabling further developments in power generation, hypersonic and orbital re-entry flights, ballistic protection, etc

- (4) The dynamic response of Hastelloy X has been investigated when subjected to shock wave loading under extreme environments for simply supported boundary condition. To establish the necessary fundamental understanding of failure mechanisms and failure modes of the material, experiments have to be carried out for different boundary conditions (clamped-free and clamped-clamped).
- (5) Since aerospace structural materials can experience shock loading from oblique angles, it is imperative to understand the performance of these materials when subjected to different shock impingement angles. By varying the shock impingement angle, the behavior of these specimens under moderate to high shock loadings has to be studied. Experiments should be carried out at high shock loadings and at extreme temperatures for different boundary conditions. High temperature DIC system can be utilized to obtain the real-time stress, strain and displacement fields.
- (6) Different high temperature capable aerospace materials are needed to be evaluated to predict their performance and structural integrity under a combination of extreme mechanical and thermal environments. Some of the materials that can be examined include currently available MAX phases,

layered materials, etc. Of particular interest to Air Force will be the evolution of damage in these materials under shock conditions when simultaneously subjected to high pressures and high temperatures.

APPENDICES

APPENDIX A: STANDARD OPERATING PROCEDURES (SOP)

SHPB

Specimen preparation:

1. The specimen dimensions should follow the below relation:

$$\frac{L}{D} = \sqrt{\frac{3\nu}{4}}$$

where L is the length, D is the diameter and ν is the Poisson's ratio of the specimen.

2. Make sure the faces of the specimen are parallel and flat (use step collet while machining metal specimens to get parallel faces). The diameter of the specimen after the test should be smaller than the diameter of the pressure bars.

Selecting the bar:

1. Determine the impedance ($\rho c A$) of the specimen.

where ρ is the density, c ($c = \sqrt{\frac{E}{\rho}}$) is the wave speed and A is the area.

2. Then select the pressure bars (steel or Aluminum) closer to the impedance of the specimen. We also have different diameters for the pressure bars.

Note: The basic thumb rule is that we use steel bars for the harder materials (metals etc..) and Aluminum bars for the softer materials (polymers, foams etc..).

3. After the pressure bars are selected, make sure the end faces of the bars are flat and parallel.
4. Align the pressure bars and striker on the mounting frame.

Experimental procedure:

- (a) Give all required connections. Connections include: Connect the BNC cables from the amplifier to the oscilloscope. Check the right channels and connect them. Make sure the amplifier (2310A) and oscilloscope are grounded. Do not change any settings on the amplifier. The amplifier has

been calibrated for 350 ohms strain gages. Please refer to manual if you wish to make any changes and let everyone in the lab know before you make any changes. Turn ON the amplifier and oscilloscope.

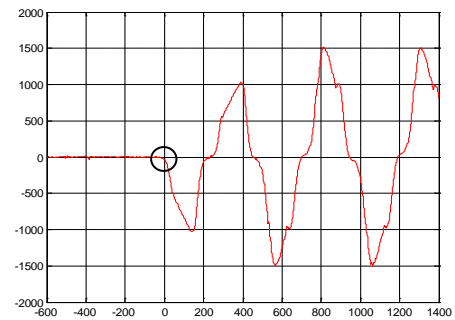
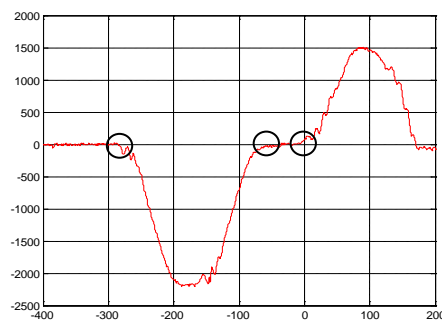
- (a) The excitation voltage and gain are set to 10V and 100 respectively. Turn the reset switch ON for all the four channels.
- (b) Check the resistance on the strain gauges and they should read around 350 ohms.
- (c) Set the voltage levels, trigger position, data duration time (2ms-4ms), for all the four channels in Oscilloscope. These values depend on the experiments.
- (d) Balance the Wheatstone bridge for all the four channels by turning the reset button.
- (e) Check whether the bars are well aligned or not, and also the projectile should be well aligned to the impact end of the incident bar.
- (f) Then make sure that the bars are moving freely, if not apply WD-40 lubricant and adjust the screws of the clamps.
- (g) Clean the interfaces of the bar and the projectile with Kim wipes and ethyl alcohol.
- (h) Push the projectile to the end of the barrel of gas gun assembly with a flexible poly rod.
- (i) Measure the dimensions of both specimen and pulse shaper. Dimensions include: diameter and thickness.
- (j) Select the striker depending on the strain rate you are trying to get. You can vary strain rate by using different pressures and different striker bars. Make sure the pulses are not getting overlapped. If the pulses are getting overlapped, use the shorter striker bar. (Thumb rule: The longer the striker, the lower the strain rate. The higher the pressure, the higher the strain rate).
- (k) Lubricate both faces of the test specimen with Molybdenum disulfide lubricant and sandwich the specimen between the bars and align the specimen with respect to bar center.

- (l) Place the pulse shaper at the impact end of the incident bar with a thin layer of KY jelly grease (if you are using lead pulse shaper) and align it with respect to bar center. We generally use clay and lead pulse shapers. These give us very good results for harder materials, but for the softer materials, you can try different pulse shapers. These include paper, copper etc.
- (m) Release the nitrogen gas from the gas tank into the gas gun chamber until the required pressure level is achieved.
- (n) Arm the oscilloscope to capture the strain gage voltage signals and make sure the arm holds until you release the projectile. If the arm is not holding, adjust trigger levels. (Note: if you are getting high noise in your signals more than 20mv, turn off the tube lights before the experiment).
- (o) Once again, ensure that the specimen is well aligned between the bars and verify the status of the trigger hold before pressing the solenoid valve release button.
- (p) Press solenoid valve control box button to release the projectile.
- (q) Save captured voltage pulses onto a USB drive for further analysis of the data.
- (r) A MATLAB program is written to read the data from the pulses and analyze the pulses using the one-dimensional wave theory stress and strain equations. After the experiments are performed, the pulses are used along with the MATLAB program to determine the equilibrium and true stress-strain plots of the specimen.
- (s) After the experiment is completed, turn off the cylinder and make sure all the left over nitrogen gas in the gas chamber is released.
- (t) After the data is transferred from the oscilloscope to USB drive, verify that in your computer and turn off the amplifier and oscilloscope.

Analyzing the results:

1. There are two MATLAB codes to analyze the data. 1. Verify_Equilibrium and
2. Steel/aluminum_SHPB. Use the appropriate codes to analyze the data. Depending on the bars you used, the respective code has to be used.

2. Make sure the code has the right properties and dimensions of the pressure bars you used. These include diameter, wave speed, and diameter.
3. If we use hollow tubes, make sure you have the right dimensions in the code. For solid bars, dimensions for the hollow tube should be zero.
4. First run the verify equilibrium code. Make sure the data you get from the oscilloscope has the following names for the four channels. TEK00000, TEK00001, TEK00002, and TEK00003. The code recognizes these names. Make sure the codes and the data are in the same folder.
5. TEK00000 and TEK00001 represent incident and reflected pulses (channel 1 and channel 2). TEK00002 and TEK00003 represent the transmitted pulse (channel 3 and channel 4). The code averages channel 1 and channel 2. And channel 3 and channel 4.
6. The code converts the voltage output to microstrains and balances.
7. Default values for filtering are given in the code. For incident and reflected pulse, default value of 0.2 ($fn=0.2$) is used and for transmitted pulse, a value of 0.05 ($fn=0.05$) is used. Depending on the noise you get, change the values of fn . The value of ' fn ' ranges from 0.001 to 0.99. Higher value of ' fn ' means, the pulses were not filtered. Decrease the value of ' fn ' if you would like to filter more. You can use different values for incident and transmitted pulses.
8. When you run the code, you get two figures. Figure 1 gives the incident and reflected pulses. Figure 2 gives the transmitted pulse.

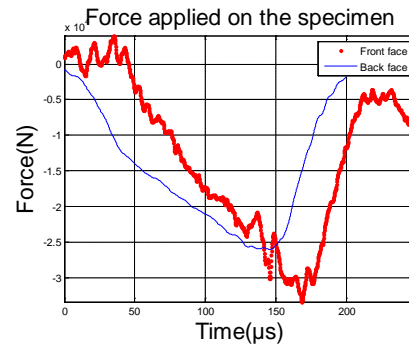


9. Note the incident starting time, incident end time, reflected starting time and transmitted starting time as shown in the above figures. You can zoom the

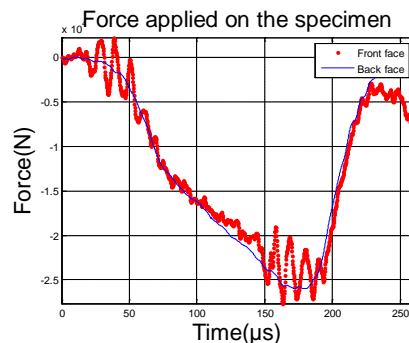
pulses by pressing 'zoom in' button at the top to get the right times. Then go to MATLAB main window and press 'ENTER'.

10. Input the values you found out and press 'ENTER'.
11. Now you will get 3 more figures. Figure 3 shows the incident, reflected and transmitted pulses. Figure 4 shows the incident, reflected and transmitted pulses you picked on before. Figure 5 shows the force ratio. Front face represents the forces calculated on the incident and reflected pulses. Back face represents the force calculated on the transmitted pulse. Ideally, these two fronts and back face should match perfectly.
12. Various factors decide the equilibrium. These include type of material tested, strain rate etc..
13. Make sure the incident and reflected pulses start at the same time on Figure 4.

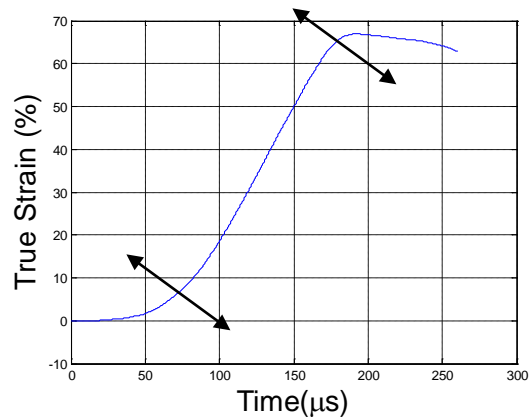
On the first trial, you might end up something as below



14. Go back to the times you found for the incident, reflected and transmitted pulses. Never change the times of reflected and transmitted pulses. Shift the incident pulse to either side and try for different values until you get decent equilibrium. For the case shown above, by shifting the time of the incident pulse, the below equilibrium was obtained.



15. Save this figure in to the respective folder. Also save the new times of the pulses.
16. Now open the SHPB code and make sure you have the same value for filter as in the verify_equilibrium code.
17. Enter the specimen thickness and diameter in inches.
18. Again, you get two figures. Figure 1 gives the incident and reflected pulses. Figure 2 gives the transmitted pulse.
19. Go to main 'MATLAB' window and enter the final times here.
20. You get Eng. stress strain curve (Figure 3) and True stress-strain curve (Figure 4).
21. Follow the directions of the Figure 4.
22. Pick two points to calculate the slope. You can pick at the initial elastic region of the true stress-strain curve.
23. You will end up with figure 5. Pick two points at the linear region as shown below.



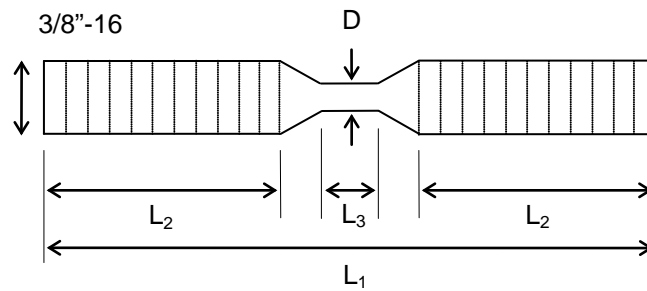
24. Go to MATLAB main window and you can see the strain rate. Note down this value. Next you will end up with final figure (Figure 6). This is eng. strain rate vs. time.
25. Be careful when you pick up the strain rate points. Consider the following points
 - a. Make sure the region you pick is in the equilibrium.

- b. For foam materials, you might not get very good equilibrium and constant strain rate. So calculate the strain rate over the entire loading duration.

Tensile SHPB:

Procedure:

1. The specimen dimensions are given below. These dimensions vary with the material tested. For metals, the below dimensions can be used. To perform experiments at lower strain rate, increase the gage diameter (D) to 0.2". For plastics, use gage length of 0.2" and gage diameter of 0.2".



D (Diameter) = 0.15"

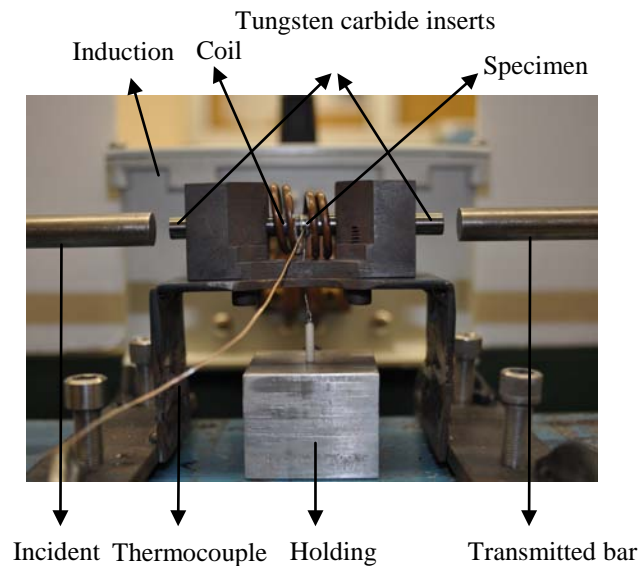
$L_1 = 1.5$ "

$L_2 = 0.56$ "

2. Selecting the bar is same as explained before.
3. Experimental procedure is also similar to the above. Here, you place the pulse shaper on the flange. You can use paper, clay or lead.
4. Different striker bars can be used to perform experiments at different strain rates. Make sure the striker bar slides freely on the bars.
5. The specimen will be threaded at both ends to the pressure bars. There is no need to use the lubricant.
6. The connections remain the same as explained before. You can use the same amplifier and oscilloscope, and same settings.
7. The MATLAB codes have been modified and use the appropriate code to perform your analysis. The steps to run the code is same as explained for compression SHPB.

Compression SHPB at elevated temperatures:

1. The tungsten carbide inserts will be used. The specimen will be sandwiched between these inserts.
2. The diameter of the specimen should be smaller than the inserts. The below figure shows the set up.



3. For experiments at elevated temperatures, the SHPB apparatus in conjunction with the induction coil heating system will be utilized as shown in Fig. 2.
4. A special fixture is used to load the specimen.
5. The inserts were used to eliminate the temperature gradient in the bars and thus protect the strain gages mounted on them.
6. The impedance of the inserts was matched with the bars; hence they do not disturb the stress wave profiles in the bar. The impedance matching requires the diameter of these tungsten carbide inserts to be smaller than the main pressure bars. This is the reason for the specimen diameter for high temperature testing being smaller than that for room temperature testing.
7. By varying the power, higher temperatures can be achieved.
8. The induction coil heating system has a power control box, remote to start and stop, a cooling unit and cooling supply (blue box) to reserve water. Make sure

the blue box has sufficient distilled water. The copper coils are connected to the cooling unit and it is placed around the inserts.

9. First turn ON the blue box, then the power supply. The power supply needs the larger output in the DPML lab.
10. Make sure the wheel on the cooling unit is spinning smoothly and fast. If not, do not do the experiment. Increase the power supply, to heat the specimen.
11. When the regulator is turned ON, it should give a click sound after around 30s. If it does not, turn it off and try again. If the problem persists, turn off the regulator and the problem can be determined.
12. Turning ON the power supply regulator, it will read 'cycle continuous' on the remote (smallest one), which is desired.
13. The system should already be set to manual power output again, which will allow to control the power. If it is not set, you can do by using the switch located to the immediate right of the dial on the regulator.
14. Make sure the dial on the regulator is zero, so there will be no immediate power output.
15. Now press 'start' button on the remote (small one that reads the display).
16. The bars were kept apart initially, later the specimen and carbide inserts were heated in isolation to the desired temperature (usually about 20-50°C higher than the test temperature) and soon after the bars were brought manually into contact with the specimen. The temperature of the specimen was monitored using a 0.127mm chromel-alumel thermocouple, which was spot welded onto the specimen.
17. In most of the experiments, it takes less than two minutes to heat the specimen to the required temperature and it takes less than 10 seconds to bring the pressure bars into contact with the tungsten inserts and fire the gun.
18. Once the temperature is reached, hit 'stop' on the display and turn off the regulator and the induction heater. Now trigger the oscilloscope. If you trigger the oscilloscope before, due to magnetic fields from the induction heater, you will see a lot of noise.

19. Allow the cooling unit to run for some time so that it reaches room temperature.
20. All other experimental procedure, data capturing, and analyzing the results remain the same as explained in compression SHPB section.

Note:

1. Always make sure the yield strength of the material you are testing is never beyond the yield strength pressure bars.
2. For testing ceramics of high strength, we need to use inserts so as to protect the bars from plastic deformation.

SHOCK TUBE

Checklist Before Experiments:

Shock Tube Related:

- Do you have enough **GAS** and **GAS PRESSURE**?
- Do you have enough **MYLAR SHEETS**?

Dump Tank Related:

- Is the support **FIXTURE** tight in the dump tank?
- Are the supports in the right **SPAN** position?
- According to your experiment, do you need the **EXTRA SPACERS** for the support?
- Is the side window, **LEXAN SHEET**, clean?
- Are the back windows, **LEXAN SHEETS**, clean?
- Are the back windows, **LEXAN SHEETS**, **1/2 in.** thick?

Visualization System Related:

- Does every **LIGHT** work fine?
- Does every **CAMERA** work fine?
- Does **LAPTOP** work fine?

Specimen Related:

- Have you measured the specimen's **SIZE**?
- Have you measured the specimen's **WEIGHT**?
- Is your **SPECKLE PATTERN** OK?
- Have you taken the **pre-blast IMAGES** of the specimen?

Checklist During Experiments:

Shock Tube Related:

- Have you changed the **MYLARS**?
- Are all the screw connections **TIGHT**?
- Have you put the **PRESSURE SENSORS** in the shock tube?
- Is the shock tube **PERPENDICULAR** to the supports, and centrally located?

Dump Tank Related:

- Is the specimen in the right position and secure?
- Is the shock tube close enough to the specimen, 1/16 in?
- Have you put the side doors on the dump tank?
- If no back side DIC system is required, have you installed a good protection for the back side LEXAN windows ?

DIC System Related:

- Have you double checked the camera **CABLE CONNECTIONS**?
- Is the back view camera system **PERPENDICULAR** to the back side window?
- Is the side view camera **PERPENDICULAR** to the side window and specimen?
- Have you set the right **FRAME RATE**?
- Have you done the **BLACK CALIBRATION (SHADING)**?
- Is the viewing area acceptable (make the view of the specimen as large as it can)?
- Have you **FOCUSED** on the specimen (use iris 2.8 or smaller)?
- Have you increased the **IRIS** to at least 5.6?
- Have you set **SYNC MODE** for all slave cameras (E-SYNC)?
- Have you done the correct **CALIBRATION (grids used to track particle distance)**?
- Have you set the right **TRIGGER MODE**?

- Have you double checked that the cameras can take the desired images?

Oscilloscope Related:

- Have you double checked the **CABLE CONNECTIONS** from the sensors to the channels are right?
- Have you double checked the **VOLTAGE AND TIME RANGE** setting?
- Have you double checked the **TRIGGER** setting (trigger level and position)?

ULTRAHIGH-SPEED AND HIGH-SPEED PHOTOGRAPHY SYSTEMS:

IMACON200A

Set camera facing desired event

1. Connect control i/o cable, which runs from camera to computer, to camera (should already be attached to computer)
2. Connect a BNC cable from the monitor output of the camera (clearly marked) to the stereo converter box used to connect trigger to photogenic flash light.
3. Connect a BNC cable to trigger 1 (clearly marked) on the camera, and utilizing a T joint, connect the trigger to the oscilloscope, with a second BnC branching to the make circuit used to trigger the apparatus.
4. When selecting which Photogenic to use, be sure that one is the flash with the bulb capable of producing persistent light – this will be identifiable as the bulb with an additional, smaller bulb, situated in the center of the flash ring of the rest of the bulb.
5. **FOR CAMERA SETTINGS, put camera into Focus mode and set the following:**
 - a. Set Iris to f2.8
 - b. Set exposure to 5 microsec
 - c. Set Gain to 5
6. To focus camera, set flash with the ability to provide a constant light source to model, so it provides light with which to focus the camera. Focus the camera as you would any other camera, by use of the lens manual focus. **NOTE:** The camera must be in focus mode in order to focus the lens.
7. Once camera, flash, and trigger are set, open the camera software on the computer system.
8. Program provides instruction on setting any additional necessary settings, which can be tailored to your experiment
9. **MAKE NOTE:**
 - a. The flash has a rise time of 100 microseconds – be sure that the preflash delay is at least that much

- b. Set MCP to 3 or 4 in computer software – the higher the #, the higher the brightness
- c. The camera delay must also be tailored to your experiment – know how long your event takes, what part of it you wish to photograph, and how long it takes before that happens. The Imacon, though indeed quite mighty, only takes 16 pictures, so you must be sure not to miss your event!

10. TAKE CARE:

- a. **When changing the lens, be sure that the shutter of the camera is closed – if it is open, and there is no lens on the camera, ambient light or any sudden flashes can/will destroy the ISOs and the prisms, rendering the camera useless.**
- b. **When testing the flash for operation, do not look directly into it, or flash it while others are doing so – the flash is EXTREMELY intense, and can cause disorientation and result in injury.**

11. FINAL NOTE: The Imacon 200 was the first of its kind, and is worth \$500,000. Treat it with respect – handle it and its components with care

TEST AND CAMERA PROCEDURE

Physical Setup – Prior to any software

1. Set up lamps
2. Keep lens caps on cameras
3. Plug in cameras
 1. Turn on master
 2. Turn on slave
 3. Wait for “sync in” light on slave camera before starting any software
 4. Make sure IP light is also on

Software Setup

1. Start software – PFV
2. Go to Cam2 window
 1. Right click
 1. CAM options
 1. I/O
 1. Set sync in to “ON CAM POS”
 1. E-Sync shows up in window
3. Set frame rate to 20,000 fps (or desired rate)
4. Shading
 1. Make sure lens cap is on
 1. Click calibrate
 2. Do this for each camera!!!
5. Now all set with software setup

Camera Setup (Focus and Calibration)

1. Take lens caps off
2. Focus and set aperture on the lens itself
 1. Set aperture to 2.8 initially for focusing the camera

2. Maximize window of interest in the software for focusing and hit fit
3. Set aperture to 5.6 for calibration
4. Repeat for each camera
3. Calibrate the Cameras
 1. Trig Mode = Random, 1 frame
 2. Hit Record button in software
 3. Move the calibration sheet and hit the trigger button repeatedly while rotating and translating the cal sheet
 4. Once sufficient images (>100) are captured hit record done
4. Data Save Tab
 1. Select the folder to save the calibration images
 1. Save CAM 1 (Cal_0_), Type = TIFF
 2. Save CAM 2 (Cal_1_), Type = TIFF
 3. Run Through the calibration process in VIC-3D

Camera Usage (Actual Test)

1. In the camera software
 1. Camera Tab
 1. Hit Display “Live”
 2. Set Trigger mode to “END”
 3. Hit record button (software) one time
 1. Light goes to orange, and will say Trig In
 4. Hit the Trigger (physical) button to begin recording
 5. Hit the Trigger button again to stop recording
 1. The software will record the images for the 1 second prior to the stop recording push. Therefore you should stop the recording as soon as possible after the event or you will miss the data.
 6. DO NOT TURN OFF THE CAMERAS UNTIL THE DATA HAS BEEN SAVED

7. Check the start point of motion with the red slider bar (the middle number is the current frame)
 1. Hit left facing arrow to set begin point to current frame
 2. Play until end of motion and hit stop
 3. Hit right arrow to set end of frames

You have now isolated the frames that comprise the event

Data Save

1. Set the folder for the data to be saved to
 1. This is different than the folder the calibration is saved to
2. Select Camera 1
 1. File names (Data_0_), Type = TIFF
 2. Save
3. Select Camera 2
 1. File names (Data_1_), Type = TIFF
 2. Save

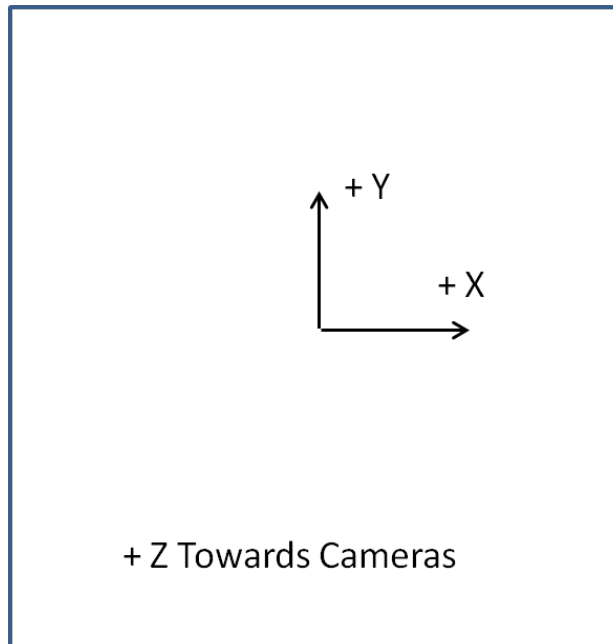
DATA CALIBRATION AND POST PROCESSING

1. Open VIC-3-D Program
2. Click Grid Icon (Cal Images)
 1. Find Calibration images from test
 2. Open all
3. Click caliper button
 1. Select Target (12x12x9 or whatever used during test)
 2. Extract
 3. Auto
 4. Calibrate
 1. Standard Deviation should be <0.1 and should have used at least 75 images
 5. Now you are done with the calibration part

4. Click the speckle images icon
 1. Select the images recorded during the test
 2. Under AOI tools tab
 1. Select the type of view area (rectangle, polygon, etc.)
 2. Select the view area
 3. Take the green box and move to a area of low deformation with a high quality speckle dot
 4. Click the “?” icon
 1. Dic_0 → camera 1
 2. Dic_1 → camera 2
 3. Verify that both cameras are seeing the dot with a checkmark next to the image by scrolling through the images with the down arrow. If there is not a chackmar next to each image then go back and select a new green box location
 4. Click close
 5. Now all ready for post processing
 5. Click the “start analysis” button
 1. Run
 2. The code will run through the images with Z Displacement initially
 3. Done
 6. Data drop down menu
 1. Post processing
 1. Calculate curvature
 2. Calculate strain
 3. Calculate velocity
 1. Input time step as the inter frame time
 4. Close
 7. Data tab under AOI Tools
 1. Can click on the individual pictures now

2. Right click to change contour levels
3. Plot tools → Autoscale
 1. Uncheck Boxes
4. Contour, set range
5. Right click to create animations
 1. Different coding methods increase or decrease the file size
6. Inspector tools
 1. Point, Line etc.
 1. 'X' icon to extract time histories

DIC Coordinate System



ENERGY ANALYSIS

This manual is designed for the steps to use the energy and impulse analysis code.

(1) Obtain the original data

The original data of shock tube experiments are from the Tektronix oscilloscope (TDS3014 or 3014C). The data must have following name:

First channel: TEK00000.csv

Second channel: TEK00001.csv

Normally, there are two columns in these files. The unit of the first column is second (s). The unit of the second column is voltage (v). Please copy these files into the folder named “experimental data backup”.

(2) Analyze the original data. This step is to analyze the original data to obtain the shock wave velocity, the peak pressure and the modified pressure profiles.

This step is carried out in the folder named “original data analysis”. In this folder, the m file named profile_analysis.m is necessary. Other files can be deleted or replaced. You must copy the original data files into this folder and then run the code. The running process is as follow,

- (1) The code will first ask you how many plys you use in the experiment. This information is only for your record. It does not matter the analysis process.
- (2) The code will ask you the sensitivity of the sensors. This value is given in the box of the sensors. This value means how many milli-voltage related to 1 psi.
- (3) Then, a figure with two plots of the pressure profiles will be given. Look at this figure carefully and determine an approximate biggest time before the first jump time of channel 1. (This time should be less than and as close as possible to the first jump time of channel 1. Normally, should not be farer from the first jump time than 200 microsecond)

- (4) Then the code will inform you as follow,
“The peak and velocity data have been saved into the file, which is named peak&velocity.txt and in the same folder of this code.
There are two more pressure data files in this folder:
inc_sp.dat
ref_sp.dat
They can be used for energy and impulse evaluation.
The code will give some plots to verify your data.
Please double check them very carefully.
press any key to continue”
- (5) After pressing any key, the code will give four images:
Figure 1 Original Data
Figure 2 Modified Pressure Profiles
Figure 3 Pressure profile of Channel 1 with key point marks
Figure 4 Pressure profile of Channel 2 with key point marks
Look at these figures very carefully, especially Figure 3 and 4. If the jump points and peak points are not right, you may need to manually pick up the jump points and peak points.
- (6) There will be three saved files in the same folder,
inc_sp.dat
ref_sp.dat
peak&velocity.txt
The first two files will be used to analyze the energy and impulse. There are two column data in these two files. The first column is time with unit second (s). The second column is pressure data with unit psi.
The last file records the physical parameters, which needs to be input in the energy and impulse analysis.
- (7) Please cut these three data files into the folder named “experimental data backup” and delete all of these files in the current folder.

(3) Analyze the incident and remaining energy and impulse

This step is to use the data obtained in step 2 to analyze the incident and remaining energy and impulse in a shock tube experiment.

This step is carried out in the folder named “gas energy and impulse analysis”. In this folder, seven m files are necessary. They are,

Main code: energy_impulse_analysis.m

Function 1: load_data.m

Function 2: skip_points.m

Function 3: density_change.m

Function 4: sound_speed.m

Function 5: velocity_change.m

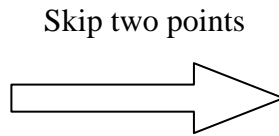
Function 6: spline_integ.m

Other files can be deleted or replaced. You must copy the data files: inc_sp.dat and ref_sp.dat, into this folder and the correlated blank test data file, inc.dat, from the folder named “blank test data”. The code running process is as follow,

- (1) The code will first show the format and unit of the data. Please be sure that the data should be the exact format.
- (2) Then the code will give the total number of the data and ask you how many points you want to skip. This means if the original data is

Original Data

1	4
2	8
3	5
4	11
5	15
6	7
7	6
8	17
9	12



New Data

1	4
4	11
7	6
10	19

- (3) Then the code will ask you to input physical parameters obtained in step 2 (saved in peak&velocity.txt).
- (4) The code will calculate the physical parameter profiles. This process is automatic.
- (5) Then the code will integrate the parameter profiles to obtain the energy components. This process is automatic.
- (6) Finally, the code will ask you to input the name of the file which you want to save data into. Then all of the data will be saved into filename_gas_energy.mat. The energy and impulse components are saved into ten files as follow,

filename_incident_internal_E.dat	incident internal energy
filename_remaining_internal_E.dat	remaining internal energy
filename_incident_translational_E.dat	incident translation energy
filename_remaining_translational_E.dat	remaining translational energy
filename_incident_work_E.dat	work done by the incident gas
filename_remaining_work_E.dat	work done by the gas behind the reflected shock wave
filename_total_incident_E.dat	total incident energy
filename_total_remaining_E.dat	total remaining energy
filename_total_energy_loss.dat	absolute difference between the total incident and remaining energies
filename_total_impulse.dat	total impulse

Please copy and save these data into a safe folder.

- (4) Analyze the deformation energy of the gas, momentum and kinetic energy of the specimen

This step is to use the data obtained in step 2 and the high-speed side-view images to analyze the deformation energy of the gas, momentum and kinetic energy of the specimen in a shock tube experiment.

This step is carried out in the folder named “specimen momentum and energy”. In this folder, only one m files, Deformation_momentum_kinetic_photron.m, are necessary. Other files can be deleted or replaced. You must copy the data files: ref_sp.dat, and a series of high-speed images into this folder. The code running process is as follow,

(1) The code will first show the format and unit of the data. Please be sure that the data should be the exact format.

(2) load the time series of the images

You will have three ways to load the time series of the images.

(i) The time between two frames is same. You can input total number of frames and time between two frames. Then the code will generate the time series automatically.

(ii) The time between two frames is not same. You can input total number of frames and input time between two frames frame by frame.

(iii)The time between two frames is not same. The time between two frames is not same. Then you can just load that time series data file.

You can choose anyone and following the instruction.

(3) Length calibration. You can choose any image for length calibration. You will need to choose two points on this image and the vertical distance between these two points will be used to calibrate the length. Therefore, you need to know one real vertical scale between two points on the image.

For example:

(i) the span of the supports is 6 inches

(ii) the outer diameter of the shock tube is 5 inches

The process will repeat three times. Thus, totally you will pick six times. Please follow the instruction.

(4) Then you can do real measurement. Normally, you need to measure the deformation shape of the front face for every image. For each image, you

need to choose seven points on the front face. The code will let you pick up the top point of the front face first. Then it will let you pick up the bottom point of the front face. After this, the code will base on these two points to draw seven lines with equivalent distance. Please pick up the points from the top to the bottom.

- (5) The code will ask you to input the mass of the specimen.
- (6) The code will ask you to input the name of the file which you want to save you data into.

APPENDIX B: MORE DETAILS OF CHAPTER 4

Experimental Results

Dynamic Constitutive Response at Room Temperature

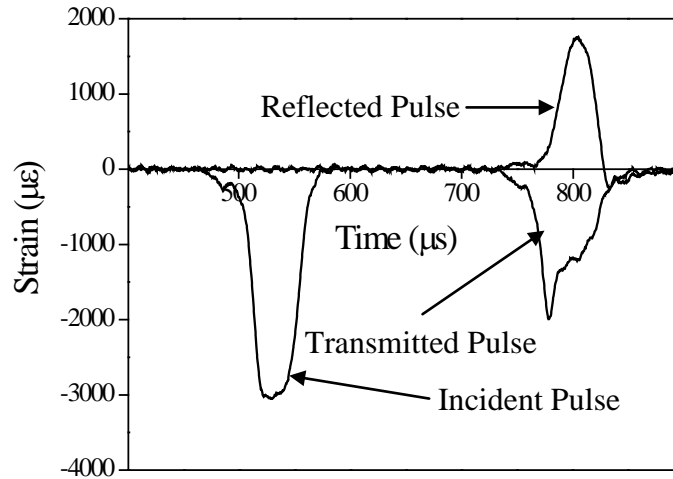


Fig. 1 Typical real-time strain pulses obtained from strain gages mounted on the bars for an average strain rate of 2800/s.

The real time strain-pulses obtained for Ti_2AlC at an average strain rate of 2500/s are shown in Fig 1. The clay pulse shaper used in all these experiments helped to reduce high frequency oscillations in the incident stress wave and improved the force equilibrium conditions at the specimen-bar interface.

The dynamic true stress-true strain curve for different strain rates ranging from 1500/s to 4500/s are plotted for Ti_2AlC at room temperature in Fig 2. Ti_2AlC shows no rate dependency under dynamic loading for a strain rate range of 1500-4500/s. The value of maximum dynamic compressive strength varies between 450MPa – 600MPa for all the four different strain rates tested. The failure initiates at true strain of 1-3%

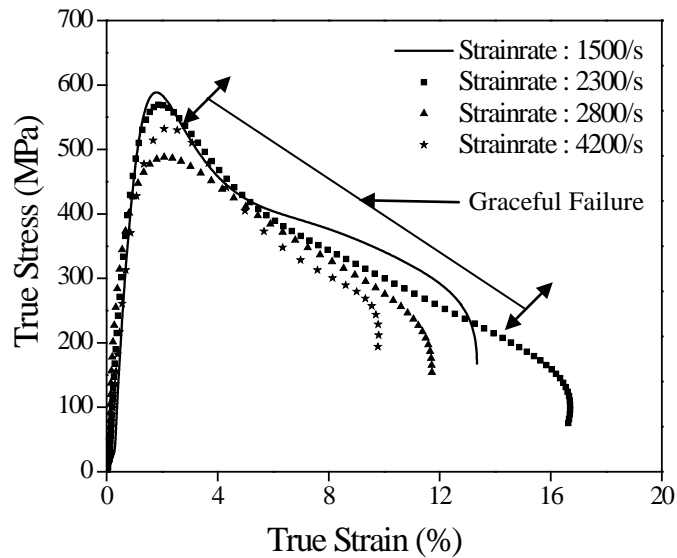


Fig. 2 True compressive stress-strain curve of Ti_2AlC under dynamic loading at room temperature.

and the maximum true strain is between 9-16%. Also the material shows more graceful failure to brittle failure. At the peak stress, the failure initiates and the material shows softening behavior. As a result of this, the value of the true stress decreases as the true strain increases.

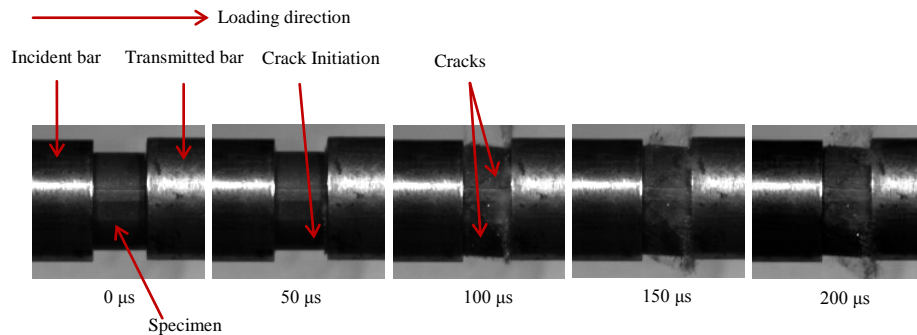


Fig 3. Real time deformations of Ti_2AlC under dynamic loading at room temperature for a strain rate of 2800/s.

Fig 3 shows the real-time deformations of Ti_2AlC under dynamic loading at room temperature for a strain rate of 2800/s. At $t=50 \mu s$, the crack initiates at the lower

right of the specimen, and starts propagating through the specimen as shown in Fig 5. By $t=100 \mu\text{s}$, more cracks are clearly visible and they have completely propagated through the specimen. After this time, the damage begins to grow and the outer edge of the specimen breaks off, while the center part of the specimen stays intact.

Dynamic Constitutive Response at Elevated Temperatures

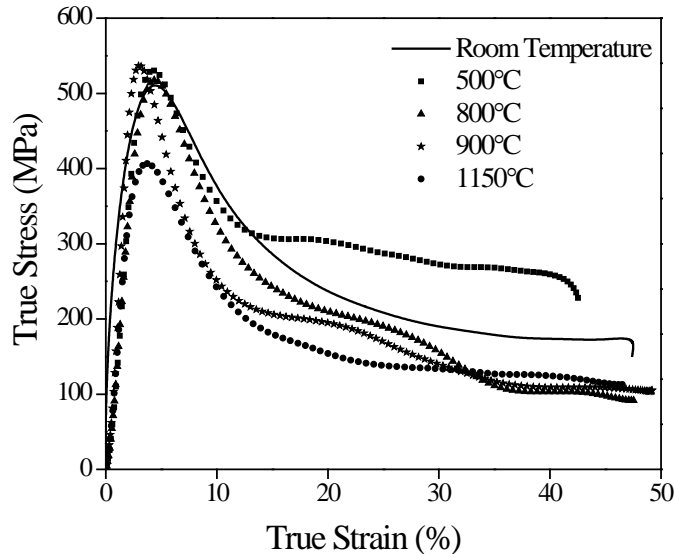


Fig. 4 True compressive stress-strain curve of Ti_2AlC under dynamic loading at elevated temperatures and a strain rate of about 3500/s.

A series of experiments were conducted to investigate the dynamic constitutive behavior of Ti_2AlC at different temperatures under identical strain rate of about 3500/s. Fig. 4 shows the dynamic true stress-strain curves for Ti_2AlC at different temperatures. All experiments were carried out with the same striker bar and at the same pressure. It can be noticed from the figure that, as the temperature increases, there is no significant change in the maximum compressive strength till up to 900°C and the value of maximum compressive stress is about 520MPa. But at 1150°C, the material shows a significant decrease in the maximum compressive strength and the

value drops to around 400MPa. Even at high temperatures, the material exhibits graceful failure. The failure initiates at a true strain of 2-6% and reaches a maximum true strain of 45-50%.

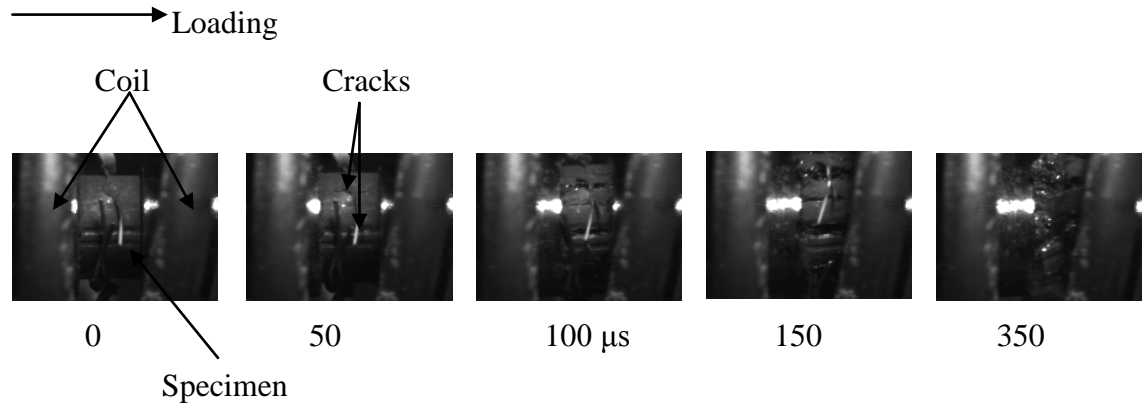


Fig. 5 Real-time deformations of Ti₂AlC under dynamic loading at 500°C.

Fig. 5 shows the real-time deformations of Ti₂AlC under dynamic loading at 500°C. Similar to room temperature experiments, the failure initiates at the peak stress and the outer edge of the specimen breaks off while the center part of the specimen remains primarily intact as shown in Fig. 5. However, the damage is more severe at high temperatures when compared to room temperature. This is directly related to the material softening at elevated temperatures.

APPENDIX C: SAFETY GUIDELINES FOR EXPERIMENTAL EQUIPMENT

SHPB

1. Never perform experiment without the help of other students
 - a. For ease of conducting a safe and efficient experiment
2. Make sure proper precautions are made prior to experiment
 - a. Wear safety glasses at all times
 - b. Long sleeve shirts and shoes should be worn, no open toe shoes or sandals
 - c. Make sure all wires and gauges are adhered correctly and prepared properly
3. Make sure proper bars are being used depending upon specific materials being tested (steel or aluminum bars)
 - a. Solid-Solid Bar (hard materials)
 - b. Solid-Hollow Bar (soft materials)
 - c. Hollow-Hollow (real soft materials)
4. **DO NOT PRESSURIZE GUN UNTIL YOU ARE ABOUT TO FIRE**
 - a. Do not put fingers between bars, i.e. striker and incident bar or incident and transmitter bar when SHPB is pressurized
 - b. Do not stand in front of muzzle or try to load striker bar when pressurized
 - c. Do not leave bar unattended after pressurized
 - d. If adjustments are needed, vent the pressure beforehand
5. Conduct yourself in a mature and responsible manner at all times in the laboratory
6. Make sure to yell “firing” when experiment is about to be run and SHPB is being pressurized, keep outside doors closed so no one walks in
7. Make sure everyone in the lab, helping or not with the experiment, is aware an experiment will be taking place

SHOCK TUBE

1. Do not stand near shock tube when it is being fired
 - a. Stand no closer than 30 feet in any direction
 - b. Stand next to person who controls Helium Tank
2. Wear ear and eye protection
3. Warn everyone around you that shock tube is to be fired
 - a. Make sure Fluids Labs and Microfluidics labs know
 - b. Make sure no classes are going on in Design Studio
 - c. Make sure Design Studio students are not there
 - i. If Design Studio is occupied, and no class is going on, ask students to leave for the test
4. Double check to make sure no one is in specimen lab
5. Check to make sure door to outside is closed and locked
6. Have the shock tube area roped off prior to test
7. Place “warning sign” in front of Microfluidics lab door and close divider off to design studio
8. Be sure to yell “firing” when releasing gas and also around the pressure where the diaphragm is expected to burst
9. Make sure bolts are completely tightened in the enclosure at end of shock tube.
10. Make sure all lexan is in place and both sliding doors are closed
11. Attach vacuum if sample that is to be blasted will cause excessive debris
12. **If for any reason someone comes within 30 feet of tube shut off gas immediately and ask person to leave**

Procedure For Running a Safe Shock Tube Experiment

1. Load up cart in DPML lab with proper equipment that is to be used
 - a. Oscilloscope, High Speed Camera, proper cables, extension cords, duct tape, research notebook, pressure sensors, mylar sheets, etc
 - b. Ask someone to help you move the cart and camera

- i. Under no circumstance is the High Speed Camera to be moved by less than 2 people.
 - ii. This includes loading and unloading the camera
2. Enter Shock Tube area through garage door and place cart in position
3. Set up Camera in proper position
4. Set up flash bulbs and/or proper lights
5. Attach cables to necessary components and to triggers
6. Once High Speed Camera and components are set up, then place sample in enclosure
 - a. Use rubber band for positioning and then tape the sample in place
 - b. Adjust camera for experiment and focus on sample
7. Set up computer software (Imacon200, or Photron SA1)
8. Trigger camera and adjust images accordingly
9. Once Camera and computer are in place, properly set up oscilloscope place pressure sensors in the shock tube
10. Make sure everything is turned on and set up properly for given test
 - a. Camera images and triggers for both oscilloscope and camera are dependent on the number of plies being used
11. Make sure mylar is in place between driver and driven section
12. Once mylar is in place and both the camera and oscilloscope are set up properly, double check sample and make sure it is in place and shock tube muzzle is touching it.
13. Check everything over one more time and make sure nothing triggered prematurely
14. Make sure tank is completely shut and **follow the safety rules**
15. If sample is known to make mess attach vacuum to enclosure tank Go to helium tank and slowly begin releasing gas into the shock tube
16. Remember to yell “firing” when loading and when burst is expected
17. Once sample has been blasted, shut off gas and proceed to checking the scope and camera for data

18. Make sure to save data to respected positions
 - a. Camera data saved under “users”
 - b. Oscilloscope data saved on floppy and then on your computer
 - i. Double check to make sure data is there
19. Remove sample from shock tube and piece back together
 - a. Once the piece pertaining to the sample have been collected and the sample put back together as well as possible, **take pictures**
 - i. Remember the longer you wait the more time the sample has to creep back and lose shape...which means losing crucial information

APPENDIX D: MATLAB Code

Code to calculate and plot thermo-mechanical stress fields for dynamic curving cracks

under steady-state and transient loading conditons

```
clear all;
close all;
clc;
%%

format long
%general constants
mue=210e9;           % shear modulus
rho=6000;           % density
nue=0.16;           % posson ratio
k=2*nue/(1-2*nue); % delta
a0=5.9e-6;          % thermal expansion
at=1e-5;
crack_length=0.01;
q0=200;             % temperature constants
q1=50;
q2=50;
q0_dot=100;

%The constants in the stress functions
K1D=5e6;             %input('Enter the value of K1:');           % mode
% mode 1 stress intensity factor
K2D=0.2*K1D;        % mode 2 stress
% mode 2 stress intensity factor
Kef=sqrt(K1D^2+K2D^2);
K1D_dot=1e8;
K2D_dot=2e7;
%Nonhomogeneous constants
gamma=0.5;
gamma1=0.2; % thermal constant
zeta=-2;           %input('Enter the value of nonhomogeneity factor:');
% mechanical constant
%("Enter gradation angle(deg):');
%beta=-(beta);     %(negative angle used in rotation)

ac = a0*((1+(gamma1*crack_length)));

%%
TD=0.005;% input('the domain for fringe generation= ');
NOP=202; %input('Number of points =');
ds=2*TD/(NOP-1);
xc=[-TD:ds:TD];
yc=[-TD:ds:TD];
count_i=0;
idata=1;

cs=sqrt(mue/rho);
```

```

cl=cs*sqrt(2+k);
sr=0.5;%input('sr='); %ratio of crack speed to shear wave speed at
crack tip
c=sr*cs; %c=3000; % crack-tip speed
c_dot=1e7; % acceleration of crack-tip

kc=20; % (Curvature)
beta=20*pi/180;
al=sqrt(1-(c/cl)^2);
as=sqrt(1-(c/cs)^2);

%end
count_i=0;
%% % constants
A0=((4*(1+(as^2)))/((4*al*as)-
((1+(as^2))^2)))*(K1D/(3*mue*sqrt(2*pi)));
A0_dot=((4*(1+(as^2)))/((4*al*as)-
((1+(as^2))^2)))*(K1D_dot/(3*mue*sqrt(2*pi)));

B0=(-2*al)/(1+(as^2))*A0;
B0_dot=(-2*al)/(1+(as^2))*A0_dot;

C0=((8*as)/(3*(4*as*al-((1+(as^2))^2)))*(K2D/(mue*sqrt(2*pi)));
C0_dot=((8*as)/(3*(4*as*al-
((1+(as^2))^2)))*(K2D_dot/(mue*sqrt(2*pi)));

D0=((1+(as^2))/(2*as))*C0;
D0_dot=((1+(as^2))/(2*as))*C0_dot;

A1 = -3/4;

Dl_A0 = -3 * (sqrt(c)) * ( rho / (mue *(k+2))) *
(sqrt(c)*(A0_dot+((c_dot)/(2*c))*A0));

Dl_C0 = -3 * (sqrt(c)) * ( rho / (mue *(k+2))) *
(sqrt(c)*(C0_dot+((c_dot)/(2*c))*C0));

Bl_A0 = 1.5 * ((c^2) / (al^2)) * ((rho/(mue *(k + 2)))^2) * A0 *
c_dot;

Bl_C0 = 1.5 * ((c^2) / (al^2)) * ((rho/(mue *(k + 2)))^2) * C0 *
c_dot;

Ds_B0 = -3 * (c) * (rho/mue) * B0_dot ;

Ds_D0 = -3 * (c) * (rho/mue) * D0_dot ;

Bs_B0 = 1.5 * ((c^2) / (as^2)) * ((rho/mue )^2) * B0 * c_dot;

Bs_D0 = 1.5 * ((c^2) / (as^2)) * ((rho/mue )^2) * D0 * c_dot;

```

%%

```
Q1_1 = -(zeta*(cos(beta)))*(A0/(4*(al^2)));
Q1_2 = (zeta*(sin(beta)))*(C0/(4*(al^1)));
Q1_3 = -(rho/(mue*(k+2))) * ( -((c^2)/(8*(al^3)))*kc*C0) -
((c^2)/(8*(al)))*kc*C0 - ((c^2)/(4*(al)))*kc*C0 +
(((c_dot)/(4*(al^2)))*A0) );
Q1_4 = ((Dl_A0)/(6*(al^2))) + ((Bl_A0)/(12*(al^2))) ;
Q1 = Q1_1 + Q1_2 + Q1_3 + Q1_4;

Q2_1 = -(zeta*(cos(beta)))*(C0/(4*(al^2)));
Q2_2 = -(zeta*(sin(beta)))*(A0/(4*(al^1)));
Q2_3 = -(rho/(mue*(k+2))) * ( ((c^2)/(8*(al^3)))*kc*A0) +
((c^2)/(8*(al)))*kc*A0 + ((c^2)/(4*(al)))*kc*A0 +
(((c_dot)/(4*(al^2)))*C0) );
Q2_4 = ((Dl_C0)/(6*(al^2))) + ((Bl_C0)/(12*(al^2))) ;
Q2 = Q2_1 + Q2_2 + Q2_3 + Q2_4;

Q3 = (-2/5)*(zeta/(k+2))*(1/((al^2)-(as^2)))*(B0*(sin(beta))) -
(D0*(cos(beta))*as));

Q4 = (-2/5)*(zeta/(k+2))*(1/((al^2)-(as^2)))*(B0*(cos(beta))*as) +
(D0*(sin(beta)));

Q5 = ((rho/(mue*(k+2))) * ( -((c^2)/(16*(al^3)))*3*kc*A0) +
((c^2)/(16*(al)))*3*kc*A0) ) + (( Bl_C0)/(8*(al^2)));

Q6 = ((rho/(mue*(k+2))) * ( -((c^2)/(16*(al^3)))*3*kc*C0) +
((c^2)/(16*(al)))*3*kc*C0) ) - (( Bl_A0)/(8*(al^2)));

R1_1 = -(zeta*(cos(beta)))*(D0/(4*(as^2)));
R1_2 = (zeta*(sin(beta)))*(B0/(4*(as^1)));
R1_3 = (rho/(mue)) * ( ((c^2)/(8*(as^3)))*kc*B0) +
((c^2)/(8*(as)))*kc*B0 + ((c^2)/(4*(as)))*kc*B0 -
(((c_dot)/(4*(as^2)))*D0) );
R1_4 = ((Ds_D0)/(6*(as^2))) + ((Bs_D0)/(12*(as^2))) ;
R1 = R1_1 + R1_2 + R1_3 + R1_4;

R2_1 = -(zeta*(cos(beta)))*(B0/(4*(as^2)));
R2_2 = -(zeta*(sin(beta)))*(D0/(4*(as^1)));
R2_3 = -(rho/(mue)) * ( ((c^2)/(8*(as^3)))*kc*D0) +
((c^2)/(8*(as)))*kc*D0 + ((c^2)/(4*(as)))*kc*D0 +
(((c_dot)/(4*(as^2)))*B0) );
R2_4 = ((Ds_B0)/(6*(as^2))) + ((Bs_B0)/(12*(as^2))) ;
R2 = R2_1 + R2_2 + R2_3 + R2_4;

R3 = (2/5)*(zeta*k)*(1/((al^2)-(as^2)))*(C0*(sin(beta))) -
(A0*(cos(beta))*al));

R4 = (2/5)*(zeta*k)*(1/((al^2)-(as^2)))*(C0*(cos(beta))*al) +
(A0*(sin(beta)));
```

```

R5 = ((rho/(mue)) * ( -(c^2)/(16*(as^3))*3*kc*D0 ) +
      ((c^2)/(16*(as))*3*kc*D0 ) ) + (( Bs_B0)/(8*(as^2)));

R6 = ((rho/(mue)) * ( -(c^2)/(16*(as^3))*3*kc*B0 ) +
      ((c^2)/(16*(as))*3*kc*B0 ) ) - (( Bs_D0)/(8*(as^2)));

S1 = (k*(1-(al^2)))+2;
S2 = (k*(1+(al^2)))+2;
S3 = (k*(1-(as^2)))+2;

S4 = k-((al^2)*(k+2));
S5 = k+((al^2)*(k+2));
S6 = k-((as^2)*(k+2));

S7 = 1+(as^2);
S8 = 1+(al^2);
S9 = (as^2)-1;
S10 = (as^2)+1;

T1 = 1/(al^2);
T2 = (T1-1);
T3 = (((3*k)+2)/(k+2))*(ac/((al^2)-1));
T4 = ac*(((3*k)+2)/(k+2))*(1/(6*at))*(1+(zeta*crack_length));
T5 = (1+(zeta*crack_length));

%%

%Expreseion for Stress

r_base = 0.0001 : 0.0001 : 0.005 ;
theta_base = -pi : (pi/180) : +pi ;
for i = 1 : length(r_base)
    for j = 1 : length(theta_base)
        r(i,j) = r_base(i);
        t(i,j) = theta_base(j);
        x(i,j) = r(i,j)*cos(t(i,j));
        y(i,j) = r(i,j)*sin(t(i,j));
        rl(i,j) = sqrt((x(i,j)^2) + ((al*y(i,j))^2));
        tl(i,j) = atan2(( al * y(i,j)), x(i,j) );
        rs(i,j) = sqrt((x(i,j)^2) + ((as*y(i,j))^2));
        ts(i,j) = atan2(( as * y(i,j)),x(i,j) );
        x_bar(i,j)=x(i,j);
        y_bar(i,j)=y(i,j);
    end
end
end

```

```

for i = 1 : length(r_base)
    for j = 1 : length(theta_base)

        s11_1(i,j)      = ((3*S1/4)*A0*(r1(i,j)^(-1/2))*cos(tl(i,j)/2))-
        ((3*S1/4)*C0*(r1(i,j)^(-1/2))*sin(tl(i,j)/2));
        s11_2(i,j)      = ((3*as/2)*B0*(rs(i,j)^(-
        1/2))*cos(ts(i,j)/2))+((3*as/2)*D0*(rs(i,j)^(-1/2))*sin(ts(i,j)/2));
        s11_3(i,j)      =
        ((3*Q1*S2)+(2*Q6*S1)+((15/2)*R3*al))*(r1(i,j)^(1/2))*cos(tl(i,j)/2);
        s11_4(i,j)      = ((3*Q2*S2)-(2*Q5*S1)-
        ((15/2)*R4*al))*(r1(i,j)^(1/2))*sin(tl(i,j)/2);
        s11_5(i,j)      =
        (((3/4)*Q1*S1)+(2*Q6*S2))*(r1(i,j)^(1/2))*cos(3*tl(i,j)/2);
        s11_6(i,j)      = (((-
        3/4)*Q2*S1)+(2*Q5*S2))*(r1(i,j)^(1/2))*sin(3*tl(i,j)/2);
        s11_7(i,j)      = -((Q6/4)*S1)*(r1(i,j)^(1/2))*cos(7*tl(i,j)/2);
        s11_8(i,j)      = -((Q5/4)*S1)*(r1(i,j)^(1/2))*sin(7*tl(i,j)/2);
        s11_9(i,j)      =
        ((4*R5*as)+((15/4)*Q4*S3))*(rs(i,j)^(1/2))*cos(ts(i,j)/2);
        s11_10(i,j)     =
        ((4*R6*as)+((15/4)*Q3*S3))*(rs(i,j)^(1/2))*sin(ts(i,j)/2);
        s11_11(i,j)     = (1.5*R2*as)*(rs(i,j)^(1/2))*cos(3*ts(i,j)/2);
        s11_12(i,j)     = (1.5*R1*as)*(rs(i,j)^(1/2))*sin(3*ts(i,j)/2);
        s11_13(i,j)     = ((R5/2)*as)*(rs(i,j)^(1/2))*cos(7*ts(i,j)/2);
        s11_14(i,j)     = ((-R6/2)*as)*(rs(i,j)^(1/2))*sin(7*ts(i,j)/2);

        s11_15(i,j)     = 0;%2*T3*q0*((r(i,j)^(1/2)))*cos(t(i,j)/2);
%temperature terms
        s11_16(i,j)     =
        0;%(T4*q0_dot*(r1(i,j)^(5/2)))*cos(tl(i,j)/2)*((k*((0.5*T1)+((1/32)*T
        1*T2)+(1/2)+((19/32)*T2)))+(T1)+((1/16)*T1*T2));
        s11_17(i,j)     =
        0;%(T4*q0_dot*(r1(i,j)^(5/2)))*cos(3*tl(i,j)/2)*((k*((3/16)*T1)-
        ((9/128)*T1*T2)-(3/16)-((39/128)*T2)))+(3/8)*T1-((9/64)*T1*T2));
        s11_18(i,j)     =
        0;%(T4*q0_dot*(r1(i,j)^(5/2)))*cos(5*tl(i,j)/2)*((k*((1/10)*T1)-
        ((1/16)*T1*T2)-(1/10)-((3/16)*T2)))+(1/5)*T1-((1/8)*T1*T2));
        s11_19(i,j)     =
        0;%(T4*q0_dot*(r1(i,j)^(5/2)))*cos(7*tl(i,j)/2)*((k*((-
        1/64)*T1*T2)+(1/64)*T2))-((1/32)*T1*T2));

        s11_20(i,j)     = -
        ((3*k)+2)*ac*((q0*(r(i,j)^(1/2))*cos(t(i,j)/2)+(q1*r(i,j)*sin(t(i,j)
        ))+(q2*(r(i,j)^(3/2))*cos(3*t(i,j)/2)));
        s11_21(i,j)     = -
        ((3*k)+2)*ac*((1/4)*gamma*q0*(r(i,j)^(3/2))*(((sin(beta)*sin(t(i,j)/
        2))-(cos(beta)*cos(t(i,j)/2)))));
        s11_22(i,j)     =
        ((3*k)+2)*ac*((T5*c)/(4*at))*((q0*(r(i,j)^(3/2))*cos(t(i,j)/2));
        s11_23(i,j)     = -
        ((3*k)+2)*ac*(T5/(6*at))*((q0_dot*(r(i,j)^(5/2))*cos(t(i,j)/2));

        s22_1(i,j)      = ((3*S4/4)*A0*(r1(i,j)^(-1/2))*cos(tl(i,j)/2))-
        ((3*S4/4)*C0*(r1(i,j)^(-1/2))*sin(tl(i,j)/2));

```

```

s22_2(i,j) = -((3*as/2)*B0*(rs(i,j)^(-1/2))*cos(ts(i,j)/2))-
((3*as/2)*D0*(rs(i,j)^(-1/2))*sin(ts(i,j)/2));
s22_3(i,j) = ((3*Q1*S5)+(2*Q6*S4)-
((15/2)*R3*al))*(r1(i,j)^(1/2))*cos(tl(i,j)/2);
s22_4(i,j) = ((3*Q2*S5)-
(2*Q5*S4)+((15/2)*R4*al))*(r1(i,j)^(1/2))*sin(tl(i,j)/2);
s22_5(i,j) =
(((3/4)*Q1*S4)+(2*Q6*S5))*(r1(i,j)^(1/2))*cos(3*tl(i,j)/2);
s22_6(i,j) = (((-
3/4)*Q2*S4)+(2*Q5*S5))*(r1(i,j)^(1/2))*sin(3*tl(i,j)/2);
s22_7(i,j) = -((Q6/4)*S4)*(r1(i,j)^(1/2))*cos(7*tl(i,j)/2);
s22_8(i,j) = -((Q5/4)*S4)*(r1(i,j)^(1/2))*sin(7*tl(i,j)/2);
s22_9(i,j) = ((-
4*R5*as)+((15/4)*Q4*S6))*(rs(i,j)^(1/2))*cos(ts(i,j)/2);
s22_10(i,j) = ((-
4*R6*as)+((15/4)*Q3*S6))*(rs(i,j)^(1/2))*sin(ts(i,j)/2);
s22_11(i,j) = (-1.5*R2*as)*(rs(i,j)^(1/2))*cos(3*ts(i,j)/2);
s22_12(i,j) = (-1.5*R1*as)*(rs(i,j)^(1/2))*sin(3*ts(i,j)/2);
s22_13(i,j) = ((-R5/2)*as)*(rs(i,j)^(1/2))*cos(7*ts(i,j)/2);
s22_14(i,j) = ((R6/2)*as)*(rs(i,j)^(1/2))*sin(7*ts(i,j)/2);

s22_15(i,j) = 0;%-2*T3*q0*((r(i,j)^(1/2)))*cos(t(i,j)/2);
%temperature terms
s22_16(i,j) =
0;%(T4*q0_dot*(r1(i,j)^(5/2)))*cos(tl(i,j)/2)*((k*((0.5*T1)+((1/32)*T
1*T2)+(1/2)+((19/32)*T2))) +(1)+((19/16)*T2));
s22_17(i,j) =
0;%(T4*q0_dot*(r1(i,j)^(5/2)))*cos(3*tl(i,j)/2)*((k*((3/16)*T1)-
((9/128)*T1*T2)-(3/16)-((39/128)*T2))) -((3/8)-((39/64)*T2));
s22_18(i,j) =
0;%(T4*q0_dot*(r1(i,j)^(5/2)))*cos(5*tl(i,j)/2)*((k*((1/10)*T1)-
((1/16)*T1*T2)-(1/10)-((3/16)*T2))) -((1/5)-((3/8)*T2));
s22_19(i,j) =
0;%(T4*q0_dot*(r1(i,j)^(5/2)))*cos(7*tl(i,j)/2)*((k*((-
1/64)*T1*T2)+((1/64)*T2))) +(1/32)*T2));

s22_20(i,j) = -
((3*k)+2)*ac*((q0*(r(i,j)^(1/2))*cos(t(i,j)/2)+(q1*r(i,j)*sin(t(i,j)
))+((q2*(r(i,j)^(3/2))*cos(3*t(i,j)/2)))));
s22_21(i,j) = -
((3*k)+2)*ac*((1/4)*gamma*q0*(r(i,j)^(3/2))*(((sin(beta)*sin(t(i,j)/
2))-((cos(beta)*cos(t(i,j)/2))))));
s22_22(i,j) =
((3*k)+2)*ac*((T5*c)/(4*at))*((q0*(r(i,j)^(3/2))*cos(t(i,j)/2)));
s22_23(i,j) = -
((3*k)+2)*ac*((T5)/(6*at))*((q0_dot*(r(i,j)^(5/2))*cos(t(i,j)/2)));

s12_1(i,j) = ((3*al/2)*A0*(r1(i,j)^(-
1/2))*sin(tl(i,j)/2))+((3*al/2)*C0*(r1(i,j)^(-1/2))*cos(tl(i,j)/2));
s12_2(i,j) = ((3*S7/4)*B0*(rs(i,j)^(-1/2))*sin(ts(i,j)/2))-
((3*S7/4)*D0*(rs(i,j)^(-1/2))*cos(ts(i,j)/2));
s12_3(i,j) = ((4*Q5*al)-
((15/4)*R4*S8))*(r1(i,j)^(1/2))*cos(tl(i,j)/2);

```

```

s12_4(i,j) = ((4*Q6*al)-
((15/4)*R3*S8))*(rl(i,j)^(1/2))*sin(tl(i,j)/2);
s12_5(i,j) = (((3/2)*Q2*al))*(rl(i,j)^(1/2))*cos(3*tl(i,j)/2);
s12_6(i,j) = (((3/2)*Q1*al))*(rl(i,j)^(1/2))*sin(3*tl(i,j)/2);
s12_7(i,j) = ((Q5/2)*al)*(rl(i,j)^(1/2))*cos(7*tl(i,j)/2);
s12_8(i,j) = ((-Q6/2)*al)*(rl(i,j)^(1/2))*sin(7*tl(i,j)/2);
s12_9(i,j) = ((3*R1*S9)-
(2*R6*S7)+((15/2)*Q3*as))*(rs(i,j)^(1/2))*cos(ts(i,j)/2);
s12_10(i,j) = ((3*R2*S9)+(2*R5*S10)-
((15/2)*Q4*as))*(rs(i,j)^(1/2))*sin(ts(i,j)/2);
s12_11(i,j) = ((-
(3/4)*R1*S7)+(2*R6*S9))*(rs(i,j)^(1/2))*cos(3*ts(i,j)/2);
s12_12(i,j) =
(((3/4)*R2*S7)+(2*R5*S9))*(rs(i,j)^(1/2))*sin(3*ts(i,j)/2);
s12_13(i,j) = ((R6/4)*S7)*(rs(i,j)^(1/2))*cos(7*ts(i,j)/2);
s12_14(i,j) = ((R5/4)*S7)*(rs(i,j)^(1/2))*sin(7*ts(i,j)/2);

s12_15(i,j) = 0;%-2*T3*q0*((r(i,j)^(1/2)))*sin(t(i,j)/2);
%temperature terms
s12_16(i,j) =
0;%((T4/al)*q0_dot*(rl(i,j)^(5/2)))*sin(tl(i,j)/2)*((1/16)*T2);
s12_17(i,j) =
0;%((T4/al)*q0_dot*(rl(i,j)^(5/2)))*sin(3*tl(i,j)/2)*((3/8)+((30/128)
*T2));
s12_18(i,j) =
0;%((T4/al)*q0_dot*(rl(i,j)^(5/2)))*sin(5*tl(i,j)/2)*((1/5)+((1/8)*T2
));
s12_19(i,j) =
0;%((T4/al)*q0_dot*(rl(i,j)^(5/2)))*sin(7*tl(i,j)/2)*((-1/32)*T2);

s11a(i,j) =
(s11_1(i,j)+s11_2(i,j)+s11_3(i,j)+s11_4(i,j)+s11_5(i,j));
s11b(i,j) =
(s11_6(i,j)+s11_7(i,j)+s11_8(i,j)+s11_9(i,j)+s11_10(i,j));
s11c(i,j) =
(s11_11(i,j)+s11_12(i,j)+s11_13(i,j)+s11_14(i,j)+s11_15(i,j));
s11d(i,j) =
(s11_16(i,j)+s11_17(i,j)+s11_18(i,j)+s11_19(i,j)+s11_20(i,j)+s11_21(i
,j)); %s11_22(i,j)+s11_23(i,j)

s11(i,j)=(mue*exp(zeta*(x_bar(i,j))))*(s11a(i,j)+s11b(i,j)+s11c(i,j)+
s11d(i,j))+(A1*K1D);

s22a(i,j) =
(s22_1(i,j)+s22_2(i,j)+s22_3(i,j)+s22_4(i,j)+s22_5(i,j));
s22b(i,j) =
(s22_6(i,j)+s22_7(i,j)+s22_8(i,j)+s22_9(i,j)+s22_10(i,j));
s22c(i,j) =
(s22_11(i,j)+s22_12(i,j)+s22_13(i,j)+s22_14(i,j)+s22_15(i,j));

```

```

        s22d(i,j) =
(s22_16(i,j)+s22_17(i,j)+s22_18(i,j)+s22_19(i,j)+s22_20(i,j)+s22_23(i
,j));%+s22_22(i,j)+s22_23(i,j)

s22(i,j)=(mue*exp(zeta*(x_bar(i,j))))*(s22a(i,j)+s22b(i,j)+s22c(i,j)+
s22d(i,j));

        s12a(i,j) =
(s12_1(i,j)+s12_2(i,j)+s12_3(i,j)+s12_4(i,j)+s12_5(i,j));
        s12b(i,j) =
(s12_6(i,j)+s12_7(i,j)+s12_8(i,j)+s12_9(i,j)+s12_10(i,j));
        s12c(i,j) =
(s12_11(i,j)+s12_12(i,j)+s12_13(i,j)+s12_14(i,j)+s12_15(i,j));
        s12d(i,j) = (s12_16(i,j)+s12_17(i,j)+s12_18(i,j)+s12_19(i,j));

s12(i,j)=(mue*exp(zeta*(x_bar(i,j))))*(s12a(i,j)+s12b(i,j)+s12c(i,j)+
s12d(i,j));

        tmax(i,j)=sqrt((((s11(i,j)-s22(i,j))/2)^2)+(s12(i,j)^2));

end
end

% figure(1)
% plot(t(20,:)*180/pi,s11(20,:),'-r'); hold on;
% ylabel('\sigma_x_x (MPa)', 'FontName', 'Timesnewroman')
% xlabel('\theta (degrees)', 'FontName', 'Timesnewroman')
% title('\sigma_x_x Plot')
%
% figure(2)
% plot(t(20,:)*180/pi,s22(20,:),'-r'); hold on;
% ylabel('\sigma_y_y (MPa)', 'FontName', 'Timesnewroman')
% xlabel('\theta (degrees)', 'FontName', 'Timesnewroman')
% title('\sigma_y_y Plot')
%
% figure(3)
% plot(t(20,:)*180/pi,s12(20,:),'-r'); hold on;
% ylabel('\sigma_x_y (MPa)', 'FontName', 'Timesnewroman')
% xlabel('\theta (degrees)', 'FontName', 'Timesnewroman')
% title('\sigma_x_y Plot')

% figure(4)
% contour(x_bar,y_bar,tmax,50); hold on;
% ylabel('y (m)', 'FontName', 'Timesnewroman')
% xlabel('x (m)', 'FontName', 'Timesnewroman')
% title('Only Homogeneous \sigma_x_x')
% colorbar
% line([-0.005,0],[0,0]);
% xlim([-0.003 0.003])
% ylim([-0.003 0.003])

```

```

% print -dtiffnocompression Only_Homogeneous_sigma_y_y ;
%
% figure(5)
% contour(x_bar,y_bar,s22,50); hold on;
% ylabel('y (m)', 'FontName', 'Timesnewroman')
% xlabel('x (m)', 'FontName', 'Timesnewroman')
% title('Only Homogeneous \sigma_y_y')
% colorbar
% line([-0.005,0],[0,0]);
% xlim([-0.003 0.003])
% ylim([-0.003 0.003])
%
% figure(6)
% contour(x_bar,y_bar,s12,50); hold on;
% ylabel('y (m)', 'FontName', 'Timesnewroman')
% xlabel('x (m)', 'FontName', 'Timesnewroman')
% title('Only Homogeneous \sigma_x_y')
% colorbar
% line([-0.005,0],[0,0]);
% xlim([-0.003 0.003])
% ylim([-0.003 0.003])
% figure(3)
% contour(x_bar,y_bar,s12,100); hold on;
% ylabel('y (m)', 'FontName', 'Timesnewroman')
% xlabel('x (m)', 'FontName', 'Timesnewroman')
% title('Only Homogeneous \stau_x_y')
% colorbar
% line([-0.005,0],[0,0]);
% xlim([-0.003 0.003])
% ylim([-0.003 0.003])
%
% figure(4)
% contour(x_bar,y_bar,tmax,30); hold on;
% ylabel('y (m)', 'FontName', 'Timesnewroman')
% xlabel('x (m)', 'FontName', 'Timesnewroman')
% title('Only Homogeneous \stau_m_a_x')
% colorbar
% line([-0.005,0],[0,0]);
% xlim([-0.003 0.003])
% ylim([-0.003 0.003])

% figure(3)
% plot(t(20,:)*180/pi,s12(20,:),'-o')
% ylabel('\tau_x_y(MPa)', 'FontName', 'Timesnewroman')
% xlabel('\theta(degrees)', 'FontName', 'Timesnewroman')
% title('Only Homogeneous \tau_x_y')

% figure(9)
%

% figure(100)
% plot(x_bar(:,1), s22(:,1),'-k');hold on;

```

```

% figure(101)
% plot(x_bar(:,1), s12(:,1),'-k')

PP = polyfit(x_bar(:,1),s22(:,1),4);
QQ = polyfit(x_bar(:,1),(((s12(:,1))-(s12(:,361)))/2),4);
%QQ = polyfit(x_bar(:,1),s12(:,1),4);

% figure(100)
% plot(x_bar(:,1), s22(:,1), '-k'); hold on;
% plot(x_bar(:,1), (PP(1)*x_bar(:,1).^4 + PP(2)*x_bar(:,1).^3 +
PP(3)*x_bar(:,1).^2 + PP(4)*x_bar(:,1) + PP(5)), 'or')
%
% figure(101)
% plot(x_bar(:,1), s12(:,1), '-k'); hold on;
% plot(x_bar(:,1), (QQ(1)*x_bar(:,1).^4 + QQ(2)*x_bar(:,1).^3 +
QQ(3)*x_bar(:,1).^2 + QQ(4)*x_bar(:,1) + QQ(5)), 'or')

L_ploy(1) = PP(1)/5;
L_ploy(2) = PP(2)/4;
L_ploy(3) = PP(3)/3;
L_ploy(4) = PP(4)/2;
L_ploy(5) = PP(5)/1;

M_ploy(1) = QQ(1)/5;
M_ploy(2) = QQ(2)/4;
M_ploy(3) = QQ(3)/3;
M_ploy(4) = QQ(4)/2;
M_ploy(5) = QQ(5)/1;

for i = 1 : length(x_bar(:,1)) - 1
    Load_P2(i) = ((L_ploy(1)*x_bar(i,1)^5 + L_ploy(2)*x_bar(i,1)^4 +
L_ploy(3)*x_bar(i,1)^3 + L_ploy(4)*x_bar(i,1)^2 +
L_ploy(5)*x_bar(i,1)^1) ...
- (L_ploy(1)*x_bar(i+1,1)^5 + L_ploy(2)*x_bar(i+1,1)^4 +
L_ploy(3)*x_bar(i+1,1)^3 + L_ploy(4)*x_bar(i+1,1)^2 +
L_ploy(5)*x_bar(i+1,1)^1));

    Load_Q2(i) = ((M_ploy(1)*x_bar(i,1)^5 + M_ploy(2)*x_bar(i,1)^4 +
M_ploy(3)*x_bar(i,1)^3 + M_ploy(4)*x_bar(i,1)^2 +
M_ploy(5)*x_bar(i,1)^1) ...
- (M_ploy(1)*x_bar(i+1,1)^5 + M_ploy(2)*x_bar(i+1,1)^4 +
M_ploy(3)*x_bar(i+1,1)^3 + M_ploy(4)*x_bar(i+1,1)^2 +
M_ploy(5)*x_bar(i+1,1)^1));

    c_mid(i)=(x_bar(i,1)+x_bar(i+1,1))/2;
    d(i) = abs(c_mid(i));

end
for i = 1 : length(x_bar(:,1)) - 1
PP1=polyfit(c_mid,Load_P2,4);
QQ1=polyfit(c_mid,Load_Q2,4);
c1(i) = (x_bar(i,1);%+x_bar(i+1,1))/2;

```

```

Load_P(i) =
PP1(1)*c1(i).^4+PP1(2)*c1(i).^3+PP1(3)*c1(i).^2+PP1(4)*c1(i).^1+PP1(5
);
Load_Q(i) =
QQ1(1)*c1(i).^4+QQ1(2)*c1(i).^3+QQ1(3)*c1(i).^2+QQ1(4)*c1(i).^1+QQ1(5
);
d1(i) = abs(c1(i));%-0.0000000000029;
d1(i) = abs(c1(i));%-0.0000000000046;
end
% figure(301)
% plot(x_bar(1:49,1),Load_P2);
% plot(x_bar(1:49,1),Load_P,'k');
%
% figure(302)
% plot(x_bar(1:49,1),Load_Q,'k');
% plot(x_bar(1:49,1),Load_Q2);

correction_s11_1 = zeros(length(r_base),length(theta_base));
sum_correction_s11_1 = zeros(length(r_base),length(theta_base));
correction_s22_1 = zeros(length(r_base),length(theta_base));
sum_correction_s22_1 = zeros(length(r_base),length(theta_base));
correction_s12_1 = zeros(length(r_base),length(theta_base));
sum_correction_s12_1 = zeros(length(r_base),length(theta_base));
correction_s11_2 = zeros(length(r_base),length(theta_base));
sum_correction_s11_2 = zeros(length(r_base),length(theta_base));
correction_s22_2 = zeros(length(r_base),length(theta_base));
sum_correction_s22_2 = zeros(length(r_base),length(theta_base));
correction_s12_2 = zeros(length(r_base),length(theta_base));
sum_correction_s12_2 = zeros(length(r_base),length(theta_base));

for m = 1 : length(Load_P)
    b1 = d1(m); % for sigmay
    b2 = d1(m); % for tauxy
    b3 = d1(m); %for sigmax
    %b = -x_bar(m,1) + ((x_bar(1,1)-x_bar(2,1))/2);

    for n = 1 : length(r_base)
        for o = 1 : length(theta_base)
            r_1_1(n,o) = sqrt( ((x_bar(n,o) + b1)^2) + (y_bar(n,o)^2)
);
            theta_1_1(n,o) = atan2( y_bar(n,o),(x_bar(n,o)+b1) );
            r_1_2(n,o) = sqrt( ((x_bar(n,o) + b2)^2) + (y_bar(n,o)^2)
);
            theta_1_2(n,o) = atan2( y_bar(n,o),(x_bar(n,o)+b2) );

            r_1_3(n,o) = sqrt( ((x_bar(n,o) + b3)^2) + (y_bar(n,o)^2)
);
            theta_1_3(n,o) = atan2( y_bar(n,o),(x_bar(n,o)+b3) );
%             Load_P(m) = 100;
%             Load_Q(m) = 100;

```

```

        real_z_1(n,o) = (Load_P(m) * sqrt(b1)/pi)* ( 1/
(r_1_1(n,o)*sqrt(r(n,o)))) * cos ( theta_1_1(n,o) + t(n,o)/2 );
        imag_z_1(n,o) = -(Load_P(m) * sqrt(b1)/pi)* ( 1/
(r_1_1(n,o)*sqrt(r(n,o)))) * sin ( theta_1_1(n,o) + t(n,o)/2 );
        real_z_1_prime(n,o) = -(Load_P(m) * sqrt(b1)/pi) * (
(1/(2*r_1_1(n,o)*(r(n,o)^1.5))) * cos(theta_1_1(n,o) + 1.5*t(n,o)) +
(1/(sqrt(r(n,o))*(r_1_1(n,o)^2)))* cos(2*theta_1_1(n,o) + t(n,o)/2));
        imag_z_1_prime(n,o) = (Load_P(m) * sqrt(b1)/pi) * (
(1/(2*r_1_1(n,o)*(r(n,o)^1.5))) * sin(theta_1_1(n,o) + 1.5*t(n,o)) +
(1/(sqrt(r(n,o))*(r_1_1(n,o)^2)))* sin(2*theta_1_1(n,o) + t(n,o)/2));
        real_z_2(n,o) = (Load_Q(m) * sqrt(b2)/pi)* ( 1/
(r_1_2(n,o)*sqrt(r(n,o)))) * cos ( theta_1_2(n,o) + t(n,o)/2 );

        imag_z_2(n,o) = -(Load_Q(m) * sqrt(b2)/pi)* ( 1/
(r_1_2(n,o)*sqrt(r(n,o)))) * sin ( theta_1_2(n,o) + t(n,o)/2 );

        real_z_2_prime(n,o) = -(Load_Q(m) * sqrt(b2)/pi) * (
(1/(2*r_1_2(n,o)*(r(n,o)^1.5))) * cos(theta_1_2(n,o) + 1.5*t(n,o)) +
(1/(sqrt(r(n,o))*(r_1_2(n,o)^2)))* cos(2*theta_1_2(n,o) + t(n,o)/2));

        imag_z_2_prime(n,o) = (Load_Q(m) * sqrt(b2)/pi) * (
(1/(2*r_1_2(n,o)*(r(n,o)^1.5))) * sin(theta_1_2(n,o) + 1.5*t(n,o)) +
(1/(sqrt(r(n,o))*(r_1_2(n,o)^2)))* sin(2*theta_1_2(n,o) + t(n,o)/2));

        real_z_1_s11(n,o) = (Load_P(m) * sqrt(b3)/pi)* ( 1/
(r_1_3(n,o)*sqrt(r(n,o)))) * cos ( theta_1_3(n,o) + t(n,o)/2 );
        imag_z_1_s11(n,o) = -(Load_P(m) * sqrt(b3)/pi)* ( 1/
(r_1_3(n,o)*sqrt(r(n,o)))) * sin ( theta_1_3(n,o) + t(n,o)/2 );
        real_z_2_prime_s11(n,o) = -(Load_Q(m) * sqrt(b3)/pi) * (
(1/(2*r_1_3(n,o)*(r(n,o)^1.5))) * cos(theta_1_3(n,o) + 1.5*t(n,o)) +
(1/(sqrt(r(n,o))*(r_1_3(n,o)^2)))* cos(2*theta_1_3(n,o) + t(n,o)/2));
        imag_z_2_s11(n,o) = -(Load_Q(m) * sqrt(b3)/pi)* ( 1/
(r_1_3(n,o)*sqrt(r(n,o)))) * sin ( theta_1_3(n,o) + t(n,o)/2 );

        correction_s11_1(n,o) = real_z_1_s11(n,o) -
y(n,o)*imag_z_1_s11(n,o);
        correction_s22_1(n,o) = real_z_1(n,o) +
y(n,o)*imag_z_1(n,o);
        correction_s12_1(n,o) = -y(n,o)*real_z_1(n,o);
        correction_s11_2(n,o) = y(n,o)*real_z_2_prime_s11(n,o)+
2*imag_z_2_s11(n,o);
        correction_s22_2(n,o) = -y(n,o)*real_z_2_prime(n,o);
        correction_s12_2(n,o) = -y(n,o)*imag_z_2_prime(n,o) +
real_z_2(n,o);

        end
    end
    sum_correction_s11_1= sum_correction_s11_1 + correction_s11_1;
    sum_correction_s22_1= sum_correction_s22_1 + correction_s22_1;
    sum_correction_s12_1= sum_correction_s12_1 + correction_s12_1;
    sum_correction_s11_2= sum_correction_s11_2 + correction_s11_2;
    sum_correction_s22_2= sum_correction_s22_2 + correction_s22_2;
    sum_correction_s12_2= sum_correction_s12_2 + correction_s12_2;

```

```

end

% for u=1:length(sum_correction_s11_1)
%     if t(u)<0
%
%         final_s22 =

% figure(3002)
%     contour(x_bar,y_bar,s22      +      sum_correction_s22_1      +
sum_correction_s22_2,50)
% colorbar
% ylabel('y (m)','FontName','Timesnewroman')
% xlabel('x (m)','FontName','Timesnewroman')
% title('Only Homogeneous \sigma_y_y')
% colorbar
% line([-0.005,0],[0,0]);
%
% figure(1001)
% plot(x_bar(:,1), -(sum_correction_s12_2(:,4)), '-k'); hold on;
% %plot(x_bar(:,311), -sum_correction_s12_2(:,311), '-k'); hold on;
% %figure(1002)
% plot(x_bar(:,1),s12(:,1)); hold on;
% plot(x_bar(:,311),s12(:,311));

% figure(1002)
%     plot(x_bar(:,1),
(sum_correction_s12_1(:,1)+sum_correction_s12_2(:,1)), '-r'); hold
on;
% %plot(x_bar(:,311), -sum_correction_s12_2(:,311), '-k'); hold on;
% %figure(1002)
% plot(x_bar(:,1),s12(:,1)); hold on;
% %plot(x_bar(:,311),s12(:,311));

% figure(1002)
% plot(x_bar(:,1), -sum_correction_s22_2(:,1), '-k'); hold on;

%Field copying from +- 3 degress from point load to the same as 3
degress
%one
%sum_correction_s22_x
(sum_correction_s22_1(:,3)+sum_correction_s22_1(:,4))/2;
sum_correction_s22_1(:,1) = sum_correction_s22_1(:,3);
sum_correction_s22_1(:,2) = 0.99*sum_correction_s22_1(:,3);
sum_correction_s22_1(:,3) = 0.98*sum_correction_s22_1(:,3);
% sum_correction_s22_1(:,4) = sum_correction_s22_1(:,3);
%sum_correction_s22_1(:,361) = sum_correction_s22_1(:,357);
sum_correction_s22_1(:,361) = sum_correction_s22_1(:,359);
sum_correction_s22_1(:,360) = sum_correction_s22_1(:,359);
% sum_correction_s22_1(:,359) = sum_correction_s22_1(:,358);

```

```

%Field copying from +- 3 degrees from point load to the same as of 3
degrees
%one

sum_correction_s12_2(:,1) = 1.14*sum_correction_s12_2(:,4);
sum_correction_s12_2(:,2) = 1.06*sum_correction_s12_2(:,4);
sum_correction_s12_2(:,3) = 1.05*sum_correction_s12_2(:,4);
sum_correction_s12_2(:,361) = 1.14*sum_correction_s12_2(:,358);
sum_correction_s12_2(:,360) = 1.11*sum_correction_s12_2(:,358);
sum_correction_s12_2(:,359) = 1.1*sum_correction_s12_2(:,358);

%Field copying from +- 3 degress from point load to the same as 3
degress
%one

sum_correction_s11_1(:,1) = sum_correction_s11_1(:,2);
sum_correction_s11_1(:,2) = sum_correction_s11_1(:,3);
sum_correction_s11_1(:,3) = sum_correction_s11_1(:,4);
sum_correction_s11_1(:,361) = sum_correction_s11_1(:,358);
sum_correction_s11_1(:,360) = sum_correction_s11_1(:,358);
sum_correction_s11_1(:,359) = sum_correction_s11_1(:,358);

% Reversing field of correction_Q field

% for i = 1 : 181
%     sum_correction_s12_2(:,i) = -sum_correction_s12_2(:,i);
% end

% figure(3001)
% contour(x_bar,y_bar,sum_correction_s22_1,50)
% colorbar
%
% figure(3002)
% contour(x_bar,y_bar,sum_correction_s22_2,100)
% colorbar
%
% figure(3003)
% contour(x_bar,y_bar,sum_correction_s12_1,50)
% colorbar
%
% figure(3004)
% contour(x_bar,y_bar,sum_correction_s12_2,100)
% colorbar

% final_s22= s22 + sum_correction_s22_1 - sum_correction_s22_2 ;
% final_s11 = s11 + sum_correction_s11_1 - sum_correction_s11_2;
% final_s12 = s12 + sum_correction_s12_1 - sum_correction_s12_2;
%s22(:,361) = -s22(:,361);
%s11(:,361) = -s11(:,361);
% for i = 1 : 181
%     sum_correction_s12_2(:,i) = -sum_correction_s12_2(:,i);
% end
for (i=1:length(r_base))
    for (j=1:length(theta_base))

```

```

        final_s11(i,j) = s11(i,j)
+sum_correction_s11_1(i,j)+sum_correction_s11_2(i,j);

end
    end

for (i=1:length(r_base))
    for (j=1:length(theta_base))
if t(i,j)>1.7;

        final_s22(i,j) = s22(i,j) -
sum_correction_s22_1(i,j)+sum_correction_s22_2(i,j);

else

        final_s22(i,j) = s22(i,j)
+sum_correction_s22_1(i,j)+sum_correction_s22_2(i,j);

end
    end
end
for (i=1:length(r_base))
    for (j=1:length(theta_base))
if t(i,j)<-0.85;

        final_s12(i,j) = s12(i,j) -
sum_correction_s12_1(i,j)+sum_correction_s12_2(i,j);
else

        final_s12(i,j) = s12(i,j) +sum_correction_s12_1(i,j)-
sum_correction_s12_2(i,j);

end
    end
end
    for i = 1 : length(r_base)
        for j = 1 : length(theta_base)
            final_tmax(i,j)=sqrt((((final_s11(i,j)-
final_s22(i,j))/2)^2)+(final_s12(i,j)^2));

            sigmal(i,j)=((final_s11(i,j)+final_s22(i,j))/2)+sqrt((((final_s11(i,j)
)-final_s22(i,j))/2)^2)+(final_s12(i,j)^2));
            sed(i,j)=(1/(4*(mue*exp(zeta*x_bar(i,j)))))*((1-nue)*((
final_s11(i,j))^2+ (final_s22(i,j))^2)-(2*nue* final_s11(i,j)*
final_s22(i,j)))+(2*(( final_s12(i,j))^2)));
            N(i,j) = sigmal(i,j)/(1e7);
        end
    end

```

```

end
%randtheta
for (i=1:length(r_base))
    for (j=1:length(theta_base))

s11r(i,j)=(final_s11(i,j)*(cos(t(i,j)))^2)+(final_s22(i,j)*(sin(t(i,j)
))^2)+(2*final_s12(i,j)*(cos(t(i,j))*sin(t(i,j))));

s22r(i,j)=(final_s11(i,j)*(sin(t(i,j)))^2)+(final_s22(i,j)*(cos(t(i,j)
))^2)-(2*final_s12(i,j)*(cos(t(i,j))*sin(t(i,j))));
s12r(i,j)=(-
final_s11(i,j)*(cos(t(i,j))*sin(t(i,j)))+(final_s22(i,j)*(sin(t(i,j)
)*cos(t(i,j)))+(final_s12(i,j)*((cos(t(i,j)))^2-(sin(t(i,j)))^2));
N1(i,j) = s22r(i,j)/1e7;
    end
end
% figure(1)
% plot(t(20,:)*180/pi,final_s11(20,:),'-r'); hold on;
% ylabel('\sigma_x_x (MPa)','FontName','Timesnewroman')
% xlabel('\theta (degrees)','FontName','Timesnewroman')
% title('\sigma_x_x Plot')
%
% figure(2)
% plot(t(20,:)*180/pi,final_s22(20,:),'-r'); hold on;
% ylabel('\sigma_y_y (MPa)','FontName','Timesnewroman')
% xlabel('\theta (degrees)','FontName','Timesnewroman')
% title('\sigma_y_y Plot')
%
% figure(3)
% plot(t(20,:)*180/pi,final_s12(20,:),'-r'); hold on;
% ylabel('\sigma_x_y (MPa)','FontName','Timesnewroman')
% xlabel('\theta (degrees)','FontName','Timesnewroman')
% title('\sigma_x_y Plot')

% figure(9004)
% plot(x_bar(:,361), (sum_correction_s12_2(:,361)), '-k'); hold on;
% plot(x_bar(:,1), (sum_correction_s12_2(:,1)), '-or'); hold on;
% %plot(x_bar(:,311), -sum_correction_s12_2(:,311), '-k'); hold on;
% %figure(1002)
% plot(x_bar(:,1),s12(:,1)); hold on;
% plot(x_bar(:,361),s12(:,361),'r'); hold on;
%
% plot(x_bar(:,311),s12(:,311));
% figure(9001)
% plot(x_bar(:,361), (sum_correction_s12_2(:,361)), '-k'); hold on;
% plot(x_bar(:,1), (sum_correction_s12_2(:,1)), '-or'); hold on;
% %plot(x_bar(:,311), -sum_correction_s12_2(:,311), '-k'); hold on;
% %figure(1002)
% plot(x_bar(:,1),s22(:,361)); hold on;
% %plot(x_bar(:,311),s12(:,311));
%
% figure(9002)
% plot(x_bar(:,361), (sum_correction_s12_2(:,361)), '-k'); hold on;
% plot(x_bar(:,361), (sum_correction_s12_1(:,361)), '-or'); hold on;
% %plot(x_bar(:,311), -sum_correction_s12_2(:,311), '-k'); hold on;

```

```

% %figure(1002)
% plot(x_bar(:,1),s12(:,361)); hold on;
% %plot(x_bar(:,311),s12(:,311));
%
% figure(9003)
% plot(x_bar(:,361), (sum_correction_s11_2(:,361)), '-k'); hold on;
% plot(x_bar(:,361), (sum_correction_s11_1(:,361)), '-or'); hold on;
% %plot(x_bar(:,311), -sum_correction_s12_2(:,311), '-k'); hold on;
% %figure(1002)
% plot(x_bar(:,1),s11(:,361)); hold on;
% %plot(x_bar(:,311),s12(:,311));

% figure(5001)
% plot(t(20,:)*180/pi,s22(20,:),'-o'); hold on;
% % plot(t(20,:)*180/pi,sum_correction_s22_1(20,:)); hold on;
% % plot(t(20,:)*180/pi,sum_correction_s22_2(20,:),'r'); hold on;
% plot(t(20,:)*180/pi,final_s22(20,:),'-or'); hold on;
% % ylabel('\sigma_y_y (MPa)', 'FontName', 'Timesnewroman')
% % xlabel('\theta (degrees)', 'FontName', 'Timesnewroman')
% % title('\sigma_y_y Plot')
%
%
% figure(5002)
% plot(t(20,:)*180/pi,s12(20,:),'-o');hold on;
% plot(t(20,:)*180/pi,final_s12(20,:),'-or'); hold on;
% plot(t(20,:)*180/pi,sum_correction_s12_1(20,:)); hold on;
% plot(t(20,:)*180/pi,sum_correction_s12_2(20,:),'or'); hold on;
% ylabel('\tau_x_y (MPa)', 'FontName', 'Timesnewroman')
% xlabel('\theta (degrees)', 'FontName', 'Timesnewroman')
% title('\tau_x_y Plot')
%
% figure(5003)
% % plot(t(20,:)*180/pi,s12(20,:),'-o');hold on;
%
plot(t(20,1:361)*180/pi,(final_tmax(20,1:361)/(Kef/sqrt(2*pi*0.002)))
,'-o'); hold on;
% % plot(t(20,:)*180/pi,sum_correction_s12_1(20,:)); hold on;
% % plot(t(20,:)*180/pi,sum_correction_s12_2(20,:),'or'); hold on;
% % plot(t(20,:)*180/pi,final_s12(20,:),'or'); hold on;
% ylabel('\tau_m_a_x / (K_e_f_f / \surd(2\pir))', 'FontName', 'Timesnewroman', 'FontSize', 16)
% xlabel('\theta (degrees)', 'FontName', 'Timesnewroman', 'FontSize', 16)
% xlim([-180 180])
% %ylim([0 1.41])
%
legend('k=20,\beta=20^o', 'k=40,\beta=20^o', 'k=60,\beta=20^o', 'FontName', 'Timesnewroman', 'FontSize', 12);
%
legend('q_0=0', 'q_0=1000', 'q_0=2000');%,'k=20,\beta=20');%,'C/C_s=0.6', 'C/C_s=0.4');
% figure(2001)
%
% figure(5004)
%plot(t(20,:)*180/pi,s12(20,:),'-o');hold on;

```

```

plot(t(20,1:361)*180/pi,(sigma1(20,1:361)/(Kef/sqrt(2*pi*0.002))),':g
','Linewidth',1.5); hold on;
%plot(t(20,:)*180/pi,sum_correction_s12_1(20,:)); hold on;
%plot(t(20,:)*180/pi,sum_correction_s12_2(20,:),'or'); hold on;
ylabel('\sigma_1 / (K_e_f_f / \surd(2\pir))','FontName','Timesnewroman','FontSize',16)
xlabel('\theta (degrees)','FontName','Timesnewroman','FontSize',16)
xlim([-180 180])
%ylim([-0.5 2.5])

%legend('k=20,\beta=20^o','k=40,\beta=20^o','k=60,\beta=20^o','FontName',
'Timesnewroman','FontSize',12);

legend('q_0=0','q_0=100','q_0=200');%,'k=20,\beta=20');%,'C/C_s=0.6',
'C/C_s=0.4');

figure(5005)
%plot(t(20,:)*180/pi,s12(20,:),'-o');hold on;
plot(t(20,1:361)*180/pi,(s22r(20,1:361)/(Kef/sqrt(2*pi*0.002))), '--
k','Linewidth',1.5); hold on;
%plot(t(20,:)*180/pi,sum_correction_s12_1(20,:)); hold on;
%plot(t(20,:)*180/pi,sum_correction_s12_2(20,:),'or'); hold on;
ylabel('\sigma_\theta_\theta / (K_e_f_f / \surd(2\pir))','FontName','Timesnewroman','FontSize',16)
xlabel('\theta (degrees)','FontName','Timesnewroman','FontSize',16)
xlim([-180 180])
%ylim([-0.5 2.5])

%legend('k=20,\beta=20^o','k=40,\beta=20^o','k=60,\beta=20^o','FontName',
'Timesnewroman','FontSize',12);

legend('q_0=0','q_0=100','q_0=200');%,'k=20,\beta=20');%,'C/C_s=0.6',
'C/C_s=0.4');

figure(5006)
% plot(t(20,:)*180/pi,s12(20,:),'-o');hold on;
plot(t(20,1:361)*180/pi,(sed(20,1:361)),'-^'); hold on;
%plot(t(20,:)*180/pi,sum_correction_s12_1(20,:)); hold on;
%plot(t(20,:)*180/pi,sum_correction_s12_2(20,:),'or'); hold on;
ylabel('S (N.m/m^3)','FontName','Timesnewroman','FontSize',14)
xlabel('\theta (degrees)','FontName','Timesnewroman','FontSize',14)
xlim([-180 180])
% ylim([0 18e5])
%legend('k=20,\beta=20^o','k=40,\beta=20^o','k=60,\beta=20^o');
legend('\zeta = -0.4','\zeta = 0','\zeta = 0.4');
%
legend('q_0=0','q_0=1000','q_0=2000');%,'k=20,\beta=20');%,'C/C_s=0.6',
'C/C_s=0.4');

% contour(x_bar,y_bar,final_s22,100); hold on;
% ylabel('y (m)','FontName','Timesnewroman')
% xlabel('x (m)','FontName','Timesnewroman')
% title('Only Homogeneous \sigma_y_y')

```

```

% colorbar
% line([-0.005,0],[0,0]);
% xlim([-0.003 0.003])
% ylim([-0.003 0.003])
% %print -dtiffnocompression Only_Homogeneous_sigma_y_y ;

% figure(3001)
% contour(x_bar,y_bar,final_s12,100); hold on;
% ylabel('y (m)', 'FontName', 'Timesnewroman')
% xlabel('x (m)', 'FontName', 'Timesnewroman')
% title('Only Homogeneous \stau_x_y')
% colorbar
% line([-0.005,0],[0,0]);
% xlim([-0.003 0.003])
% ylim([-0.003 0.003])
%
% figure(4001)
% [cc,h] = contour(x_bar,y_bar,final_tmax,30); hold on;
% ylabel('\zeta_2 (m)', 'FontName', 'Timesnewroman')
% xlabel('\zeta_1 (m)', 'FontName', 'Timesnewroman')
% title('\Tau_m_a_x')
% colorbar
% line([-0.005,0],[0,0]);
% xlim([-0.003 0.003])
% ylim([-0.003 0.003])
% H=clabel(cc,h, 'manual');
% set(H, 'FontSize', 10, 'FontWeight', 'bold', 'Color', 'red')
% axis square;
% grid on;

figure(6001)
%v = [30];
v = [1 2 3 4 5 6 7 8 9 11 13 15 17 19 21 23 25 30 40 50];
[cc,h] = contour(x_bar/0.003,y_bar/0.003,N,v); hold on;
ylabel('\zeta_2/h ', 'FontName', 'Timesnewroman', 'FontSize', 14)
xlabel('\zeta_1/h ', 'FontName', 'Timesnewroman', 'FontSize', 14)
%title('\sigma_1')
%colorbar
line([-1,0],[0,0], 'LineWidth', 5, 'Color', 'black');
xlim([-1 1])
ylim([-1 1])
H=clabel(cc,h, 'manual');
set(H, 'FontSize', 10, 'FontWeight', 'bold', 'Color', 'red')
axis square;
grid on;

figure(6002)
%v1 = [30];
v1 = [1 2 3 4 5 6 7 8 9 11 13 15 17 19 21 23 25 30 40 50];
[cc,h] = contour(x_bar/0.003,y_bar/0.003,N1,v1); hold on;
ylabel('\zeta_2/h ', 'FontName', 'Timesnewroman', 'FontSize', 14)
xlabel('\zeta_1/h ', 'FontName', 'Timesnewroman', 'FontSize', 14)
%title('\sigma_theta_theta')
%colorbar

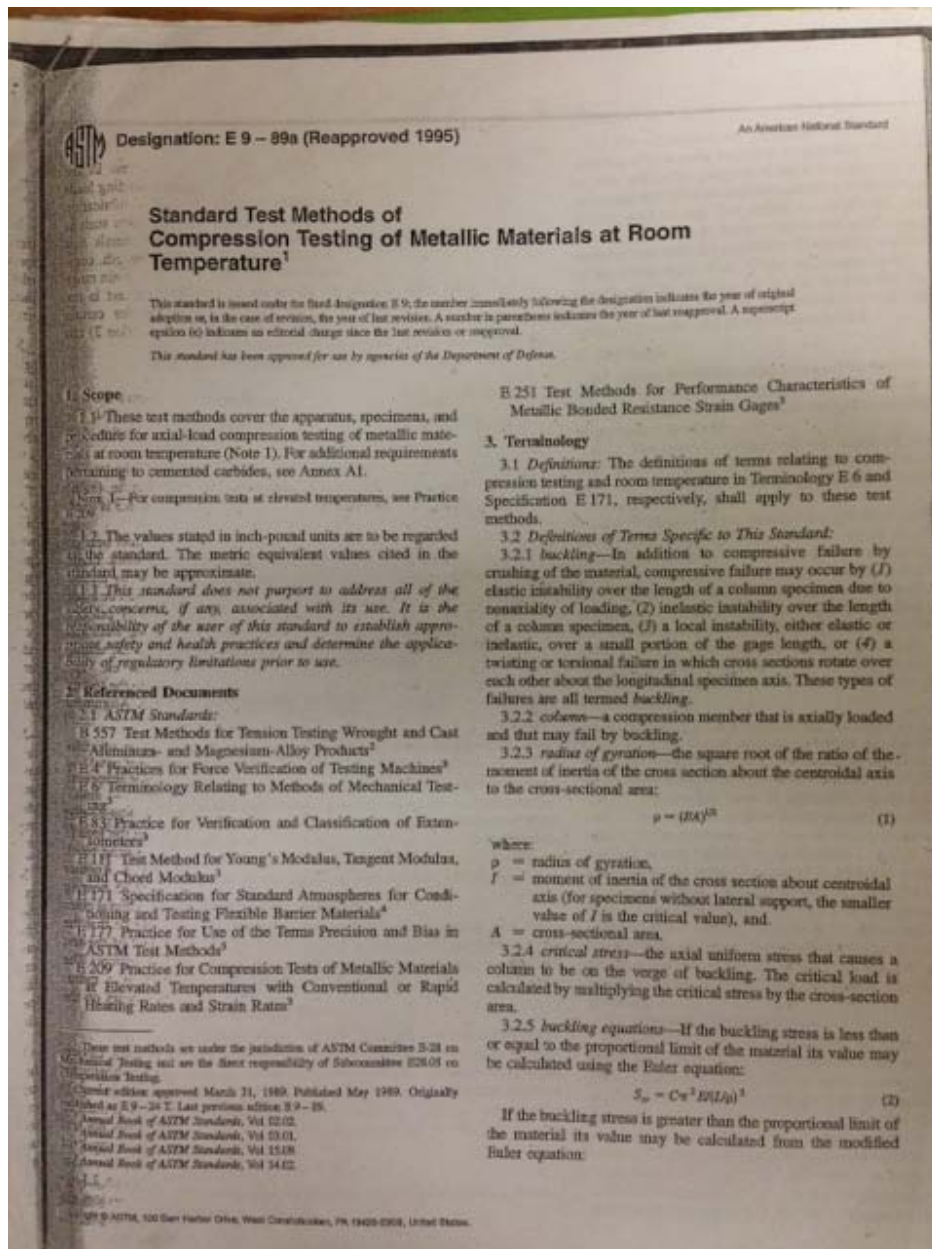
```

```
line([-1,0],[0,0], 'LineWidth',5, 'Color', 'black');  
xlim([-1 1])  
ylim([-1 1])  
H=clabel(cc,h, 'manual');  
set(H, 'FontSize',10, 'FontWeight', 'bold', 'Color', 'red')  
axis square;  
grid on;
```

APPENDIX E: ASTM STANDARDS

ASTM E 9 – 89a

Standard Test Methods of Compression Testing of Metallic Materials at Room Temperature



BIBLIOGRAPHY

- Abotula, S., Shukla, A., and Chona, R., “Dynamic constitutive behavior of Hastelloy X under thermo-mechanical loads”, *Journal of Materials Science* 46 (2011) 4971-4979.
- Amini, M. R., Amirkhizi, A. V., and Nemat-Nasser, S., “Numerical modeling of response of monolithic and bilayer plates to impulsive loading”, *International Journal of Impact Engineering*, 37(2010) 90-102.
- Amini, M. R., Isaacs, J. B., and Nemat-Nasser S., “Experimental investigation of response of monolithic and bilayer plates to impulsive loading”, *International Journal of Impact Engineering*, 37(2010) 82-89.
- Chalivendra, V. B., “Asymptotic analysis of transient curved crack in functionally graded materials”, *International Journal of Solids & Structures*, 44(2007) 465-479.
- Chen, W., Zhang, B., and Forrestal, M.J., “A split Hopkinson bar technique for low-impedance materials”, *Experimental Mechanics*, 39 (1998) 81–85.
- Chen, W., Song, B., Frew, D. J., and Forrestal, M. J., “Dynamic Small Strain Measurements of a metal Specimen with a Split Hopkinson Pressure Bar”, *Experimental Mechanics*, 43(2003) 20-23.
- Courant, R., and Friedrichs, K.O., “Supersonic flow and shock waves”, *Interscience Publishers*, New York, 1948.
- Fleck, N. A., and Deshpande, V. S., “The resistance of clamped sandwich beams to shock loading”, *Journal of Applied Mechanics*, 71 (2004) 386-401.

- Follansbee, P. S., “The Hopkinson bar mechanical testing”, *metals handbook, 9th ed.*, ASM, Metals Park, Ohio. 8(1985) 198-217.
- Freund, L. B., “Dynamic fracture mechanics”, *Cambridge University Press*, Cambridge (1990).
- Gardner, N., Wang, E., Kumar, P., and Shukla, A., “Blast mitigation in a sandwich composite using graded core with polyurea interlayer”, *Experimental Mechanics*, 2011. DOI 10.1007/s11340-011-9517-9.
- Gardner, N., Wang, E., and Shukla A., “Performance of functionally graded sandwich beams under shock wave loading”, *Composite Structures*, 2011. DOI 10.1016/j.compstruct.2011.12.006.
- Gray, G. T., “Classical split-Hopkinson pressure bar technique”. ASM handbook, 8(2000), Mechanical Testing and Evaluation, *ASM International*, Materials Park, OH, 44073-0002.
- Gupta, S., and Shukla, A., “Blast performance of marine foam core sandwich composites at extreme temperatures”, *Experimental Mechanics*, 52(2012) 1521-1534.
- Johnson, G. R., and Cook, W. H., “A constitutive model and data for metals subjected to large strains, high strain rates and high temperatures”. *Proceedings of seventh international symposium on ballistics*, The Hague, The Netherlands, 1983 541-547.
- Kidane, A., Chalivendra, V. B., and Shukla, A., “Thermo-mechanical stress fields and strain energy associated with a propagating crack”. *Acta Mechanica*. 215(2010) 57-69.

- Kidane, A., Chalivendra, V. B., Shukla, A., and Chona, R., “Dynamic crack propagation in graded materials under thermo-mechanical loading”. *Engineering Fracture Mechanics*, 77(2010) 2864-2880.
- Kolsky, H.. “An Investigation of the mechanical properties of materials at very high strain rates of loading”. *Proceeding of Physics Society*, 62(1949) 676-700.
- Kumar, P., LeBlanc, J., Stargel, D., and Shukla, A., “Effect of plate curvature on blast response of aluminum panels”, *Impact Engineering*, 46(2012) 74-85.
- LeBlanc, J., Shukla, A., Rousseau, C., and Bogdanovich, A., “Shock loading of three-dimensional woven composite materials”, *Composite Structures*, 79(2007) 344- 355.
- Li, N., Sutton, M., Li, X., and Schreier, H., “Full-field thermal deformation measurements in a scanning electron microscope by 2D digital image correlation”, *Experimental Mechanics* 48(2008) 635-646.
- Nurick, G. N., Olson, M. D., Fagnan, and J. R., Levin, A., “Deformation and tearing of blast-loaded stiffened square plates”.. *International Journal of Impact Engineering* 16(1995) 273-291.
- Nurick, G. N., and Shave, G. C., “ The deformation and tearing of thin square plates subjected to impulsive loads -An experimental study”, *International Journal of Impact Engineering*, 18(1996) 99-116.
- Pan, B., Wu, D., Wang, Z., and Xia, Y., “High-temperature digital image correlation method for full-field deformation measurement at 1200 °C”, *Measurement Science and Technology*, 22(2011) 11pages.

- Pan, B., Wu, D., and Xia, Y., “High-temperature deformation field measurement by combining transient aerodynamic heating simulation system and reliability-guided digital image correlation”, *Optics and Lasers in Engineering*, 48(2010) 841-848.
- Tekalur, S. A., Shukla, A., and Shivakumar, K., “Blast resistance of polyurea based layered composite materials”, *Composite Structures*, 84 (2008) 271-281.
- Tekalur, S.A., Bogdanovich, A.E. and Shukla, A., “Shock loading response of sandwich panels with 3-D woven E-glass composite skins and stitched foam core”, *Composite Science and Technology* (2008), doi:10.1016/j.compscitech.2008.03.017.
- Tiwari, V., Sutton, M. A., and McNeill, S. R., “Assessment of high-speed imaging systems for 2D and 3D deformation measurements: Methodology Development and Validation”, *Experimental Mechanics*, 47(2007) 561-579.
- Tiwari, V., Sutton, M. A., McNeill, S. R., Xu, S., Deng, X., Fourney, W.L., and Bretall, D., “Application of 3D image correlation for full-field transient plate deformation measurements during blast loading”, *International Journal of Impact Engineering*, 36(2009) 862-874.
- Wang, E., Gardner, N., and Shukla, A., “The blast resistance of sandwich composites with stepwise graded cores”, *International Journal of Solids and Structures*, 46 (2009) 3492-3502.
- Wang, E., and Shukla, A., “Analytical and experimental evaluation of energies during shock wave loading”, *International Journal of Impact Engineering*, 37 (2010) 1188-1196.

Wang, E., Wright, J., and Shukla, A., “Analytical and experimental study on the fluid structure interaction during air blast loading”, *Journal of Applied Physics*, 110(2011) 114901-114901-114912.

Wang, L. L., “Foundation of stress waves”, Elsevier, 2007.

Wang, E., “Blast resistance and energy mitigation behavior of sandwich composite materials”, *Ph.D Dissertation*, University of Rhode Island, 2010.

Wright, J., Shock tubes. *John Wiley and Sons Inc*, New York, 1961.